

University of Windsor

## Scholarship at UWindor

---

Electronic Theses and Dissertations

Theses, Dissertations, and Major Papers

---

2006

### Anode electrocatalysts for direct borohydride fuel cells.

Mohammed Hassan Atwan  
*University of Windsor*

Follow this and additional works at: <https://scholar.uwindsor.ca/etd>

---

#### Recommended Citation

Atwan, Mohammed Hassan, "Anode electrocatalysts for direct borohydride fuel cells." (2006). *Electronic Theses and Dissertations*. 1187.

<https://scholar.uwindsor.ca/etd/1187>

This online database contains the full-text of PhD dissertations and Masters' theses of University of Windsor students from 1954 forward. These documents are made available for personal study and research purposes only, in accordance with the Canadian Copyright Act and the Creative Commons license—CC BY-NC-ND (Attribution, Non-Commercial, No Derivative Works). Under this license, works must always be attributed to the copyright holder (original author), cannot be used for any commercial purposes, and may not be altered. Any other use would require the permission of the copyright holder. Students may inquire about withdrawing their dissertation and/or thesis from this database. For additional inquiries, please contact the repository administrator via email ([scholarship@uwindsor.ca](mailto:scholarship@uwindsor.ca)) or by telephone at 519-253-3000ext. 3208.

**Anode Electrocatalysts  
For  
Direct Borohydride Fuel Cells**

by

**Mohammed Hassan Atwan**

**A Dissertation  
Submitted to the Faculty of Graduate Studies and Research  
through Engineering Materials  
In Partial Fulfillment of the Requirements for  
the Degree of Doctor of Philosophy at the  
University of Windsor**

**Windsor, Ontario, Canada**

**2006**

**© 2006 Mohammed H. Atwan**



Library and  
Archives Canada

Bibliothèque et  
Archives Canada

Published Heritage  
Branch

Direction du  
Patrimoine de l'édition

395 Wellington Street  
Ottawa ON K1A 0N4  
Canada

395, rue Wellington  
Ottawa ON K1A 0N4  
Canada

*Your file* *Votre référence*  
*ISBN: 978-0-494-17138-7*  
*Our file* *Notre référence*  
*ISBN: 978-0-494-17138-7*

**NOTICE:**

The author has granted a non-exclusive license allowing Library and Archives Canada to reproduce, publish, archive, preserve, conserve, communicate to the public by telecommunication or on the Internet, loan, distribute and sell theses worldwide, for commercial or non-commercial purposes, in microform, paper, electronic and/or any other formats.

The author retains copyright ownership and moral rights in this thesis. Neither the thesis nor substantial extracts from it may be printed or otherwise reproduced without the author's permission.

**AVIS:**

L'auteur a accordé une licence non exclusive permettant à la Bibliothèque et Archives Canada de reproduire, publier, archiver, sauvegarder, conserver, transmettre au public par télécommunication ou par l'Internet, prêter, distribuer et vendre des thèses partout dans le monde, à des fins commerciales ou autres, sur support microforme, papier, électronique et/ou autres formats.

L'auteur conserve la propriété du droit d'auteur et des droits moraux qui protègent cette thèse. Ni la thèse ni des extraits substantiels de celle-ci ne doivent être imprimés ou autrement reproduits sans son autorisation.

---

In compliance with the Canadian Privacy Act some supporting forms may have been removed from this thesis.

Conformément à la loi canadienne sur la protection de la vie privée, quelques formulaires secondaires ont été enlevés de cette thèse.

While these forms may be included in the document page count, their removal does not represent any loss of content from the thesis.

Bien que ces formulaires aient inclus dans la pagination, il n'y aura aucun contenu manquant.

  
**Canada**

## ABSTRACT

Colloidal Os and Os-alloys, Pt and Pt-alloys, Au and Au alloys, Ir and Ir-alloys, and Pd and Pd alloys (1:1 atomic ratio for all alloys) supported on Vulcan XC-72 (20 wt% metal) were prepared according to the Bönneiman method and investigated for their electrocatalytic activity with respect to methanol and borohydride oxidation for Os and with respect to borohydride oxidation only for Pt, Au, Ir, and Pd for fuel cell applications. Voltammetry on static and rotating electrodes, chronoamperometry and chronocoulometry were performed on the colloidal catalysts immobilized on glassy carbon with the help of a Nafion<sup>®</sup> 117 solution acting as the ionic conductor and binder of the catalyst layer. Insights were gained with regard to the  $\text{BH}_4^-$  electro-oxidation mechanism, and apparent kinetic parameters were determined such as Tafel slopes, exchange current densities, heterogeneous rate constants, and the total number of electrons involved. The electrolytes were: 0.5 M  $\text{H}_2\text{SO}_4$  for methanol oxidation and 2M NaOH for borohydride oxidation, respectively. The fundamental studies were followed by direct borohydride fuel cell experiments using a 2 M NaOH - 2 M  $\text{NaBH}_4$  solution on the anode side, 5 mg  $\text{cm}^{-2}$  colloidal anode catalyst load and Nafion<sup>®</sup> 117 membrane. The cathode was a conventional  $\text{O}_2$  gas diffusion electrode with 4 mg  $\text{cm}^{-2}$  Pt.

Voltammetry results showed that the Os-based materials were catalytically inactive with respect to methanol oxidation in acid media. It was found that all three pure colloidal Os (10, 20 and 30 %wt) materials showed catalytic activity in cyclic voltammetry experiments toward the oxidation of borohydride. Chronopotentiometry experiments with a current step of 25 mA  $\text{cm}^{-2}$  showed that the 20 %wt Os gave the lowest anodic overpotential, about 0.3 V, of the Os-based materials.

On Pt and its alloys, cyclic voltammetry (CV) results show that colloidal Pt and colloidal Pt-alloys were electrochemically active toward borohydride oxidation with oxidation potentials ranging between -0.85 and +0.3 V vs. a mercury/mercury oxide reference electrode (MOE). Of the investigated colloidal catalysts, the Pt-Ir alloy gave the highest voltammetric  $\text{BH}_4^-$  oxidation current densities at potentials more negative than about -0.2 V vs. MOE, which is ultimately the domain of interest for borohydride fuel cells. Pt-Ir showed oxidation peaks at the most negative potentials, -0.85 V due to  $\text{H}_2$  oxidation and -0.27 V corresponding to direct  $\text{BH}_4^-$  oxidation. Fuel cell test results show

that although Pt-Au gave a higher coulombic efficiency due to eight-electron oxidation, Pt-Ir and Pt-Ni were the most active catalysts and they were characterized by a three-electron oxidation of  $\text{BH}_4^-$ .

For Au and Au-alloys, the CV results show that they were electrochemically active toward borohydride oxidation with oxidation potentials ranging between -0.7V to 0.35V vs. MOE. Colloidal Au-Pt shows the highest peak current and a negative oxidation potential, followed by Au-Pd with a lower peak current. Fuel cell test results show that Pt-Au was the most active catalyst characterized by  $\sim 8$  electron oxidation of  $\text{BH}_4^-$ .

For Ir and its alloys, fuel cell test results show that Ir-Pd and Ir-Pt are the most active catalysts for the oxidation of  $\text{BH}_4^-$ .

For colloidal Pd and Pd-alloys, fuel cell test results show that Pd-Ir and Pd-Ni are the most active catalysts for the oxidation of  $\text{BH}_4^-$ .

Colloidal Ir-Ni, Pd-Ir, Pt-Ni and Pt-Ir, showed the highest fuel cell performance. For Ir-Ni, Pd-Ir, Pt-Ir, and Pt-Ni colloids, a cell operating at 0.5 V can give current densities of 50, 49, 46, and 44  $\text{mA cm}^{-2}$ , respectively at 298 K.

Finally, it has been demonstrated that a  $\text{TiO}_2$  addition has a significant positive impact on the electrocatalytic activities of Pt and Pd; while it has a dramatic negative impact on the catalytic activity of Ir.

**DEDICATION**

**To My Parents**

**Especially to the Memory of My Mother**

**and to  
my wife Nedhal**

**and my children,  
Yousif, Safana, Yehya**

## ACKNOWLEDGEMENTS

I would like to express my gratitude to my supervisors Dr. Derek Northwood and Dr. Elod Gyenge. They have always been extremely generous with their time, knowledge and ideas and allowed me great freedom in this research. Their enthusiastic approach to research, their endless excitement for fuel cells and their pleasant personalities have made this experience all the more enjoyable and I am greatly appreciative.

I would also like to thank my committee members; Dr. Ahmet Alpas, Dr. Randy Bowers, and Dr. David Ting for their helpful discussions and for their advice.

I would like to thank Dr. Charles Macdonald, of the Chemistry and Biochemistry Department, for several months of using his lab facilities in preparing the colloidal catalysts, and for the useful discussions.

I am also extremely grateful to Mr. John Robinson for his assistance in performing and analyzing SEM images and EDS and XRD results for all my colloidal samples, and for helpful discussions.

To Patrick Seguin, many thanks, for his help in installing my computer and fixing its trouble shootings, and for downloading the required software.

Many thanks to Steve Budinsky, Tim Bolger, Andy Jenner, Rob Dumouchelle, and Marc St. Pierre, of the Technical Support Center, at the University of Windsor, for their technical assistance.

Special thanks go to Horace Lam, Peter Roberts, and Graham Liebelt, at the Technical Centre, Chemical and Biotechnological Department, the University of British Columbia, for their technical assistance.

To Ms. Barb Denomey and Ms. Rosemarie Gignac, I extend special thanks for all their help during my study period.

To the Graduate Faculty many thank for all of their help, especial thank to Mrs. Svetlana Georgieva.

The financial support from the Natural Science and Engineering Research Council of Canada (NSERC) is gratefully acknowledged.

Finally, I also would like to express my sincere appreciation to my wife Nedhal, and my children Yousif, Safana, and Yehya with special thanks for their patience and supports in so many ways.

## **STATEMENT OF ORIGINALITY**

I certify that this thesis, and the research to which it refers, are the product of my own work, and that any ideas or quotations from the work of the other people, published or otherwise, are fully acknowledged in accordance with the standard referencing practice of the discipline. I acknowledge the helpful guidance and support of my supervisors, Professor Derek Northwood and Professor Elod Gyenge.



## TABLE OF CONTENTS

ABSTRACT	iii
DEDICATION	v
ACKNOWLEDGEMENTS	vi
STATEMENT OF ORIGINALITY	vii
LIST OF TABLES	xii
LIST OF FIGURES	xiv
NOMENCLATURE	xxviii
ACRONYMS	xxx

### CHAPTER

<b>I.</b>	<b>CHAPTER 1</b>	
	<b>INTRODUCTION</b>	
	1.1. General	1
	1.2. Direct Liquid Fuel Cell Research and Development	2
	1.2.1. Why a Direct Borohydride Fuel Cell?	2
	1.3. References	5
<b>II.</b>	<b>CHAPTER 2</b>	
	<b>LITERATURE SURVEY</b>	
	2.1. Fuel Cell Technology	6
	2.1.1. Principle of Operation	7
	2.2. Fuel Cell Performance	8
	2.2.1. Ideal and Actual performance	8
	2.2.1.1. Activation Polarization	8
	2.2.1.2. Ohmic Polarization	9
	2.2.1.3. Concentration Polarization	9
	2.2.1.4. Reactant crossover and internal current losses	9
	2.3. Overall Cell Voltage	9
	2.4. Fuel Cell Efficiency	11
	2.5. Fuel Cells vs. Heat Engine	11
	2.6. Fuel Cell Types	12
	2.6.1. Proton Exchange Membrane Fuel Cells (PEMFC)	13

2.6.2. Alkaline Fuel Cells (AFC)	14
2.6.3. Phosphoric Acid Fuel Cells (PAFC)	15
2.6.4. Molten Carbonate Fuel Cells (MCFC)	16
2.6.5. Solid Oxide Fuel Cells (SOFC)	16
2.6.6. PEM-Based Direct Liquid Fuel Cells	17
2.6.6.1. Direct Methanol Fuel Cells (DMFC)	17
2.6.6.2. Direct Formic Acid Fuel Cells (DFAFC)	18
2.6.6.3. Direct Borohydride Fuel Cells (DBFC)	19
2.7. Fuel Cell Systems	20
2.8. Fuel Cell Application	21
2.9. Heterogeneous Catalysis	21
2.9.1. Catalysis by Metals	23
2.9.1.1. Transition Metals as Catalysts	23
2.9.1.2. Reactions on Metals	23
2.9.2. Principles of Catalytic Action	24
2.9.2.1. Metal Catalytic Mechanisms	25
2.9.3. Electrocatalysis	26
2.9.3.1. Electrocatalysts Design	27
2.9.3.2. Factors Affecting Electrocatalytic Properties	27
2.9.4. Effect of Support Type on the Catalytic Activity	28
2.9.5. Preparation of Colloidal Nanoparticles	28
2.9.5.1. Chemical Methods of preparing supported colloid metal(s)	29
2.9.5.1.1. Colloidal method	30
2.9.5.1.2. Impregnation method	32
2.9.5.1.3. Microemulsion method	32
2.10. Borohydride	33
2.10.1. Borohydride Hydrolysis	34
2.10.2. Borohydride Oxidation	37
2.10.3. Direct Borohydride Fuel Cells (DBFC) Literature	42
2.11. References	45

### **III. CHAPTER 3**

#### **EXPERIMENTAL METHODS**

3.1. Electrocatalyst Preparation	49
3.2. Working Electrode Preparation	64
3.3. Experimental Cell Set Up	64
3.4. Electrochemical Measurement Systems and Related Electrochemical Parameters	65
3.5. Fuel Cell Set Up and MEA Preparation	66
3.5.1. MEA Preparation	66
3.5.2. Fuel Cell Set Up	67
3.6. Electrochemical Measurement Methods	68
3.6.1. Electrode Kinetics	69
3.6.1.1. Activation Polarization	69

3.6.1.1.1. Exchange Current Density ( $i_o$ ) and Tafel Slope ( $b_a$ )	69
3.6.1.1.2. Concentration Polarization	72
3.6.2. Cyclic Voltammetry	73
3.6.2.1. Theory of voltammetry	75
3.6.3. Chronoamperometry	76
3.6.3.1. Theory of Chronoamperometry	77
3.6.4. Chronocoulometry	78
3.6.4.1. Theory of Chronocoulometry	79
3.6.5. Chronopotentiometry	80
3.6.6. Summary of Electrochemical Techniques Employed in this Study	81
3.7. References	81

#### IV. CHAPTER 4

##### RESULTS AND DISCUSSION

4.1. Osmium and Osmium-Alloys	83
4.1.1. Comparative Cyclic Voltammetry of Methanol on Os and Os-alloys	83
4.1.2. Cyclic Voltammetry of $\text{BH}_4^-$ on Os and Os-alloys	85
4.1.3. Effect of Thiourea on the Electro-oxidation of $\text{BH}_4^-$ on Os	87
4.1.4. Chronopotentiometry	88
4.1.5. Chronoamperometry	89
4.1.6. Summary	90
4.2. Platinum and Platinum Alloys	91
4.2.1. Voltammetry of borohydride oxidation on static electrodes	91
4.2.2. Voltammetry of borohydride oxidation on rotating electrodes	99
4.2.3. Chronopotentiometry	104
4.2.4. Chronoamperometry and Coulometry	105
4.2.5. Fuel cell performance	113
4.2.6. Summary	117
4.3. Gold and Gold Alloys	118
4.3.1. Voltammetry of borohydride oxidation on static electrodes	118
4.3.2. Voltammetry of borohydride oxidation on rotating electrodes	124
4.3.3. Chronopotentiometry	128
4.3.4. Chronoamperometry and Coulometry	129
4.3.5. Fuel cell performance	135
4.3.6. Summary	138
4.4. Iridium and Iridium Alloys	139
4.4.1. Voltammetry of borohydride oxidation on static electrodes	139
4.4.2. Voltammetry of borohydride oxidation on rotating electrodes	145

4.4.3. Chronopotentiometry	149
4.4.4. Chronoamperometry and Coulometry	150
4.4.5. Fuel cell performance	156
4.4.6. Summary	159
4.5. Palladium and Palladium Alloys	160
4.5.1. Voltammetry of borohydride oxidation on static electrodes	160
4.5.2. Voltammetry of borohydride oxidation on rotating electrodes	165
4.5.3. Chronopotentiometry	168
4.5.4. Chronoamperometry and Coulometry	169
4.5.5. Fuel cell performance	175
4.5.6. Summary	177
4.6. Overall Comparison of the Best of the Catalyst Groups	178
4.6.1. Voltammetry of borohydride oxidation on static electrodes	178
4.6.2. Voltammetry of borohydride oxidation on rotating electrodes	180
4.6.3. Chronopotentiometry	181
4.6.4. Chronoamperometry and Coulometry	182
4.6.5. Fuel cell performance	183
4.6.6. Summary	185
4.7. Effect of Titanium Dioxide Addition	186
4.7.1. Voltammetry of borohydride oxidation on static electrodes	186
4.7.2. Voltammetry of borohydride oxidation on rotating electrodes	194
4.7.3. Chronopotentiometry	198
4.7.4. Chronoamperometry and Coulometry	199
4.7.5. Summary	205
4.8. References	206
<b>V. CONCLUSIONS</b>	<b>208</b>
<b>VI. RECOMMENDATIONS FOR FUTURE WORK</b>	<b>211</b>
<b>VITA AUCTORIS</b>	<b>213</b>
<b>PUBLICATIONS AND PRESENTATIONS</b>	<b>214</b>

## LIST OF TABLES

### Chapter 2

2.6.1. Characteristics of major types of fuel cells.	12
2.10.1. Summary of Borohydride Hydrolysis Literature.	36
2.10.2. Summary of Borohydride Oxidation Literature.	42
2.10.3. Summary of direct borohydride fuel cell processes literature.	45

### Chapter 3

3.1.1. Stoichiometric amounts of the reacted species.	53
3.1.2. Summary of materials/chemicals related information.	54
3.6. Summary of the formulas used, the measured and calculated parameters.	81

### Chapter 4

4.2.1. Apparent Tafel slopes, exchange current densities, total number of electrons exchanged, $n$ , and the activation energy for $\text{BH}_4^-$ oxidation at 298 K, for supported colloidal Pt and Pt-alloys catalysts.	104
4.2.2. Apparent heterogeneous rate constants for $\text{BH}_4^-$ oxidation at $-0.4$ V vs. MOE and 298 K calculated from chronocoulometry.	113
4.3.1. Apparent Tafel slopes, exchange current densities, total number of electrons exchanged, $n$ , and the activation energy for $\text{BH}_4^-$ oxidation at 298 K, for supported colloidal Au and Au-alloys catalysts.	128
4.3.2. Apparent heterogeneous rate constants for $\text{BH}_4^-$ oxidation at $-0.4$ V vs. MOE and 298 K calculated from chronocoulometry.	135
4.4.1. Apparent Tafel slopes, exchange current densities, total number of electrons exchanged, $n$ , and the activation energy for $\text{BH}_4^-$ oxidation at 298 K, for supported colloidal Ir and Ir-alloys catalysts.	149
4.4.2. Apparent heterogeneous rate constants for $\text{BH}_4^-$ oxidation at $-0.4$ V vs. MOE and 298 K calculated from chronocoulometry.	156
4.5.1. Apparent Tafel slopes, exchange current densities, total number of electrons exchanged, $n$ , and the activation energy for $\text{BH}_4^-$ oxidation at 298 K, for supported colloidal Pd and Pd-alloys catalysts.	168
4.5.2. Apparent heterogeneous rate constants for $\text{BH}_4^-$ oxidation at $-0.4$ V vs. MOE and 298 K calculated from chronocoulometry.	174
4.6.1. Summary of peak currents and potentials of the best of the catalyst group at $0.1$ M $\text{NaBH}_4$ and $100$ $\text{mV s}^{-1}$ .	179
4.6.2. Apparent Tafel slopes, exchange current densities, total number of electrons exchanged, $n$ , and the activation energy for $\text{BH}_4^-$ oxidation at 298 K, for supported colloidal of different catalysts.	181
4.6.3. Apparent heterogeneous rate constants for $\text{BH}_4^-$ oxidation at $-0.4$ V vs.	

MOE and 298 K calculated from chronocoulometry.	182
4.7.1. Apparent Tafel slopes, exchange current densities, total number of electrons exchanged, $n$ , and the activation energy for $\text{BH}_4^-$ oxidation at 298 K, for supported (on C and on C+TiO <sub>2</sub> ) colloidal catalysts.	197
4.7.2. Apparent heterogeneous rate constants for $\text{BH}_4^-$ oxidation at $-0.4$ V vs. MOE and 298 K calculated from chronocoulometry.	204

## LIST OF FIGURES

### Chapter 2

2.1.1. a) Grove's water electrolysis experiment; b) Grove's fuel cell demonstration [2].	6
2.1.2. Schematic diagram of fuel cell [6].	7
2.2.1. Ideal and actual fuel cell voltage vs. current [5].	8
2.3.1. The anodic and cathodic polarizations [5].	10
2.3.2. Relationship between the power density and the voltage [7].	10
2.5.1. Comparison of the processes involved in an ICE and a fuel cell [10].	11
2.5.2. Efficiency and power output comparison between fuel cells and IC engines [10].	12
2.6.1. A schematic illustration of polymer electrolyte fuel cell [13].	13
2.6.2. Typical cell potential vs. current density plot for major types of fuel cells [11].	14
2.6.3. Nafion structure: white zone is the sulphate ions which transport $H^+$ [1].	14
2.6.4. A schematic illustration of the alkaline fuel cell [13].	15
2.6.5. A schematic illustration of phosphoric acid fuel cell [13].	15
2.6.6. A schematic illustration of the molten carbonate fuel cell [13].	16
2.6.7. A schematic illustration of the solid oxide fuel cell [13].	17
2.6.8. A schematic illustration of direct methanol fuel cell [17].	18
2.6.9. A schematic illustration of direct borohydride fuel cell [28].	19
2.7.1. Expanded view of PEM Fuel Cell Stack [29].	20
2.7.2. FC integrated system [30].	20
2.9.1. Catalysis knowledge development [33].	21
2.9.2. A supported nanoparticle heterogeneous catalysts [33].	22
2.9.3. Reaction cycle of a heterogeneous catalytic reaction.	24
2.9.4. A schematic of a) Langmuir-Hinshelwood, b) Riedel-Eley, c) Precursor Mechanism [35].	25
2.9.5. Adsorption site on various surfaces [33].	25
2.9.6. Schematic illustration of metal nanoparticles preparation methods [50].	29
2.9.7. The main preparation steps of supported metal nanoparticles [51].	30
2.9.8. Structure model of polymer-protected metallic colloids [53].	30
2.9.9. Chemical methods to synthesize supported platinum nanoparticles with different size control methodologies [51].	31
2.9.10. a) Electrostatic stabilization of nanostructured metal colloids; b) steric stabilization of nanostructured metal colloids [54].	32
2.10.1. Shows how $B-H$ bond serves as a source of $H^-$ [56].	33
2.10.2. Capacity comparison when hydrogen was stored in different ways [71].	35
2.10.3. Schematic illustration of Inding and Snyder cell [79].	39
2.10.4. Performance of direct borohydride fuel cell stacks [71].	44

### Chapter 3

3.1.1. Electrocatalysts colloids preparation apparatus.	49
3.1.2. Electrocatalysts annealing and reducing processes equipment.	52

3.1.3. Powder EDS analysis showing the elemental distributions in Vulcan XC72R carbon black.	55
3.1.4. Powder EDS analysis showing the metals distributions in 20wt% (1:1 atomic ratio) colloidal Pt and Pt-Au.	55
3.1.5. Powder EDS analysis showing the metals distributions in 20wt% (1:1 atomic ratio) colloidal Pt-Ni and Pt-Ir.	56
3.1.6. Powder EDS analysis showing the metals distributions in 20wt% colloidal Au.	56
3.1.7. Powder EDS analysis showing the metals distributions in 20wt% (1:1 atomic ratio) colloidal Au-Ag, Au-Ni and Au-Pd.	57
3.1.8. Powder EDS analysis showing the metals distributions in 20wt% (1:1 atomic ratio) colloidal Ir, Ir-Ag, Ir-Ni, and Ir-Pd.	58
3.1.9. Powder EDS analysis showing the metals distributions in 20wt% (1:1 atomic ratio) colloidal Pd, Pd-Ag, and Pd-Ni.	59
3.1.10. X-ray diffraction pattern of powder Vulcan XC 72R carbon black.	60
3.1.11. X-ray diffraction pattern of powder 20wt% (1:1 atomic ratio) colloidal Pt and Pt-alloys, showing [111], [200], [220], and [311] reflections of the fcc lattice of metallic Pt and its alloys.	60
3.1.12. X-ray diffraction pattern of powder 20wt% (1:1 atomic ratio) colloidal Au and Au-alloys, showing [111], [200], [220], and [311] reflections of the fcc lattice of metallic Au and its alloys.	61
3.1.13. X-ray diffraction pattern of powder 20wt% (1:1 atomic ratio) colloidal Ir and Ir-alloys, showing [111], [200], [220], and [311] reflections of the fcc lattice of metallic Ir and its alloys.	62
3.1.14. X-ray diffraction pattern of powder 20wt% (1:1 atomic ratio) colloidal Pd and Pd-alloys, showing [111], [200], [220], and [311] reflections of the fcc lattice of metallic Pd and its alloys.	63
3.3.1. Set-up of the conventional three electrode cell.	65
3.4.1. Electrochemical instrumentation (PAR 363A) for stationary and (Volta Lab 80) for rotating disc tests.	66
3.5.1. Lyntech fuel cell test station.	68
3.6.1. Net anodic, zero, and net cathodic overall reactions of a redox electrode. Arrow direction represents the electron flow [15].	70
3.6.2. Experimental determination of exchange current density $i_o$ and Tafel slope $b$ [18].	72
3.6.3. A schematic representation shows the effect of Tafel slope $b$ on $i_o$ and the overpotential [17].	72
3.6.4. (a) the potential sweep, and (b) corresponding current response [16].	74
3.6.5. Cyclic voltammogram for a reversible electron transfer reaction [16].	74
3.6.6. The essentials of chronoamperometry (a) Potential step, (b) Concentration variation with distance, and (c) Current-time response [18].	77
3.6.7. A current-time response for a potential step experiment. The potential step is chosen so that, a) The reaction is diffusion control, b) Kinetically controlled, and c) Mixed controlled [24].	78
3.6.8. Chronocoulometric response for 10 mM Cd <sup>2+</sup> in 1 M Na <sub>2</sub> SO <sub>4</sub> [18].	80
3.6.9. Variation of potential with time for a step change in applied current [18].	80



## Chapter 4

- 4.1.1. Cyclic voltammogram of 1 M methanol in 0.5 M H<sub>2</sub>SO<sub>4</sub> on colloidal Os. Scan rate 50 mV s<sup>-1</sup>, temperature 295 K. 84
- 4.1.2. Cyclic voltammogram of 1 M methanol in 0.5 M H<sub>2</sub>SO<sub>4</sub> on 20 %wt colloidal Os-Mo, Os-Sn and Os-V (1:1 atomic ratio). Scan rate 50 mV s<sup>-1</sup>, temperature 295 K. 84
- 4.1.3. Cyclic voltammetry of 0.03 M NaBH<sub>4</sub> in 2 M NaOH on colloidal 20%wt Os. Alloy load 30 μg cm<sup>-2</sup>. Temperature 295 K. 85
- 4.1.4. Cyclic voltammetry of 0.03 M NaBH<sub>4</sub> in 2 M NaOH on colloidal 20%wt (1:1 atomic ratio) Os-Mo, Os-V and Os-Sn. Alloy load 30 μg cm<sup>-2</sup>. 295 K 86
- 4.1.5. Concentration dependence of the peak current I<sub>p</sub> for the oxidation of 0.03 M BH<sub>4</sub><sup>-</sup> in 2 M NaOH with 1.5x10<sup>-3</sup> M TU on colloidal 20wt% Os at 298 K. 86
- 4.1.6. Cyclic voltammogram obtained on 10 %wt colloidal Os electrode in 2 M NaOH in the absence and in the presence of 0.03 M NaBH<sub>4</sub> and 1.5x10<sup>-3</sup> M TU. Scan rate 100 mV s<sup>-1</sup>. Temperature 295 K. 87
- 4.1.7. Chronopotentiogram of 0.03 M NaBH<sub>4</sub> in 2 M NaOH on 10, 20 and 30%wt colloidal Os electrodes with 30 μg cm<sup>-2</sup> Os load each. Current density step: from 0 to 25 mA cm<sup>-2</sup>. Temperature 298 K. 88
- 4.1.8. Chronopotentiometry of 0.03 M Na BH<sub>4</sub> in 2 M NaOH on colloidal 20%wt Os-Mo, Os-V and Os-Sn. Metal load of 30 μg cm<sup>-2</sup>. Temperature 295 K. 89
- 4.1.9. Chronoamperometry of 0.1 M BH<sub>4</sub><sup>-</sup> in 2M NaOH with 1.5x10<sup>-3</sup> M TU on colloidal 10wt%, 20wt% and 30%wt Os , potential step from -0.8 to 0.3 V vs. Ag/AgCl, KCl<sub>std</sub>, at 298 K. 89
- 4.1.10. Chronoamperometry of 0.1 M BH<sub>4</sub><sup>-</sup> in 2 M NaOH with 1.5x10<sup>-3</sup> M TU on colloidal 20wt% (50/50atomic) OsMo, OsSn and OsV, potential step from -0.8 to 0.3 V vs. Ag/AgCl, KCl<sub>std</sub>, at 298 K. 90
- 4.1.11. Chronoamperometry response on colloidal 20%wt Os as a function of NaBH<sub>4</sub> concentration in 2 M NaOH. Potential step from - 0.8 to + 0.3 V vs. Ag/AgCl, KCl<sub>std</sub>. Temperature 295 K. 90
- 4.2.1 Linear voltammogram of BH<sub>4</sub><sup>-</sup> oxidation on colloidal Pt catalyst using static electrode showing the effect of BH<sub>4</sub><sup>-</sup> concentration. Scan rate 100 mV s<sup>-1</sup>, 298 K. Inset legend indicates the NaBH<sub>4</sub> concentration in 2 M NaOH. 91
- 4.2.2. Linear voltammogram of BH<sub>4</sub><sup>-</sup> oxidation on colloidal Pt-Au catalyst using static electrode showing the effect of BH<sub>4</sub><sup>-</sup> concentration. Scan rate 100 mV s<sup>-1</sup>, 298 K. Inset legend indicates the NaBH<sub>4</sub> concentration. 91
- 4.2.3 Linear voltammogram of BH<sub>4</sub><sup>-</sup> oxidation on colloidal Pt-Ni catalyst using static electrode showing the effect of BH<sub>4</sub><sup>-</sup> concentration. Scan rate 100 mV s<sup>-1</sup>, 298 K. Inset legend indicates the NaBH<sub>4</sub> concentration. 92
- 4.2.4. Linear voltammogram of BH<sub>4</sub><sup>-</sup> oxidation on colloidal Pt-Ir catalyst using static electrode showing the effect of BH<sub>4</sub><sup>-</sup> concentration. Scan rate 100 mV s<sup>-1</sup>, 298 K. Inset legend indicates the NaBH<sub>4</sub> concentration. 92
- 4.2.5. Linear voltammogram of BH<sub>4</sub><sup>-</sup> oxidation on colloidal Pt-Ag catalyst using static electrode showing the effect of BH<sub>4</sub><sup>-</sup> concentration. Scan rate 100 mV s<sup>-1</sup>, 298 K. Inset legend indicates the NaBH<sub>4</sub> concentration. 93

4.2.6. Linear voltammogram of $\text{BH}_4^-$ oxidation on colloidal Ni catalyst using static electrode showing the effect of $\text{BH}_4^-$ concentration. Scan rate $100 \text{ mV s}^{-1}$ , 298 K. Inset legend indicates the $\text{NaBH}_4$ concentration in 2 M NaOH.	95
4.2.7. Linear voltammogram of $\text{BH}_4^-$ oxidation on colloidal Ag catalyst using static electrode showing the effect of $\text{BH}_4^-$ concentration. Scan rate $100 \text{ mV s}^{-1}$ , 298 K. Inset legend indicates the $\text{NaBH}_4$ concentration in 2 M NaOH	95
4.2.8. The concentration dependence of the peak current density on colloidal Pt and Pt-alloys. Scan rate $100 \text{ mV s}^{-1}$ , 298 K.	96
4.2.9. Linear voltammogram of $\text{BH}_4^-$ oxidation on colloidal Pt catalyst using static electrode showing the effect of Scan rate. $\text{NaBH}_4$ concentration 0.03 M, 298 K. Inset legend indicates the scan rates.	96
4.2.10. Linear voltammogram of $\text{BH}_4^-$ oxidation on colloidal Pt-Au catalyst using static electrode showing the effect of Scan rate. $\text{NaBH}_4$ concentration 0.03 M, 298 K. Inset legend indicates the scan rates.	97
4.2.11. Linear voltammogram of $\text{BH}_4^-$ oxidation on colloidal Pt-Ni catalyst using static electrode showing the effect of Scan rate. $\text{NaBH}_4$ concentration 0.03 M, 298 K. Inset legend indicates the scan rates.	97
4.2.12. Linear voltammogram of $\text{BH}_4^-$ oxidation on colloidal Pt-Ir catalyst using static electrode showing the effect of Scan rate. $\text{NaBH}_4$ concentration 0.03 M, 298 K. Inset legend indicates the scan rates.	98
4.2.13. Linear voltammogram of $\text{BH}_4^-$ oxidation on colloidal Pt-Ag catalyst using static electrode showing the effect of Scan rate. $\text{NaBH}_4$ concentration 0.03 M, 298 K. Inset legend indicates the scan rates.	98
4.2.14. The scan rate dependence of the peak current densities obtained on the colloidal Pt and Pt-alloys catalysts: $\text{NaBH}_4$ concentration 0.03 M, 298 K.	99
4.2.15. Linear voltammetry of $\text{BH}_4^-$ oxidation on colloidal Pt catalysts using rotating electrodes: the effect of rotation rate and temperature. Scan rate $5 \text{ mV s}^{-1}$ , 298 K and 313 K. $\text{NaBH}_4$ concentration 0.3 M in 2 M NaOH. Inset legend indicates the rotation rate per minute.	100
4.2.16. Linear voltammetry of $\text{BH}_4^-$ oxidation on colloidal Pt-Au catalysts using rotating electrodes: the effect of rotation rate and temperature. Scan rate $5 \text{ mV s}^{-1}$ , 298 K and 313 K. $\text{NaBH}_4$ concentration 0.3 M in 2 M NaOH. Inset legend indicates the rotation rate per minute.	100
4.2.17. Linear voltammetry of $\text{BH}_4^-$ oxidation on colloidal Pt-Ni catalysts using rotating electrodes: the effect of rotation rate and temperature. Scan rate $5 \text{ mV s}^{-1}$ , 298 K and 313 K. $\text{NaBH}_4$ concentration 0.3 M in 2 M NaOH. Inset legend indicates the rotation rate per minute.	101
4.2.18. Linear voltammetry of $\text{BH}_4^-$ oxidation on colloidal Pt-Ir catalysts using rotating electrodes: the effect of rotation rate and temperature. Scan rate $5 \text{ mV s}^{-1}$ , 298 K and 313 K. $\text{NaBH}_4$ concentration 0.3 M in 2 M NaOH. Inset legend indicates the rotation rate per minute.	101
4.2.19. Linear voltammetry of $\text{BH}_4^-$ oxidation on colloidal Pt-Ag catalysts using rotating electrodes: the effect of rotation rate and temperature. Scan rate $5 \text{ mV s}^{-1}$ , 298 K and 313 K. $\text{NaBH}_4$ concentration 0.3 M in 2 M NaOH. Inset legend indicates the rotation rate per minute.	102

4.2.20. Tafel plots for the supported colloidal Pt and Pt-alloys catalysts generated from the rotating disk electrode data. 298 K.	102
4.2.21. Chronopotentiometry of $\text{BH}_4^-$ oxidation on colloidal Pt and Pt-alloys catalysts. Current step from 0 to 10 $\text{mA cm}^{-2}$ . 0.5 M $\text{NaBH}_4$ in 2 M $\text{NaOH}$ . 298 K.	105
4.2.22. Chronoamperometry of $\text{BH}_4^-$ oxidation on colloidal Pt catalyst. Potential steps from $-0.9$ V vs. MOE to $-0.6$ , $-0.4$ and $-0.2$ V vs. MOE, respectively. 0.5 M $\text{NaBH}_4$ in 2 M $\text{NaOH}$ . 298 K.	106
4.2.23. Chronoamperometry of $\text{BH}_4^-$ oxidation on colloidal Pt-Au catalyst. Potential steps from $-0.9$ V vs. MOE to $-0.6$ , $-0.4$ and $-0.2$ V vs. MOE, respectively. 0.5 M $\text{NaBH}_4$ in 2 M $\text{NaOH}$ . 298 K.	106
4.2.24. Chronoamperometry of $\text{BH}_4^-$ oxidation on colloidal Pt-Ni catalyst. Potential steps from $-0.9$ V vs. MOE to $-0.6$ , $-0.4$ and $-0.2$ V vs. MOE, respectively. 0.5 M $\text{NaBH}_4$ in 2 M $\text{NaOH}$ . 298 K.	107
4.2.25. Chronoamperometry of $\text{BH}_4^-$ oxidation on colloidal Pt-Ir catalyst. Potential steps from $-0.9$ V vs. MOE to $-0.6$ , $-0.4$ and $-0.2$ V vs. MOE, respectively. 0.5 M $\text{NaBH}_4$ in 2 M $\text{NaOH}$ . 298 K.	107
4.2.26. Chronoamperometry of $\text{BH}_4^-$ oxidation on colloidal Pt-Ag catalyst. Potential steps from $-0.9$ V vs. MOE to $-0.6$ , $-0.4$ and $-0.2$ V vs. MOE, respectively. 0.5 M $\text{NaBH}_4$ in 2 M $\text{NaOH}$ . 298 K.	108
4.2.27. Cottrell plot generated from the chronoamperometry data of potential step from $-0.9$ V to $-0.2$ V vs. MOE.	109
4.2.28. Cottrell plot generated from the chronoamperometry data of potential step from $-0.9$ V to $-0.4$ V vs. MOE.	110
4.2.29. Cottrell plot generated from the chronoamperometry data of potential step from $-0.9$ V to $-0.6$ V vs. MOE.	110
4.2.30 Cumulative charge density as a function of square root of time (Anson plot) generated from the chronoamperometry data of potential step from $-0.9$ V to $-0.2$ V vs. MOE.	111
4.2.31. Cumulative charge density as a function of square root of time (Anson plot) generated from the chronoamperometry data of potential step from $-0.9$ V to $-0.4$ V vs. MOE.	111
4.2.32. Cumulative charge density as a function of square root of time (Anson plot) generated from the chronoamperometry data of potential step from $-0.9$ V to $-0.6$ V vs. MOE.	112
4.2.33. Direct borohydride fuel cell polarization curves at 298 K and 333 K: Anode catalyst (Pt) load 5 $\text{mg cm}^{-2}$ . 2 M $\text{NaBH}_4$ – 2 M $\text{NaOH}$ . Cathode catalyst (Pt) load 4 $\text{mg cm}^{-2}$ . $\text{O}_2$ flow rate 200 $\text{ml min}^{-1}$ at 2.7 atm.	114
4.2.34. Direct borohydride fuel cell polarization curves at 298 K and 333 K: Anode catalyst (Pt-Au) load 5 $\text{mg cm}^{-2}$ . 2 M $\text{NaBH}_4$ – 2 M $\text{NaOH}$ . Cathode catalyst (Pt) load 4 $\text{mg cm}^{-2}$ . $\text{O}_2$ flow rate 200 $\text{ml min}^{-1}$ at 2.7 atm.	114
4.2.35. Direct borohydride fuel cell polarization curves at 298 K and 333 K: Anode catalyst (Pt-Ni) load 5 $\text{mg cm}^{-2}$ . 2 M $\text{NaBH}_4$ – 2 M $\text{NaOH}$ . Cathode catalyst (Pt) load 4 $\text{mg cm}^{-2}$ . $\text{O}_2$ flow rate 200 $\text{ml min}^{-1}$ at 2.7 atm.	115

4.2.36. Direct borohydride fuel cell polarization curves at 298 K and 333 K: Anode catalyst (Pt-Ir) load $5 \text{ mg cm}^{-2}$ . $2 \text{ M NaBH}_4 - 2 \text{ M NaOH}$ . Cathode catalyst (Pt) load $4 \text{ mg cm}^{-2}$ . $\text{O}_2$ flow rate $200 \text{ ml min}^{-1}$ at 2.7 atm.	115
4.2.37. Direct borohydride fuel cell polarization curves at 298 K and 333 K: Comparison between the colloidal catalysts prepared in the present work (Pt, Pt-Au, Pt-Ni and Pt-Ir). Anode catalyst load $5 \text{ mg cm}^{-2}$ . $50 \text{ ml min}^{-1} 2 \text{ M NaBH}_4 - 2 \text{ M NaOH}$ . Cathode catalyst (Pt) load $4 \text{ mg cm}^{-2}$ . $\text{O}_2$ flow rate $200 \text{ ml min}^{-1}$ at 2.7 atm.	116
4.2.38. Direct borohydride fuel cell polarization curve at 298 K: Comparison Between commercial Pt-Ru and the colloidal catalysts prepared in the present work (Pt, Pt-Au, Pt-Ni and Pt-Ir). Anode catalyst load $5 \text{ mg cm}^{-2}$ . $50 \text{ ml min}^{-1} 2 \text{ M NaBH}_4 - 2 \text{ M NaOH}$ . Cathode catalyst (Pt) load $4 \text{ mg cm}^{-2}$ . $\text{O}_2$ flow rate $200 \text{ ml min}^{-1}$ at 2.7 atm.	117
4.3.1. Linear voltammogram of $\text{BH}_4^-$ oxidation on colloidal Au catalyst using static electrode showing the effect of $\text{BH}_4^-$ concentration. Scan rate $100 \text{ mV s}^{-1}$ , 298 K. Inset legend indicates the $\text{NaBH}_4$ concentration.	118
4.3.2. Linear voltammogram of $\text{BH}_4^-$ oxidation on colloidal Au-Pd catalyst using static electrode showing the effect of $\text{BH}_4^-$ concentration. Scan rate $100 \text{ mV s}^{-1}$ , 298 K. Inset legend indicates the $\text{NaBH}_4$ concentration.	118
4.3.3. Linear voltammogram of $\text{BH}_4^-$ oxidation on colloidal Au-Ni catalyst using static electrode showing the effect of $\text{BH}_4^-$ concentration. Scan rate $100 \text{ mV s}^{-1}$ , 298 K. Inset legend indicates the $\text{NaBH}_4$ concentration.	119
4.3.4. Linear voltammogram of $\text{BH}_4^-$ oxidation on colloidal Au-Ag catalyst using static electrode showing the effect of $\text{BH}_4^-$ concentration. Scan rate $100 \text{ mV s}^{-1}$ , 298 K. Inset legend indicates the $\text{NaBH}_4$ concentration.	119
4.3.5. The concentration dependence of the peak current density on colloidal Au and Au-Alloys. Scan rate $100 \text{ mV s}^{-1}$ , 298 K.	121
4.3.6. Linear voltammogram of $\text{BH}_4^-$ oxidation on colloidal Au catalyst using static electrode showing the effect of Scan rate. $\text{NaBH}_4$ concentration $0.03 \text{ M}$ , 298 K. Inset legend indicates the scan rates.	122
4.3.7. Linear voltammogram of $\text{BH}_4^-$ oxidation on colloidal Au-Pd catalyst using static electrode showing the effect of Scan rate. $\text{NaBH}_4$ concentration $0.03 \text{ M}$ , 298 K. Inset legend indicates the scan rates.	122
4.3.8. Linear voltammogram of $\text{BH}_4^-$ oxidation on colloidal Au-Ni catalyst using static electrode showing the effect of Scan rate. $\text{NaBH}_4$ concentration $0.03 \text{ M}$ , 298 K. Inset legend indicates the scan rates.	123
4.3.9. Linear voltammogram of $\text{BH}_4^-$ oxidation on colloidal Au-Ag catalyst using static electrode showing the effect of Scan rate. $\text{NaBH}_4$ concentration $0.03 \text{ M}$ , 298 K. Inset legend indicates the scan rates.	123
4.3.10. The scan rate dependence of the peak current densities obtained on the colloidal Au and Au-alloys catalysts: $\text{NaBH}_4$ concentration $0.03 \text{ M}$ , 298 K.	124
4.3.11. Linear voltammetry of $\text{BH}_4^-$ oxidation on colloidal Au catalysts using rotating electrodes: the effect of rotation rate and temperature. Scan rate $5 \text{ mV s}^{-1}$ , 298 K and 313 K. $\text{NaBH}_4$ concentration $0.3 \text{ M}$ in $2 \text{ M NaOH}$ . Inset legend indicates the rotation rate per minute.	125

4.3.12. Linear voltammetry of $\text{BH}_4^-$ oxidation on colloidal Au-Pd catalysts using rotating electrodes: the effect of rotation rate and temperature. Scan rate $5 \text{ mV s}^{-1}$ , 298 K and 313 K. $\text{NaBH}_4$ concentration 0.3 M in 2 M NaOH. Inset legend indicates the rotation rate per minute.	125
4.3.13. Linear voltammetry of $\text{BH}_4^-$ oxidation on colloidal Au-Ni catalysts using rotating electrodes: the effect of rotation rate and temperature. Scan rate $5 \text{ mV s}^{-1}$ , 298 K and 313 K. $\text{NaBH}_4$ concentration 0.3 M in 2 M NaOH. Inset legend indicates the rotation rate per minute.	126
4.3.14. Linear voltammetry of $\text{BH}_4^-$ oxidation on colloidal Au-Ag catalysts using rotating electrodes: the effect of rotation rate and temperature. Scan rate $5 \text{ mV s}^{-1}$ , 298 K and 313 K. $\text{NaBH}_4$ concentration 0.3 M in 2 M NaOH. Inset legend indicates the rotation rate per minute.	126
4.3.15. Tafel plots for the supported colloidal Au and Au-alloys catalysts generated from the rotating disk electrode data. 298 K.	127
4.3.16. Chronopotentiometry of $\text{BH}_4^-$ oxidation on colloidal Au and Au-alloys catalysts. Current step: from 0 to $10 \text{ mA cm}^{-2}$ . 0.5 M Na $\text{BH}_4$ in 2 M NaOH. 298 K.	129
4.3.17. Chronoamperometry of $\text{BH}_4^-$ oxidation on colloidal Au catalyst. Potential steps from $-0.9 \text{ V vs. MOE}$ to $-0.6$ , $-0.4$ and $-0.2 \text{ V vs. MOE}$ , respectively 0.5 M $\text{NaBH}_4$ in 2 M NaOH. 298 K.	130
4.3.18. Chronoamperometry of $\text{BH}_4^-$ oxidation on colloidal Au-Pd catalyst. Potential steps from $-0.9 \text{ V vs. MOE}$ to $-0.6$ , $-0.4$ and $-0.2 \text{ V vs. MOE}$ , respectively 0.5 M $\text{NaBH}_4$ in 2 M NaOH. 298 K.	130
4.3.19. Chronoamperometry of $\text{BH}_4^-$ oxidation on colloidal Au-Ni catalyst. Potential steps from $-0.9 \text{ V vs. MOE}$ to $-0.6$ , $-0.4$ and $-0.2 \text{ V vs. MOE}$ , respectively 0.5 M $\text{NaBH}_4$ in 2 M NaOH. 298 K.	131
4.3.20. Chronoamperometry of $\text{BH}_4^-$ oxidation on colloidal Au-Ag catalyst. Potential steps from $-0.9 \text{ V vs. MOE}$ to $-0.6$ , $-0.4$ and $-0.2 \text{ V vs. MOE}$ , respectively 0.5 M $\text{NaBH}_4$ in 2 M NaOH. 298 K.	131
4.3.21. Cottrell plot generated from the chronoamperometry data of potential step from $-0.9 \text{ V}$ to $-0.2 \text{ V vs. MOE}$ .	132
4.3.22. Cottrell plot generated from the chronoamperometry data of potential step from $-0.9 \text{ V}$ to $-0.4 \text{ V vs. MOE}$ .	132
4.3.23. Cottrell plot generated from the chronoamperometry data of potential step from $-0.9 \text{ V}$ to $-0.6 \text{ V vs. MOE}$ .	133
4.3.24. Cumulative charge density as a function of square root of time (Anson plot) generated from the chronoamperometry data of potential step from $-0.9 \text{ V}$ to $-0.2 \text{ V vs. MOE}$ .	133
4.3.25. Cumulative charge density as a function of square root of time (Anson plot) generated from the chronoamperometry data of potential step from $-0.9 \text{ V}$ to $-0.4 \text{ V vs. MOE}$ .	134
4.3.26. Cumulative charge density as a function of square root of time (Anson plot) generated from the chronoamperometry data of potential step from $-0.9 \text{ V}$ to $-0.6 \text{ V vs. MOE}$ .	134

4.3.27. Direct borohydride fuel cell polarization curves at 298 K and 333 K: Anode catalyst (Au) load $5 \text{ mg cm}^{-2}$ . $2 \text{ M NaBH}_4 - 2 \text{ M NaOH}$ . Cathode catalyst (Pt) load $4 \text{ mg cm}^{-2}$ . $\text{O}_2$ flow rate $200 \text{ ml min}^{-1}$ at 2.7 atm.	136
4.3.28. Direct borohydride fuel cell polarization curves at 298 K and 333 K: Anode catalyst (Au-Pd) load $5 \text{ mg cm}^{-2}$ . $2 \text{ M NaBH}_4 - 2 \text{ M NaOH}$ . Cathode catalyst (Pt) load $4 \text{ mg cm}^{-2}$ . $\text{O}_2$ flow rate $200 \text{ ml min}^{-1}$ at 2.7 atm.	136
4.3.29. Direct borohydride fuel cell polarization curves at 298 K and 333 K: Comparison between the colloidal Au and Au-alloys catalysts prepared. Anode catalyst load $5 \text{ mg cm}^{-2}$ . $85 \text{ ml min}^{-1} 2 \text{ M NaBH}_4 -$ $2 \text{ M NaOH}$ . Cathode catalyst (Pt) load $4 \text{ mg cm}^{-2}$ . $\text{O}_2$ flow rate $200$ $\text{ml min}^{-1}$ at 2.7 atm.	137
4.3.30. Direct borohydride fuel cell polarization curve at 298 K: Comparison between commercial Pt-Ru and the colloidal Au and Au-alloys catalysts. Anode catalyst load $5 \text{ mg cm}^{-2}$ . $50 \text{ ml min}^{-1} 2 \text{ M NaBH}_4 - 2 \text{ M NaOH}$ . Cathode catalyst (Pt) load $4 \text{ mg cm}^{-2}$ . $\text{O}_2$ flow rate $200 \text{ ml min}^{-1}$ at 2.7 atm.	137
4.4.1. Linear voltammogram of $\text{BH}_4^-$ oxidation on colloidal Ir catalyst using static electrode showing the effect of $\text{BH}_4^-$ concentration. Scan rate $100 \text{ mV s}^{-1}$ , 298 K. Inset legend indicates the $\text{NaBH}_4$ concentration.	139
4.4.2. Linear voltammogram of $\text{BH}_4^-$ oxidation on colloidal Ir-Ni catalyst using static electrode showing the effect of $\text{BH}_4^-$ concentration. Scan rate $100 \text{ mV s}^{-1}$ , 298 K. Inset legend indicates the $\text{NaBH}_4$ concentration.	139
4.4.3. Linear voltammogram of $\text{BH}_4^-$ oxidation on colloidal Ir-Pd catalyst using static electrode showing the effect of $\text{BH}_4^-$ concentration. Scan rate $100 \text{ mV s}^{-1}$ , 298 K. Inset legend indicates the $\text{NaBH}_4$ concentration.	140
4.4.4. Linear voltammogram of $\text{BH}_4^-$ oxidation on colloidal Ir-Ag catalyst using static electrode showing the effect of $\text{BH}_4^-$ concentration. Scan rate $100 \text{ mV s}^{-1}$ , 298 K. Inset legend indicates the $\text{NaBH}_4$ concentration.	140
4.4.5. The concentration dependence of the peak current density on colloidal Ir and Ir-alloys. Scan rate $100 \text{ mV s}^{-1}$ , 298 K.	142
4.4.6. Linear voltammogram of $\text{BH}_4^-$ oxidation on colloidal Ir catalyst using static electrode showing the effect of Scan rate. $\text{NaBH}_4$ concentration $0.03 \text{ M}$ , 298 K. Inset legend indicates the scan rates.	143
4.4.7. Linear voltammogram of $\text{BH}_4^-$ oxidation on colloidal Ir-Ni catalyst using static electrode showing the effect of Scan rate. $\text{NaBH}_4$ concentration $0.03 \text{ M}$ , 298 K. Inset legend indicates the scan rates.	143
4.4.8. Linear voltammogram of $\text{BH}_4^-$ oxidation on colloidal Ir-Pd catalyst using static electrode showing the effect of Scan rate. $\text{NaBH}_4$ concentration $0.03 \text{ M}$ , 298 K. Inset legend indicates the scan rates.	144
4.4.9. Linear voltammogram of $\text{BH}_4^-$ oxidation on colloidal Ir-Ag catalyst using static electrode showing the effect of Scan rate. $\text{NaBH}_4$ concentration $0.03 \text{ M}$ , 298 K. Inset legend indicates the scan rates.	144
4.4.10. The scan rate dependence of the peak current densities obtained on the colloidal Ir and Ir-alloys catalysts: $\text{NaBH}_4$ concentration $0.03 \text{ M}$ , 298 K.	145

4.4.11. Linear voltammetry of $\text{BH}_4^-$ oxidation on colloidal Ir catalysts using rotating electrodes: the effect of rotation rate and temperature. Scan rate $5 \text{ mV s}^{-1}$ , 298 K and 313 K. $\text{NaBH}_4$ concentration 0.3 M in 2 M NaOH. Inset legend indicates the rotation rate per minute.	146
4.4.12. Linear voltammetry of $\text{BH}_4^-$ oxidation on colloidal Ir-Ni catalysts using rotating electrodes: the effect of rotation rate and temperature. Scan rate $5 \text{ mV s}^{-1}$ , 298 and 313 K. $\text{NaBH}_4$ concentration 0.3 M in 2 M NaOH. Inset legend indicates the rotation rate per minute.	146
4.4.13. Linear voltammetry of $\text{BH}_4^-$ oxidation on colloidal Ir-Pd catalysts using rotating electrodes: the effect of rotation rate and temperature. Scan rate $5 \text{ mV s}^{-1}$ , 298 K and 313 K. $\text{NaBH}_4$ concentration 0.3 M in 2 M NaOH. Inset legend indicates the rotation rate per minute.	147
4.4.14. Linear voltammetry of $\text{BH}_4^-$ oxidation on colloidal Ir-Ag catalysts using rotating electrodes: the effect of rotation rate and temperature. Scan rate $5 \text{ mV s}^{-1}$ , 298 K and 313 K. $\text{NaBH}_4$ concentration 0.3 M in 2 M NaOH. Inset legend indicates the rotation rate per minute.	147
4.4.15. Tafel plots for the supported colloidal Ir and Ir-alloys catalysts generated from the rotating disk electrode data. 298 K.	148
4.4.16. Chronopotentiometry of $\text{BH}_4^-$ oxidation on colloidal Ir and Ir-alloys catalysts. Current step: from 0 to $10 \text{ mA cm}^{-2}$ . 0.5 M Na $\text{BH}_4$ in 2 M NaOH. 298 K.	150
4.4.17. Chronoamperometry of $\text{BH}_4^-$ oxidation on colloidal Ir catalyst. Potential steps from $-0.9 \text{ V vs. MOE}$ to $-0.6$ , $-0.4$ and $-0.2 \text{ V vs. MOE}$ , respectively 0.5 M $\text{NaBH}_4$ in 2 M NaOH. 298 K.	151
4.4.18. Chronoamperometry of $\text{BH}_4^-$ oxidation on colloidal Ir-Ni catalyst. Potential steps from $-0.9 \text{ V vs. MOE}$ to $-0.6$ , $-0.4$ and $-0.2 \text{ V vs. MOE}$ , respectively 0.5 M $\text{NaBH}_4$ in 2 M NaOH. 298 K.	151
4.4.19. Chronoamperometry of $\text{BH}_4^-$ oxidation on colloidal Ir-Pd catalyst. Potential steps from $-0.9 \text{ V vs. MOE}$ to $-0.6$ , $-0.4$ and $-0.2 \text{ V vs. MOE}$ , respectively 0.5 M $\text{NaBH}_4$ in 2 M NaOH. 298 K.	152
4.4.20. Chronoamperometry of $\text{BH}_4^-$ oxidation on colloidal Ir-Ag catalyst. Potential steps from $-0.9 \text{ V vs. MOE}$ to $-0.6$ , $-0.4$ and $-0.2 \text{ V vs. MOE}$ , respectively 0.5 M $\text{NaBH}_4$ in 2 M NaOH. 298 K.	152
4.4.21. Cottrell plot generated from the chronoamperometry data of potential step from $-0.9 \text{ V}$ to $-0.4 \text{ V vs. MOE}$ .	153
4.4.22. Cottrell plot generated from the chronoamperometry data of potential step from $-0.9 \text{ V}$ to $-0.4 \text{ V vs. MOE}$ .	153
4.4.23. Cottrell plot generated from the chronoamperometry data of potential step from $-0.9 \text{ V}$ to $-0.6 \text{ V vs. MOE}$ .	154
4.4.24. Cumulative charge density as a function of square root of time (Anson plot) generated from the chronoamperometry data of potential step from $-0.9 \text{ V}$ to $-0.2 \text{ V vs. MOE}$ .	154
4.4.25. Cumulative charge density as a function of square root of time (Anson plot) generated from the chronoamperometry data of potential step from $-0.9 \text{ V}$ to $-0.4 \text{ V vs. MOE}$ .	155

4.4.26. Cumulative charge density as a function of square root of time (Anson plot) generated from the chronoamperometry data of potential step from $-0.9\text{ V}$ to $-0.6\text{ V}$ vs. MOE.	155
4.4.27. Direct borohydride fuel cell polarization curves at 298 K and 333 K: Anode catalyst (Ir-Pt) load $5\text{ mg cm}^{-2}$ . 2 M $\text{NaBH}_4$ – 2 M $\text{NaOH}$ . Cathode catalyst (Pt) load $4\text{ mg cm}^{-2}$ . $\text{O}_2$ flow rate $200\text{ ml min}^{-1}$ at 2.7 atm.	157
4.4.28. Direct borohydride fuel cell polarization curves at 298 K and 333 K: Anode catalyst (Ir-Ni) load $5\text{ mg cm}^{-2}$ . 2 M $\text{NaBH}_4$ – 2 M $\text{NaOH}$ . Cathode catalyst (Pt) load $4\text{ mg cm}^{-2}$ . $\text{O}_2$ flow rate $200\text{ ml min}^{-1}$ at 2.7 atm.	157
4.4.29. Direct borohydride fuel cell polarization curves at 298 K and 333 K: Anode catalyst (Ir-Pd) load $5\text{ mg cm}^{-2}$ . 2 M $\text{NaBH}_4$ – 2 M $\text{NaOH}$ . Cathode catalyst (Pt) load $4\text{ mg cm}^{-2}$ . $\text{O}_2$ flow rate $200\text{ ml min}^{-1}$ at 2.7 atm.	158
4.4.30. Direct borohydride fuel cell polarization curves at 298 K and 333 K: Comparison between the colloidal catalysts prepared in the present work (Ir-Pt, Ir-Ni and Ir-Pd). Anode catalyst load $5\text{ mg cm}^{-2}$ . $50\text{ ml min}^{-1}$ 2 M $\text{NaBH}_4$ – 2 M $\text{NaOH}$ . Cathode catalyst (Pt) load $4\text{ mg cm}^{-2}$ . $\text{O}_2$ flow rate $200\text{ ml min}^{-1}$ at 2.7 atm.	159
4.5.1. Linear voltammogram of $\text{BH}_4^-$ oxidation on colloidal Pd catalyst using static electrode showing the effect of $\text{BH}_4^-$ concentration. Scan rate $100\text{ mV s}^{-1}$ , 298 K. Inset legend indicates the $\text{NaBH}_4$ concentration.	160
4.5.2. Linear voltammogram of $\text{BH}_4^-$ oxidation on colloidal Pd-Ni catalyst using static electrode showing the effect of $\text{BH}_4^-$ concentration. Scan rate $100\text{ mV s}^{-1}$ , 298 K. Inset legend indicates the $\text{NaBH}_4$ concentration.	160
4.5.3. Linear voltammogram of $\text{BH}_4^-$ oxidation on colloidal Pd-Ag catalyst using static electrode showing the effect of $\text{BH}_4^-$ concentration. Scan rate $100\text{ mV s}^{-1}$ , 298 K. Inset legend indicates the $\text{NaBH}_4$ concentration.	161
4.5.4. The concentration dependence of the peak current density on colloidal Pd and Pd-alloys catalysts. Scan rate $100\text{ mV s}^{-1}$ , 298 K.	162
4.5.5. Linear voltammogram of $\text{BH}_4^-$ oxidation on colloidal Pd catalyst using static electrode showing the effect of Scan rate. $\text{NaBH}_4$ concentration 0.03 M, 298 K. Inset legend indicates the scan rates.	163
4.5.6. Linear voltammogram of $\text{BH}_4^-$ oxidation on colloidal Pd-Ni catalyst using static electrode showing the effect of Scan rate. $\text{NaBH}_4$ concentration 0.03 M, 298 K. Inset legend indicates the scan rates.	163
4.5.7. Linear voltammogram of $\text{BH}_4^-$ oxidation on colloidal Pd-Ag catalyst using static electrode showing the effect of Scan rate. $\text{NaBH}_4$ concentration 0.03 M, 298 K. Inset legend indicates the scan rates.	164
4.5.8. The scan rate dependence of the peak current densities obtained on the colloidal Pd and Pd-alloys catalysts: $\text{NaBH}_4$ concentration 0.03 M, 298 K.	164
4.5.9. Linear voltammetry of $\text{BH}_4^-$ oxidation on colloidal Pd catalysts using rotating electrodes: the effect of rotation rate and temperature. Scan rate $5\text{ mV s}^{-1}$ , 298 K and 313 K. $\text{NaBH}_4$ concentration 0.3 M in 2 M $\text{NaOH}$ . Inset legend indicates the rotation rate per minute.	165



4.5.10. Linear voltammetry of $\text{BH}_4^-$ oxidation on colloidal Pd-Ni catalysts using rotating electrodes: the effect of rotation rate and temperature. Scan rate $5 \text{ mV s}^{-1}$ , 298 K and 313 K. $\text{NaBH}_4$ concentration 0.3 M in 2 M NaOH. Inset legend indicates the rotation rate per minute.	166
4.5.11. Linear voltammetry of $\text{BH}_4^-$ oxidation on colloidal Pd-Ag catalysts using rotating electrodes: the effect of rotation rate and temperature. Scan rate $5 \text{ mV s}^{-1}$ , 298 K and 313 K. $\text{NaBH}_4$ concentration 0.3 M in 2 M NaOH. Inset legend indicates the rotation rate per minute.	166
4.5.12. Tafel plots for the supported colloidal Pd and Pd-alloys catalysts generated from the rotating disk electrode data. 298 K.	167
4.5.13. Chronopotentiometry of $\text{BH}_4^-$ oxidation on colloidal Pd and Pd-alloys catalysts Current step: from 0 to $10 \text{ mA cm}^{-2}$ . 0.5 M $\text{NaBH}_4$ in 2 M NaOH. 298 K.	169
4.5.14. Chronoamperometry of $\text{BH}_4^-$ oxidation on colloidal Pd catalyst. Potential steps from $-0.9 \text{ V vs. MOE}$ to $-0.6$ , $-0.4$ and $-0.2 \text{ V vs. MOE}$ , respectively 0.5 M $\text{NaBH}_4$ in 2 M NaOH. 298 K.	170
4.5.15. Chronoamperometry of $\text{BH}_4^-$ oxidation on colloidal Pd-Ni catalyst. Potential steps from $-0.9 \text{ V vs. MOE}$ to $-0.6$ , $-0.4$ and $-0.2 \text{ V vs. MOE}$ , respectively 0.5 M $\text{NaBH}_4$ in 2 M NaOH. 298 K.	170
4.5.16. Chronoamperometry of $\text{BH}_4^-$ oxidation on colloidal Pd-Ag catalyst. Potential steps from $-0.9 \text{ V vs. MOE}$ to $-0.6$ , $-0.4$ and $-0.2 \text{ V vs. MOE}$ , respectively 0.5 M $\text{NaBH}_4$ in 2 M NaOH. 298 K.	171
4.5.17. Cottrell plot generated from the chronoamperometry data of potential step from $-0.9 \text{ V}$ to $-0.2 \text{ V vs. MOE}$ .	171
4.5.18 Cottrell plot generated from the chronoamperometry data of potential step from $-0.9 \text{ V}$ to $-0.4 \text{ V vs. MOE}$ .	172
4.5.19. Cottrell plot generated from the chronoamperometry data of potential step from $-0.9 \text{ V}$ to $-0.6 \text{ V vs. MOE}$ .	172
4.5.20. Cumulative charge density as a function of square root of time (Anson plot) generated from the chronoamperometry data of potential step from $-0.9 \text{ V}$ to $-0.2 \text{ V vs. MOE}$ .	173
4.5.21. Cumulative charge density as a function of square root of time (Anson plot) generated from the chronoamperometry data of potential step from $-0.9 \text{ V}$ to $-0.4 \text{ V vs. MOE}$ .	173
4.5.22. Cumulative charge density as a function of square root of time (Anson plot) generated from the chronoamperometry data of potential step from $-0.9 \text{ V}$ to $-0.6 \text{ V vs. MOE}$ .	174
4.5.23. Direct borohydride fuel cell polarization curves at 298 K and 333 K: Anode catalyst (Pd) load $5 \text{ mg cm}^{-2}$ . 2 M $\text{NaBH}_4$ – 2 M NaOH. Cathode catalyst (Pt) load $4 \text{ mg cm}^{-2}$ . $\text{O}_2$ flow rate $200 \text{ ml min}^{-1}$ at 2.7 atm.	175
4.5.24. Direct borohydride fuel cell polarization curves at 298 K and 333 K: Anode catalyst (Pd-Ir) load $5 \text{ mg cm}^{-2}$ . 2 M $\text{NaBH}_4$ – 2 M NaOH. Cathode catalyst (Pt) load $4 \text{ mg cm}^{-2}$ . $\text{O}_2$ flow rate $200 \text{ ml min}^{-1}$ at 2.7 atm.	176
4.5.25. Direct borohydride fuel cell polarization curves at 298 K and 333 K: Anode catalyst (Pd-Au) load $5 \text{ mg cm}^{-2}$ . 2 M $\text{NaBH}_4$ – 2 M NaOH. Cathode catalyst (Pt) load $4 \text{ mg cm}^{-2}$ . $\text{O}_2$ flow rate $200 \text{ ml min}^{-1}$ at 2.7 atm.	176

4.5.26. Direct borohydride fuel cell polarization curves at 298 K and 333 K: Comparison between the colloidal catalysts prepared in the present work (Pd, Pd-Ir, and Pd-Au). Anode catalyst load $5 \text{ mg cm}^{-2}$ . $50 \text{ ml min}^{-1}$ $2 \text{ M NaBH}_4 - 2 \text{ M NaOH}$ Cathode catalyst (Pt) load $4 \text{ mg cm}^{-2}$ . $\text{O}_2$ flow rate $200 \text{ ml min}^{-1}$ at 2.7 atm.	177
4.6.1. Linear voltammogram of $\text{BH}_4^-$ oxidation on colloidal catalysts using static electrode. $\text{NaBH}_4$ concentration $0.03 \text{ M BH}_4^-$ in $2 \text{ M NaOH}$ . Scan rate $100 \text{ mV s}^{-1}$ , 298 K.	178
4.6.2. Linear voltammogram of $\text{BH}_4^-$ oxidation on colloidal catalysts using static electrode. $\text{NaBH}_4$ concentration $0.1 \text{ M}$ in $2 \text{ M NaOH}$ . Scan rate $100 \text{ mV s}^{-1}$ , 298 K.	179
4.6.3. Linear voltammetry of $\text{BH}_4^-$ oxidation on colloidal catalysts using rotating electrodes: Rotation per minute 500. Scan rate $5 \text{ mV s}^{-1}$ , 298. $\text{NaBH}_4$ concentration $0.3 \text{ M}$ in $2 \text{ M NaOH}$ .	180
4.6.4. Chronopotentiometry of $\text{BH}_4^-$ oxidation on colloidal catalysts. Current step: from 0 to $10 \text{ mA cm}^{-2}$ . $0.5 \text{ M Na BH}_4$ in $2 \text{ M NaOH}$ . 298 K.	181
4.6.5. Chronoamperometry of $\text{BH}_4^-$ oxidation on colloidal catalysts. Potential steps from $-0.9 \text{ V}$ to $-0.2 \text{ V}$ vs. MOE, respectively $0.5 \text{ M NaBH}_4$ in $2 \text{ M NaOH}$ . 298 K.	182
4.6.6. Direct borohydride fuel cell polarization curves at 298 K: Comparison between the colloidal catalysts. Anode catalyst load $5 \text{ mg cm}^{-2}$ . $85 \text{ ml min}^{-1}$ $2 \text{ M NaBH}_4 - 2 \text{ M NaOH}$ . Cathode catalyst (Pt) load $4 \text{ mg cm}^{-2}$ . $\text{O}_2$ flow rate $200 \text{ ml min}^{-1}$ at 2.7 atm.	184
4.6.7. Direct borohydride fuel cell polarization curves at 333 K: Comparison between the colloidal catalysts. Anode catalyst load $5 \text{ mg cm}^{-2}$ . $85 \text{ ml min}^{-1}$ $2 \text{ M NaBH}_4 - 2 \text{ M NaOH}$ . Cathode catalyst (Pt) load $4 \text{ mg cm}^{-2}$ . $\text{O}_2$ flow rate $200 \text{ ml min}^{-1}$ at 2.7 atm.	184
4.7.1. Linear voltammogram of $\text{BH}_4^-$ oxidation on colloidal Pt catalysts using static electrodes showing the effect of $\text{BH}_4^-$ concentration: a) The colloidal supported on C-Black: b) The colloidal supported on 90wt% C-Black and 10wt% $\text{TiO}_2$ . Scan rate $100 \text{ mV s}^{-1}$ , 298 K. Inset legend indicates the $\text{NaBH}_4$ concentration in $2 \text{ M NaOH}$ .	187
4.7.2. Linear voltammogram of $\text{BH}_4^-$ oxidation on colloidal Pd catalysts using static electrodes showing the effect of $\text{BH}_4^-$ concentration: The colloidal supported on 90wt% C-Black and 10wt% $\text{TiO}_2$ . Scan rate $100 \text{ mV s}^{-1}$ , 298 K. Inset legend indicates the $\text{NaBH}_4$ concentration in $2 \text{ M NaOH}$ .	187
4.7.3. Linear voltammogram of $\text{BH}_4^-$ oxidation on colloidal Ir catalysts using static electrodes showing the effect of $\text{BH}_4^-$ concentration: The colloidal supported on 90wt% C-Black and 10wt% $\text{TiO}_2$ . Scan rate $100 \text{ mV s}^{-1}$ , 298 K. Inset legend indicates the $\text{NaBH}_4$ concentration in $2 \text{ M NaOH}$ .	188
4.7.4. The concentration dependence of the peak current density on colloidal Pt/(C-Black) and Pt/(C-Black+ $\text{TiO}_2$ ) catalysts. Scan rate $100 \text{ mV s}^{-1}$ , 298 K.	189
4.7.5. The concentration dependence of the peak current density on colloidal Pd/(C-Black) and Pd/(C-Black+ $\text{TiO}_2$ ) catalysts. Scan rate $100 \text{ mV s}^{-1}$ , 298 K.	189
4.7.6. The concentration dependence of the peak current density on colloidal Ir/(C-Black) and Ir/(C-Black+ $\text{TiO}_2$ ) catalysts. Scan rate $100 \text{ mV s}^{-1}$ , 298 K.	190

4.7.7. Linear voltammogram of $\text{BH}_4^-$ oxidation on colloidal Pt catalysts using static electrodes showing the effect of scan rate: The colloidal supported on 90wt% C-Black and 10wt% $\text{TiO}_2$ . $\text{NaBH}_4$ concentration 0.03 M, 298 K. Inset legend indicates the scan rates.	190
4.7.8. Linear voltammogram of $\text{BH}_4^-$ oxidation on colloidal Pd catalysts using static electrodes showing the effect of scan rate: The colloidal supported on 90wt% C-Black and 10wt% $\text{TiO}_2$ . $\text{NaBH}_4$ concentration 0.03 M, 298 K. Inset legend indicates the scan rates.	191
4.7.9. Linear voltammogram of $\text{BH}_4^-$ oxidation on colloidal Ir catalysts using static electrodes showing the effect of scan rate: The colloidal supported on 90wt% C-Black and 10wt% $\text{TiO}_2$ . $\text{NaBH}_4$ concentration 0.03 M, 298 K. Inset legend indicates the scan rates.	191
4.7.10. The scan rate dependence of the peak current densities obtained on the colloidal Pt/(C-Black) and Pt/(C-Black+ $\text{TiO}_2$ ) catalysts: $\text{NaBH}_4$ concentration 0.03 M, 298 K.	192
4.7.11. The scan rate dependence of the peak current densities obtained on the colloidal Pd/(C-Black) and Pd/(C-Black+ $\text{TiO}_2$ ) catalysts: $\text{NaBH}_4$ concentration 0.03 M, 298 K.	193
4.7.12. The scan rate dependence of the peak current densities obtained on the colloidal Ir/(C-Black) and Ir/(C-Black+ $\text{TiO}_2$ ) catalysts: $\text{NaBH}_4$ concentration 0.03 M, 298 K.	193
4.7.13. Linear voltammetry of $\text{BH}_4^-$ oxidation on colloidal Pt catalysts using rotating electrodes: the effect of rotation rate and temperature. The colloidal supported on 90wt% C-Black and 10wt% $\text{TiO}_2$ . Scan rate $5 \text{ mV s}^{-1}$ , 298 K and 313 K. $\text{NaBH}_4$ concentration 0.3 M in 2 M NaOH. Inset legend indicates the rotation rate per minute.	194
4.7.14. Linear voltammetry of $\text{BH}_4^-$ oxidation on colloidal Pd catalysts using rotating electrodes: the effect of rotation rate and temperature. The colloidal supported on 90wt% C-Black and 10wt% $\text{TiO}_2$ . Scan rate $5 \text{ mV s}^{-1}$ , 298 K and 313 K. $\text{NaBH}_4$ concentration 0.3 M in 2 M NaOH. Inset legend indicates the rotation rate per minute.	195
4.7.15. Linear voltammetry of $\text{BH}_4^-$ oxidation on colloidal Ir catalysts using rotating electrodes: the effect of rotation rate and temperature. The colloidal supported on 90wt% C-Black and 10wt% $\text{TiO}_2$ . Scan rate $5 \text{ mV s}^{-1}$ , 298 K and 313 K. $\text{NaBH}_4$ concentration 0.3 M in 2 M NaOH. Inset legend indicates the rotation rate per minute.	195
4.5.16. Tafel plots for the supported colloidal Pt/(C-Black) and Pt/(C-Black+ $\text{TiO}_2$ ) catalysts generated from the rotating disk electrode data. 298 K and 313 K.	196
4.5.17. Tafel plots for the supported colloidal Pd/(C-Black) and Pd/(C-Black+ $\text{TiO}_2$ ) catalysts generated from the rotating disk electrode data. 298 K and 313 K.	196
4.5.18. Tafel plots for the supported colloidal Ir/(C-Black) and Ir/(C-Black+ $\text{TiO}_2$ ) catalysts generated from the rotating disk electrode data. 298 K and 313 K.	197

4.7.19. Chronopotentiometry of $\text{BH}_4^-$ oxidation on colloidal Pt/(C-Black) and Pt/(C-Black+ $\text{TiO}_2$ ) catalysts. Current step: from 0 to $10 \text{ mA cm}^{-2}$ . 0.5 M $\text{NaBH}_4$ in 2 M $\text{NaOH}$ . 298 K.	198
4.7.20. Chronopotentiometry of $\text{BH}_4^-$ oxidation on colloidal Pd/(C-Black) and Pd/(C-Black+ $\text{TiO}_2$ ) catalysts. Current step: from 0 to $10 \text{ mA cm}^{-2}$ . 0.5 M $\text{NaBH}_4$ in 2 M $\text{NaOH}$ . 298 K.	198
4.7.21. Chronopotentiometry of $\text{BH}_4^-$ oxidation on colloidal Ir/(C-Black) and Ir/(C-Black+ $\text{TiO}_2$ ) catalysts. Current step: from 0 to $10 \text{ mA cm}^{-2}$ . 0.5 M $\text{NaBH}_4$ in 2 M $\text{NaOH}$ . 298 K.	199
4.7.22. Chronoamperometry of $\text{BH}_4^-$ oxidation on Pt/(C-Black) and Pt/(C-Black+ $\text{TiO}_2$ ) catalysts. Potential steps from $-0.9 \text{ V}$ to $-0.2 \text{ V}$ vs. MOE. 0.5 M $\text{NaBH}_4$ in 2 M $\text{NaOH}$ . 298 K.	199
4.7.23. Chronoamperometry of $\text{BH}_4^-$ oxidation on Pd/(C-Black) and Pd/(C-Black+ $\text{TiO}_2$ ) catalysts. Potential steps from $-0.9 \text{ V}$ to $-0.2 \text{ V}$ vs. MOE. 0.5 M $\text{NaBH}_4$ in 2 M $\text{NaOH}$ . 298 K.	200
4.7.24. Chronoamperometry of $\text{BH}_4^-$ oxidation on colloidal Ir/(C-Black) and Ir/(C-Black+ $\text{TiO}_2$ ) catalysts. Potential steps from $-0.9 \text{ V}$ to $-0.2 \text{ V}$ vs. MOE. 0.5 M $\text{NaBH}_4$ in 2 M $\text{NaOH}$ . 298 K.	200
4.7.25. Cottrell plot generated from the chronoamperometry data for colloidal Pt catalyst supported on 90wt% C-balk and 10wt% $\text{TiO}_2$ . Potential steps from $-0.9 \text{ V}$ to $-0.6$ , $-0.4$ and $-0.2 \text{ V}$ vs. MOE.	201
4.7.26. Cottrell plot generated from the chronoamperometry data for colloidal Pd catalyst supported on 90wt% C-balk and 10wt% $\text{TiO}_2$ . Potential steps from $-0.9 \text{ V}$ to $-0.6$ , $-0.4$ and $-0.2 \text{ V}$ vs. MOE.	202
4.7.27. Cottrell plot generated from the chronoamperometry data for colloidal Ir catalyst supported on 90wt% C-balk and 10wt% $\text{TiO}_2$ . Potential steps from $-0.9 \text{ V}$ to $-0.6$ , $-0.4$ and $-0.2 \text{ V}$ vs. MOE.	202
4.7.28. Cumulative charge density as a function of square root of time (Anson plot) generated from the chronoamperometry data for colloidal Pt catalyst supported on 90wt% C-balk and 10wt% $\text{TiO}_2$ . Potential steps from $-0.9 \text{ V}$ vs. MOE to $-0.6$ , $-0.4$ and $-0.2 \text{ V}$ vs. MOE.	203
4.7.29. Cumulative charge density as a function of square root of time (Anson plot) generated from the chronoamperometry data for colloidal Pd catalyst supported on 90wt% C-balk and 10wt% $\text{TiO}_2$ . Potential steps from $-0.9 \text{ V}$ vs. MOE to $-0.6$ , $-0.4$ and $-0.2 \text{ V}$ vs. MOE.	203
4.7.30. Cumulative charge density as a function of square root of time (Anson plot) generated from the chronoamperometry data for colloidal Ir catalyst supported on 90wt% C-balk and 10wt% $\text{TiO}_2$ . Potential steps from $-0.9 \text{ V}$ vs. MOE to $-0.6$ , $-0.4$ and $-0.2 \text{ V}$ vs. MOE.	204

## NOMENCLATURE

Symbol	Meaning	Units
$A$	Active surface area,	$\text{cm}^2$
$A_s$	Superficial surface area,	$\text{cm}^2$
$b$	Tafel slope	V / decade
$b_a$	Anodic Tafel slope	V / decade
$b_c$	Cathodic Tafel slope	V / decade
$C$	Concentration	$\text{mol cm}^{-3}$
$C^O$	Bulk concentration	$\text{mol cm}^{-3}$
$C^S$	Surface concentration	$\text{mol cm}^{-3}$
$C_O$	Concentration of species O	$\text{mol cm}^{-3}$
$C_R$	Concentration of species R	$\text{mol cm}^{-3}$
$D, D_o$	Diffusion coefficient	$\text{cm}^2 \text{s}^{-1}$
$E$	Cell Potential	V
$E^o$	Standard potential	V
$E_e$	Equilibrium potential	V
$E_a$	Anode potential	V
$E_c$	Cathode potential	V
$E_P$	Peak potential	V
$F$	Faraday's constant	$\text{C mol}^{-1}$
$G$	Gibbs free energy	$\text{kJ mol}^{-1}$
$H$	Enthalpy	$\text{kJ mol}^{-1}$
$\varepsilon$	Porosity	
$I$	Current density	$\text{A cm}^{-2}$
$i$	Current	A
$i_o$	Exchange current density	$\text{A cm}^{-2}$
$i_a$	Anodic current	A
$i_c$	Cathodic current	A
$i_L$	Limiting current density	$\text{A cm}^{-2}$
$i_p$	Peak current	A
$J$	Flux	$\text{mol cm}^{-2} \text{s}^{-1}$
$k^o$	Standard heterogeneous rate constant	$\text{cm s}^{-1}$
$k_a$	Oxidation heterogeneous rate constant	$\text{cm s}^{-1}$
$k_c$	Reduction heterogeneous rate constant	$\text{cm s}^{-1}$
$k_h$	Heterogeneous rate constant	$\text{cm s}^{-1}$
$N_A$	Avogadro's number	$\text{mol}^{-1}$

$n$	Number of electrons	
$O$	Oxidized species	
$P$	Pressure	Pa, atm
$Q$	Chronocoulometric charge	C
$Q_{in}$	Heat	$\text{kJ mol}^{-1}$
$R$	a) Gas constant	$\text{J K}^{-1} \text{mol}^{-1}$
	b) Resistance	$\Omega$
	c) Reduced species	
$S$	Entropy	$\text{kJ K}^{-1} \text{mol}^{-1}$
$T$	Temperature	K
$t$	Time	s
$V$	Scan rate	$\text{V s}^{-1}$
$V$	Volume	$\text{cm}^3$
$W$	Work	$\text{kJ mol}^{-1}$
$W_{el}$	Electrical work	
$x$	Distance from electrode	cm

### Greek

$\alpha_a$	Anodic transfer coefficient	
$\alpha_b$	Cathodic transfer coefficient	
$\eta$	Overpotential, $\eta = E - E_e$	V
$\eta_{ohm}$	Ohmic overpotential	V
$\eta_{act}$	Activation overpotential	V
$\eta_{conc}$	Concentration overpotential	V
$\zeta$	Efficiency	

## ACRONYMS

AFC	Alkaline fuel cell
DMFC	Direct methanol fuel cell
DFAFC	Direct formic acid fuel cell
DBFC	Direct borohydride fuel cell
MCFC	Molten carbonate fuel cell
MOE	Mercuric (Hg/HgO) reference electrode
MEA	Membrane electrode assembly
PEMFC	Proton exchange membrane fuel cell
PAFC	Phosphoric acid fuel cell
SOFC	Solid oxide fuel cell
SCE	Saturated calomel electrode
SMSE	Saturated mercurous sulfate electrode
SSE	Saturated silver/silver chloride electrode
SHE	Standard hydrogen electrode
TST	Transition State Theory

# CHAPTER 1

## INTRODUCTION

### 1.1. General

It is clear that a clean and secure form of energy is one of the world's main priorities. Fuel cells and hydrogen are amongst the most promising technological solutions. Yet, it is difficult to answer the question, "Are these systems any where near close to commercial reality?" The path is challenging, but ongoing worldwide efforts give hope that success is on the horizon [1]. The performance and commercialization of fuel cells depend to a large extent on the electrode materials performance, in particular that of the electrocatalysts.

It was thought that the availability of energy was inexhaustible. Oil, fossil fuel, and coal, were so cheap that no one was concerned about their consumption. Lately, people have realized that fossil fuel supplies are limited, and have started looking for alternative sources that are clean and inexhaustible in order to avoid similar problems in the future [2]. Several factors should be considered in estimating the remaining life-time for the existing resources in the world. These factors include the total remaining resources, the present rate of consumption, and the future rate of consumption, taking into account the rise in demand due to both population and economic growth [2].

Fuel cells are a reasonable choice, since they operate on hydrogen which is an abundant and less polluting fuel source. A fuel cell is an electrochemical device which combines hydrogen fuel with oxygen to produce electricity and heat, releasing water as a byproduct. Fuel cells are a clean, environmentally friendly, versatile, reliable and efficient power source.

The engineering complexity and high costs can be overcome by replacing hydrogen as the fuel with a liquid that can be fed directly to a fuel cell. A conventional storage tank is then required instead of a gas storage tank or a fuel reformer plus storage tank [3].



## **1.2. Direct Liquid Fuel Cell (DLFC) Research and Development**

Portable fuel cell demands have increased in the past several years. The technologies of such fuel cell types that are under development are materials-related rather than system and/or process related. Fuel cell manufacturers have put an emphasis on developing the polymer electrolyte membrane, electrode catalysts, and the fuel to be used. To avoid the crossover phenomenon which is encountered in DLFCs using a Nafion membrane, which was originally designed to be utilized in pure hydrogen-fed fuel cells, a new electrolyte must be developed. To enhance the reaction speed for better fuel utilization and a more efficient fuel cell, a more active and cost effective electrocatalyst must be developed.

In the last two decades, direct methanol fuel cells [4-7] have attracted the most attention of all the direct liquid fuel cells, since methanol can be easily and cheaply synthesized from primary sources. Direct methanol fuel cells (DMFC) offer advantages in the storage of fuel, but currently show rather low power densities, thus limiting their use in many portable applications. The major unresolved problems with DMFCs such as CO poisoning of catalysts and fuel crossover [7], have encouraged some investigators to look for alternative fuels rather than organic base fuels (e.g., methanol, ethanol, formic acid, etc.).

### **1.2.1. Why a Direct Borohydride Fuel Cell (DBFC)?**

Hydrazine [8-13] and Borohydride [14-22] have been suggested as alternative fuels since the early 1960s and have come into prominence once again after three decades of hiatus.

Direct hydrazine fuel cells (DHFC) that utilize a cation polymer electrolyte suffer from fuel crossover and the evolution of hydrogen and formation of ammonia, some of which can crossover to the cathode compartment thus affecting its performance [11-13]. In addition, hydrazine is toxic if inhaled or swallowed and is an irritant if absorbed through the skin. Severe exposure to hydrazine vapour may cause temporary blindness [hydrazine MSDS]. Ammonia is evolved from a side reaction and itself is toxic and harmful if

inhaled and may cause severe irritation of the respiratory tract [ammonia MSDS]. All these concerns mitigate against hydrazine being a good candidate for portable fuel cell applications.

Recently, direct borohydride fuel cells have emerged as a direct liquid fuel cell alternative. They are considered as both a potential source of hydrogen, and an environmentally friendly aqueous fuel. Borohydride is oxidized in an aqueous alkaline medium to meta-borate and water. The theoretical cell voltage of a DBFC is 1.64 V [23], which is higher than that of DMFC, direct formic acid fuel cells (DFAFC), DHFC, and pure hydrogen fed fuel cells, with theoretical cell voltages of 1.2 V [4-7], 1.45 V [24], 1.56 [11], and 1.23 V [23], respectively. In addition, DBFCs do not suffer from CO poisoning which affects the catalyst activity and do not emit ammonia or CO<sub>2</sub>, the environmentally unfriendly gases, to the atmosphere.

The main drawback of DBFCs is the hydrolysis of borohydride as a side reaction, producing H<sub>2</sub> affecting, therefore, the fuel utilization. However, it has been found that by altering the NaOH and NaBH<sub>4</sub> concentrations and using a supported catalyst on a conductive and high surface area support can help suppress, or even prevent, the hydrolysis reaction [19, 20].

Given the fact that these fuel cells are technically limited by electrocatalyst activity, a new more active and cost effective supported electrocatalyst is required for the direct liquid borohydride fuel cells to be brought to the commercialization stage. The focus of this dissertation is the examination of borohydride oxidation on a total of 35 mono- and bi-metallic colloidal, precious and non-precious, metals and alloys (including Ni, Zr, Cu, Ag, Au, Pt, Pd, Ir, and Os) supported on Vulcan XC72R carbon black, in order to find more active electrocatalysts than that previously and/or currently investigated catalysts as anode electrocatalysts for DBFC such as NiB<sub>2</sub>-, Pt- and Pd-plated on Ni (1965); Au-Pt deposited on C-cloth (1999); AB<sub>2</sub> powder (2003); and supported and unsupported Pt on carbon (2004).

Following a cyclic voltammetry (CV) examination of all 35 electrocatalysts, 23 were chosen for further study based on their peak potentials: a higher peak current and more negative oxidation peak potentials are required for fuel cell applications. In general, the electrocatalysts that exhibited attractive oxidation peak potentials were based on

precious (noble) metals, although some precious metal/non-precious metal alloys showed a more attractive oxidation peak current/potential behaviour than some precious metals. The 23 electrocatalysts chosen for further study included Os-, Pt-, Au-, Pd-, and Ir-group materials.

In order to better compare these electrocatalysts for potential fuel cell applications, their electrochemical activity toward the oxidation of borohydride was characterized using chronoamperometry, chronopotentiometry, chronocoulometry, rotating disc electrode (RDE). Based on the RDE results, 9 out of 23 electrocatalysts were chosen for fuel cell station tests.

### 1.3. References

1. R. Anthony Mang, Hydrogen: Energy, Fuel Cell and Hydrogen Technologies Go Global, The Globe and Mail Newspaper, Sep. 24 (2004) B9.
2. G. J. Aubrecht II, Energy, Prentice Hall, NY (1995) 180-208.
3. C. H. Hamann, A. Hammentt, W. Vielstich, Electrochemistry, Wiley-VCH, NY (1999) 376.
4. B. D. McNicol, D. A. J Rand. Power Sources for Electrical Vehicles, Elsevier, NY (1984) 807-838.
5. A. S. Arico, S. Srinivasan, V. Antonucci, Fuel Cells, 1(2) (2001) 133-161.
6. L. Carrette. K. A. Friedrich. U. Stimming, Chemphyschem, 1(2000) 163-193.
7. C. Lamy, A. Lima, V. LeRhun, F. Delime, C. Coutanceau, J. Leger, J. Power Sources, 105 (2002) 283-296.
8. M. R. Anrew, W. J. Gressler, J. K. Johnson, R.T. Short, K. R. Williams, J. Appl. Electrochem. 2 (1972) 327.
9. S. G. Meibuhr, J. Electrochem. Soc., 121 (1974) 1264.
10. K. Tamura, T. Kahara, J. Electrochem. Soc., 123 (1976) 776.
11. K. Ymada, K. Yasuda, H. Tanaka, Y. Miyazaki, T. Kobayashi, J. Power Sources, 122 (2003) 132-137.
12. K. Ymada, , K. Asazawa, K. Yasuda, T. Ioroi, H. Tanaka, Y. Miyazaki, T. Kobayashi, J. Power Sources, 115 (2003) 236-242.
13. K. Ymada, , K. Yasuda, N. Fujiwara, Z. Siroma, H. Tanaka, Y. Miyazaki, T. Kobayashi, J. Power Sources, 115 (2003) 236-242.
14. M. E. Indig, R. N. Snyder, J. Elec. Soc., 109 (1962) 1104-1106.
15. R. Jasinski, Electrochemical Tech., 391-20 (1965) 40-43.
16. S. C. Amendola, P. Onnerud, M. T. Kelly, P. J. Petillo, S. L. Shap-Goldman, M. Binder, J. Power Sources, 84 (1999) 130-133.
17. B. Liu, Z. P. Li, S. Suda, J. Electrochem, Soc., 150 (30) (2003) A398-A402.
18. Z. P. Li, B. H. Liu, K. Arai, S. Suda, J. Electrochem. Soc., 150(7) (2003) A868-A872.
19. Z. P. Li, B. H. Liu, K. Arai, K. Asaba, S. Suda, J. Power Sources, 126 (2004) 28-33.

20. B. Liu, Z. P. Li, S. Suda, *Electrochimica Acta*, 49 (19) (2004) 3097-3105.
21. E. Gyenge, *Electrochimica Acta*, 49 (2004) 965-978.
22. J. Kim, H. Kim, Y. Kang, M. Song, S. Rajendran, S. Han, D. Jung, J. Lee, J. *Electrochem. Soc.*, 151 (7) (2004) A1038-A1043.
23. S. Suda et al., *Material Stage*, Oct. 10, 1 (7) (2001) 14-17,  
([www.kucel.hydrogen.co.jp/1-6](http://www.kucel.hydrogen.co.jp/1-6)).
24. C. Rice, S. Ha, R. I. Masel, P. Waszczuk, A. Wieckowski, T. Barnard, *J. Power Sources*, 111 (2002) 83-89.

## CHAPTER 2

### LITERATURE SURVEY

#### 2.1. Fuel Cell Technology

Sir William Grove, a British lawyer turned scientist, is considered to be the father of the fuel cell. During his water electrolysis experiments in 1839, he suggested, that electricity can be produced by reversing the electrolysis process [1], Fig. 2.1.1.

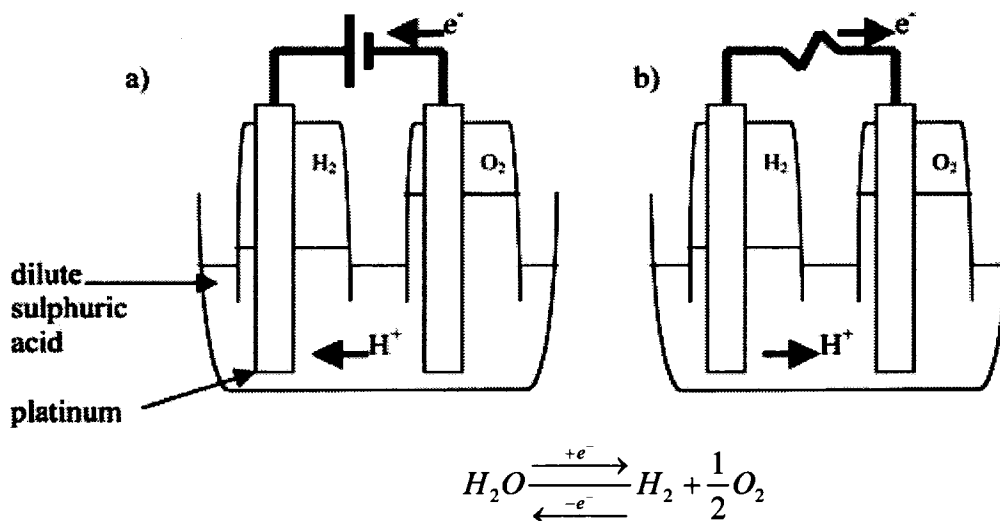


Fig.2.1.1a) Grove's water electrolysis experiment; b) Grove's fuel cell demonstration [2].

Mond and Langer, almost fifty years later in 1889, were the first to make a practical fuel cell. Their failure in obtaining a good performance level (only 3.5 mA cm<sup>-2</sup> at 0.73 V) was ascribed to a shortage in knowledge of electrode kinetics and materials availability [3]. The electrochemical approach of producing electricity was set aside because of the discovery of the oil and the invention of the internal combustion engine. Sir Francis Bacon in 1959 was the first to make a successful fuel cell, where he demonstrated 5-kilowatt and 6-kilowatt fuel cells which were licensed for space applications and powered a welding machine [3].

The new modern of fuel cells is said to have begun between 1960 and 1965, after the NASA Apollo space program started using the alkaline fuel cell [1]. Then, researchers started looking for applications other than space vehicles. Kordesch was the

first to build an alkaline fuel cell car in the 1970s [4]. Nowadays, fuel cell technology is being applied to all aspects of energy generation.

### 2.1.1. Principle of Operation

A fuel cell is an electrochemical device that converts the chemical energy of a fuel directly into electricity without any intermediate thermal or mechanical processes. In contrast, in the internal combustion engine, the combustion of the reactants releases energy in form of heat which can be used to produce electricity [5]. A schematic representation of a fuel cell is shown in Fig.2.1.2.

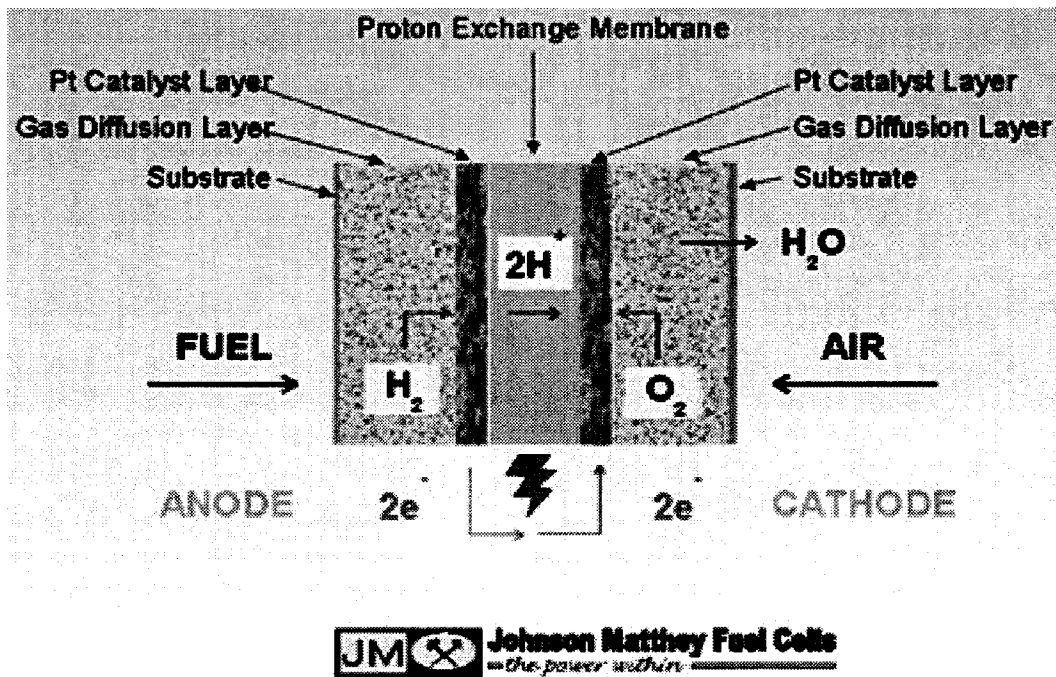


Fig.2.1.2. Schematic diagram of fuel cell [6].

Figure 2.1.2 shows that a fuel cell consists of end plates that contain the fuel and oxidant flow-fields, and the MEA that consists of a cation or anion conductive membrane, as well as anode and cathode catalyst layers, which are backed by a conductive substrate (usually carbon cloth) that acts as a diffusion layer as well as an electron conductor.

## 2.2. Fuel Cell Performance

### 2.2.1. Ideal and Actual performance

Gibbs Free Energy for an electrochemical reaction can be used to predict the reversible cell voltage [5].

$$\Delta G = - nFE_e \quad (2.2.1)$$

Due to the cell polarization ( $\eta$ ), or losses, the actual cell voltage is always less than the equilibrium potential,  $E_e$ . The known types of cell polarization are; ohmic polarization ( $\eta_{ohm}$ ), activation polarization ( $\eta_{act}$ ), and concentration polarization ( $\eta_{conc.}$ ). Other losses include reactant crossover and internal current losses [7], Fig. 2.2.1.

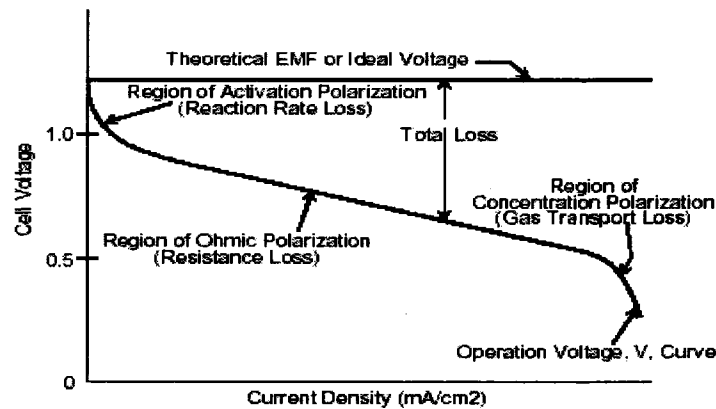


Fig.2.2.1. Ideal and actual fuel cell voltage vs. current [5].

#### 2.2.1.1. Activation Polarization

The sluggishness of the electrochemical reaction is considered an intrinsic property of the electrodes. Thus, an extra voltage drop is required for the electrochemical reaction to proceed and cause a current to flow. This voltage is called the activation overpotential ( $\eta_{act}$ ) and is expressed as [5]:

$$\eta_{act} = \frac{RT}{\alpha nF} \ln \frac{i}{i_o} \quad (2.2.2)$$

where  $\alpha$  is the electron transfer coefficient of the reaction at the electrode being addressed,  $i_o$  is the exchange current density,  $n$  is the number of electrons transferred, and  $F$  is the Faraday constant.

### 2.2.1.2. Ohmic Polarization

Ohmic polarization is attributed to the resistance both to the electron transfer through the cell materials including the electrode, and to the ion transfer through the electrolyte. The ohmic overpotential can be calculated as follow [5]:

$$\eta_{ohm} = iR \quad (2.2.3)$$

Where  $i$  is the current density and  $R$  is the total cell resistance (electronic, ionic, and contact resistance).

### 2.2.1.3. Concentration Polarization

A concentration gradient formed due to the depletion of the fuel at the electrode causes this kind of polarization. This type of loss can be determined using the following equation [5]:

$$\eta_{conc} = \frac{RT}{\alpha nF} \ln \left( 1 - \frac{i}{i_L} \right) \quad (2.2.4)$$

where  $i_L$  is the limiting current density.

### 2.3.1.4. Reactant crossover and internal current losses

Fuel crossover is one of the major drawbacks of most Polymer Exchange Membrane Fuel Cell (PEMFC) systems. Fuel migration through the electrolyte to the cathode can cause a decrease in the cathode performance, and thus, to a loss in overall fuel cell efficiency [7].

## 2.3. Overall Cell Voltage

The actual cell voltage is given by the formula,

$$E_{cell} = \Delta E_e - \sum \eta, \text{ where } \sum \eta = |\eta_c| - |\eta_a| - iR, \text{ and } \Delta E_e = E_{c,e} - E_{a,e} \quad (2.3.1)$$

Equation (2.3.1) shows that as the current flows in a fuel cell, the cell voltage decreases due to electrode and ohmic polarization, Fig.2.3.1.



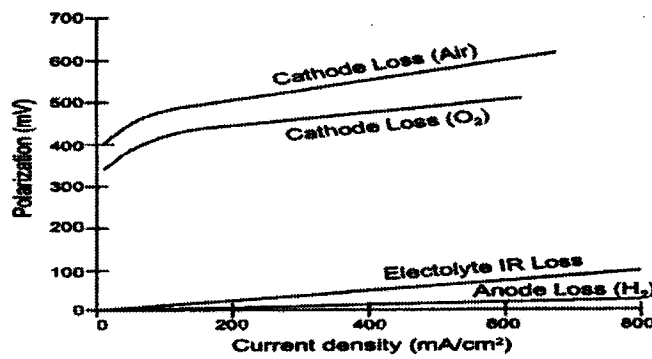


Fig.2.3.1. The anodic and cathodic polarization in a hydrogen fuel cell [5].

Researchers are attempting to minimize these losses by improving the electrocatalysts, the membrane, the electrode structure, and other fuel cell components [5].

In order to meet fuel cell application requirements, the operating conditions (e.g., temperature, pressure, fuel composition, reactant utilization, current density, etc., in addition to fuel cell power) have to be optimized, because they have a significant impact on performance. Therefore, it is important for designers to know the required cell voltage and current density, to ensure a better design. As an example, for automotive applications where a high current density output is required, a small volume, light weight, lower voltage fuel cell is preferred. Fig. 2.3.2 shows how a fuel cell can be operated economically by optimizing its efficiency and operating costs according to the specified current density and voltage [7].

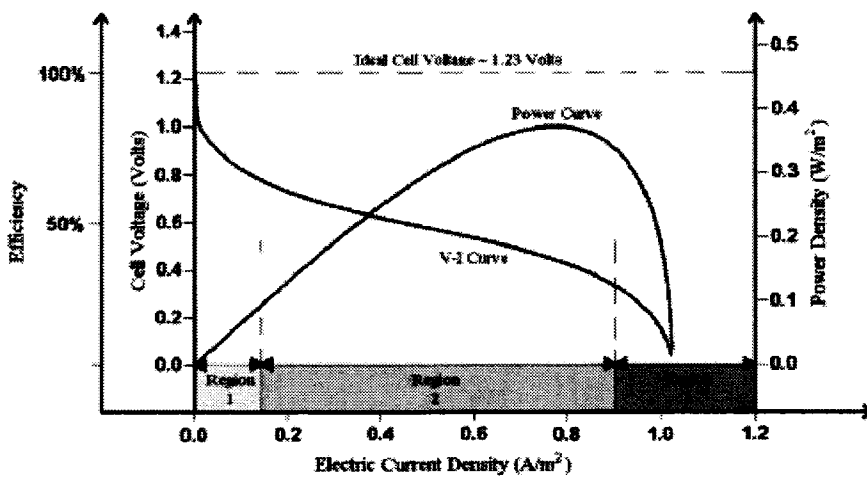


Fig.2.3.2. Relationship between the power density and cell voltage. Region 1: Activation, Region 2: ohmic, and Region 3: concretion polarization [7].

## 2.4. Fuel Cell Efficiency

Because the heat input is equal to the change in enthalpy for the reaction, i.e.,  $Q_{in} = -\Delta H$ , the electrochemical efficiency is defined as the ratio of the available Gibbs free energy of the reaction to the change in stored chemical energy, i.e., for an irreversible reaction, the ideal efficiency ( $\zeta$ ) is given by [8, 9]

$$\zeta = \frac{\Delta G_R}{\Delta H_R} \quad (2.4.1)$$

where  $\Delta G_R$  and  $\Delta H_R$  are the Gibbs free energy and enthalpy of reaction, respectively.

Therefore, eq. 2.4.1 can be rewritten as follows [4];

$$\zeta_p = \frac{nFE_{cell}}{\Delta H_R}, \text{ where } \zeta_p \text{ is the practical efficiency} \quad (2.4.2)$$

The electrochemical efficiency ( $\zeta_{el}$ ) can also be expressed as a voltage efficiency [4].

$$\zeta_{el} = \frac{E}{E^o} \quad (2.4.3)$$

## 2.5. Fuel Cells vs. Heat Engine

More than a century ago, power plant efficiencies ranged between 2 to 3%, while efficiencies of today's plants range between 35 to 40% [1]. Fig. 2.5.1 compares the fuel cell, where there is no intermediate heat process, and the internal combustion engine (ICE). Fig. 2.5.2 compares the efficiencies of fuel cells and other conventional systems [10].

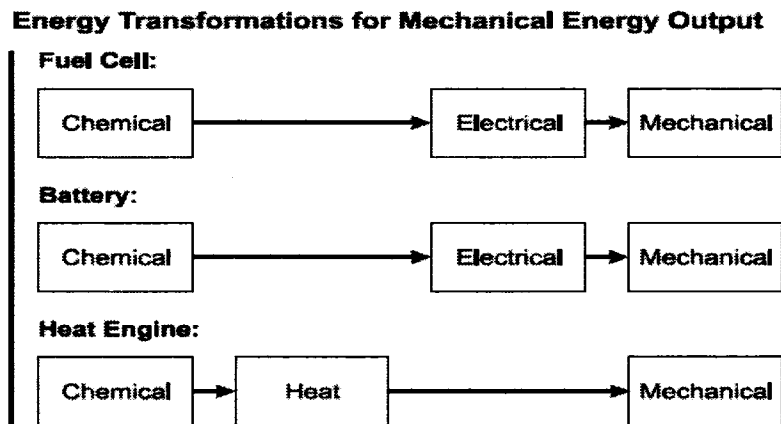


Fig.2.5.1. Comparison of the processes involved in an ICE and a fuel cell [10].

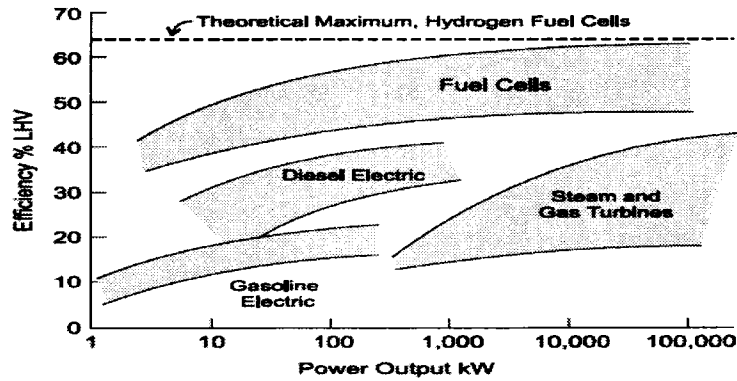


Fig. 2.5.2. Comparison of the efficiency and power output of fuel cells and IC engines [10].

## 2.6. Fuel Cell Types

Fuel cells are typically classified according to the type of electrolyte employed. The electrolyte determines the operating temperature range, the catalysts to be used, and the electrochemical reactions that occur in the fuel cell. Table 2.6.1 shows the reactants and products, and the operating conditions of the well known types of fuel cell (adapted from Ref. [11] with the addition of DBFC data).

Table 2.6.1. Characteristics of major types of fuel cells (adapted from Ref. [11] with the addition of DBFC data).

Characteristic	Type of Fuel Cell						
	PEMFC	DMFC	DBFC	AFC	PAFC	MCFC	SOFC
Electrolyte	Proton Exchange Membrane	Proton Exchange Membrane	Proton Exchange Membrane	KOH	Phosphoric Acid	Molten Carbonate	Solid Oxide
Operating Temperature	50-90 °C	50 to < 130 °C	50 to 100 °C	50-250 °C	180-200 °C	650 °C	750-1050 °C
Charge Carrier	H <sup>+</sup>	H <sup>+</sup>	Na <sup>+</sup>	OH <sup>-</sup>	H <sup>+</sup>	CO <sup>3-</sup>	O <sup>2-</sup>
Electrocatalysts	Pt	Pt	Zr-Ni, Pt, Pt-Au	Pt, Ni/NiO <sub>x</sub>	Pt	Ni/LiNiO <sub>x</sub>	Ni/Perovskites
Fuel	H <sub>2</sub>	CH <sub>3</sub> OH	NaBH <sub>4</sub>	H <sub>2</sub>	H <sub>2</sub>	H <sub>2</sub> & CO	H <sub>2</sub> & CO
Poisoning	CO > 10 ppm	Adsorbed Intermediates	No poisoning, but H <sub>2</sub> evolution	CO, CO <sub>2</sub>	CO > 1%, H <sub>2</sub> S > 0.5 ppm	H <sub>2</sub> S > 0.5 ppm	H <sub>2</sub> S > 1 ppm
Applications	Portable, Transportation	Portable, Transportation	Portable, Transportation	Space	Power Generation, Transportation	Power Generation /Cogeneration	Power Generation/ Cogeneration

### 2.6.1. Proton Exchange Membrane Fuel Cells (PEMFC)

Considered as low temperature fuel cells (Fig. 2.6.1), PEMFCs operate in a temperature range between room temperature and 100 °C. In comparison to other fuel cells PEMs deliver a high power density (Fig. 2.6.2). Therefore they can offer both low volume and weight [5].

PEMFC is named after the proton-exchange polymer membrane (PEM) electrolyte that is used. General Electric invented this technology in the early 1960s for use in space programs of NASA. Today, the automotive industry is demonstrating PEM type fuel cells in prototype cars. General Electric's Plug Power has been using PEM fuel cell to supply electricity for small size houses since 1988. The Nafion membrane (Fig. 2.6.3), produced by Du Pont, is being widely used as an electrolyte in PEMFCs, because it has a high conductivity and low equivalent weight (g/equivalent, i.e., the amount of a polymer equal in grams to its equivalent weight). Colloidal platinum and platinum alloys, supported on carbon black, are being used as both cathode and anode electrocatalysts [12].

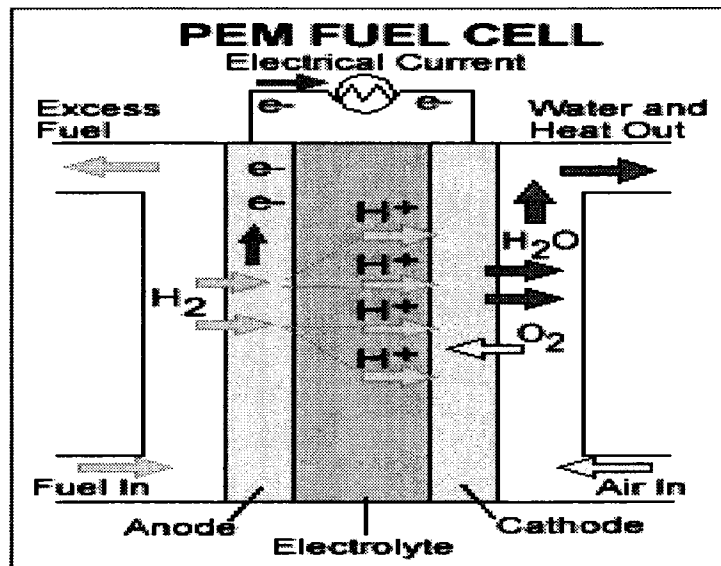


Fig.2.6.1. A schematic illustration of polymer electrolyte fuel cell [13].

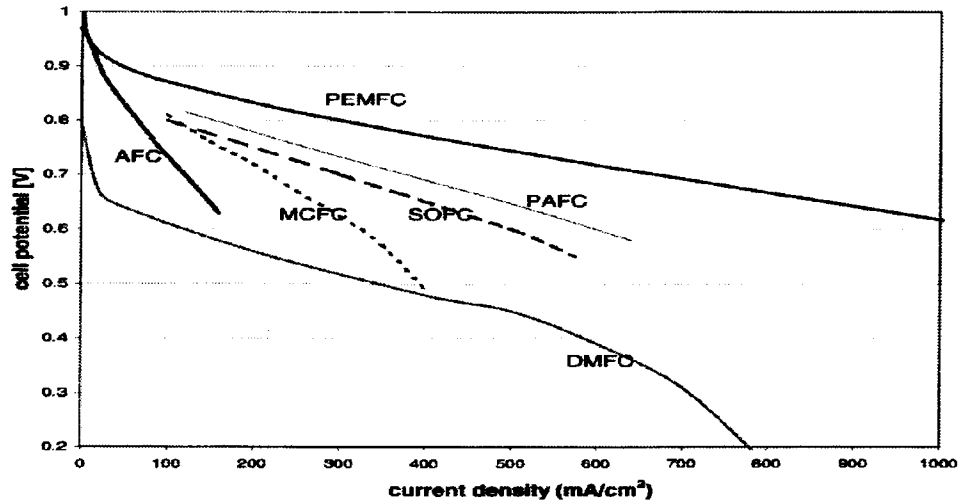


Fig. 2.6.2. Typical cell potential vs. current density plot for major types of fuel cells [11].

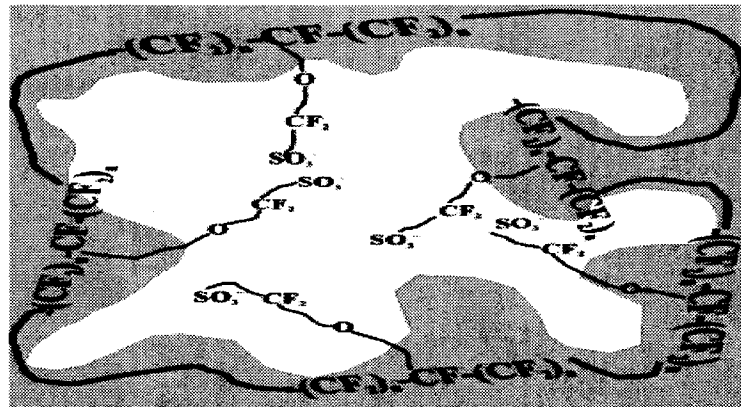


Fig.2.6.3. Nafion structure: white zone is the sulphate ions which transport  $H^+$  [1].

### 2.6.2. Alkaline Fuel Cells (AFC)

AFC operating temperature is between 50-250°C. The enhancement of its efficiency compared to acidic electrolyte fuel cells is attributed to the kinetically faster oxygen reduction in an alkaline electrolyte. This type of fuel cell was used by NASA in the 1960s in the Apollo space program.

Supported platinum is being used as the anode and cathode electrocatalysts; non-noble metals, Ni and Ag have also been used. Carbonation is the main drawback in AFCs. It is caused by  $CO_2$ , which originally exists in the air or forms during the fuel oxidation reactions [14]. This drawback can be partially solved by circulating the electrolyte to avoid the build up of carbonates [1].

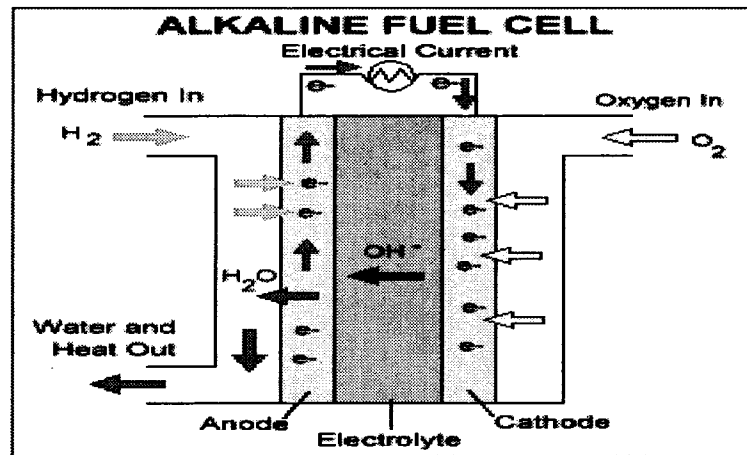


Fig.2.6.4. A schematic illustration of the alkaline fuel cell [13].

### 2.6.3. Phosphoric Acid Fuel Cells (PAFC)

The PAFC-type fuel cell is shown schematically in Fig.2.6.5. It operates at a medium temperature range between 150 and 200 °C, which gives this type of fuel cell enhanced performance, because the reaction rate is highly affected by the temperature according to Arrhenius equation [1]. Platinum-based electrocatalysts are being used in PAFCs for both the anode and the cathode electrodes [15]. Today, PAFCs with capacities over 75 MW are being used worldwide as stationary power plants [16].

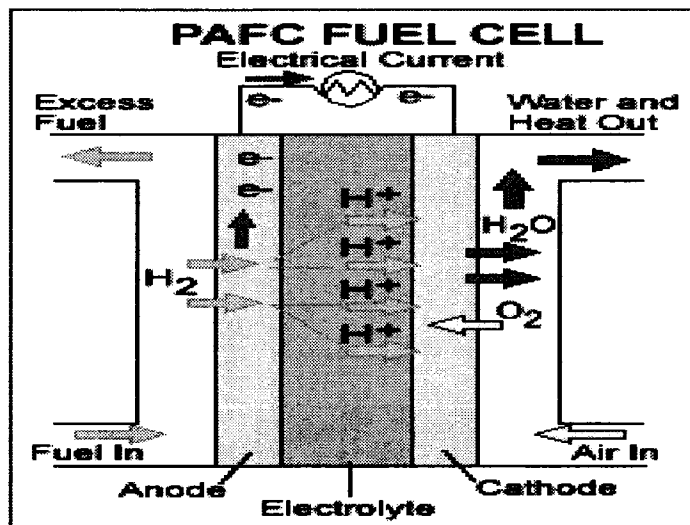


Fig.2.6.5. A schematic illustration of phosphoric acid fuel cell [13].

#### 2.6.4. Molten Carbonate Fuel Cells (MCFC)

The idea of using coal directly to produce electricity from a fuel cell was behind the invention of the MCFC, Fig.2.6.6, in the 1960s. Natural gas, rather than coal, is being used today to enhance the MCFC efficiency. Under high temperature (around 650°C) operating conditions, the hydrocarbons can be internally reformed [5].  $\text{Li}_2\text{CO}_3/\text{Na}_2\text{CO}_3$  materials stabilized in an alumina-based matrix are widely used today as the electrolyte. Ni is used as an anode electrocatalyst. Al and Cr are being added to the Ni anode electrocatalyst to enhance its corrosion resistance. Lithiated NiO materials also have been used as cathode electrocatalysts [5, 1].

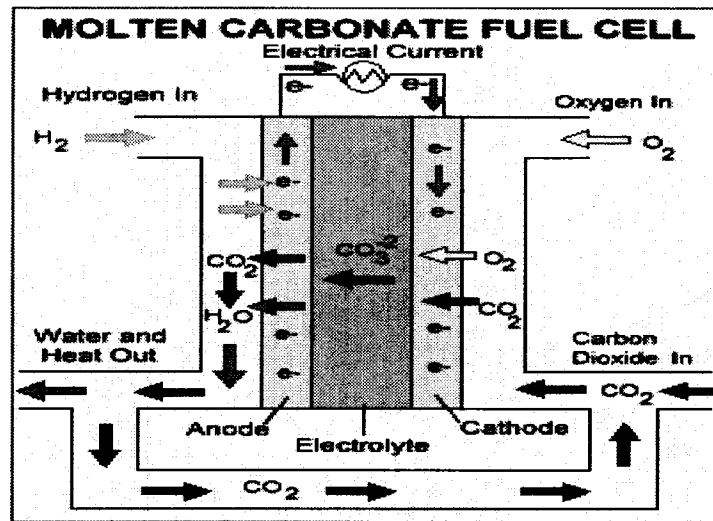


Fig.2.6.6. A schematic illustration of the molten carbonate fuel cell [13].

#### 2.6.5. Solid Oxide Fuel Cells (SOFC)

This high temperature fuel cell (Fig.2.6.7) operates at around 750-1050°C, which facilitates the ionic conductivity of the ceramic material and the internal reforming of hydrocarbon fuels. It uses a ceramic solid-phase electrolyte such as yttria stabilized zirconia ( $\text{Y}_2\text{O}_3\text{-ZrO}_2$ ). Ruthenium supported on either  $\text{TiO}_2$  or  $\text{LaCrO}_3$  has been found to be the best anode electrocatalyst, while doped lanthanum manganite ( $\text{LaMnO}_3$ ) is being used as a cathode electrocatalyst [5].

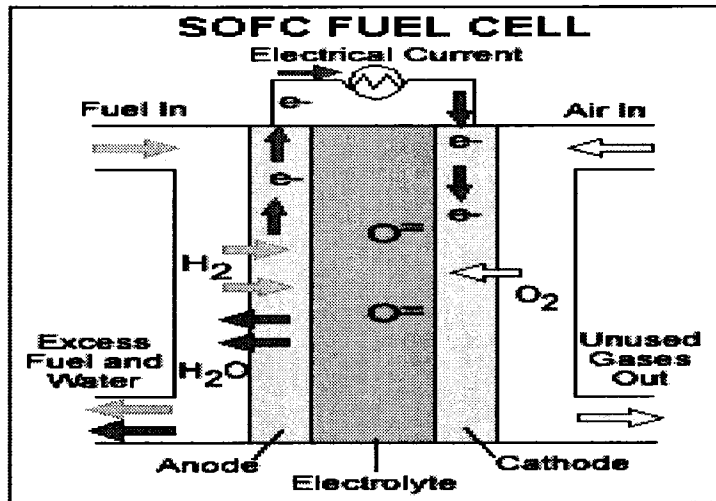


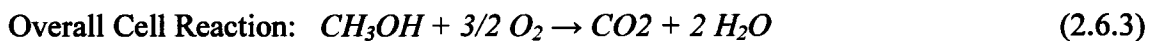
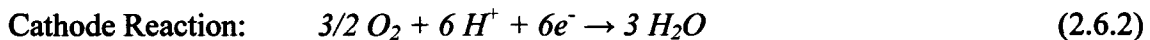
Fig. 2.6.7. A schematic illustration of the solid oxide fuel cell [13].

## 2.6.6. PEM-Based Direct Liquid Fuel Cells

### 2.6.6.1. Direct Methanol Fuel Cells (DMFC)

The DMFC (Fig.2.6.8) operates between room temperature and 100°C; methanol is fed directly into the fuel cell. Poor anode electrocatalyst activity and methanol cross-over from the anode to the cathode are the major drawbacks facing the development of DMFCs. Thus, Pt-Ru supported on carbon has been found to be the most active anode electrocatalyst, while supported platinum is widely used for the cathode electrocatalyst [17]. In addition to minimizing fuel cross-over, solving the poisoning problem resulting from CO formation is the key for developing this type of fuel cell, [17].

Reactions:





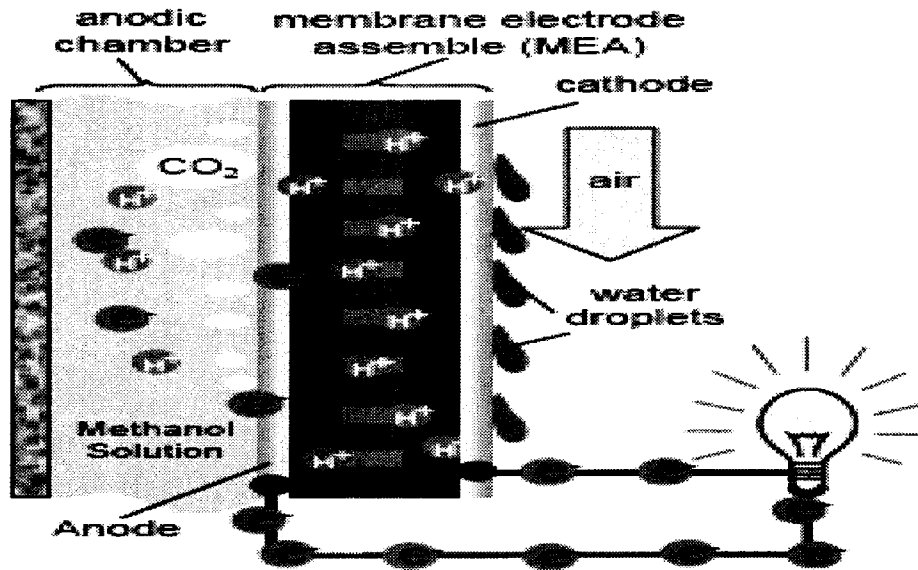
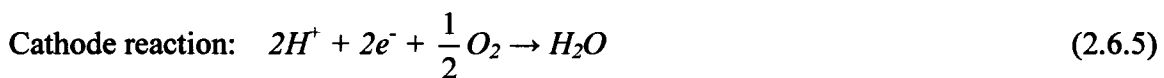
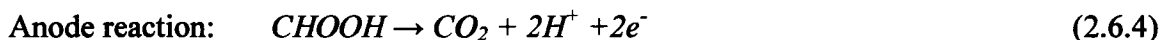


Fig. 2.6.8. A schematic illustration of direct methanol fuel cell [18].

#### 2.6.6.2. Direct Formic Acid Fuel Cells (DFAFC)

This relatively new direct liquid fuel cell is presently under development for use in portable applications [19-23]. Schematically, it can be illustrated using the same diagram as for DMFC (Fig. 2.6.8). It has some common features with DMFCs in that it suffers from formic acid cross over as well as the poisoning problem resulting from CO formation. The only advantage in using formic acid as a fuel is its better theoretical electromotive force (EMF) compared to hydrogen and DMFC [20, 21]. Reactions:



The reaction mechanisms on a platinum surface are as follows [20, 21]:



Palladium and its alloys seem to be the most active as anode electrocatalysts [19, 20, 23]. Several studies have been carried out by Masel *et al.* in order to optimize palladium and palladium alloys for use in formic acid electro-oxidation [19, 20, 23].

### 2.6.6.3. Direct Borohydride Fuel Cells (DBFC)

The direct borohydride fuel cells, Fig.2.6.9, were first proposed in the early 1960s [24]. The open circuit voltage of the borohydride-air fuel cell is  $1.64\text{ V}$ . With hydrogen peroxide as the source of oxygen on the cathode side, it is possible to obtain a theoretical voltage of  $2.25\text{ V}$  [25]. The reactions in fuel cells using borohydride and oxygen are given in equations 2.6.10, 2.6.11, and 2.6.12 [26]. Catalysts for oxygen reduction for DBFCs are same as those being used for the PEMs and DMFCs [27, 28]. The development of a more active anode catalyst is still ongoing.

#### Reactions

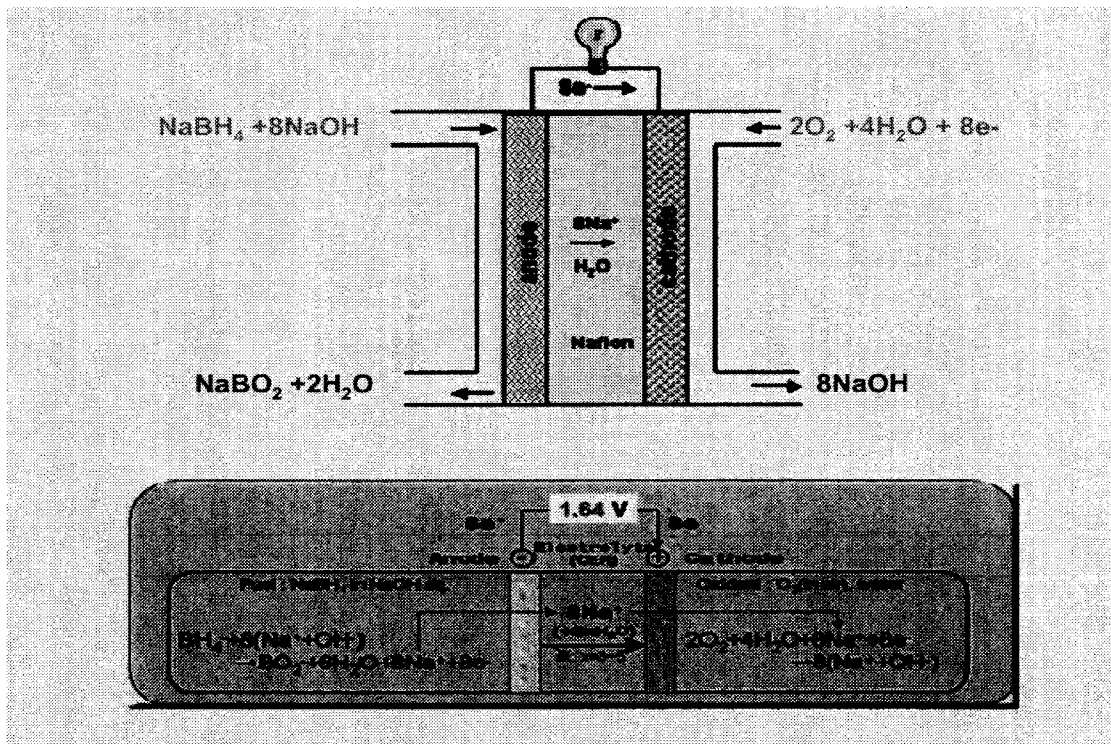
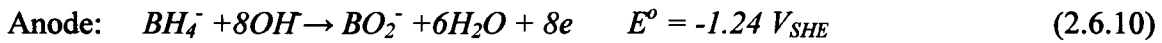


Fig. 2.6.9. A schematic illustration of direct borohydride fuel cell [29].

## 2.7. Fuel Cell Systems

A single cell delivers insufficient voltage for most applications. Accordingly, cells must be combined in a series to form a stack (Fig.2.7.1) in order to deliver the required voltage. These stacks are assembled into modules in conjunction with the auxiliary equipment. Auxiliary equipment includes fuel processing, power conditioning, heat recovery, heating or cooling, etc., and the required control system, to fit the desired application (Fig.2.7.2).

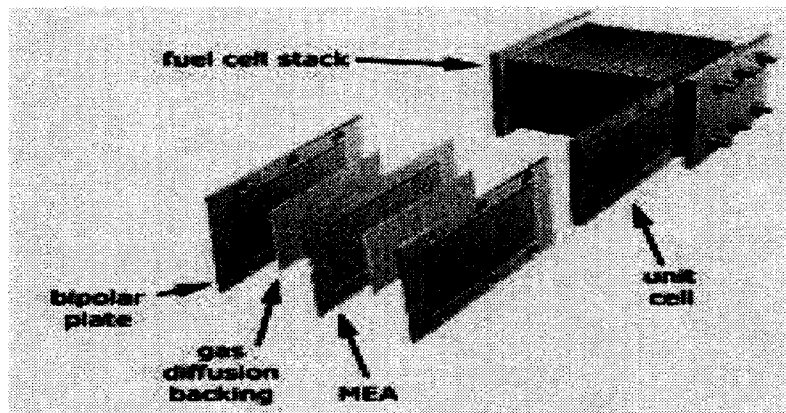


Fig.2.7.1. Expanded view of PEM Fuel Cell Stack [30].

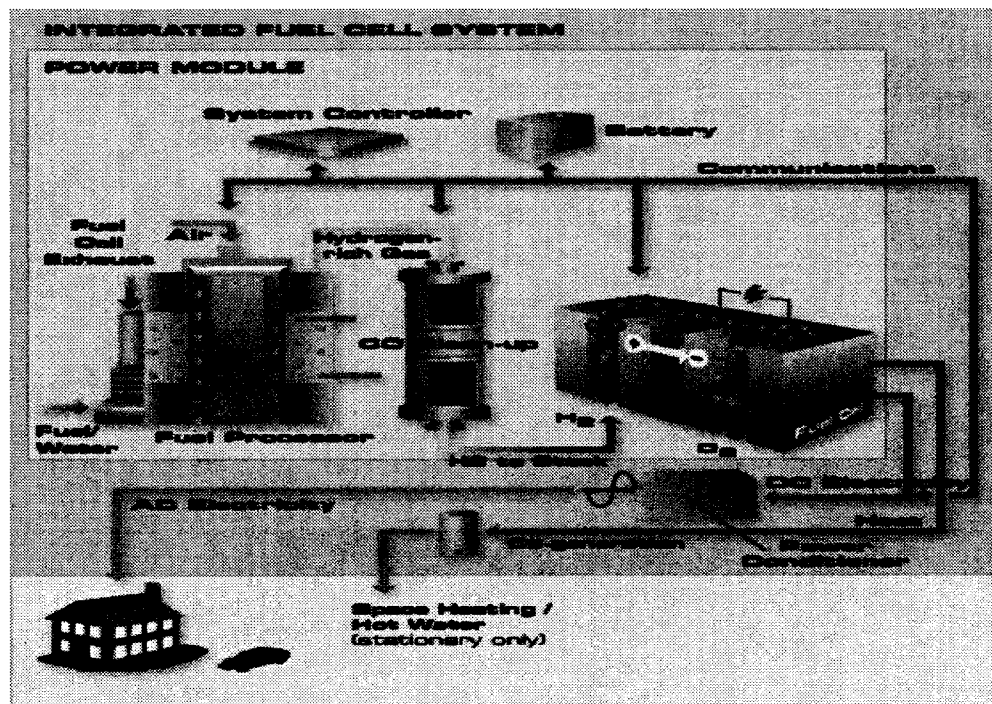


Fig.2.7.2. FC integrated system [31].

## 2.8. Fuel Cell Applications

The target applications for low temperature fuel cells include transport, portable and remote (small scale) power plant applications. Large scale power plants are the target applications for high temperature fuel cells [4, 5].

## 2.9. Heterogeneous Catalysis

The substance that initiates a reaction, without itself being consumed, is called a catalyst, as defined by Berzelius in 1836 [32]. The main reason behind using a catalyst is to enhance the reaction rate by lowering its activation energy. In 1834, Grove [32] proved that a platinum filament was a good catalyst for the decomposition of water vapour into hydrogen and oxygen. Subsequent catalyst development has led to dramatically lower catalyst production costs. Continuing research and development in this field led to a better understanding of catalytic action and to cleaner and cheaper production processes [33]. Fig. 2.9.1 shows the chronological knowledge development in heterogeneous catalysis between 1800 and 2000, which makes it possible to relate the catalytic activity to the composition and the structure of materials [34].

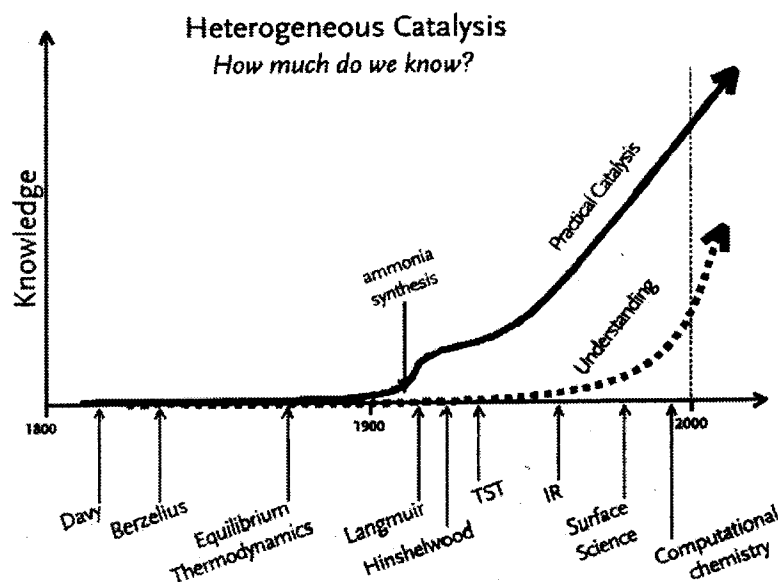


Fig. 2.9.1. Heterogeneous catalysis: knowledge development [34].

Reactions occur at the solid surfaces in heterogeneous catalysis, unlike in homogeneous catalysis where both catalysts and reactants are in the same phase. For precious metals to be used as heterogeneous catalysts, nanoparticles are supported on an inert or conductive porous structure (see Fig. 2.9.2) [34].

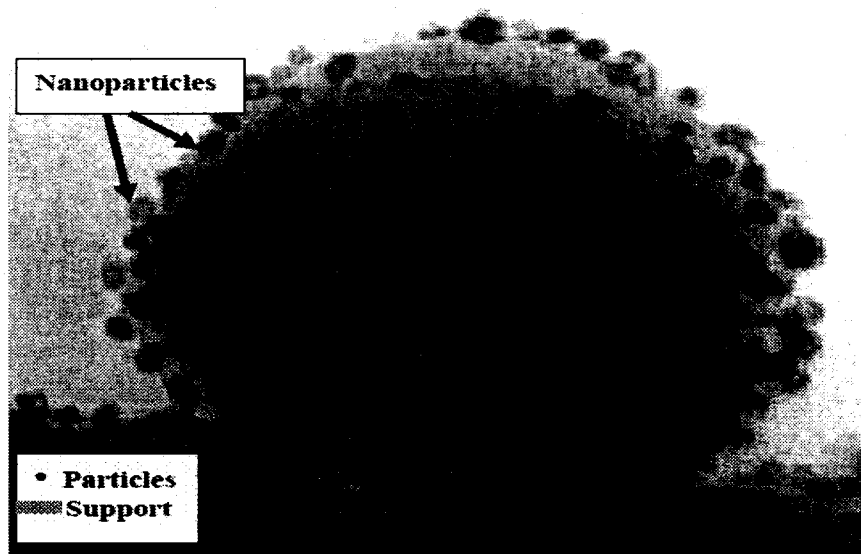


Fig. 2.9.2. A supported nanoparticle heterogeneous catalysts [34].

The use of nanoparticle materials as catalysts is still in its early stages. The basic concept of manufacturing heterogeneous metal colloid catalysts using a precursor was developed in the 1990s. Due to its importance in fuel cells and other advanced technologies, research and development in this field is ongoing worldwide [35]. A material that contains an active material, metal or metal oxide, dispersed on a high surface area, stable support, is defined as a heterogeneous catalyst [36].

Supported metals, transition metal oxides and sulfides, solid acids and bases, and immobilized enzymes are the main heterogeneous catalyst types [36]. Electrocatalysts are also considered as heterogeneous catalysts. Heterogeneous catalysts are considered as the workhorses of the chemical, petrochemical, and fuel cell industries [34].

### **2.9.1. Catalysis by Metals**

The chemical, petroleum, and petrochemical industries are widely utilizing transition metal cluster compounds, and/or supported metal catalysts, in their production processes [36].

#### **2.9.1.1. Transition Metals as Catalysts**

Transition metals are characterized by their ability to form compounds with variable oxidation states, due to the presence of *d* electrons, and unfilled *d* orbitals. These compounds are able to donate, or accept, electrons during chemical reactions. Since they chemisorb hydrogen, Co, Rh, Ir, Ni, Pd, and Pt are being used widely as catalysts for hydrogenation reactions [38].

#### **2.9.1.2. Reactions on Metals**

Six primary reactions occur on metals [36]: 1) simple molecular adsorption reactions, 2) dissociative adsorption reactions, 3) bond scission reactions, 4) addition reactions, 5) recombination reactions and, 6) desorption reactions.

The catalytic action cycle starts with adsorption, in which the molecules come into contact with the metal surface and stick, Fig. 2.9.3 [34]. In molecular adsorption there is no bond breaking; it does happen in dissociative adsorption. This step is followed by addition and recombination reactions; product desorption will be the final step in the catalytic action cycle [36].

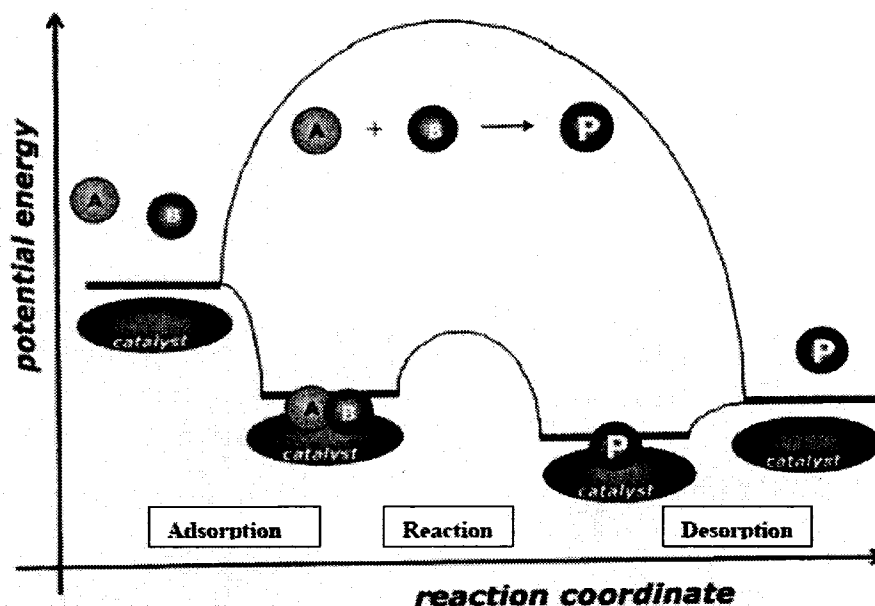


Fig. 2.9.3. Reaction cycle of a heterogeneous catalytic reaction [34].

## 2.9.2. Principles of Catalytic Action

The changing of the local environment around the reactants is the main catalyst action. Berzelius (1836) (see bibliography of Chap. 12 in [36]) proposed that the catalyst changed the rate by modifying the forces between the reactants to stimulate the reactions. Sabatier (1913) (see bibliography of Chap. 12 in [36]) suggested that the catalysts stabilized intermediates, thereby promoting a reaction. Perrin (1919) (see bibliography of Chap. 12 in [36]) suggested that catalysts were able to transfer energy into the reactants and thereby overcome the energy requirements needed to activate molecules [36].

It can be seen clearly from Fig. 2.9.3 that the catalyst can provide an alternative more complex reaction path but with a lower activation energy, and hence the catalytic reaction rate is much higher than that of uncatalyzed reaction [34]. Moreover, the catalyst cannot change the thermodynamics but the kinetics, i.e., it can accelerate the reaction at much lower temperatures and pressures, but does not affect the equilibrium. In other words, the catalysts cannot promote a reaction that is thermodynamically unfavorable [34].

### 2.9.2.1. Metal Catalytic Mechanisms

Helping initiate reactions, stabilizing the intermediates, holding the reactants in close proximity and in the right configuration to react, stretching bonds, and donating or accepting electrons are the main ways in which the metal can catalyze the reaction [36]. Fig. 2.9.4 shows the reaction mechanisms on metals; Langmuir-Hinshelwood, Riedel-Eley, and the precursor mechanism. In the first mechanism, all of the reactants are adsorbed, while, only one reactant is adsorbed in the second one, and one reactant is adsorbed strongly and the other is adsorbed weakly in the third mechanism.

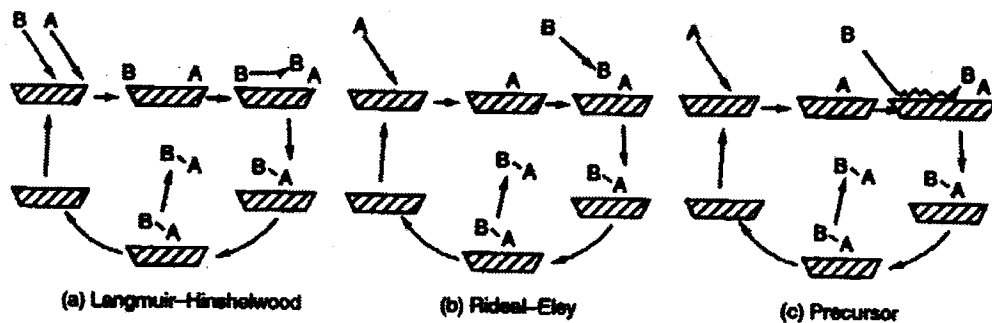


Fig.2.9.4. A schematic of (a) Langmuir-Hinshelwood, (b) Riedel-Eley, (c) Precursor mechanism for the reaction  $A+B=AB$  [36].

The most preferred adsorption sites on metals are shown in Fig. 2.9.5 [34]. They are bridge sites (long or short), and hollow sites (three or four fold in character) [34].

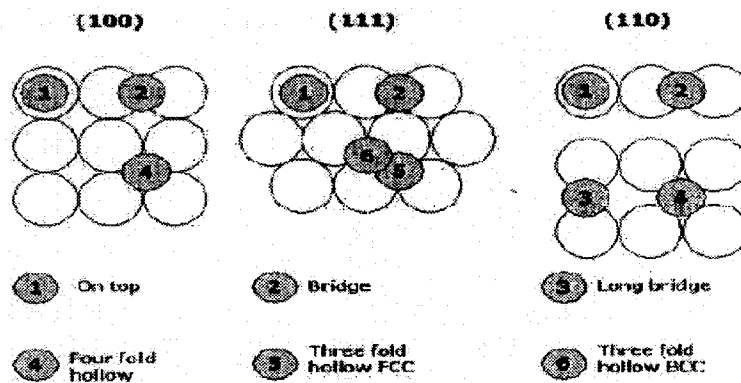


Fig.2.9.5. Adsorption site on various surfaces [34].



### 2.9.3. Electrocatalysis

Fuel cell technology as part of electrochemical energy conversion is most affected area by advances in electrocatalysis [39]. Electrocatalysis is defined as the study of how reactions can be enhanced at electrodes [40]. The term *electrocatalysis* combines two important subdisciplines of physical chemistry: electrochemistry and catalysis [39]. Advances in electrocatalysis require understanding the electron, ion, and atom transfer reactions [39]. Electrocatalysis processes involve adsorption, reaction, and desorption steps for both reactants and products at the electrode surface. During these processes, in addition to the adsorption of reactants, many bond-breaking steps occur; therefore the electrode surface acts as an electron donor or acceptor, and as a reaction site [39, 40]. The fuel oxidation and oxygen reduction at the fuel cell electrodes requires bond formation to adsorb and stabilize the reactants, intermediates, and the products. Therefore, fuel cells are restricted by the activity of the electrocatalysts used. Accordingly, more active electrocatalysts will result in better, and less costly, fuel cells [40].

The main requirements for fuel cell electrocatalysts are good electron conductivity, stability in the fuel cell environment, and good adsorption characteristics for reactants and/or intermediates. Electronic and geometric factors play an important role in electrocatalysis. The availability of vacant d-orbitals in an atomic structure produces chemisorption bonds with the adsorbable reactant species. It has been proven that, in addition to crystal orientation, crystal defects also can affect the electrocatalytic activity; these defects serve as highly energetic sites where adsorption can occur at high rates [15]. Geometric factors also play an important role when a specific orientation and close proximity distance are required for a reaction to happen [36]. The long-term goal of electrocatalysis research is the ability to design electrocatalysts for specific reactions with correct numbers and steric geometries of the adjacent sites [15].

### 2.9.3.1. Electrocatalyst Design

It has not been easy thus far, to design electrocatalysts from theoretical considerations [40]. The dependence of electrocatalysis on adsorption is the reason behind choosing the transition metals as electrocatalysts; the adsorption process is highly affected by the availability of unpaired d-electrons and unfilled d-orbitals that can form bonds, as explained in section 2.9.2.1. Additionally, the geometric arrangement of catalyst centers is important, because it affects the proximity and the configuration of the reactants [37]. The catalysts investigated in this study were chosen based on previous related studies on borohydride oxidation and fuel cell processes, and on the literature related to kinetics, heterogeneous catalysts, and electrocatalysts [8, 9, 15, 32-45].

### 2.9.3.2. Factors Affecting Electrocatalytic Properties

Factors that affect the electrocatalyst properties can be understood by examining the parameters in the formula [35]:

$$I = isw \quad (2.9.1)$$

where  $I$ , is the normalized current density ( $A\text{ cm}^{-2}$ , geometric surface area),  $i$ , is the specific current density ( $A\text{ cm}^{-2}$ , real surface area),  $s$  the specific surface area of catalyst ( $\text{cm}^2\text{ g}^{-1}$ , real surface area), and  $w$  is the catalyst load ( $\text{g cm}^{-2}$ , geometric surface area).

To design a cost effective electrocatalyst, it is important to increase  $i$  and/or  $s$  and not  $w$ . Alloying (adding atom), can enhance the  $i$  value. Dispersing the catalyst as nanoparticles over a high surface area support increases the  $s$  value. The increase in  $i$  and  $s$  will increase  $I$  accordingly [35]. Therefore, clusters and colloids are the best choice to be used as electrocatalysts [38]. Moreover, it has been proven that the particle size (particle size of 5 nm and less is highly influenced by the metal-support interaction), ad atom, and the support type can dramatically enhance the intrinsic catalytic activity [35].

#### **2.9.4. Effect of Support Type on the Catalytic Activity of Nanoparticles**

It is important to support the catalyst as nanoparticles on high specific surface area support in order to reduce the cost and to conserve the catalyst resources [35]. The catalyst supports for industrial applications are chosen on the basis of their high surface area, thermal, chemical, and mechanical properties stabilities [35]. It was claimed that, in addition to its main role in preventing recrystallization of metal particles, the support can promote specific electronic properties as well as geometrical features of the supported nanoparticles [35]. The degree of the metal-support interaction it depends on both particle size and the nature of the support [35]. Support on an insulating substrate such as  $\text{Al}_2\text{O}_3$  or  $\text{SiO}_2$  leads to a weak metal-support interaction. However, support on a semiconducting substrate such as  $\text{Nb}_2\text{O}_5$  and  $\text{TiO}_2$  leads to a strong metal-support interaction [35]. Supporting on conducting carriers like carbon black leads to a very strong metal-support interaction and this can lead to significant electronic modifications of metal nanoparticles of sizes lower than 5 nm [35]. Carbon black has been widely used as a nanoparticle catalyst support for polymer exchange membrane fuel cells. Haruta was the first to discover that supporting gold on  $\text{TiO}_2$  can highly enhanced its catalytic activity toward CO oxidation [46, 47]. This work inspired many other researchers to support noble metals on different supports rather than carbon black, e.g.,  $\text{TiO}_2$ ,  $\text{CoO}_4$ ,  $\text{Fe}_2\text{O}_3$ ,  $\text{CeO}_2$  [48-51].

#### **2.9.5. Preparation of Colloidal Nanoparticles**

Physical and chemical routes are being used to prepare metallic nanoparticles (Fig. 2.9.6). The physical methods take place with atomization of metals in a vacuum by thermal evaporation or sputtering, while in the chemical methods the precursor(s) are first converted to a metal atom(s) which then coalesce to form nanoparticles. Chemical methods are preferable over the physical methods from a mass production point of view [52]. The advantages of the chemical over the physical method are: a uniform size of bimetallic nanoparticles can be achieved; a ready and deep penetration of the bimetallic nanoparticles into the inner regions of the support (e.g., carbon powder), whereas the

physical methods generate nanoparticles which can not penetrate very far into the carbon powder; and is more difficult to get a uniform nanoparticle size [53].

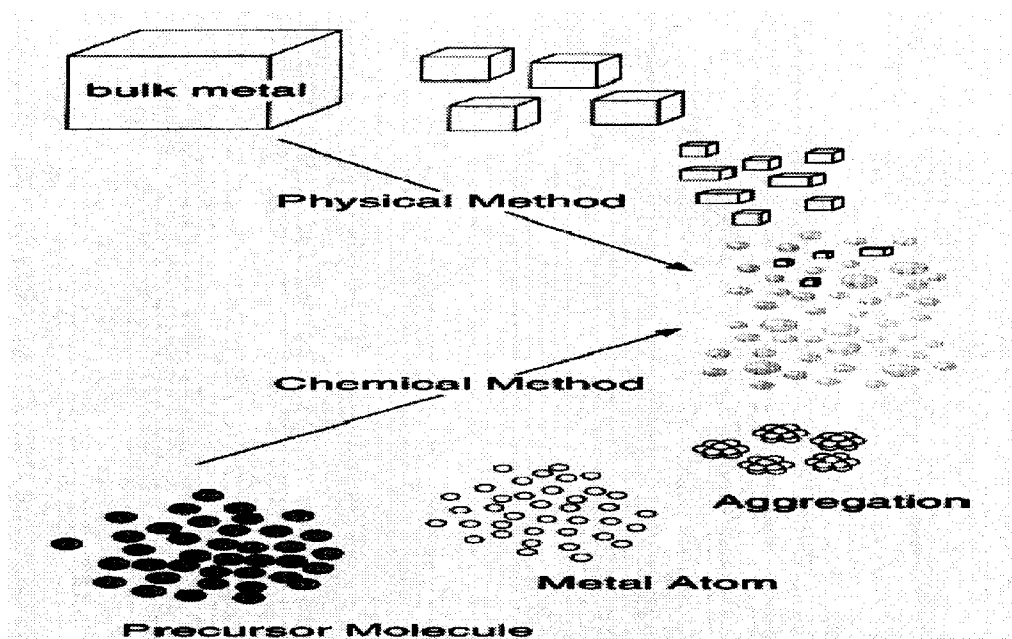


Fig.2.9.6. Schematic illustration of metallic nanoparticle preparation methods [52].

#### 2.9.5.1. Chemical Methods of preparing supported colloid metal(s)

Impregnation, colloid, and microemulsion methods are presently being used to prepare metal/alloy nanoparticles. In general, the preparation process starts with the dissolving of the metal precursor in an aqueous or organic liquid phase (Fig. 2.9.7). Then, the reaction between the precursor and the reducing agent initiates the conversion of ions of the precursor to metal atoms, which are then encapsulated by a stabilizing agent. Supporting the colloid on an amorphous high surface area porous support is the last step in the preparation process. The support significantly affects the metal dispersion and stability of the nanoparticles. Electrical conductivity, surface area, hydrophobicity, morphology, porosity, and corrosion resistance are the most important factors to be taken into account before choosing any support. Vulcan XC-72R is the most popular choice among the carbon black and activated carbon family for catalyst support [53].

The growth mechanisms are the main difference among the chemical methods. For example, the stabilizer prevents the agglomeration in the colloid method by

encapsulating the newly formed nanoparticles. The surfactant that is added in the microemulsion method controls the particle size by encapsulating the metal precursor before its reduction to a metal state, and the addition of a precursor to the microporous support before the reduction step, helps control the nanoparticle size in the impregnation method.

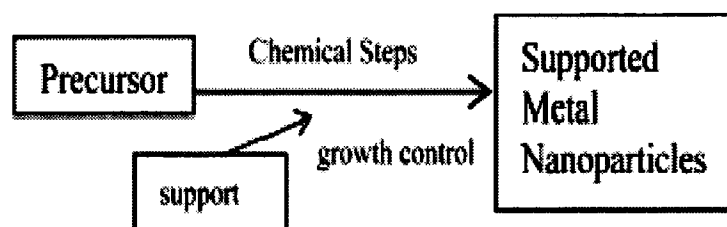


Fig.2.9.7. The main preparation steps of supported metal nanoparticles [53].

#### 2.9.5.1.1. Colloidal method

The colloidal particle size can range between 1 nm to 1  $\mu\text{m}$ . It was predicted by physicists [54] that the nanoparticle size and shape affect their electronic properties. These parameters (size, shape), have a strong impact on the catalysis processes, since the ability of the metal surface to catalyze a chemical reaction is restricted by the electron acceptance or donation processes [54].

Synthetic polymers, surfactants, and organic ligands, such as  $\text{NR}_4^+$ ,  $\text{PPh}_3$ , PVP, and PVA are the common stabilizers being used today [55]. Fig. 2.9.8 shows a schematic of the structure of a metal colloid.

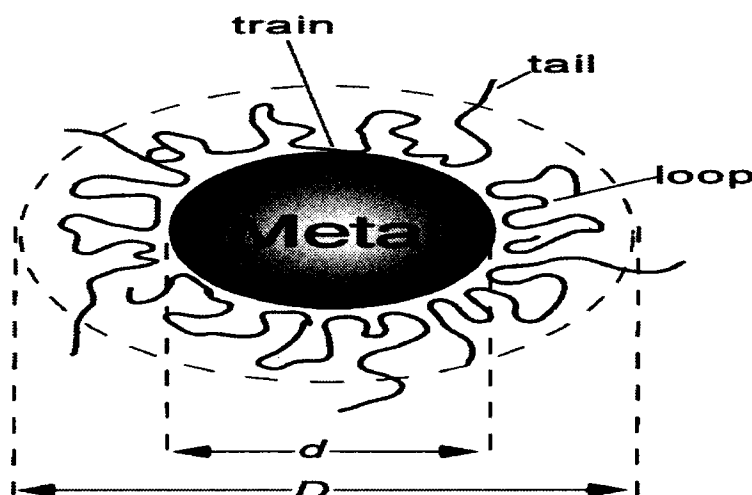


Fig.2.9.8. Structure model of polymer-protected metallic colloids [55].

The protected and unprotected colloidal methods shown in the second and third process lines of Fig. 2.9.9 are widely used today for preparing colloidal metal nanoparticles. In the case of a protective colloid, the metal precursor is reduced using a reducing agent, to form metal nanoparticles in the presence of the stabilizer agent. The stabilizer function is to achieve the distribution of colloidal metal nanoparticles by steric hindrance or by electrostatic charges. Any agglomeration into larger particles, therefore, can be prevented by the electrostatic repulsion of like charges (Fig. 2.9.10) [56].

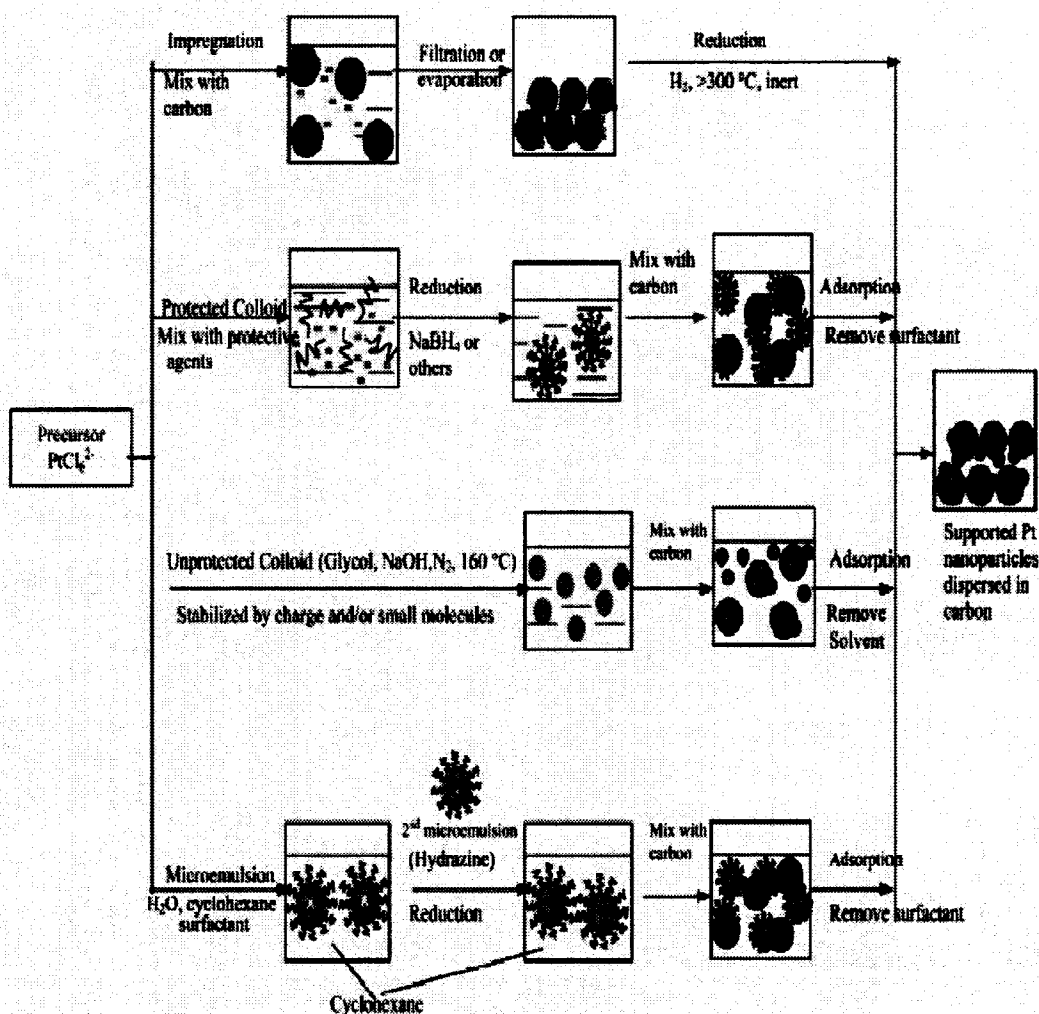


Fig. 2.9.9. Chemical methods to synthesize supported platinum nanoparticles with different size control methodologies. [53]

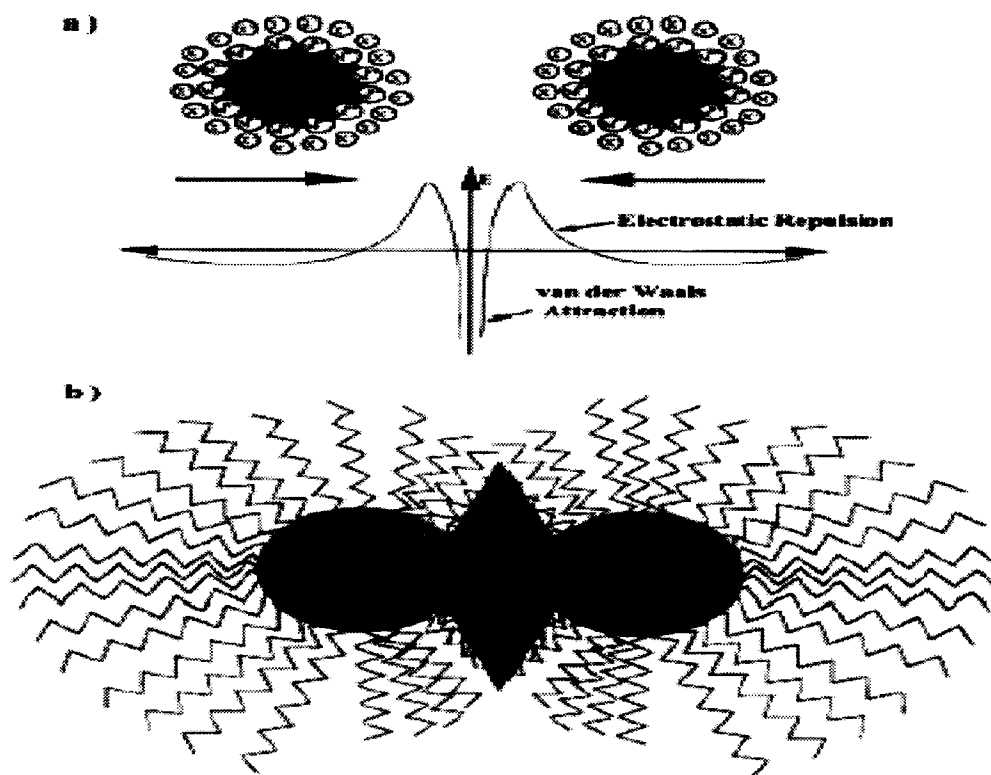


Fig. 2.9.10. a) Electrostatic stabilization of nanostructured metal colloids; b) steric stabilization of nanostructured metal colloids [56].

#### 2.9.5.1.2. *Impregnation method*

The “soaking up” of a dissolved metal precursor into the pores of a support occurs during impregnation. This method has been used for sometime for preparing electrocatalysts. The morphology of the porous substrate, the pore size distribution, and wetting of the precursor are the main factors that control the size and the distribution of particles. The method is illustrated schematically in the first process line of Fig. 2.9.9 [53].

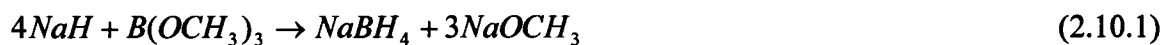
#### 2.9.5.1.3. *Microemulsion method*

The bottom process line of Fig. 2.9.9 illustrates the microemulsion method. In forming a microemulsion, a tiny drop of the precursor encapsulated by surfactant molecules is the crucial step in determining the particle size in this method. The metal precursor reduction reaction can be initiated by adding a reducing agent to a highly stirred solution for a few minutes [53].

## 2.10. Borohydride

### Overview

Sodium borohydride is a water soluble reducing agent that being used widely in organic synthesis. Reduction of carbonyls, peroxides and metal ions, as well as purification and removal of color, odor and oxidation precursors in organic chemical products are the major industrial uses. The advantages of borohydride chemistry are that it is cheap, safe in storage and use and handling, and water soluble. Moreover, sodium borohydride is derived from borax, which is abundant and widely available, and sodium borate, the fuel cell product, is a common non-toxic household item used in detergents. The world market price of sodium borohydride is \$51-\$55 per kilogram. Sodium borohydride is usually synthesized from NaH and methyl borate, which was invented by Schlesinger et al. [57].



The chemistry of sodium borohydride shows that it is a salt made up of a sodium cation,  $\text{Na}^+$ , and a borohydride anion,  $\text{BH}_4^-$ . Boron electronegativity is less than that of hydrogen, therefore, the  $\text{B-H}$  bond is polarized with boron positive and hydrogen negative. Thus,  $\text{NaBH}_4$ , and mainly the  $\text{B-H}$  bond, serves as a good source of hydride ions ( $\text{H}^-$ ), as illustrated in Fig. 2.10.1 [58].

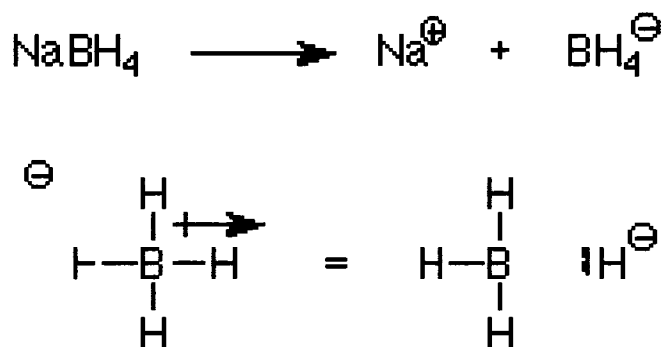


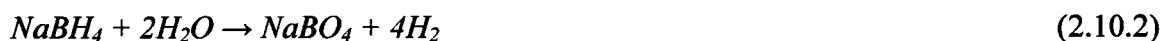
Fig. 2.10.1 Shows how  $\text{B-H}$  bond serves as a source of  $\text{H}^-$  [58].

The above figure illustrates why the complete oxidation of  $\text{NaBH}_4$  gives eight electrons, since the hydride ion,  $\text{H}^-$ , contains two electrons per proton, and upon converting this ion to a proton it will release two electrons [26].



### 2.10.1. Borohydride Hydrolysis

Hydrolysis is the evolution of the hydrogen according to the following reaction [59]:



Sodium borohydride is a powerful reducing agent in aqueous solutions, and liberates hydrogen. Hydrogen evolution greatly affects the reduction processes, and this has led to extensive studies on its hydrolysis using different electrode surfaces.

Schlesinger et al., [59-62], have conducted extensive studies of the hydrolysis of sodium borohydride. Various organic acids (benzoic, phthalic, maleic acids, etc.), metal salts (iron, cobalt, nickel) were used as reaction accelerators. They found that temperature, pH, and the nature of the catalyst have significant effects on the rate of hydrogen evolution.

Pecsok [63] studied the effect of the *pH* on the hydrolysis of sodium borohydride polarographically. The  $\text{NaBH}_4$  concentration was 0.001 M in 0.1 M KOH concentrations ( $pH = 7.7-9.5$ ), and the temperature range of 288-308 K. His main finding was that the hydrolysis of sodium borohydride is a function of *pH*.

Levy et al., [64] studied the hydrolysis kinetics at different temperatures,  $\text{NaBH}_4$  concentrations, and with different cobalt (II) chloride concentrations as a catalyst. The  $\text{NaBH}_4$  concentration was 0.13-0.56 M in 0.008 M NaOH concentrations, and the temperature range of 293-308 K. They found that the hydrolysis reaction is a first order reaction with respect to the  $\text{NaBH}_4$  concentration. They also concluded that the reaction rate constant decreases as the initial  $\text{NaBH}_4$  concentration increases at constant temperature and constant  $\text{CoCl}_2$  concentration.

Stockmayer et al., [65] studied the 0.1 M potassium borohydride hydrolysis kinetics using boric acid as a catalyst,  $\text{NH}_4\text{Cl-NaOH}$  as a buffering agent, and sodium chloride was added to bring the ionic strength to 0.16 M. Their findings were in a good agreement with the Levy et al's [64] results.

Davis et al., [66] studied of 0.001-0.05 M  $\text{NaBH}_4$  hydrolysis in aqueous solutions using normal and heavy water, boric acid-sodium hydroxide to control the solution *pH*

(7.40-14.7). Their main finding was the hydrolysis rate constant decreases as the  $pH$  increases.

Brown [67-69] studied the catalytic hydrolysis of sodium borohydride using different precious and non precious metal chlorides. They found that these salts were reduced to pure metals, and this led to an increase in the hydrolysis rate for most of the salts under investigation. They developed a technique to be able to liberate  $H_2$  rapidly. They produced a sodium borohydride pellets containing a small amount of cobalt (II) chloride, which once placed in water, immediately liberates  $H_2$ .

Gardiner and Collat [70, 71] tried to identify the intermediates during the hydrolysis process of sodium borohydride using a polarographic technique. The  $NaBH_4$  concentration was 0.02-0.05 M in 0.1 M KOH concentrations ( $pH = 9.1-12.5$ ), and at 298 K. They suggested that  $BH_3OH$  is the most probable formula for the intermediate.

Borohydride hydrolysis on metals has attracted many researchers since being used on board as a hydrogen source for portable fuel cells applications. Borohydrides show higher gravimetric capacities than metal hydrides and higher volumetric capacities than either compressed or liquefied hydrogen, Fig. 2.10.2 [72].

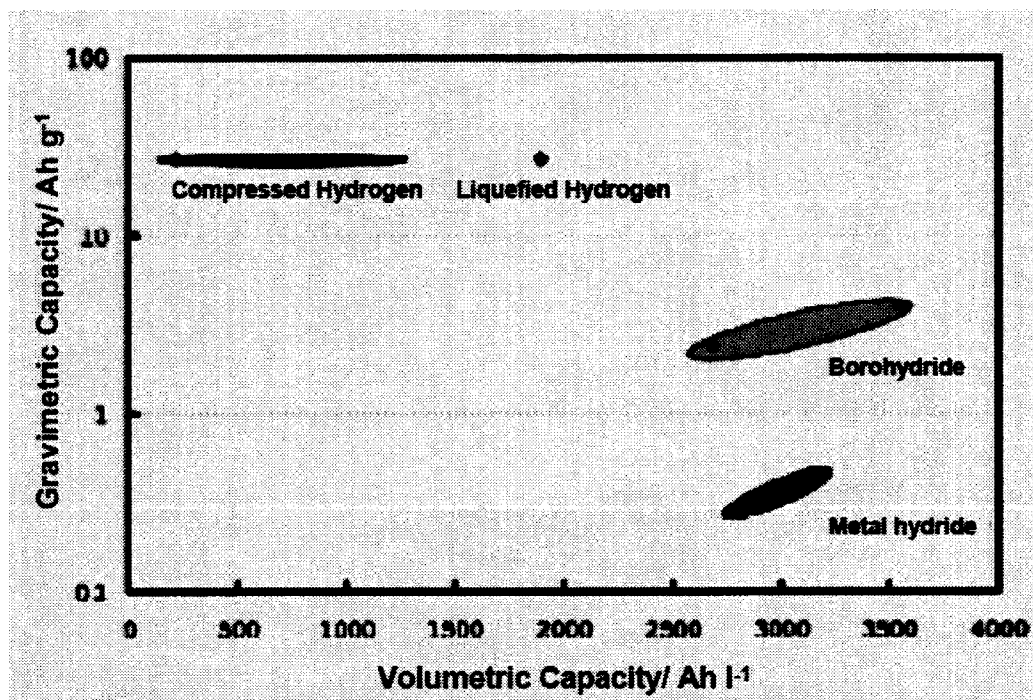


Fig.2.10.2. Capacity comparison when hydrogen is stored by different methods [73].

Today, many researchers [72-76] are trying to optimize a hydrogen storage system that uses sodium borohydride, in order to produce hydrogen on demand which can be used as a fuel for low temperature fuel cells.

Schlesinger et al. [59] had suggested early in 1953 that sodium borohydride can release 90% of the stoichiometric amount of hydrogen. Li et al. in 2003 [72], found that at a certain conditions ( $< 20\%$   $NaBH_4$  solution) sodium borohydride can release almost 100% of the stoichiometric amount of hydrogen.

Table 2.10.1 summarizes the borohydride hydrolysis on different materials under different conditions. The hydrogen evolution rates were reported only for  $Ni_xB$ , Ru/C [66], and Pt supported on different materials [65], and the rates were 200, 240, and 500  $ml\ min^{-1}$  at 298 K, respectively.

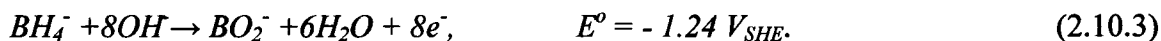
Table 2.10.1. Summary of Borohydride Hydrolysis Literature.

Ref.	Anode/ Catalysts	Geometry and Preparation Method	Solutions $NaBH_4$ Concentration	Parameters Studied	Hydrogen $ml\ min^{-1}$ [298 K]
Schlesinger et al. [59-62]	Metal Salts	N/A*	N/A	$T$ , $pH$ , and Catalyst type	N/A
Pecsok [63]	Dropping Mercury	drop	$10^{-3}$ M in 0.1 M KOH	$pH$ , $T$	N/A
Levy et al [64]	$CoCl_2$	Powder	0.13-0.56 M in 0.008 M NaOH	$T$ , $CoCl_2$ Concentration	N/A
Stockmayer et al [65]	N/A	N/A	0.01 M	$T$ , $pH$	N/A
Davis et al [66]	N/A	N/A	0.001-0.05 M	$pH$	N/A
Brown and Brown [67-69]	Metal Chlorides	Powder	1 M	Catalyst type	N/A
Gardiner and Collat [70, 71]	Dropping Mercury	drop	0.02-0.05 M in 0.001-0.1 N NaOH	$pH$ , Anode Potential	N/A
Kojima et al [73]	1. Pt-LiCoO <sub>2</sub> , 2. Pt-TiO <sub>2</sub> , 3. Pt-CoO (1:10 wt. ratio)	1. 256 mg Powder	1.6wt% $NaBH_4$ in H <sub>2</sub> O	Different Catalysts	1. 500
Hau et al. [74]	1. $Ni_xB$ , 2. Ru/C	1. 0.1 g, 2. 2wt% Ru, Powder	1.5 wt% $NaBH_4$ in 10wt% NaOH	$T$ , $pH$ , Catalyst	1. 200, 2. 240

\* Not available.

### 2.10.2. Borohydride Oxidation

The proposed complete anodic reaction for the polarographic oxidation of sodium borohydride in alkaline electrolytes is [63]:



Marshall and Widing [77] were the first to study sodium borohydride oxidation in an alkaline electrolyte using a dropping mercury electrode. Two oxidation waves were recorded at  $-0.15 V$  and  $-0.64 V$  vs. *SCE* (close to  $+0.091 V$  and  $-0.399 V$  vs. *SHE*). The wave at  $-0.15 V$  has a very high peak current compared to that at  $-0.64 V$ . They suggested that the number of electrons transferred was equal to 4, which gives a diffusion coefficient of  $10 \times 10^{-5} \text{ cm}^2 \text{ s}^{-1}$ .

Pecsok [63] extended Marshall and Widing's work in order to obtain the electrode half reaction, to confirm the hydrolysis reaction, and to measure its rate. The main point he made in his study is that  $NaBH_4$  solutions buffered at *pH* 9 or higher give a single highly irreversible anodic polarographic wave. He estimated the number of electrons transferred for the oxidation process to be 8. He also concluded that impurities were probably responsible for the presence of a small anodic peak that was found by Marshall and Widing [77]. He also proposed that the limiting current is not only a diffusion controlled process, but that the oxidation process goes through several intermediate stages, and that the peak current is proportional to the  $BH_4^-$  concentration over a wide range. Moreover, he also calculated the standard electrode potential of the anodic reaction as  $-1.23 V$  vs. standard hydrogen electrode (*SHE*).

Mochalov and Gilmanshin [78] studied the polarographic behaviour of lithium, potassium, and sodium borohydride in sodium hydroxide solution of *pH* in the range 9-11. Their potential range was between  $-2.0$  and  $0.2 V$  vs. *SCE* (close to  $-1.759 V$  and  $0.441 V$  vs. *SHE*), and the borohydride concentration range was between  $10^{-3} M$  and  $10^{-1} M$ . They found only one anodic peak at  $-0.65 V$  vs. *SCE* (close to  $-0.409 V$  vs. *SHE*), and it was directly proportional to the borohydride concentration. They also found that the peak height varied inversely with *pH*.

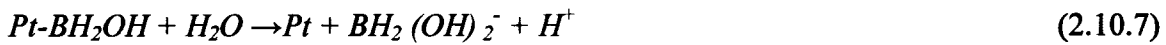
Elder et al [79, 80] studied the anodic oxidation of potassium borohydride in potassium hydroxide electrolyte on platinum (different surfaces), palladium, and nickel using an oscillographic technique. They proposed that the reaction potential is

independent of the borate ion concentration. Hydrogen evolution was observed and its rate depended on the electrode material. Thus, they found that  $BH_4^-$  oxidation is a selective reaction at certain surfaces, such as, platinum, and that hydrogen ionization is an essential electrochemical step in the oxidation of a borohydride ion. The proposed mechanisms for the  $BH_4^-$  oxidation reactions in an alkaline electrolyte and on a platinum electrode surface were as follows [80]:

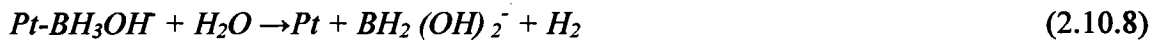
Initial step;



Rate-determining step;



Slow hydrolysis;



Complete step;



They also confirmed that the competition between the borohydride electrochemical oxidation and the accompanying hydrolysis is different from one electrode material to another.

Inding and Snyder [81] were the first to propose that sodium borohydride could be a good candidate as the anodic fuel for a direct liquid fuel cell using a borohydride solution in an alkaline electrolyte. Their experiments were conducted using 6 wt% of  $NaBH_4$  in a specified amount of 20 wt%  $NaOH$  solution, at three different temperatures 25, 45, and 75°C. They used a cell which is illustrated schematically in Fig. 2.10.3. A sintered nickel anode with 80% porosity and of 6.45  $cm^2$  area, a silver sheet cathode of 6.45  $cm^2$  area, and  $Hg/HgO$  reference electrode were used in their experiments. They found that the sodium borohydride oxidation on such an electrode, accompanied by a high rate of hydrolysis, led to the evolution of a large volume of hydrogen gas. At 25°C, a current density of 200  $mA\ cm^{-2}$  at -0.8 V vs.  $Hg/HgO$  (close to -0.7 V vs.  $SHE$ ) was

achieved. They attributed the low value of the electrons transferred ( $n \sim 4$ ), to the catalytic hydrolysis action of the nickel electrode.

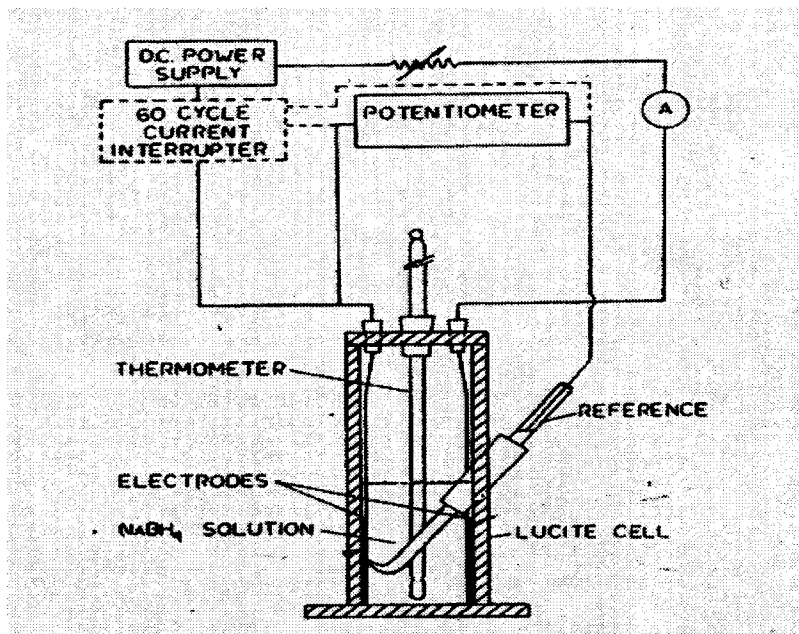
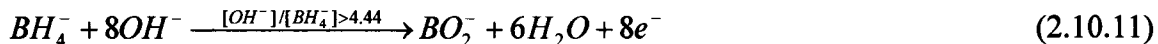
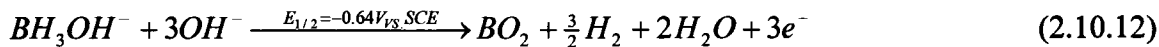


Fig.2.10.3. Schematic illustration of the Inding and Snyder cell [81].

Gardiner and Collat [70, 71, and 82] attempted to clarify the conflicting data of hydrolysis and oxidation of borohydride that was found in the polarographic literature. They tested a solution of  $0.02\text{-}0.05\text{ M NaBH}_4$  in an ammonium-ammonia buffer solution of  $\text{pH } 9.1$ , at  $25^\circ\text{C}$ . Two main oxidation peaks, at  $-0.11$  and  $-0.64\text{ V vs. SCE}$  (close to  $+0.131\text{ V}$  and  $-0.399\text{ V vs. SHE}$ ), were recorded. The first peak was ascribed to the direct borohydride oxidation, while the second to the intermediate  $\text{BH}_3\text{OH}$  oxidation. The linear proportionality of the  $\text{BH}_4^-$  oxidation peak current with the  $\text{BH}_4^-$  concentration was noticed, and in unbuffered solutions it was highly affected by the ratio of  $\text{OH}^-$  to  $\text{BH}_4^-$  concentrations. They calculated the number of the electrons transferred for the direct oxidation process to be  $8$  for the solutions that have a ratio of the  $\text{OH}^-$  to  $\text{BH}_4^-$  concentrations greater than  $4.44$ . Below this ratio ( $4.44$ ) the number of electrons exchanged drops due to the parallel hydrolysis reaction. They proposed the following reaction scheme:



↓ *Hydrolysis*



Ivanov and Tsionskii [83] studied the anodic oxidation of borohydride in 1 M NaOH at room temperature on a Pt rotating disc electrode and a wire-tip electrode. The scan rate was 0.1 V s<sup>-1</sup> and the potential range was between -1.0 and 0.5 V vs. SSC (close to -0.803 V and 0.697 V vs. SHE). They suggested that according to their results, the BH<sub>4</sub><sup>-</sup> ion is a source of adsorbed hydrogen. Their conclusion was that the BH<sub>4</sub><sup>-</sup> ion is not electrochemically active in the potential range investigated.

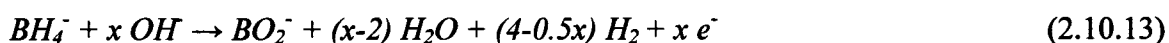
Bard et al. [84] attempted to determine the borohydride concentration in alkaline aqueous solutions using a volumetric method. A cyclic voltammetry technique was used to study the oxidation of 8.1 × 10<sup>-5</sup> to 0.013 M borohydride in 0.2 M NaOH on a disc-form gold electrode. They found that the voltammograms on a gold electrode showed a well defined shape compared to nickel and platinum electrodes. A single oxidation peak was found between -0.8 and -0.4 V vs. SMSE (close to -0.185 V and 0.215 V vs. SHE), and a linear relationship found between the peak current and borohydride concentration.

In another experiment, Bard et al. [85], tried to use a direct method to determine the diffusion coefficients using chronoamperometry of microdisk electrodes. Again they studied the oxidation of 0.2 M sodium borohydride to 1 M sodium hydroxide system on a 25 μm diameter gold microdisk to calculate the BH<sub>4</sub><sup>-</sup> diffusion coefficient. The main findings were that the number of electrons transferred for NaBH<sub>4</sub> oxidation was 7.5 ± 0.5, and that the oxidation mechanism involved a number of electrochemical and chemical steps (EC reactions), which has been supported in another study [86].

Liu et al. [87] studied the anodic oxidation of borohydride on a nickel electrode. They concluded that although the coulombic efficiency (the per cent of the recovered electrons from total available ones in the fuel) was found to be 50%, i.e., four electrons process, the polarization measurements indicated that a high power density can be achieved (i.e., at -0.88 V vs. Hg/HgO (close to -0.78 V vs. SHE) a current of 100 mA cm<sup>-2</sup> can be achieved at 200 mg cm<sup>-2</sup> catalyst load, 1.6wt% NaBH<sub>4</sub> concentration, and 293 K).

They also concluded that the electrochemical reactions can be a source of hydrogen evolution in addition to the hydrolysis reactions.

In another study [88], borohydride oxidation on *Ni*, Raney *Ni*, *Au*, *Pd*, and *Pt* was investigated in an attempt to find suitable anode electrocatalysts for borohydride fuel cells. The electrodes were prepared by mixing and grinding metal or carbon supported *Pd* and *Pt* powders with polytetrafluoroethylene (PTFE) powder, then pasting the mixture on a nickel foam ( $2.5\text{ cm} \times 2\text{ cm}$ ) and then encapsulating it using a 100 mesh nickel net, and roller-pressing to the final size. The electrode surface area was  $5\text{ cm}^2$ . Solutions used were 0.5-2.4 M  $\text{NaBH}_4$  in 6 M  $\text{NaOH}$  electrolyte. Open circuit results showed that *Ni* has the most negative potential. They also reported that the *Ni* has a high efficiency followed by *Pd*, and then *Pt*. They suggested that the  $\text{NaBH}_4$  oxidation reaction may have different paths for different electrocatalysts and environmental conditions. They also proposed that the competition between  $\text{NaBH}_4$  oxidation and hydrolysis reactions leads to the following overall anodic reaction:



where  $x$ , is the actual number of the electrons released per each  $\text{BH}_4^-$  ion.

Gyenge [89] studied the possibility of inhibiting the hydrolysis during the oxidation of borohydride on catalytic electrodes, (e.g., platinum) using thiourea (TU). It was concluded that TU inhibits the catalytic hydrolysis of  $\text{BH}_4^-$ . It was also concluded that this could improve the  $\text{BH}_4^-$  utilization efficiency and coulombic efficiency of direct borohydride fuel cells that use catalytic anodes.

Table 2.10.2 summarizes the borohydride oxidation on different materials. It is hard to compare these materials, since they have different geometries and were investigated under different conditions. Gold gave the highest fuel utilization (i.e.,  $n=8$ ), while the rest of the investigated materials showed a less than 8 electron process due to the accompanying hydrolysis reaction of borohydride on these materials. In general, materials like Pt, Pd, and Ni showed a more negative oxidation peak than that of Au.



Table 2.10.2. Summary of Borohydride Oxidation Literature.

Ref.	Anode	Geometry and preparation method	Solutions, NaBH <sub>4</sub> (M)	T, K	I <sub>a</sub> , mA cm <sup>-2</sup>	E, V	n
Marshall and Widing [77]	Dropping Mercury	drop	N/A*	298	N/A	1. -0.65 V 2. -0.15 V vs. SCE	4
Mochalov and Gilmanshin [78]	Dropping Mercury	drop	10 <sup>-3</sup> M-10 <sup>-1</sup> M	298	N/A	1. -0.65 V vs. SCE	N/A
Elder et al. [79, 80]	Pt	Smooth surface	10 <sup>-2</sup> M in 0.1 M KOH	298	N/A	N/A	4
Gardiner and Collat [70, 71, 82]	Dropping Mercury	drop	0.02-0.05 M	298		1. -0.11, 2. -0.64 V vs. SCE	N/A
Ivanov and Tsiolskii [83]	Pt	1. Pt-disc, 0.215 cm <sup>2</sup> 2. Pt-wire, 7.85x10 <sup>-3</sup> cm <sup>2</sup>	1.2 x 10 <sup>-2</sup> - 11.6 x 10 <sup>-2</sup> M in 1 M NaOH	298	N/A	N/A	N/A
Bard et al. [85, 86]	Au	Disc, 0.12 cm <sup>2</sup>	8.1x10 <sup>-3</sup> - 0.013 M in 0.2 M NaOH	298	~0.425 at 100 m V s <sup>-1</sup>	1. -0.8 to -0.4 V vs. SMSE	~8
Liu et al. [87]	Ni	Powder Ni, 5 cm <sup>2</sup>	1.64wt% NaBH <sub>4</sub> in 6 M KOH	293 313 333	100	1. ~-0.88, 2. ~ -1.0, 3. ~ -1.08	4
Liu et al. [88]	1. Pt/C, 2. Pd/C 3. Ni	carbon supported Pd and Pt powders, 5 cm <sup>2</sup>	0.5-2.4 M NaBH <sub>4</sub> in 6 M NaOH	303	1. ~ 375 2. ~ 440 3. ~ 520	-0.6 V vs. NHE	N/A
Gyenge [89]	1. Pt 2. Au	Wires, 7.85 x 10 <sup>-3</sup> cm <sup>2</sup>	1.5 x 10 <sup>-3</sup> M, in 2 M NaOH	298	N/A	1. -0.87 and -0.13 V, 2. -0.6 to +0.4 V vs. SSE	1. ~ 4 2. ~ 8

\* Not available.

### 2.10.3. Direct Borohydride Fuel Cell (DBFC) Literature

A summary of the DBFC process including a schematic diagram, operating principles and anode/cathode reactions, has been given in Section 2.6.6.3. A comparison of the DBFC with other major types of fuel cells can be found in Table 2.6.1.

Jasinski [24] was the first to test a direct borohydride fuel cell using nickel boride, palladium, and platinum as anode electrocatalysts. The first set of the electrodes were prepared by precipitating nickel boride from nickel acetate and  $KBH_4$  on a nickel plaque and an electrochemical deposit of  $Pd$  on a nickel plaque. The second electrode set was

prepared by binding the *Pt*, *Pd*, and *NiB<sub>2</sub>* powders to a nickel plaque using Teflon. *Ag* on *Ni* was used as a cathode, asbestos as a membrane, 35% *KOH* as an electrolyte, and 2% *KBH<sub>4</sub>* as a fuel. Based on half-cell results, *NiB<sub>2</sub>* had a more negative potential than *Pd*. Similarly, the fuel cell test results showed that a current of  $100 \text{ mA cm}^{-2}$  can be achieved at more negative potential on *NiB<sub>2</sub>* compared to that on *Pd*. This was attributed to the difference in the electrode surface area. Electrodes of  $9 \text{ mg cm}^{-2}$  load of commercial blacks of *Pt* and *Pd*, and a precipitated *NiB<sub>2</sub>* on *Ni* plaque were used in attempt to maintain the same surface areas of about  $25\text{-}30 \text{ m}^2 \text{ g}^{-1}$ . *NiB<sub>2</sub>* was shown to be the most active electrocatalyst compared to the *Pd* and *Pt* electrodes. It was also reported that the *KBH<sub>4</sub>/O<sub>2</sub>* cell performance was comparable to that of *H<sub>2</sub>/O<sub>2</sub>* for the same operating conditions.

Amendola et al. [90] studied the borohydride fuel cell performance of a  $3.6 \text{ cm}^2$  area of 97% *Au*-3% *Pt* which was electrochemically deposited on a carbon cloth as the anode electrocatalyst, a commercial air cathode catalyst, and an anion conductive membrane. A fuel concentration of 5% *NaBH<sub>4</sub>* in 25% *NaOH* was used. A power density of  $20 \text{ mW cm}^{-2}$  and  $60 \text{ mW cm}^{-2}$  at  $25^\circ\text{C}$  and  $70^\circ\text{C}$  respectively, and a fuel utilization of  $\sim 7$  electrons per borohydride molecule were reported. They concluded that the anion membrane may permit *BH<sub>4</sub><sup>-</sup>* crossover, thus leading to an increase in the cathode overpotential and to a loss of fuel.

Li et al. [27] studied the performance and development of a direct borohydride fuel cell. They used a *Zr-Ni*-alloy of  $0.2 \text{ g cm}^{-2}$  loading as the anode catalyst, 20wt% carbon supported *Pt* of  $2 \text{ mg cm}^{-2}$  loading as a cathode catalyst, and a Nafion membrane. The fuel concentration that was used was 10% *NaBH<sub>4</sub>* in 20wt% *NaOH*, which was pumped at a rate of  $200 \text{ ml min}^{-1}$ , and an oxidant flow rate of  $200 \text{ ml min}^{-1}$ . The migration of *Na<sup>+</sup>* ions to the cathode compartment was proven experimentally. Nafion 117's resistance to borohydride crossover was found to be high compared to Nafion 112. It was also proven that the use of a dry oxidant enhances the cathode potential, since the semi-dried membrane would lower the fuel crossover. A power density  $\sim 190 \text{ mW cm}^{-2}$  at  $85^\circ\text{C}$  was obtained. They proposed that, in order to enhance the fuel utilization, hydrogen evolved has to be minimized by choosing new anode catalysts or by making use of the evolving hydrogen as a feed to PEMFC or AFC fuel cells.

Li et al. [72] studied the performance of a direct borohydride fuel cell stack composed of ten cells each of  $6\text{ cm}^2$  area. The same materials as in their previous study, ref. [27], were used. The performance is shown in Fig 2.10.4.

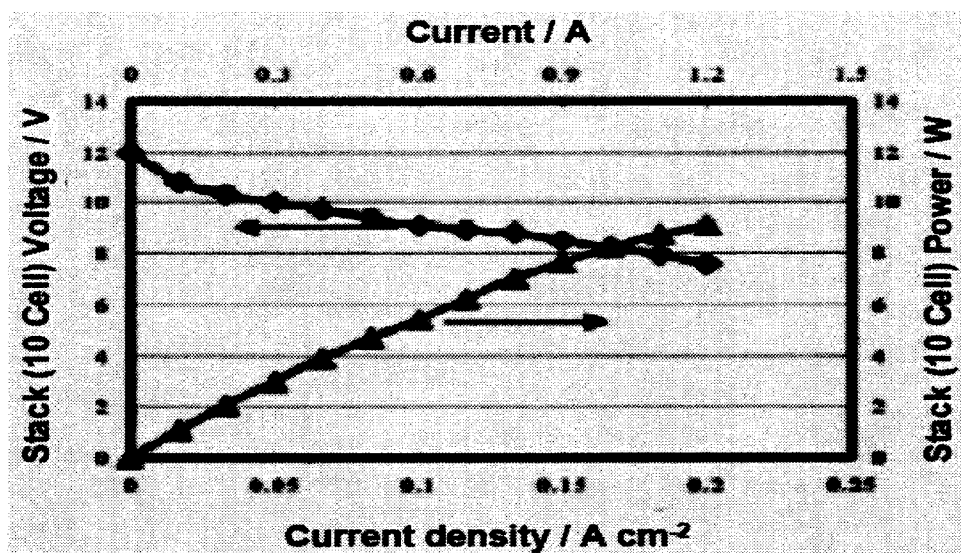


Fig.2.10.4. Performance of direct borohydride fuel cell stacks [73].

Li et al. [28] optimized the alkaline borohydride solution concentration as a fuel for fuel cells. The fuel cell and the materials were the same as in ref. [27], plus an *H-Cell* which was used to measure the open circuit and fuel crossover. A fuel of  $10\text{wt}\% \text{NaBH}_4$  in  $20\text{wt}\% \text{NaOH}$  was found to be the most suitable for a direct borohydride fuel cell. The anode was a *Zr-Ni* alloy. The open circuit potential was measured with increasing borohydride concentration. The anode performance was slightly enhanced with increasing  $\text{NaBH}_4$  concentration, while that of the cathode was significantly deteriorated, which they attributed to a high fuel crossover. Although the sodium hydroxide concentration did not affect the cell voltage, high concentrations, i.e. high viscosity, can reduce the  $\text{Na}^+$  ion mobility.

Kim et al. [91] studied both supported and unsupported *Pt* as anode catalysts for direct borohydride fuel cells. Parameters such as, catalyst load, binder, fuel concentration, and *pH* of electrolyte on the cell performance were investigated. They concluded that supported *Pt* catalyst was more active, cost effective, and showed higher coulombic efficiency than unsupported *Pt* catalysts.

Table 2.10.3 summarizes the findings for direct borohydride fuel cell processes. Despite the different anode and cathode catalysts, their loads and geometry, the

membrane types, and the operating conditions, *Pt*, *Pd*, *Ni<sub>2</sub>B*, and *Zr-Ni* showed promising performance levels. For example at a voltage of > 0.8 V, a current of 100 mA cm<sup>-2</sup> can be obtained.

Table 2.10.3 Summary of the direct borohydride fuel cell performance literature.

Ref.	Anode Materials	Geometry and Prep. Method	Load mg cm <sup>-2</sup>		Solutions/flow rates, ml min <sup>-1</sup>		Temp. K	Membrane	n	E <sub>cell</sub> , V	I, mA cm <sup>-2</sup>
			Anode	Cathode	Fuel	Oxidant					
Jasinski [24]	1. NiB <sub>2</sub> 2. Pd 3. Pt	Precipitated on, Plated on, and Powder bonded to Ni plate	9	Ag on Ni plate	2% KBH <sub>4</sub> in 25% KOH, static condition	O <sub>2</sub> , static condition	318	Asbestos	4	1. 0.95, 2. 0.88, 3. 0.87	100
Amendola et al. [90]	97%Au-3% Pt	Deposited on C-cloth, 3.5 cm <sup>2</sup>	N/A*	N/A	5% NaBH <sub>4</sub> in 25% NaOH, static condition	Air, static condition	1. 298, 2. 343	Anion exchange	N/A	1. Zero 2. ~0.57	100
Li et al. [27]	Zr-Ni alloy (AB <sub>2</sub> )	N/A	200	Pt/C =2	10% NaBH <sub>4</sub> in 20% NaOH, 200	O <sub>2</sub> = 200	1. 323, 2. 343, 3. 358	Nafion 117	N/A	1. ~0.8, 2. ~0.9, 3. ~0.98	100
Kim et al. [91]	1. Pt/C 2. Pt	Supported and unsupported Pt, 7.6 cm <sup>2</sup>	1. 1.5, 2. 6	N/A	0.5 M NaBH <sub>4</sub> in 1 M KOH, Static condition	Air, Static condition	298	6M KOH	N/A	1. ~0.18, 2. ~0.18	100

\* Not available.

## 2.11. References

1. L. Carrette, K. A. Friedrich, U. Stimming, *Chemphyschem*, 1 (2000) 162-193.
2. K. Kendall, *Emergence of Fuel Cell Products*, *Europhysics News*, 34(50) (2003), Retrieved 2003 from [www.europhysicsnews.com](http://www.europhysicsnews.com)
3. A. J. Appleby, *J. Power Sources*, 58 (2) (1996) 153-176.
4. K. Kordesch, G. Simader, *Fuel Cells and Their Applications*, VCH, NY (1996) 255, 23-50.
5. J.H. Hirschenhofer, D.B. Stauffer, R.R. Engleman, and M.G. Klett, *Fuel Cell Handbook*, U.S. Dept. of Energy, Parsons Corporation, 4<sup>th</sup> Ed. (1998). Retrieved 2002 from <http://www.seca.doe.gov/pubs/4-fuelcell.pdf>
6. Retrieved 2003 form [http://www.h2fc.com/images/Image\\_43\\_pem.gif](http://www.h2fc.com/images/Image_43_pem.gif).
7. D. S. Scott, *Int. J. Hydrogen Energy*, 29 (2004) 1203-1311.

8. S. Karthea, P. Grimes, *Physics Today*, Nov. (1994) 54-61.
9. A. Lutz, R. Larson, J. Keller, *Int. J. Hydrogen Energy*, 27 (2002) 1103-1111.
10. [www.micro-vett.it/H2/ing/fcing.html](http://www.micro-vett.it/H2/ing/fcing.html), Retrieved 2003.
11. S. Srinivasan, R. Mosdale, P. Stevens, *Annu. Rev. Energy Environ.*, 24 (1999) 281-328
12. R. Ellinger, K. Meitz, P. Perninger, S. Salchenger, W. Bandstatter, Comparison of CO<sub>2</sub> Emission Levels for Internal Combustion Engine and Fuel Cell Automotive Propulsion Systems, Environmental Sustainability Conference and Exhibition, Oct., 12-14, 2001, Graz, Austria, Society of Automotive Engineers, Inc., Warrendale, Pennsylvania, USA, Document number 2001-01-3751.
13. [http://www.eere.energy.gov/hydrogenandfuelcells/fuelcells/fc\\_types.html](http://www.eere.energy.gov/hydrogenandfuelcells/fuelcells/fc_types.html), Retrieved 2003.
14. A. K. Shulka, K. V. Ramesh, A. M. Kannan. *Proc. Indian Acad. Sci. (Chem. Sci.)*, 97 (3&4) (1986) 513-528.
15. A. J. Appleby, F. R. Foulks, *Fuel Cell Handbook*, VNB, NY (1989) 313-350.
16. <http://fuelcellworks.com>, Retrieved 2003.
17. A. S. Arico, S. Srinivasan, V. Antonucci, *Fuel Cells*, 2 (2001) 133-161.
18. [http://ho.seas.ucla.edu/members/thomas\\_cubaud/Breather.Hilton2004.pdf](http://ho.seas.ucla.edu/members/thomas_cubaud/Breather.Hilton2004.pdf), Retrieved 2003.
19. F. S. Thomas, R.I. Masel, *Surface Science*, 573 (2004) 169-175.
20. C. Rice, S. Ha, R. I. Masel, A. Wieckowski, *J. Power Sources*, 115 (2) (2003) 229-235.
21. C. Rice, S. Ha, R. I. Masel, P. Waszczuk, A. Wieckowski, T. Barnard, *J. Power Sources*, 111 (2002) 83-89.
22. Y. Zhu, S. Ha, R. I. Masel, *J. Power Sources*, 130 (2004) 8-14.
23. Y. Zhu, Z. Khan, R. I. Masel, *J. Power Sources*, 139 (2005) 15-20.
24. R. Jasinski, *Electrochemical Tech.*, 391-20 (1965) 40-43.
25. S. Suda et al., *Nikkei Electronic*, Oct. 22, 807 (2001) 130-139. Retrieved 2003 from [www.kucel.hydrogen.co.jp](http://www.kucel.hydrogen.co.jp)
26. S. Suda et al., *Material Stage*, Oct. 10, 1 (7) (2001) 14-17. Retrieved 2003 from [www.kucel.hydrogen.co.jp/1-6](http://www.kucel.hydrogen.co.jp/1-6)
27. Z. P. Li, B. H. Liu, K. Arai, S. Suda, *J. Electrochem. Soc.*, 150 (7) (2003) A868-A872.
28. Z. P. Li, B. H. Liu, K. Arai, S. Suda, *J. Power Sources*, 126 (2004) 28-33.
29. <http://merit.hydrogen.co.jp/R&D/DBFC/DBFC.html>, Retrieved 2003.
30. <http://www.tkk.fi/Units/AES/projects/renew/fuelcell/posters/fuelcells.html>, Retrieved 2003.
31. <http://www.nuvera.com/company/modules.php>, Retrieved 2003.
32. J. Thomas, W. Thomas, *Principles and practice of heterogeneous catalysis*, VCH, NY (1997) 1-55.
33. P. Stoltze, *Introduction to Heterogeneous Catalysis, Concepts and Calculations*, Dept. of Physics, Technical University of Denmark (2001). Retrieved 2002 from [www.aue.auc.dk/~stoltze/catal/book/main](http://www.aue.auc.dk/~stoltze/catal/book/main)
34. I. Chorkendorff, J. W. Niemantsverdriet, *Concepts of Modern Catalysis and Kinetics*, Wiley-VCH, Weinheim (2003).
35. A. Wieckowski, E. Savinova, C. Vayenas, *Catalysis and Electrocatalysis at*

- Nanoparticle Surfaces, Marcel Dekker Inc., NY (2003) 345-378, 745-783, 827-845, 849-875.
36. R. I. Masel, *Chemical Kinetics and Catalysis*, Wiley-Interscience, NY (2001) 689-755, 837-880, 667-743.
  37. <http://ceiba.cc.ntu.edu.tw/catalysis>, Retrieved 2003.
  38. [www.science.uwaterloo.ca/~cchieh/cact/applychem/hetrocat.html](http://www.science.uwaterloo.ca/~cchieh/cact/applychem/hetrocat.html), Retrieved 2003.
  39. J. Libkowsky, P. Ross, *Electrocatalysis*, Wiley-VCH (1998).
  40. R. Greef, P. Peat, L. Peter, D. Pletcher, J. Robinson, *Instrumental Methods in Electrochemistry*, John Wiley, NY (1985) 229-250.
  41. G. C. Bond. *Catalysis by Metals*, Academic Press, NY (1962) 407-435.
  42. V. Ponc, G. C. Bond, *Catalysis by Metals and Alloys*, Elsevier, Amsterdam (1995).
  43. A. Furstner, *Active Metals*, VCH, Germany (1996) 427-446.
  44. Y. Iwasawa, *Tailored Metal Catalysis*, D. Reidel Publishing Company, Boston (1986) 87-263.
  45. C. N. Rao, J. Gopolkrishnan, *New Directions in Solid State Chemistry*, Cambridge University Press (1997) 517-534.
  46. M. Haruta, N. Yamada, T. Kobayashi, S. Iijima, *J. Catal.* 115 (1989) 301-309.
  47. Y. Iizuka, H. Fujiki, N. Yamauchi, T. Chijiwa, S. Arai, S. Tsubota, M. Haruta, *Catalysis Today*, 36 (1997) 115-123.
  48. L. K-Minsker, I. Yuranow, E. Slavinskaia, V. Zaikovskii, A. Renker, *Catalysis Today*, 59 (2000) 61-68.
  49. K. Eguchi, H. Arai, *Applied Catalysis A: General*, 222 (2001) 359-367.
  50. H. Widijaja, K. Sekizawa, K. Eguchi, H. Arai, *Catalysis Today*, 35 (1997) 197-202.
  51. K. Sekizawa, H. Widijaja, S. Maeda, Y. Ozawa, K. Eguchi, *Catalysis Today*, 59 (2000) 69-74.
  52. N. Toshima, T. Yonezawa, *New J. Chem.*, 11 (1998) 1179-1201.
  53. K-Y Chan, J. Ding, J. Ren, S. Cheng, K. Tsang, *J. Mater Chem.*, 14 (4) (2004) 505-516.
  54. G. Schmid, *Clusters and Colloids from Theory to Applications*, VCH, NY (1994) 458-544.
  55. N. Toshima, Y. Shirasha, *Encyclopedia of Surface and Colloid Science*, NY, April (2002) 879-886.
  56. H. Bonnemann, R. Richards, *Eur. J. Inorg. Chem.* (2000) 2455-2480.
  57. ROHN and HAASS Company Web Site; Retrieved 2004 from [www.hydridessolutions.com](http://www.hydridessolutions.com)
  58. <http://chemistry2-csudh.edu/rpendarvis/oxRed.html>, Retrieved 2004.
  59. H. I. Schlesinger, H. C. Brown, A. E. Finholt, J. R. Gilbeath, H. R. Hoekstra, E. K. Hyde, *J. Am. Chem. Soc.*, 75 (1) (1953) 215-219.
  60. H. I. Schlesinger, H. C. Brown, A. E. Finholt, *J. Am. Chem. Soc.*, 75 (1) (1953) 205-209.
  61. H. I. Schlesinger, H. C. Brown, H. R. Hoekstra, *J. Am. Chem. Soc.*, 75 (1953) 199-204.
  62. H. I. Schlesinger, H. C. Brown, B. Abraham, A. C. Bond, N. Davidson, A. E. Finholt, J. R. Gilbreath, H. Hoekstra, L. Horvitz, E. K. Hyde, J. J. Katz, J. Knight, R. A. Lad, D. L. Mayfield, L. Rapp, D. M. Ritter, A. M. Schwartz, I. Sheft, L. D. Tuck, A. O. Walker, *J. Am. Chem. Soc.*, 75 (1953) 186-190.

63. R. L. Pecsok, *J. Am. Chem. Soc.*, 75 (12) (1953) 2862-2864.
64. A. Levy, J. B. Brown, C. J. Lyons, *Ind. Eng. Chem.*, 52 (3) (1960) 211-214.
65. W. H. Stockmayer, R. R. Miller, R. J. Zeto, *J. Phys. Chem.*, 65 (6) (1961) 1076-1077.
66. R. E. Davis, E. Bromels, C. L. Kibby, *J. Am. Chem. Soc.*, 84 (6) (1962) 885-892.
67. H. C. Brown, C. A. Brown, *J. Am. Chem. Soc.*, 84 (8) (1962) 1493-1494.
68. H. C. Brown, C. A. Brown, *J. Am. Chem. Soc.*, 84 (8) (1962) 1494-1495.
69. H. C. Brown, C. A. Brown, *J. Am. Chem. Soc.*, 84 (14) (1962) 2827.
70. J. A. Gardiner, J. W. Collat, *J. Am. Chem. Soc.*, 86 (15) (1964) 3165-3166.
71. J. A. Gardiner, J. W. Collat, *J. Am. Chem. Soc.*, 87 (8) (1965) 1692-1695.
72. Z. P. Li, B. H. Lin, K. Aria, N. Morigazaki, S. Suda, *J. Alloys and Comp.*, 356-357 (2003) 469-474.
73. Y. Kojima, K. Suzuki, K. Fukumoto, *Int. J. Hydrogen Energy*, 27 (2002) 1029-1034.
74. D. Hua, Y. Hanxn, A. Xinping, C. Chuansin, *Int. J. Hydrogen Energy*, 28 (2003) 1095-1100.
75. J. Kim, H. Lee, S. Han, H. Song, J. Lee, *Int. J. Hydrogen Energy*, 29 (3) (2004) 263-274.
76. C. Wu, H. Zang, B. Yi, *Catalysis Today*, 93-95 (2004) 477-483.
77. E. D. Marshal, R. A. Widing, U.S. Atomic Energy Commission Document No.2914 (1950).
78. K. N. Mochalov, G. G. Gilmanshin, *Dokl. Akad. Nauk SSSR*, 132 (1960) 134.
79. J. P. Elder, *Electrochimica Acta*, 7(4) (1962) 417-426.
80. J. P. Elder, A. Hickling, *Trans. Faraday Soc.*, 58 (1962) 1852-1864.
81. M. E. Indig, R. N. Snyder, *J. Elec. Soc.*, 109 (1962) 1104-1106.
82. J. A. Gardiner, J. W. Collat, *J. Am. Chem. Soc.*, 87 (8) (1965) 1692-1695.
83. M. V. Ivanov, M. V. Tsionskii, *Elektrokhimi IA (Rusian J. Electrochemistry)*, (25) (1989) 451-454.
84. M. V. Mirkin, A. J. Bard, *Anal. Chem.*, 63 (1991) 532-533.
85. G. Denuault, M. V. Mirkin, A.J. Bard, *J. Electroanal. Chem.*, 308 (1991) 27-38.
86. M. V. Mirkin, H. Yang, A. J. Bard, *J. Electrochem. Soc.*, 139 (1992) 2212.
87. B. Liu, Z. P. Li, S. Suda, *J. Electrochem. Soc.*, 150 (30) (2003) A398-A402.
88. B. Liu, Z. P. Li, S. Suda, *Electrochimica Acta*, 49 (19) (2004) 3097-3105.
89. E. Gyenge, *Electrochimica Acta*, 49 (2004) 965-978.
90. S. C. Amendola, P. Onnerud, M. T. Kelly, P. J. Petillo, S. L. Shap-Goldman, M. Binder, *J. Power Sources*, 84 (1999) 130-133.
91. J. Kim, H. Kim, Y. Kang, M. Song, S. Rajendran, S. Han, D. Jung, J. Lee, *J. Electrochem. Soc.*, 151 (7) (2004) A1038-A1043.

## CHAPTER 3

### EXPERIMENTAL METHODS

#### 3.1. Electrocatalysts Preparation

##### *Colloidal metal preparation technique*

The colloidal metals were prepared by a modified Bönnerman method [1], as described by Götz and Wendt [2]. In the Bönnerman method, the triethylhydroborate ( $B(C_2H_5)_3H$ ) with tetraalkylammonium ( $R_4N^+$ ) act as both reductant and colloid particle encapsulating agent, respectively. All the colloidal metals were prepared with a 20 %wt load on a Vulcan XC72R support (L. V. LAMOS Limited). An atomic ratio of 1:1 was employed for all the alloys. The reactants and reaction(s) were handled and performed in a dry nitrogen atmosphere using a glove box for the weighing in conjunction with Schlenk flasks and nitrogen lines for the reaction (Fig. 3.1.1).

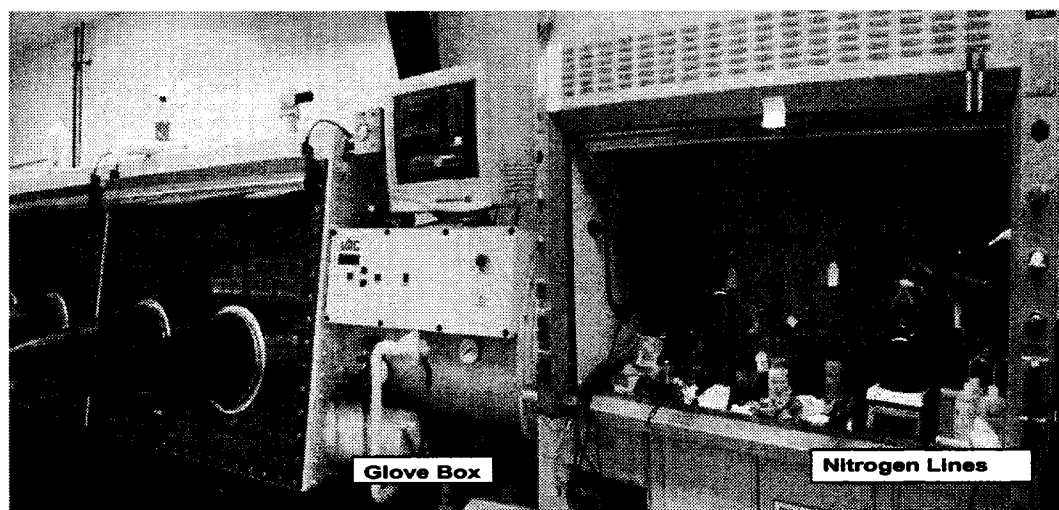


Fig. 3.1.1. Colloidal electrocatalyst preparation apparatus (University of Windsor, Dept. of Chemistry and Biochemistry).

Stoichiometric amounts of 1 M tetrabutylammonium chloride ( $(C_4H_9)_4N^+Cl^-$ ) in tetrahydrofuran (THF) (Sigma-Aldrich, >99% Anhydrous) and 1 M of lithium triethylhydroborate ( $LiB(C_2H_5)_3H$ ), or potassium triethylhydroborate ( $KBET_3H$ ) in the case of the osmium group only, were mixed to obtain a solution of 0.5 M of



tetrabutylammonium-triethylhydroborate,  $N(C_{16}H_{36})_4[BEt_3H]$ .  $LiCl$  or  $KCl$  was removed by passing the reaction products solution through a D-4 glass frit. A 50% excess 0.5 M of tetrabutylammoniumtriethyl hydroborate,  $N(C_{16}H_{36})_4[BEt_3H]$ , was added dropwise over a period of 1 h at 296 K to a stirred suspensions of anhydrous salts (Table 3.1.2) in 100 ml *THF*. Almost complete dissolution of the salt(s) occurred after stirring the deep dark coloured solution for 4 h. To destroy any unreacted reducing agent, 5 ml of acetone was added to the reaction mixture and stirred for 1 h. The solution was then added dropwise to a stirred suspension of the carbon support (Vulcan XC72R) in 100 ml *THF*. The mixture was stirred for 12 h to complete the adsorption of the surfactant protected colloidal particles on the carbon support. After the 12 h supporting step, 150 ml of ethanol (Sigma-Aldrich, 99.5%, Anhydrous) was added and stirred for 2 h. The reaction suspension was passed through a D-4 glass frit, the supported catalyst(s) was washed with ethanol several times, and then dried under a nitrogen vacuum at 296 K for 12 h. A summary of the stoichiometric amounts of the reacted species used in the preparation, and the chemicals and materials used in this study are given in Tables 3.1.1 and 3.1.2, respectively.

To investigate the role of the support in a similar method (i.e., the modified Bönnehan method), colloidal of *Pt*, *Pd* and *Ir* supported on 90wt% Vulcan XC72R carbon black plus 10wt%  $TiO_2$  (prepared in our laboratory) were also prepared (Table 3.1.1).

Annealing and reducing processes were performed to remove the protecting shell in order to enhance the catalytic activity according to the procedures recommended by Bönnehan and co-workers [3, 4, 5]. The processes were performed in three stages using a controlled tubular furnace (LINDBERG) (Fig. 3.1.2). First, the samples were heated up to 300°C for 30 min under  $N_2$  (5, BOC Gas) at a flow rate of 160 ml  $min^{-1}$ , under which most of the organic shell is decomposed. Secondly, the samples were annealed under a  $N_2/O_2$  (5, BOC Gas) mixture (10 vol.%  $O_2$ ) at a flow rate of 160 ml  $min^{-1}$  for 30 min at 300°C. Third, the samples were reduced under, 100 vol. %  $H_2$ , at flow rate of 160 ml  $min^{-1}$  for 30 min at 300°C, in order to reduce any oxidized metal(s) produced during the annealing processes. Nitrogen was purged for 5 min before and after the annealing process to avoid any contact between the oxygen and hydrogen gases. The typical particle

size produced by the Bönnerman method is between 1.5 and 10 nm (e.g., Pt = 2.8, Pd = 2.5, and Ir = 1.5 nm) [1, 3, 5].

The powder energy dispersive spectrometry (EDS) spectra for the prepared electrocatalysts corresponding to a selected zone in the powder sample indicated in the inset are shown in Figures 3.1.4 to 3.1.9. An EDS spectra was also obtained on the Vulcan XC72R, in which a trace amount of sulfur was detected (Fig. 3.1.3). Thus, in addition to the metals and the carbon from the support, the samples contained trace amounts of sulfur, which originated from the Vulcan XC72R. However, typically the post-preparation sample washing and treatment methods were effective in eliminating the *LiCl* by-product. Consequently, adsorbed *LiCl* was not detected by EDS (Figs. 3.1.4-3.1.9) for any of the samples.

The XRD pattern for the XC 72R carbon-black support is shown in Fig. 3.1.10. This pattern is typical of a non-crystalline material. The XRD patterns of the colloidal catalysts are given in Figs. 3.1.11 (Pt and Pt-alloys), 3.1.12 (Au and Au-alloys), 3.1.13 (Ir and Ir-alloys) and 3.1.14 (Pd and Pd-alloys). Examination of these XRD patterns shows a number of similarities, and some differences:

- (i) The XRD Pattern from the carbon-black support is evident in all colloidal catalyst XRD patterns.
- (ii) The XRD patterns of all colloidal catalysts can be indexed on the basis of a f.c.c. structure (the (111), (200), (220), and (311) diffraction peaks are clearly visible in all XRD patterns).
- (iii) These are small changes in the diffraction angles for (111), (200), (220), and (311) diffraction peaks which reflects the changes in lattice parameters due to the formation of solid solutions on alloying.
- (iv) All colloidal catalysts exhibit some broadening of the XRD peaks. This broadening typically shows up as wider and more intense “tails” to the diffraction peaks rather than a general broadening of the peak which can be measured as a breadth at half-peak height [6]. Such a broadening is indicative of a small crystallite size (less than 100 nm) [7], rather the general broadening which is due to microstrains (dislocations).

- (v) The amount of XRD peak broadening (more broadening of the “tails” indicating a smaller crystallite size) varies from one colloidal catalyst to another thus indicating varying crystallite sizes. Alloys exhibiting larger broadening, i.e., smaller crystallite size, include Pt-Ni, Ir, Ir-Pd, and possibly Ir-Ni.

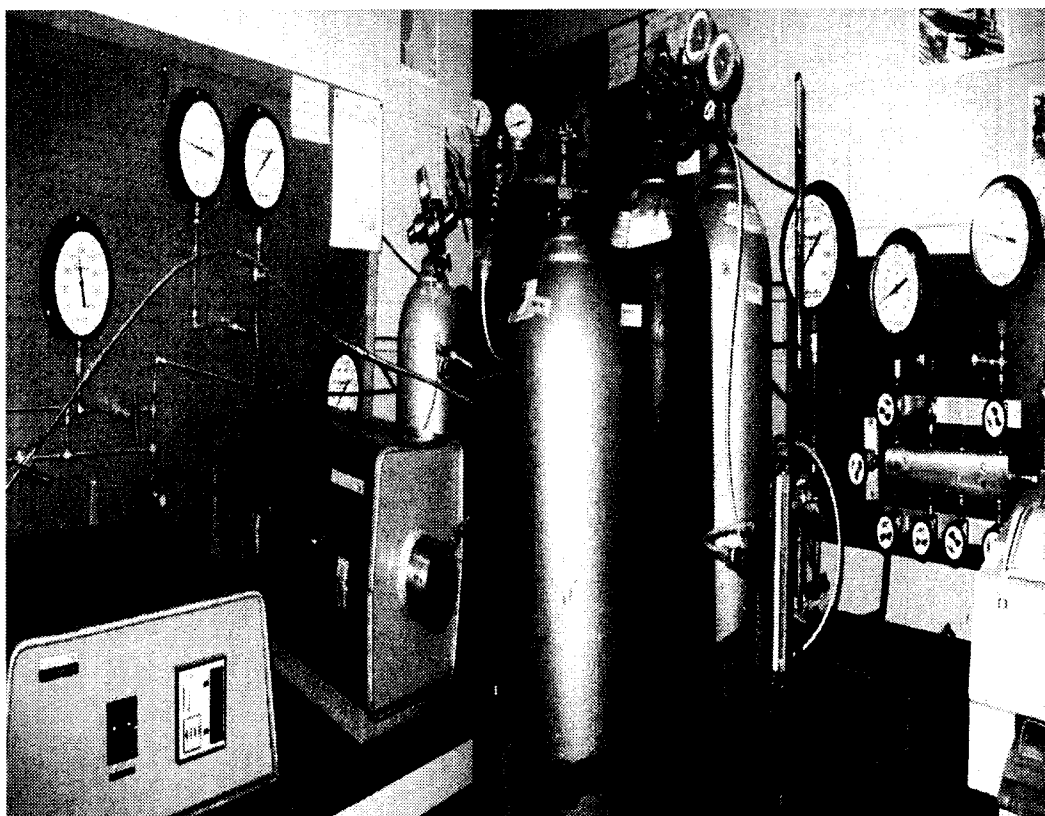


Fig.3.1.2. Electrocatalyst annealing and reducing process equipment (University of Windsor, Dept. of Mech., Automotive and Materials Eng.).

Table 3.1.1. Stoichiometric amounts of the reacted species used in preparation.

Metal Salt(s)	Metal Salt (g)	Metal Salt (mmol)	NR <sub>4</sub> [BEt <sub>3</sub> H] ml, 50% excess	C- Black (g), 20wt%	TiO <sub>2</sub> (g), 10% of C-black amount
1. OsCl <sub>3</sub>	0.2967	1.0	9	0.760	
2. OsCl <sub>3</sub> SnCl <sub>2</sub>	0.2967 0.1897	1.0 1.0	15	1.235	
3. OsCl <sub>3</sub> MoCl <sub>3</sub>	0.2967 0.2024	1.0 1.0	18	1.570	
4. OsCl <sub>3</sub> VCl <sub>3</sub>	0.2967 0.1124	1.0 1.0	18	0.964	
5. Pt Cl <sub>2</sub>	0.1329	0.5	3	0.390	
6. Pt Cl <sub>2</sub>	0.1329	0.5	3	0.341	0.0487
7. PtCl <sub>2</sub> AuCl <sub>3</sub>	0.1329 0.151	0.5 0.5	7.5	0.784	
8. PtCl <sub>2</sub> IrCl <sub>3</sub>	0.1329 0.1492	0.5 0.5	7.5	0.774	
9. PtCl <sub>2</sub> NiCl <sub>2</sub>	0.1329 0.0648	0.5 0.5	6	0.507	
10. PtCl <sub>2</sub> AgCl	0.1329 0.0716	0.5 0.5	4.5	0.605	
11. AuCl <sub>3</sub>	0.151	0.5	4.5	0.392	
13. AuCl <sub>3</sub> PdCl <sub>2</sub>	0.151 0.0886	0.5 0.5	7.5	0.819	
14. AuCl <sub>3</sub> NiCl <sub>2</sub>	0.151 0.0648	0.5 0.5	7.5	0.724	
15. AuCl <sub>3</sub> AgCl	0.151 0.0716	0.5 0.5	6	0.532	
16. PdCl <sub>2</sub>	0.0886	0.5	3	0.218	
17. PdCl <sub>2</sub>	0.0886	0.5	3	0.190	0.0275
18. PdCl <sub>2</sub> IrCl <sub>3</sub>	0.0886 0.149	0.5 0.5	7.5	0.597	
19. PdCl <sub>2</sub> NiCl <sub>2</sub>	0.0886 0.0648	0.5 0.5	6	0.330	
20. PdCl <sub>2</sub> AgCl	0.0886 0.0716	0.5 0.5	4.5	0.428	
21. IrCl <sub>3</sub>	0.149	0.5	4.5	0.384	
22. IrCl <sub>3</sub>	0.149	0.5	4.5	0.336	0.048
23. IrCl <sub>3</sub> NiCl <sub>2</sub>	0.149 0.0648	0.5 0.5	7.5	0.501	
24. IrCl <sub>3</sub> AgCl	0.149 0.0716	0.5 0.5	6	0.600	

Table 3.1.2. Summary of materials/chemicals related information.

<b>Material/ Chemical</b>	<b>Supplier</b>	<b>Purity</b>
<b>1. Osmium (III) Chloride</b>	<b>Sigma-Aldrich</b>	<b>99.9%, Anhydrous</b>
<b>2. Tin (II) Chloride</b>	<b>STREM Chemical, Inc.</b>	<b>98%, Anhydrous</b>
<b>3. Molybdenum (III) Chloride</b>	<b>STREM Chemical, Inc.</b>	<b>99.5%, Anhydrous</b>
<b>4. Vanadium (III) Chloride</b>	<b>STREM Chemical, Inc.</b>	<b>&gt;95%, Anhydrous</b>
<b>5. Platinum (II) Chloride</b>	<b>STREM Chemical, Inc.</b>	<b>99.9%, Anhydrous</b>
<b>6. Gold (II) Chloride</b>	<b>STREM Chemical, Inc.</b>	<b>99.9%, Anhydrous</b>
<b>7. Iridium (III) Chloride</b>	<b>STREM Chemical, Inc.</b>	<b>Ir% 64.29, Anhydrous</b>
<b>8. Palladium (II) Chloride</b>	<b>STREM Chemical, Inc.</b>	<b>99.9%, Anhydrous</b>
<b>9. Silver (I) Chloride</b>	<b>STREM Chemical, Inc.</b>	<b>99.9%, Anhydrous</b>
<b>10. Nickel (II) Chloride</b>	<b>STREM Chemical, Inc.</b>	<b>&gt;95%, Anhydrous</b>
<b>11. Titanium (III) Chloride</b>	<b>STREM Chemical, Inc.</b>	<b>&gt;98%, Anhydrous</b>
<b>12. NR<sub>4</sub>Cl</b>	<b>Sigma-Aldrich</b>	<b>&gt;99% Anhydrous</b>
<b>13. LiBEt<sub>3</sub>H, or KBEt<sub>3</sub>H</b>	<b>Sigma-Aldrich</b>	<b>1 M in THF, Anhydrous</b>
<b>14. THF</b>	<b>Sigma-Aldrich</b>	<b>99.9%, Anhydrous</b>
<b>15. Ethanol</b>	<b>Sigma-Aldrich</b>	<b>99.5%, Anhydrous</b>
<b>16. Vulcan XC72R</b>	<b>L. V. LAMOS Limited</b>	<b>100% Carbon Black</b>
<b>17. Oxygen</b>	<b>BOC Gas</b>	<b>5, High purity</b>
<b>18. Nitrogen</b>	<b>BOC Gas</b>	<b>5, High purity</b>
<b>19. Hydrogen</b>	<b>BOC Gas</b>	<b>5, High purity</b>

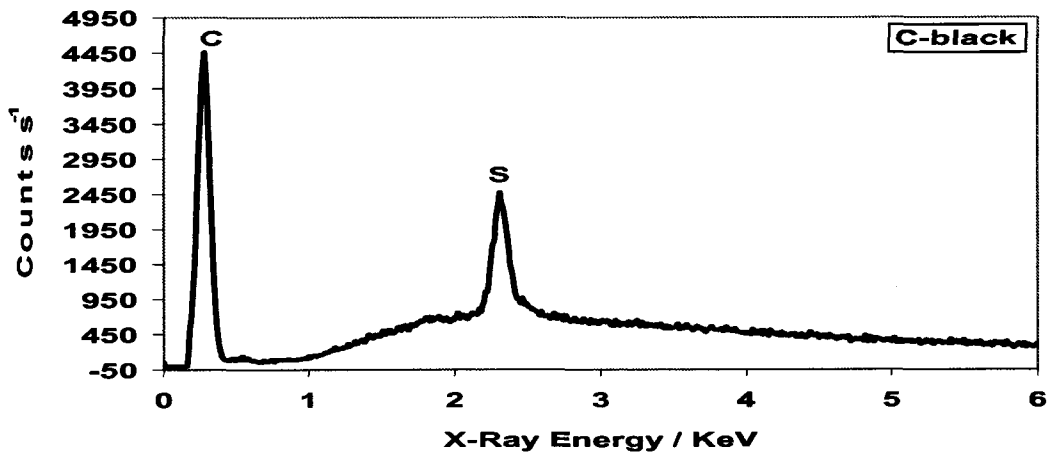


Fig. 3.1.3. Powder EDS analysis showing the elemental distributions in Vulcan XC72R carbon black.

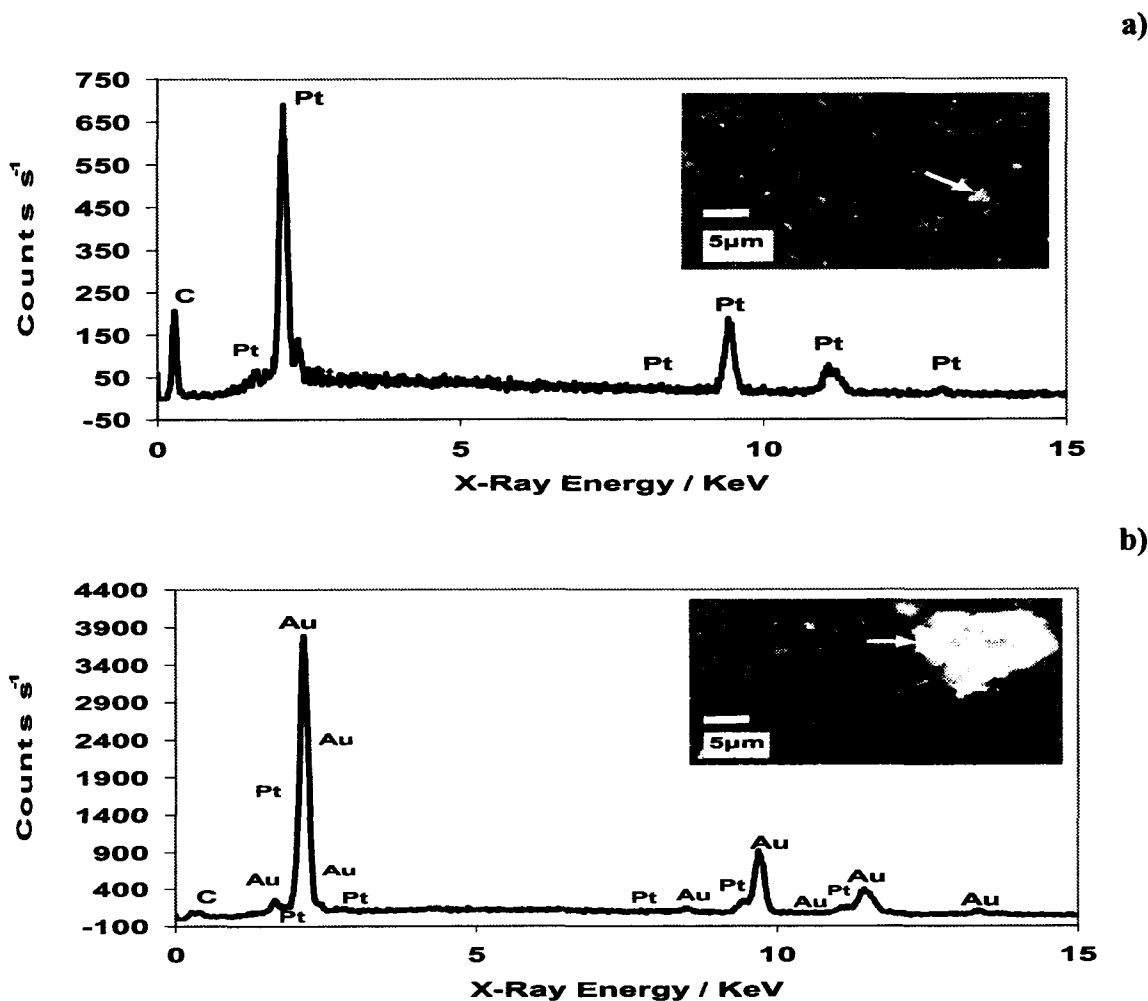


Fig.3.1.4. Powder EDS analysis showing the metal distributions in 20wt% (1:1 atomic ratio) colloidal (a) Pt and (b) Pt-Au.

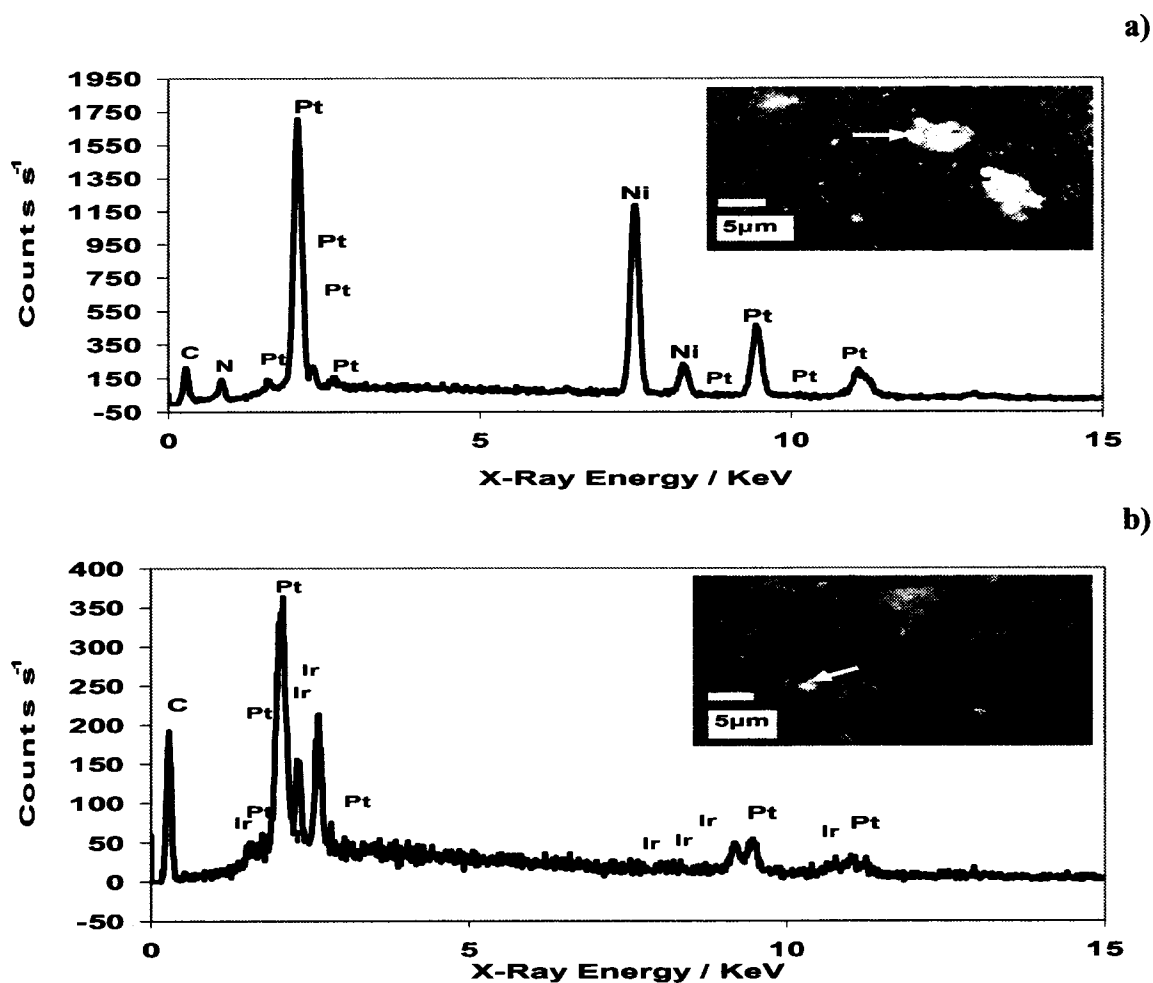


Fig. 3.1.5. Powder EDS analysis showing the metal distributions in 20wt% (1:1 atomic ratio) colloidal (a) Pt-Ni and (b) Pt-Ir.

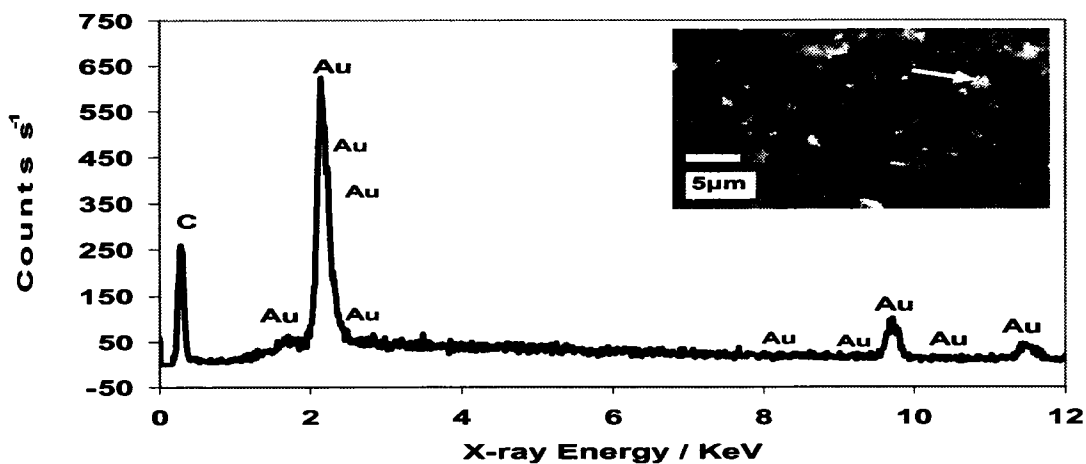


Fig. 3.1.6. Powder EDS analysis showing the metal distributions in 20wt% colloidal Au.

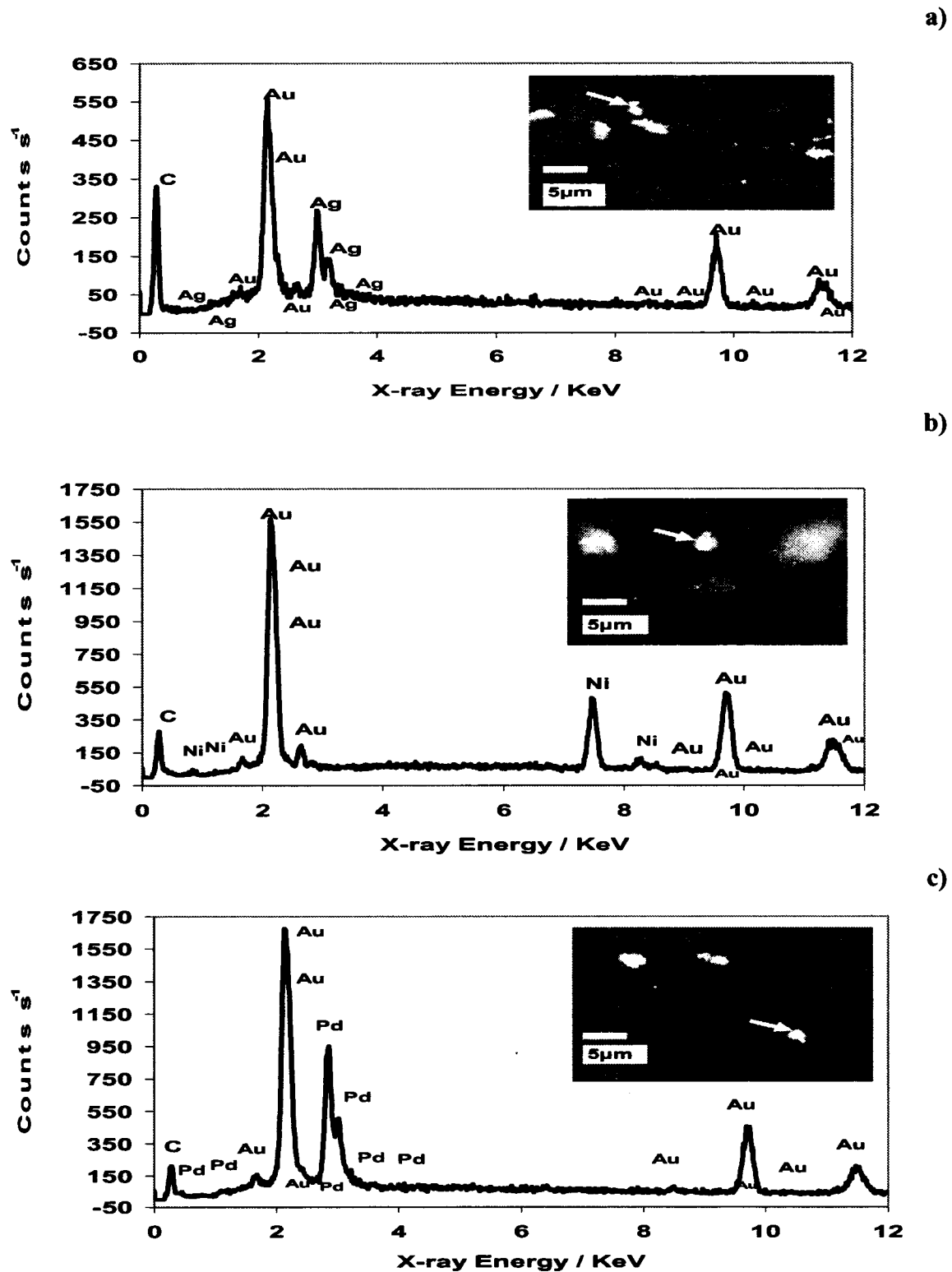


Fig. 3.1.7. Powder EDS analysis showing the metal distributions in 20wt% (1:1 atomic ratio) colloidal (a) Au-Ag, (b) Au-Ni and (c) Au-Pd.



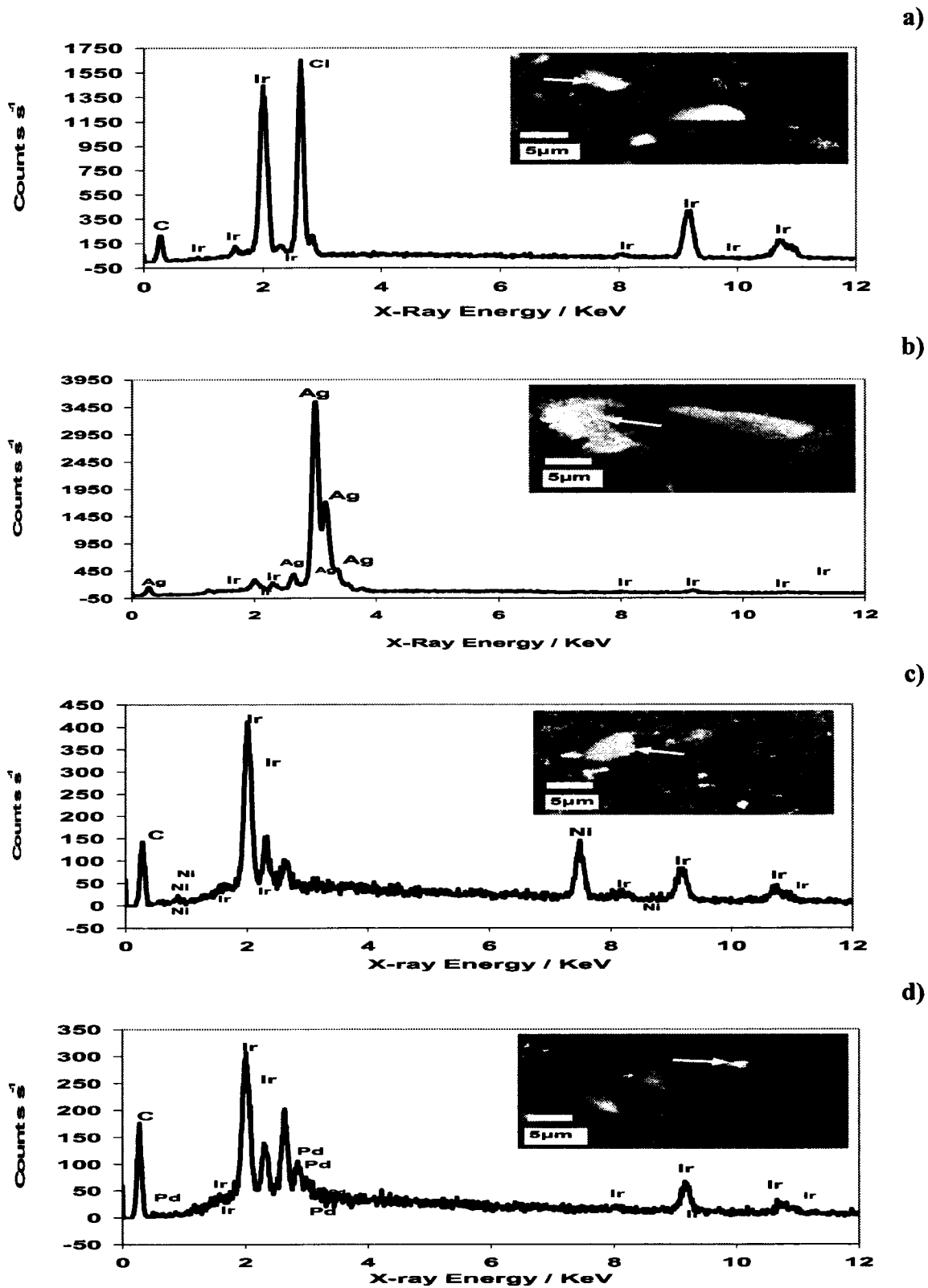


Fig.3.1.8. Powder EDS analysis showing the metal distributions in 20wt% (1:1 atomic ratio) colloidal (a) Ir, (b) Ir-Ag, (c) Ir-Ni, and (d) Ir-Pd.

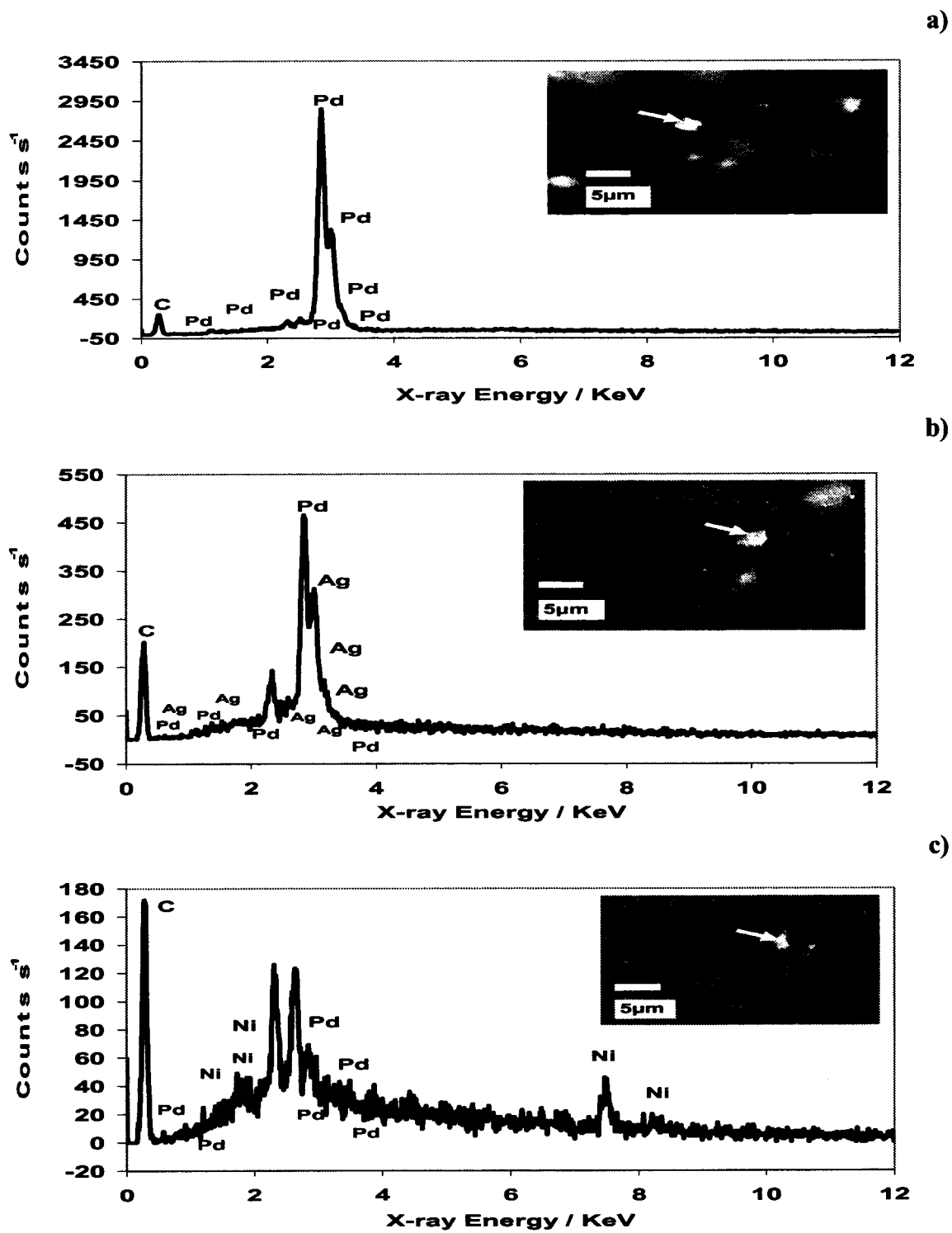


Fig. 3.1.9. Powder EDS analysis showing the metal distributions in 20wt% (1:1 atomic ratio) colloidal (a) Pd, (b) Pd-Ag, and (c) Pd-Ni.

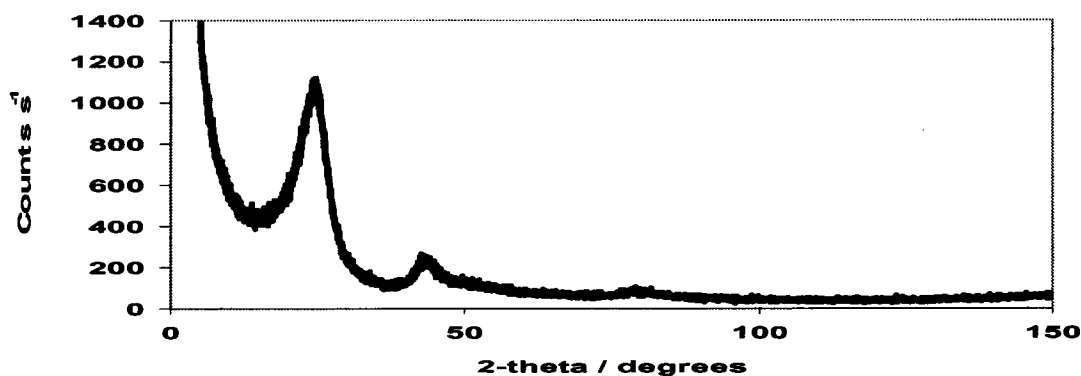


Fig. 3.1.10. X-ray diffraction pattern of powder Vulcan XC 72R carbon black.

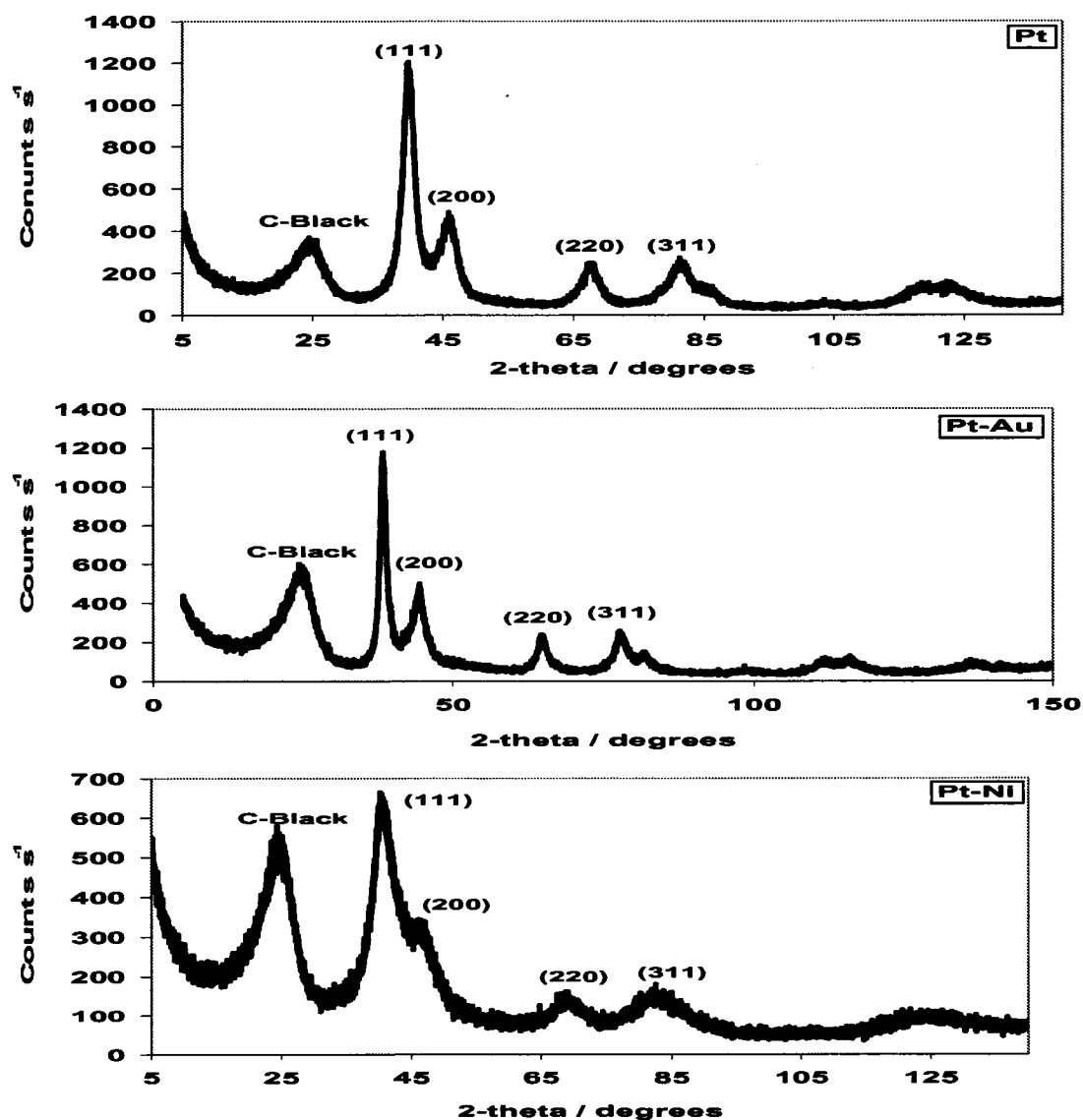


Fig. 3.1.11. X-ray diffraction patterns of powder 20wt% (1:1 atomic ratio) colloidal Pt and Pt-alloys, showing [111], [200], [220], and [311] reflections of the fcc lattice of metallic Pt and its alloys.

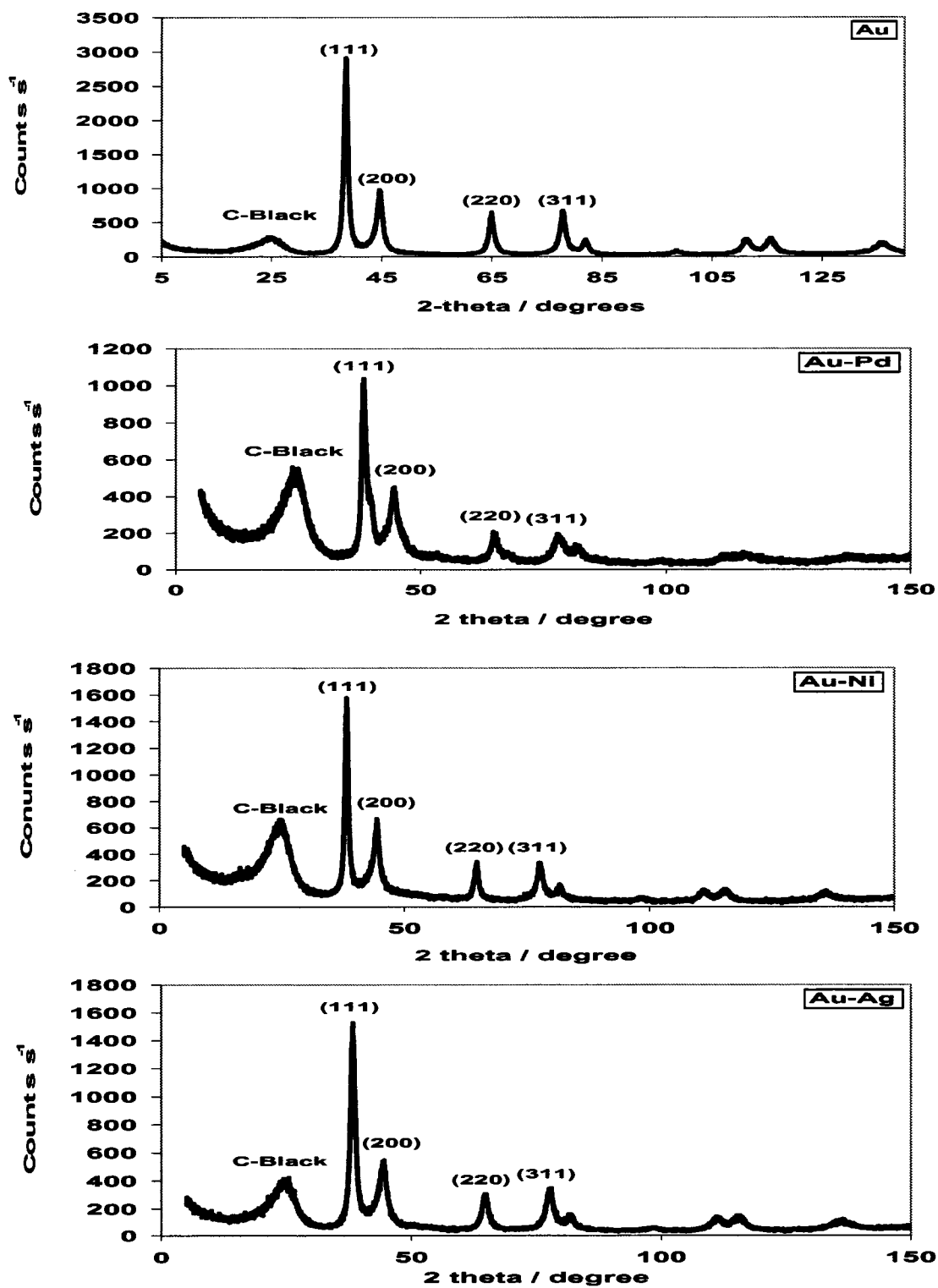


Fig. 3.1.12. X-ray diffraction patterns of powder 20wt% (1:1 atomic ratio) colloidal Au and Au-alloys, showing [111], [200], [220], and [311] reflections of the fcc lattice of metallic Au and its alloys.

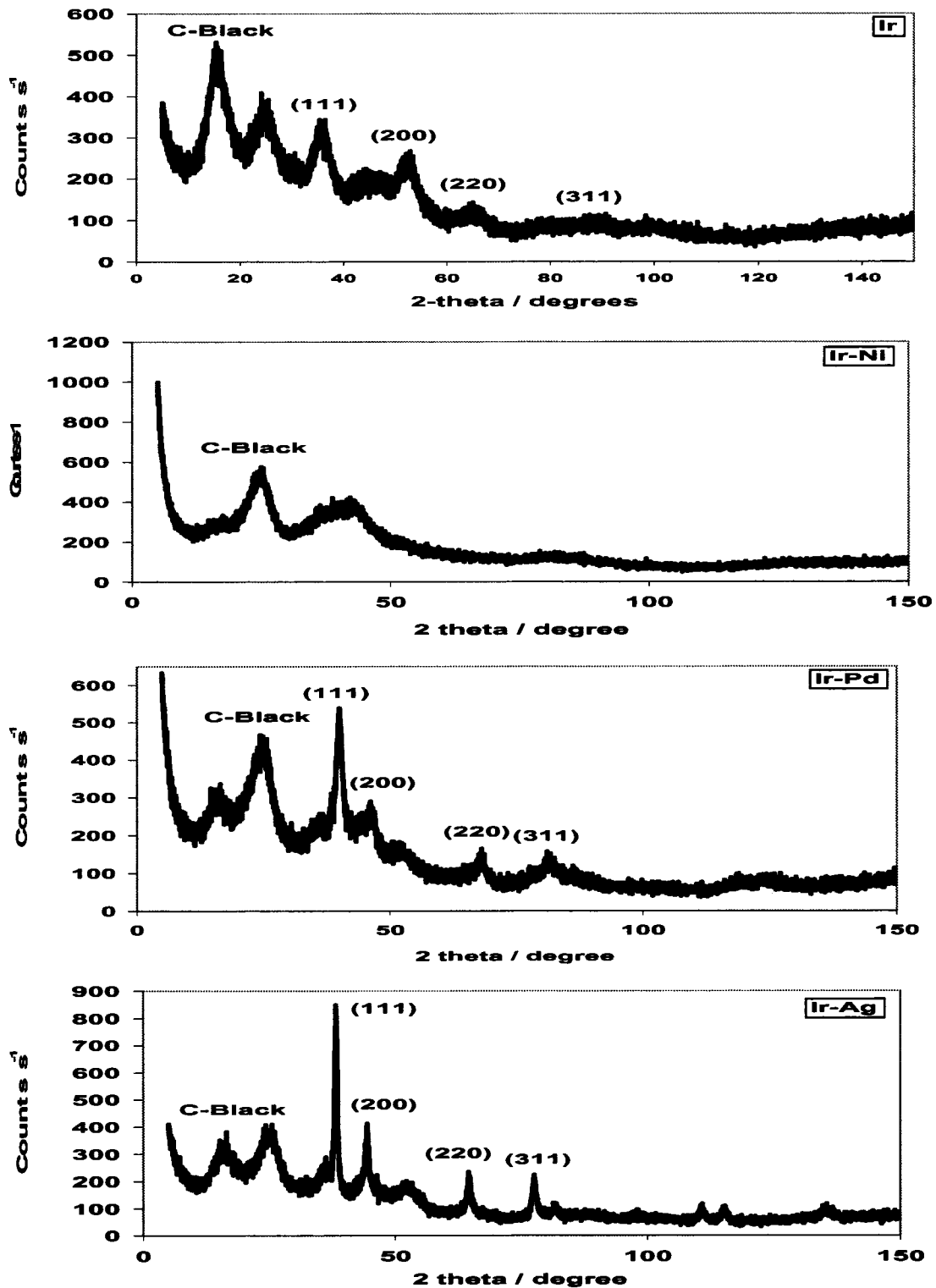


Fig. 3.1.13. X-ray diffraction patterns of powder 20wt% (1:1 atomic ratio) colloidal Ir and Ir-alloys, showing [111], [200], [220], and [311] reflections of the fcc lattice of metallic Ir and its alloys.

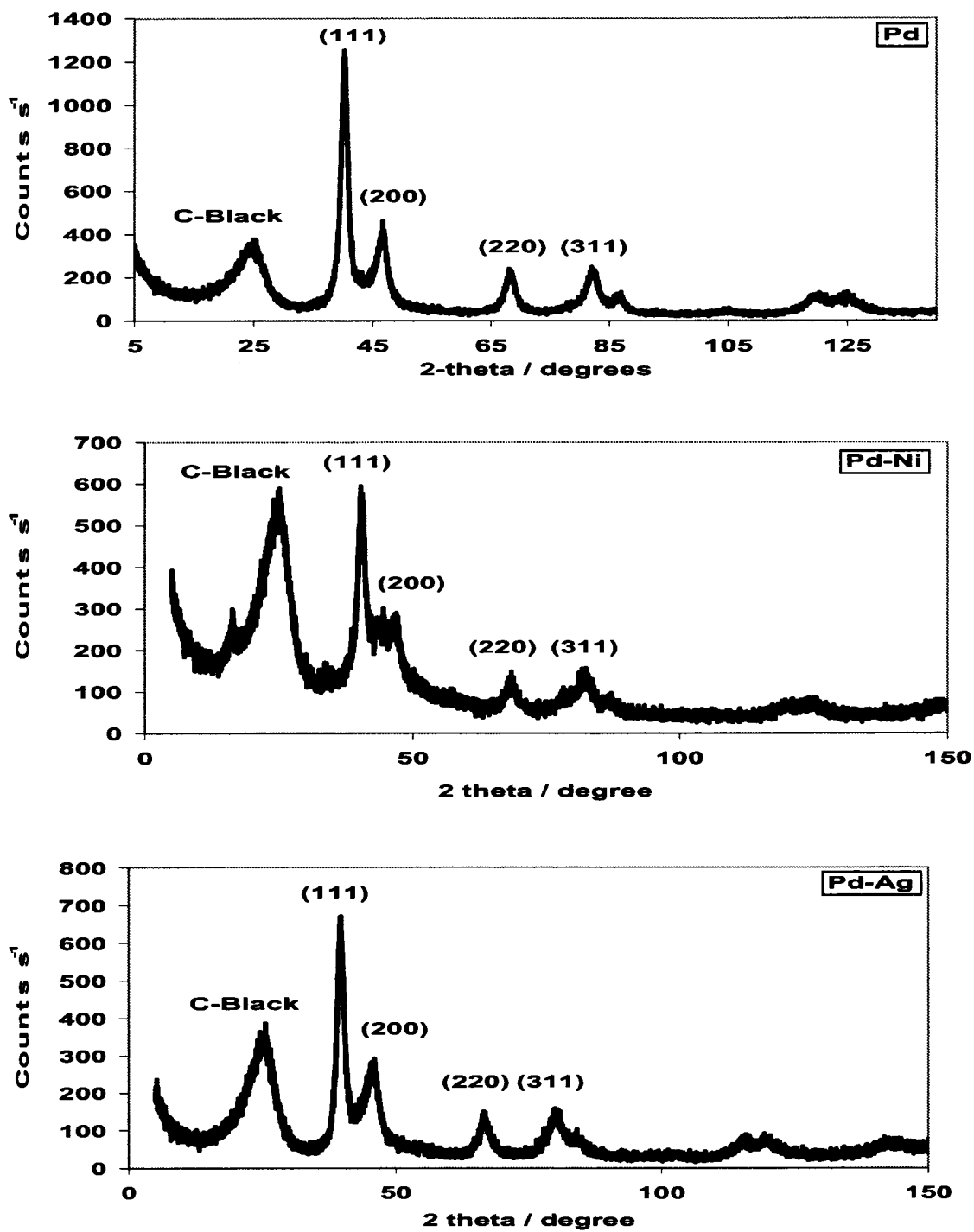


Fig. 3.1.14. X-ray diffraction patterns of powder 20wt% (1:1 atomic ratio) colloidal Pd and Pd-alloys, showing [111], [200], [220], and [311] reflections of the fcc lattice of metallic Pd and its alloys.

### 3.2. Working Electrode preparation

For the electrochemical studies (e.g., cyclic voltammetry, chrono-techniques) the supported metal colloids were fixed on a glassy carbon disk electrode of 3 mm in diameter (Electrosynthesis Inc.). Before the application of the colloid, the glassy carbon (GC) electrode was polished to a mirror finish with 1  $\mu\text{m}$  diamond paste and by 0.05  $\mu\text{m}$  alumina (Cypress System Inc. polishing kit) followed by thorough ultrasonic washing in distilled water. To create a good bonding of the supported metal colloid catalyst to the GC electrode, 5 mg of the carbon supported catalyst powder (20 % wt metal) was ultrasonically dispersed for 45 minutes in a 1 ml solution composed of 0.25 ml Nafion solution 5 % wt (Aldrich) and 0.75 ml ethanol (Aldrich). From the suspension of the supported catalyst and the Nafion, 10  $\mu\text{l}$  was carefully applied on the GC electrode surface yielding for each of the investigated catalysts a constant load per metal basis of 141  $\mu\text{g cm}^{-2}$ . The dispersed catalyst on the GC substrate was dried in a mild  $\text{N}_2$  stream for about 1 h creating a good bonding and electrical contact between the supported catalyst and the GC electrode.

### 3.3. Experimental Cell Set Up

Electrochemical tests were performed using a conventional three-electrode cell arrangement composed of the dispersed colloidal metal GC, two graphite rods with an area of  $\sim 10 \text{ cm}^2$  acting as the counter-electrodes and Hg/HgO, 2M NaOH (B20B400, Radiometer Analytical S. A.) as the reference electrode with a potential of - 0.068 V vs. Ag/AgCl, KCl<sub>std</sub> (or + 0.13 V vs. NHE). In this work all the potentials are referenced vs. Hg/HgO, 2M NaOH abbreviated as MOE. For  $\text{NaBH}_4$  oxidation, 2 M NaOH was used with  $\text{NaBH}_4$  (Alfa Aesar Inc., purity + 97 %wt) with concentrations between 0.03 and 1 M (Fig. 3.3.1).

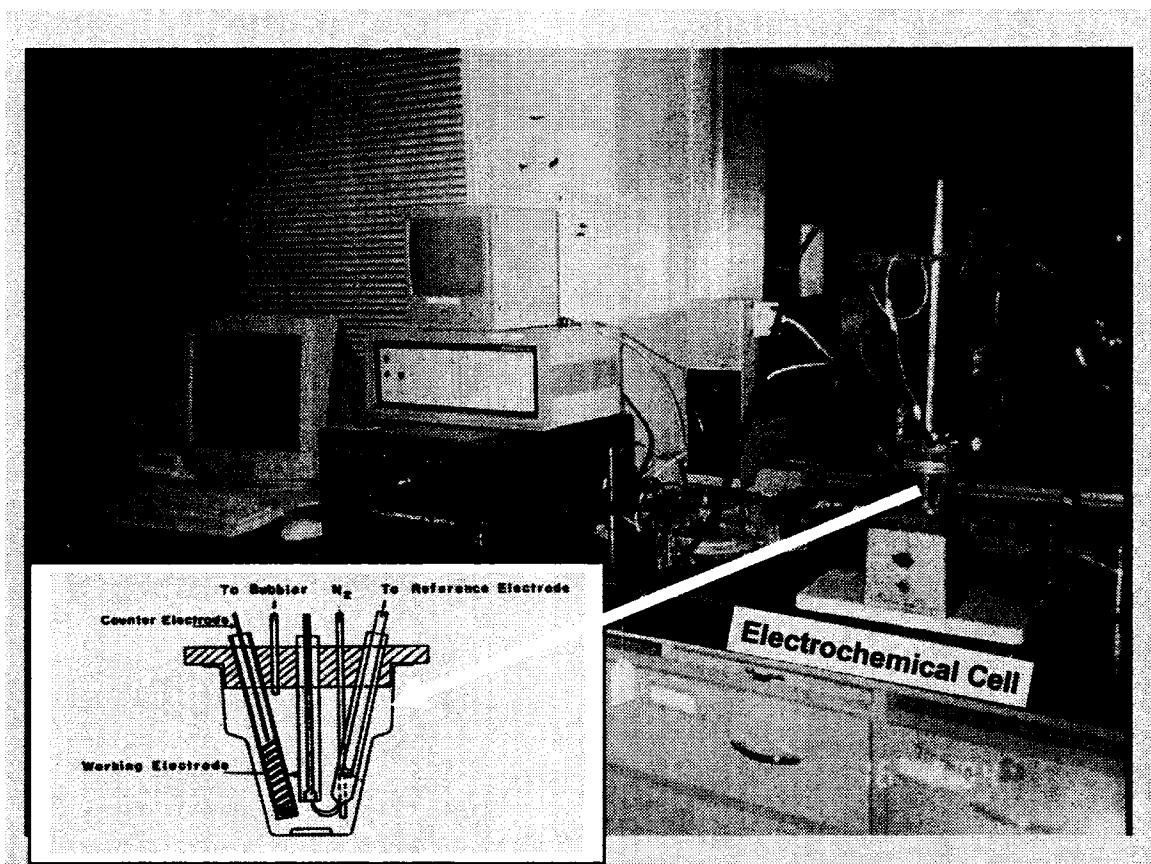


Fig.3.3.1. Set-up of conventional three electrode cell (University of British Columbia, Dept. of Chemical and Biological Eng.).

### 3.4. Electrochemical Measurement Systems

Cyclic voltammetry, chronoamperometry and chronopotentiometry experiments were carried out in  $N_2$  purged electrolytes at 295 K employing either a PAR 263A or a PARSTAT 2263 computer controlled potentiostat (Princeton Applied Research Inc.) and the associated Power Sweep and Power Step software (part of the Power Suite package). Voltammetry on a rotating disc electrode (RDE) experiments were performed by using Volta Lab 80 (PGZ402, Radiometer Analytical S. A.) in conjunction with the glassy carbon electrode tip (A35T090, Radiometer Analytical S. A.), RDE (EDI101, Radiometer Analytical S. A.), and a speed control unit (CTV101, Radiometer Analytical S. A.) (Fig.3.4.1).



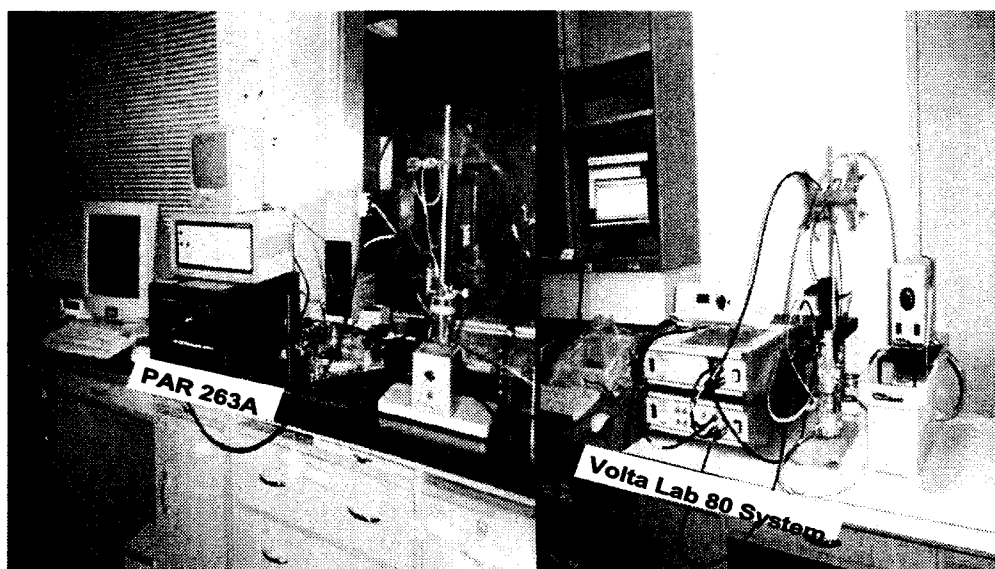


Fig.3.4.1. Electrochemical instrumentation (PAR 363A) for stationary and (Volta Lab 80) for rotating disc tests (University of British Columbia, Dept. of Chemical and Biological Eng.).

### 3.5. Fuel Cell Set Up and MEA Preparation

#### 3.5.1. MEA Preparation

Membrane electrode assemblies (MEAs) used in this study were prepared in the laboratory (University of British Columbia, Dept. of Chemical and Biological Eng.) by forming and applying the anode side onto a half-MEA with Nafion117 membrane supplied by Electrochem Inc. (EC-MEA-C1) where the cathode side consisted of 4 mg Pt cm<sup>-2</sup> and Toray carbon paper as a gas diffusion layer. The anode colloidal catalysts with a metal load of 5 mg cm<sup>-2</sup> were applied on a carbon cloth (ECCC1- 060, Electrochem. Inc.). The procedure consisted of the following steps: 5 mg cm<sup>-2</sup> on metal(s) bases of the colloidal catalyst was mixed with 1 mg cm<sup>-2</sup> Nafion 117 (i.e. corresponding volume of Nafion 5%wt solution) and 0.7 ml ethanol. The mixture was ultrasonically dispersed for 45 minutes. Afterwards, the supported catalyst suspension was applied on the carbon cloth by a technique similar to the decal method [8], followed by drying in a N<sub>2</sub> atmosphere for 12 h. The final stage in the MEA preparation was the hot pressing of the anode catalyst on the carbon cloth substrate, together with another carbon cloth acting as

the anodic backing layer onto the Nafion 117 membrane with the commercial cathode side. Hot pressing was performed at 1200 lb load for 2 min at 160 °C.

### 3.5.2. Fuel Cell Set Up

Tests on direct borohydride fuel cells were performed using the Fideris (Lyntech Industries, Inc.) FCTS MTK system in conjunction with FCPower control software and 5 cm<sup>2</sup> geometric area single fuel cell kits (Fig.3.5.1). Liquid and gas reactant pumping rates are computer controlled at a maximum of 3200 ml min<sup>-1</sup> and 10 standard liters per minute, respectively. The external reservoir capacity is 1000 ml. The heating and cooling systems capacities are both 400 watts. Inlet gas pressure ranges between 100 to 250 psi. The maximum current and voltage ratings and power dissipation are 5 A, 24 V, and 100 watts, respectively. The fuel temperature is set between ambient and 100 °C. The speed of data acquisition of this model is 108 points per minute.

The hot pressed full MEA was assembled together with the end plates using a serpentine flow path. It has been shown that this is superior to other flow paths in enhancing the mass transport inside the cell [9]. Membrane conditioning was performed by recirculating a solution of 2 M *NaOH* at 60 ml min<sup>-1</sup> and 298 K for 2 h prior to each test at open circuit voltage. The pure sodium hydroxide solution was then replaced by a 2 M *NaBH<sub>4</sub>* in 2 M *NaOH* solution at feed at rates of 20, 50, and 85 ml min<sup>-1</sup>. The oxygen flow rate was fixed at 200 ml min<sup>-1</sup> for all tests, with a gauge pressure of ~ 1.7 atm. The tests were started after the fuel cell temperature and the fuel feed flow stream temperatures reached either 298 or 333 K, respectively. The potential vs. current data were recorded.

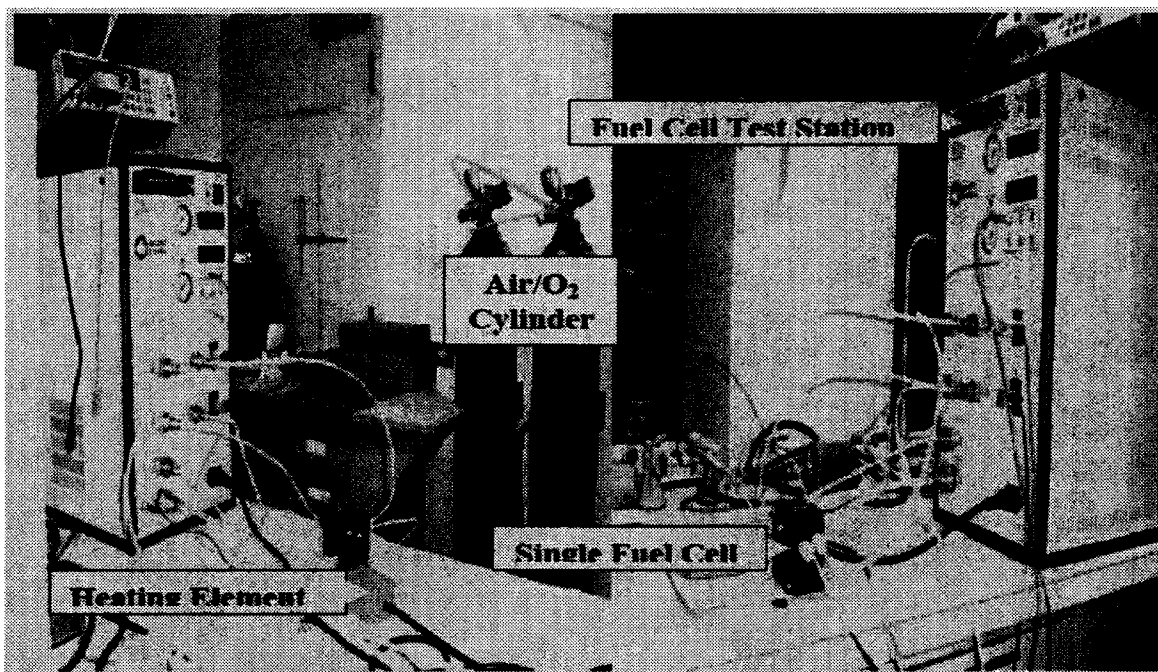


Fig.3.5.1. Lyntech fuel cell test station (University of British Columbia, Dept. of Chemical and Biological Eng.).

### 3.6. Electrochemical Measurement Methods and Related Electrochemical Parameters

In transient techniques measurements are made by perturbing the system from a steady state, and the data is recorded as a function of the perturbation until a new steady state condition is reached. Chronoamperometry (CA), chronopotentiometry (CP), chronocoulometry (CC), potential sweep methods, e.g., cyclic voltammetry (CV), and voltammetry on rotating disc electrode (RDE) are the common types of such techniques and are widely used in the determination of the kinetic parameters, and in the identification of intermediates [10].

Only certain qualitative and/or quantitative electrochemical information can be revealed by each electrochemical technique [11]. Accordingly, since electrocatalysis reactions are rather complicated, their study requires a wide range of electrochemical techniques. CV, CA, CP, CC, and capacitance measurements have been used to determine the mechanism and electrode kinetics of a reaction for an electrocatalyst. In-situ and ex-situ spectroscopic techniques are also useful in giving a detailed insight into the electrode-solution interface during the electrocatalytic reactions [12].

Potential, current, concentration and time are the essential parameters to be measured together with their governing relationships. These relationships are highly influenced by the mode of mass transfer, the kinetics of both the desired heterogeneous of electron-transfer reaction and the side chemical reactions, and the geometrics of both the working electrode and the cell [11].

### 3.6.1. Electrode Kinetics

The importance of the Tafel equation comes from the necessity of knowing the value of the overpotential ( $\eta$ ) that must be subtracted from the open circuit potential of a fuel cell in order for the electrons to flow [10]. In addition, from practical and engineering points of view, the parameters  $i_o$  and  $b_a$  are useful in comparing different electrocatalysts activities for a given electrochemical reaction [13].

#### 3.6.1.1. Activation Polarization

##### 3.6.1.1.1. Exchange Current Density ( $i_o$ ) and Tafel Slope ( $b_a$ )

Exchange current density is defined as the forward or backward reaction velocity, expressed in  $A\ cm^{-2}$ , at equilibrium [10]. A formula describing the electrode kinetics for the reaction,  $O + e^- \Leftrightarrow R$ , can be derived assuming that the electron-transfer processes are first order reactions, and that the rate of oxidation of R, or the reduction of O, depends only on the rate constant and either of their concentrations at the electrode [14]. The rate of the reaction is described by;

$$j = kC^o = \frac{i}{nFA} \quad (3.6.1)$$

The anodic current is:

$$i_a = nFAk_a C_R^o, \quad (3.6.2)$$

The cathodic current is:

$$i_c = -nFAk_c C_O^o \quad (3.6.3)$$

$k_a$  and  $k_c$  can be found from the Arrhenius expression. The substitution for  $k_a$  and  $k_c$  into eq.3.6.1 and 3.6.3 and by taking the sum of these currents, i.e.,  $i = i_a + i_c$  gives [15]:

$$i = nFA[k_a C_R^o \exp(\frac{\alpha_a nF}{RT} E) - k_c C_O^o \exp(\frac{-\alpha_c nF}{RT} E)] \quad (3.6.4)$$

Equation 3.6.4 can be written in terms the overpotential, ( $\eta$ ), as the extra potential required to overcome the energy barrier of the rate determining step to a value such that the electrode reaction proceeds at a desired rate [10]:

$$\eta = E - E_e \quad (3.6.5)$$

In addition, at equilibrium;

$$E = E_e, i_a = i_c = i_o, \text{ and } i = 0 \quad (3.6.6)$$

$$\therefore i_o = nFAk_a C_R^o \exp(\frac{\alpha_a nF}{RT} E_e) = nFAk_c C_O^o \exp(\frac{-\alpha_c nF}{RT} E_e) \quad (3.6.7)$$

The substitution of eq. 3.6.5 into eq. 3.6.4, and by making use of the equalities in eq. 3.6.6 gives a very important equation that is used widely in experimental and applied electrochemistry, and is known as Butler-Erdey-Gruz-Volmer equation (eq. 3.6.8):

$$i = i_o [\exp(\frac{\alpha_a nF}{RT} \eta) - \exp(\frac{-\alpha_c nF}{RT} \eta)] \quad (3.6.8)$$

This equation shows that the measured current is a function of  $\eta$ ,  $i_o$ ,  $\alpha_a$  and  $\alpha_c$ . It also shows that the measured current density at any overpotential is the difference of anodic and cathodic current densities (Fig. 3.6.1) [16].

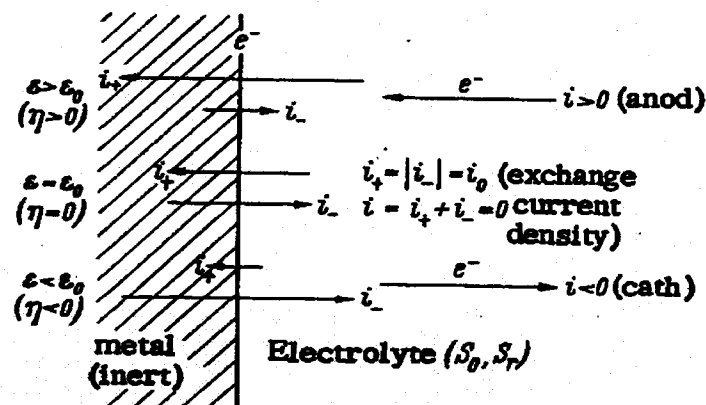


Fig. 3.6.1. Net anodic, zero, and net cathodic overall reactions of a redox electrode. Arrow direction represents the electron flow [17].

The limiting forms are:

a) High field approximation (high  $\eta$ , i.e.,  $\gg 0$ ):

At more negative overpotentials,  $i_c$  increases and  $i_a$  decreases, and accordingly the first term equation 3.6.8 becomes negligible, i.e.,

$$-i = i_o \exp\left(\frac{-\alpha_c nF}{RT} \eta\right), \text{ or} \quad (3.6.9)$$

$$\log(-i) = \log i_o - \frac{1}{b} \eta \quad (3.6.10)$$

b) Low field approximation (low  $\eta$ , i.e.,  $\ll 0$ ):

At more positive overpotentials,  $i_a$  increases and  $i_c$  decreases, and accordingly the second term of equation 3.6.8 becomes negligible, i.e.,

$$i = i_o \exp\left(\frac{\alpha_a nF}{RT} \eta\right) \quad (3.6.11)$$

$$\log i = \log i_o + \frac{\alpha_a nF}{2.3RT} \eta, \text{ or } \eta = b \log \frac{i}{i_o} \quad (3.6.12)$$

$$\text{Where } b = \frac{2.3RT}{\alpha_a nF} \text{ is defined as the Tafel slope} \quad (3.6.13)$$

The Tafel equations 3.6.10 and 3.6.12 are used widely for determining  $i_o$ , and Tafel slope  $b$ . Plotting  $\log i$  vs.  $\eta$ , the exchange current density  $i_o$  and Tafel slope  $b$ , can be determined from the intercept and the slope respectively (Fig.3.6.2) [16].

The Tafel slope ( $b$ ) and the exchange current density ( $i_o$ ) are used, from a practical point of view, as a measure for the electrocatalyst activity for a certain reaction [18, 16]. Fig. 3.6.3 shows how the Tafel slope and the exchange current densities can affect the overpotentials of two hypothetical electrocatalysts [19]. An electrocatalyst with lower values of  $b$  and higher values of  $i_o$ , will leads to a lower overpotential (eq. 3.6.12), and thus a higher electrocatalyst activity is expected [13].

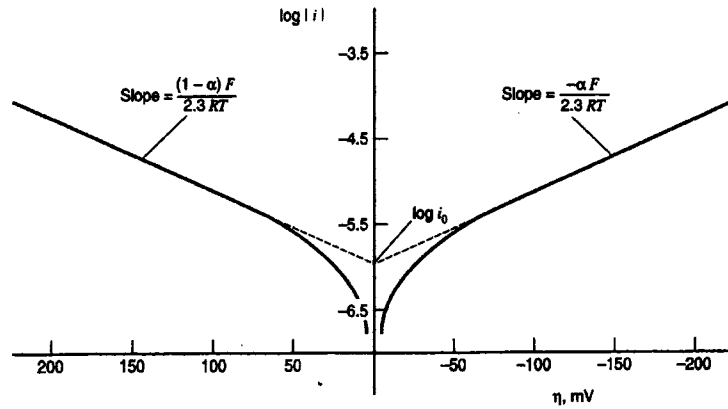


Fig.3.6.2. Experimental determination of exchange current density  $i_0$  and Tafel slope  $b$  [20].

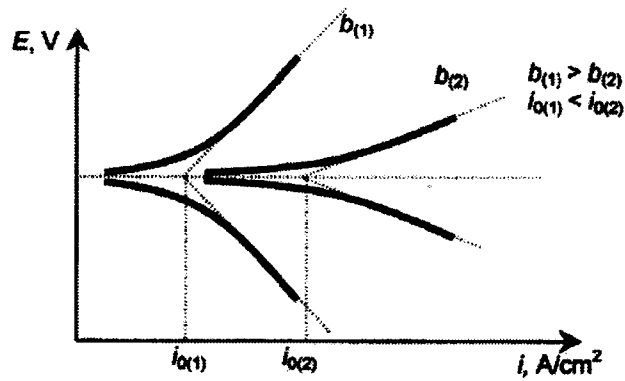


Fig. 3.6.3. A schematic representation shows the effect of Tafel slope  $b$  on  $i_0$  and the overpotential [19].

### 3.6.1.1.2. Concentration Polarization

Under mass transfer control, due to the limited diffusion rate an increase in the potential is required to maintain the desired current density. This extra potential is called concentration overpotential [21]. Consider  $C_R^o$  and  $C_R^s$  as the reactant bulk and surface concentrations of species  $R$  respectively. At high overpotentials,  $C_R^s$  reaches its minimum value and the current density can be determined by Fick's first law;

$$j = D \left( \frac{\partial C}{\partial x} \right)_{x=0}, \because j = \frac{i}{nF} \quad (3.6.14)$$

$$\therefore i = nFD \left( \frac{\partial C}{\partial x} \right)_{x=0} = nFD \frac{C_R^o - C_R^s}{\delta_N} \quad (3.6.15)$$

where,  $\delta_N$  is the Nernst diffusion layer thickness. At  $C_R^s = 0$ , the current will reach a limiting value called diffusion limited current density,  $i_L$  and eq. 3.6.15 becomes:

$$i_l = nFD \frac{C_R^o}{\delta_N} \quad (3.6.16)$$

A relationship between overpotential ( $\eta$ ), as a function of  $i$  and  $i_L$  can be developed from eqs. 3.6.15 and 3.6.16:

$$\eta_c = \frac{RT}{nF} s \ln\left(1 - \frac{i}{i_L}\right) \quad (3.6.17)$$

According to the convention, the stoichiometric factor ( $s$ ) is positive for products and negative for reactants. Therefore, it is expected that  $\eta_c$  is positive for the oxidation reaction (anodic reactions), and negative for the reduction reaction (cathodic reactions) [21].

### 3.6.2. Cyclic Voltammetry

Polarographic investigations (i.e., on a Hg drop electrode) employing the linear sweep voltammetry (LSV) and cyclic voltammetry (CV) have been used for more than 70 years and the continuous developments in the potentiostat have made it possible to apply LSV and CV techniques to a three electrode cell using virtually any solid electrode [22]. Voltammetry is defined as the interdependence of the electrode potential, the current, and the time [12]. It is usually the first technique to be employed in any electrochemical study, since it is easy to perform and provides quick and useful information about the system under investigation, especially in terms of the mechanism of the electrode reactions and the kinetics of the electron transfer process [18]. It is recommended to start with qualitative experiments before heading to semi-quantitative, and finally quantitative, experiments from which kinetic parameters can be obtained [12]. Linear sweep voltammetry (LSV) is the simplest form of such a technique, while the more useful and widely applied technique is cyclic voltammetry (CV). In both CV and LSV, the potential is scanned linearly with time in a repetitive manner (Fig. 3.6.4 and 3.6.5). The wave that peaks at a certain potential is a basic feature of the voltammogram. Scanning rate,



electrode materials, solution composition, and reactant concentration are the factors that affect the peak potential and current, and the shape of the wave. Tafel parameters, diffusion coefficient, number of electrons transferred, and electrochemical rate constant can be determined from the basic CV [13]. The characteristic peak in both CV and LSV can be explained by considering the voltage and mass transfer effects. As the voltage is swept from its initial value the current begins to flow, and it increases as the voltage is swept further to the right hand side. The peak occurs at some point where the diffusion layer has grown sufficiently above the electrode so that the diffusion rate of the reactant to the electrode surface is not fast enough to satisfy that required by the Nernst equation. At this point, the current begins to drop (Figs. 3.6.4 and 3.6.5) [23].

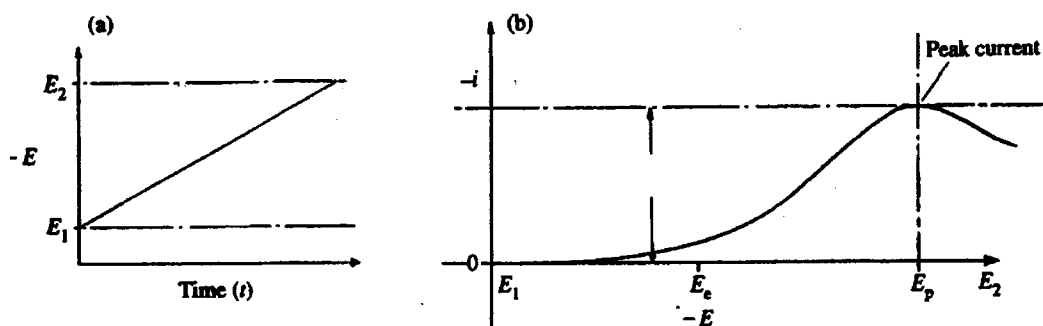


Fig. 3.6.4. (a) the potential sweep, and (b) corresponding current response [18].

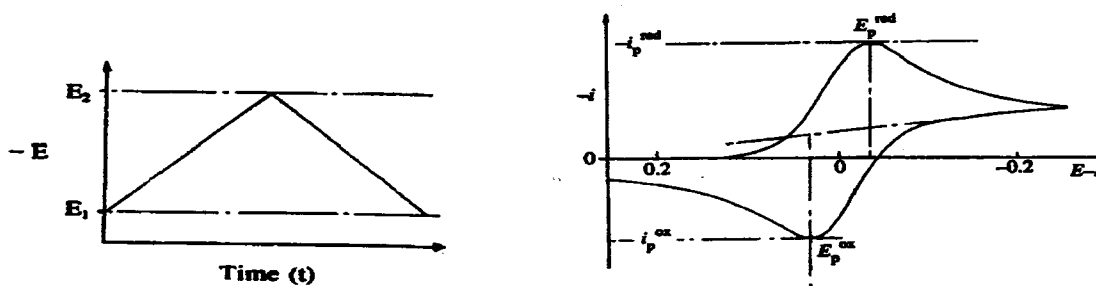


Fig. 3.6.5. Cyclic voltammogram for a reversible electron transfer reaction [18].

### 3.6.2.1. Theory of voltammetry

Fick's second law of diffusion, is the starting point in formulating the governing equation for the CV technique expressing the diffusion-limited peak current density [22].

Assume the reaction,  $R \rightarrow O + e^-$ , and for one direction diffusion:

$$\frac{\partial c}{\partial t} = D \frac{\partial^2 c}{\partial x^2}, \quad (3.6.18)$$

The boundary conditions are as follows [15]:

At  $t = 0$ , only R is present in solution:

$$(i) \ t = 0, \ x \geq 0: \ C_R = C_R^o, \quad (\text{no electrode reaction}) \quad (3.6.19)$$

$$(ii) \ t > 0, \ x \rightarrow \infty : \ C_R = C_R^o, \ (\text{bulk solution}) \quad (3.6.20)$$

(iii)  $t > 0, \ x = 0$ ;  $C_R = C_R^s = 0$ , ( diffusion-limited current), and the flux balance is

$$D_o \left( \frac{\partial C_o}{\partial x} \right)_{x=0} = D_R \left( \frac{\partial C_R}{\partial x} \right) = \frac{i}{nFA} \quad (3.6.21)$$

$$E = E_i + vt, \ \text{where } v = \frac{dE}{dt} \quad (3.6.22)$$

where  $C_R^o$  is the concentration of substance R in bulk solution, and  $C_R$  the concentration of R at any time,  $x$  is the distance from the electrode,  $t$  is the time,  $D$  is the diffusion coefficient,  $n$  is the number of the electrons,  $E$  is the potential at time  $t$ ,  $E_i$  is the starting potential,  $v$  is scanning rate, and  $R$ ,  $T$ , and  $F$  have their usual significance.

#### *Irreversible System, Slow electron transfer*

In a slow electron transfer process, the surface concentration changes slowly. Thus, the maximum gradient of the concentration is reached at more positive potentials. In such processes, diffusion is coupled with electron transfer, and as the scan rate increases the peak potential will shift to a more positive value [21]. Again, for an anodic process, and for  $t > 0, x = 0$  [21]:

$$j = k_a C_R^o = D_R \left( \frac{\partial c_R}{\partial x} \right)_{x=0} = \frac{i}{nFA} \quad (3.6.23)$$

$$k_a = k^o \exp\left[\frac{\alpha n F (E - E^o)}{RT}\right], \quad (3.6.24)$$

where  $E = E_i + vt$ , and  $k^o$  is the standard heterogeneous rate constant ( $\text{cm s}^{-1}$ ).

The solution to eq. 3.6.18 at 298 K for  $A$  in  $\text{cm}^2$ ,  $D_R$  in  $\text{cm}^2 \text{s}^{-1}$ ,  $C_R^o$  in  $\text{mol cm}^3$ , and  $v$  in  $\text{V s}^{-1}$ ,  $i_{p,a}$  in amperes will be [24]:

$$i_{p,a} = 2.99 \times 10^5 n^{3/2} A C_R^o D_R^{1/2} v^{1/2} \alpha^{1/2} \quad (3.6.25)$$

$$\therefore \alpha = \frac{2.3RT}{nbF}, \text{ therefore,}$$

$$i_{p,a} = 2.99 \times 10^5 n A C_R^o D_R^{1/2} v^{1/2} \left(\frac{2.3RT}{bF}\right)^{1/2}, \text{ or} \quad (3.6.26)$$

$$I_{p,a} = 2.99 \times 10^5 n C_R^o D_R^{1/2} v^{1/2} \left(\frac{2.3RT}{bF}\right)^{1/2} \quad (3.6.27)$$

where  $b$  is the apparent Tafel slope (V),  $C_b$  is the bulk borohydride concentration ( $\text{mol cm}^{-3}$ ),  $D$  effective  $\text{BH}_4^-$  diffusivity in the catalyst layer ( $\text{cm}^2 \text{s}^{-1}$ ),  $F$  is the faraday constant ( $\text{C mol}^{-1}$ ),  $i_p$  is the peak current (ampere),  $I_p$  is the peak current density ( $\text{A cm}^{-2}$ )  $n$  the total number of electrons involved in the oxidation,  $R$  the universal gas constant ( $\text{J mol}^{-1} \text{K}^{-1}$ ) and  $T$  temperature (K).

### 3.6.3. Chronoamperometry

Gerischer and Vielstich [24], Vielstich and Gerischer [25] were the first to develop the chronoamperometry technique (CA), in order to study the charge-transfer kinetics. For CA to be performed, a sudden potential step has to be applied, to a working electrode, from a value where no Faradic reactions takes place to a value where the reaction becomes diffusion controlled. The resulting current decay with time is then recorded (Fig.3.6.6). The ability to study the kinetics of mass-transport, charge-transfer, and adsorption are the main advantages of performing such a technique [18]. By this method, the diffusion coefficient, the heterogeneous electron-transfer rate ( $k_h$ ), the number of electrons transferred, and the charge-transfer kinetics can be determined [11].

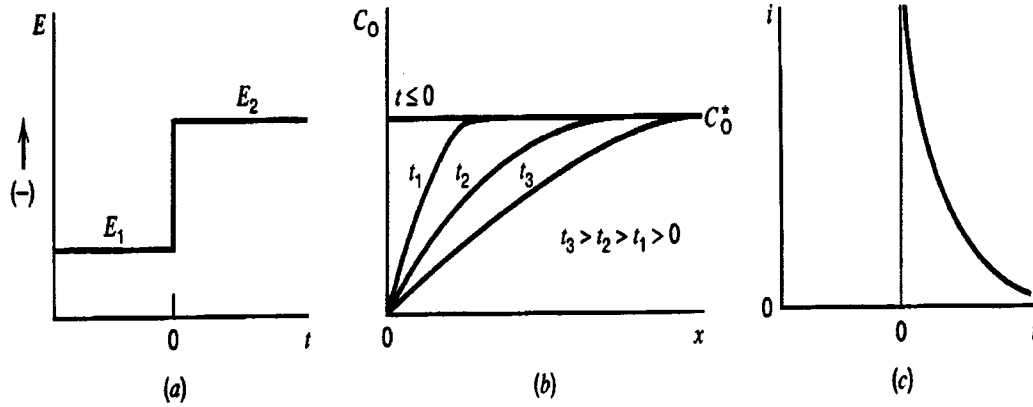


Fig. 3.6.6. The essentials of chronoamperometry (a) Potential step, (b) Concentration variation with distance, and (c) Current-time response [20].

### 3.6.3.1. Theory of Chronoamperometry

For pure diffusion problem, assume the reaction  $R \rightarrow O + e^-$ , and for one direction diffusion, can be described by Fick's second law:

$$\frac{\partial c}{\partial t} = D \frac{\partial^2 c}{\partial x^2}, \quad (3.6.18)$$

Boundary conditions [17]:

At  $x = 0, t > 0, C_R = C_R^s$ , and this surface concentration is controlled by the overvoltage,

At  $x \rightarrow \infty, t > 0, C_R = C_R^o$ , i.e., bulk concentration,

$$\text{At } t = 0, x > 0, \left( \frac{\partial C}{\partial x} \right)_{t=0} = 0,$$

$$\text{At } t > 0, x = 0, \left( \frac{\partial C}{\partial x} \right)_{x=0} = \frac{i}{nFAD_R}, \text{ from Fick's first law,}$$

The solution of the partial differential eqn. 3.6.1, using above boundary conditions is:

$$i = \frac{nFAC_R^o \sqrt{D_R}}{\sqrt{\pi \cdot t}} \left[ 1 - \exp\left(-\frac{nF\eta_c}{RT}\right) \right], \text{ or} \quad (3.6.28)$$

$$I = \frac{nFAC_R^o \sqrt{D_R}}{A_s \sqrt{\pi \cdot t}} \left[ 1 - \exp\left(-\frac{nF\eta_c}{RT}\right) \right] \quad (3.6.29)$$

where,  $I = iA_s$  is the superficial current density ( $A\text{ cm}^{-2}$ ),  $A_s$  is the superficial (geometric) electrode area,  $i$  is the current in amperes,  $A$  is the effective (electrochemically active) electrode area, and  $\eta_c$  from [21]:

$$\eta_c = \frac{RT}{nF} s \ln\left(1 - \frac{i}{i_L}\right), \text{ where } s \text{ is the stoichiometric coefficient} \quad (3.6.17)$$

Eq.3.6.28 gives the diffusion controlled time-dependence of the current density, which is well known as the Cottrell equation [17], from which the diffusion coefficient or the number of electrons transferred can be determined when  $I\sqrt{t}$  vs.  $t$  is constant [26]. Figure 3.6.7 shows the current-time responses for a step change.

In case of at  $x = 0, t > 0, C_R^s = 0$ , the Cottrell eq. (3.6.28) becomes [27]:

$$i = \frac{nFAC_R^o\sqrt{D_R}}{\sqrt{\pi \cdot t}} \quad (3.6.30)$$

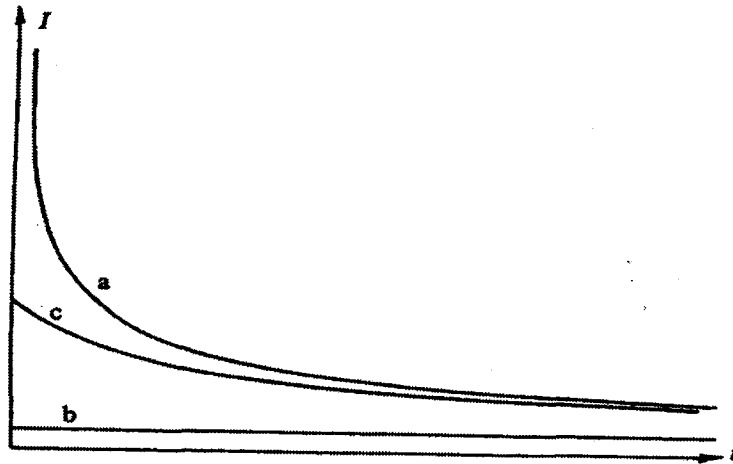


Fig. 3.6.7. A current-time response for a potential step experiment. The potential step is chosen so that, a) The reaction is diffusion control, b) Kinetically controlled, and c) Mixed controlled [26].

### 3.6.4. Chronocoulometry

Anson [14] were the first to develop this technique, which is another way of analyzing the CA data, by integrating the current, so that the charge is given as a function of time [20].

### 3.6.4.1. Theory of Chronocoulometry

#### *Irreversible System*

The interfacial electron-transfer kinetics in irreversible systems is not as fast as in case of reversible systems. Thus, the response to a potential step is influenced by parameters such as  $k_a$ ,  $k_c$ ,  $k^0$ , and  $\alpha$ , which in turn can be evaluated from those responses [18].

For a potential step from where there is no current flow to anywhere on the oxidation wave for the irreversible reaction  $R \rightarrow O + e^-$ , and for one direction diffusion on a planar electrode, the equations governing this case are [20]:

$$\frac{\partial c}{\partial t} = D \frac{\partial^2 c}{\partial x^2}, \quad (3.6.18)$$

The solution to eq. 3.6.18 will be:

$$Q = nFAk_a C_R^o \left( \frac{2t^{1/2}}{H\pi^{1/2}} - \frac{1}{H^2} \right) \quad (3.6.31)$$

and for the superficial charge density  $Q$  in  $C\text{ cm}^{-2}$ , eq. 3.6.31 becomes:

$$Q = nF \left( \frac{A}{A_s} \right) k_h C_R^o \left( \frac{2t^{1/2}}{H\pi^{1/2}} - \frac{1}{H^2} \right) \quad (3.6.32)$$

where  $H$  can be found by the relation:

$$H = \frac{\pi^{1/2}}{2t_i^{1/2}} \quad (3.6.33)$$

where  $t_i$ , is the intercept of the extrapolated linear domain on the  $t^{1/2}$  axis of the plot  $Q$  vs.  $t^{1/2}$ , Fig. 3.6.8. By knowing  $H$  and other parameters,  $k_a$  can be determined from the

linear slope  $= 2nF \left( \frac{A}{A_s} \right) k_a C_R^o / (H\pi^{1/2})$ .

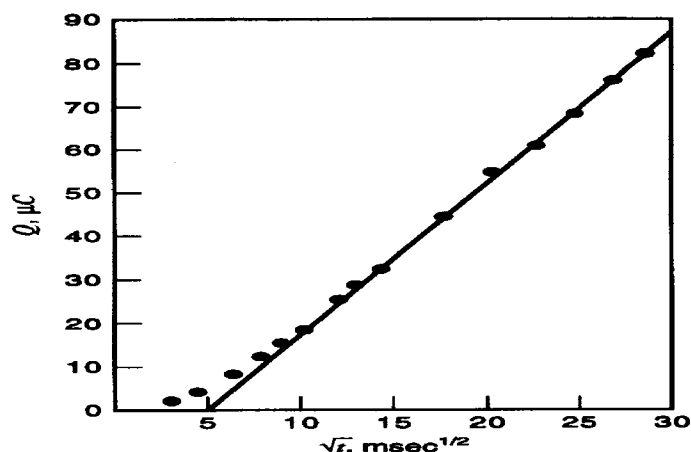


Fig. 3.6.8. Chronocoulometric response for 10 mM  $\text{Cd}^{2+}$  in 1 M  $\text{Na}_2\text{SO}_4$  [20].

### 3.6.5. Chronopotentiometry

Chronopotentiometry (CP), or constant-current, theory was first proposed by Weber (1879), Sand (1901), Karoglanoff (1906), and Rosebrugh and Miller (1910) (References 126-129 in [11]). It was described experimentally by Gierst and Juliard (1953), Delahay and Mamantov (1955), and Reilly, Everett, and Johns (1955) (References 132-134 in [11]).

It is performed by applying a current step to the working electrode and the measured potential with time is recorded (Fig 3.6.9).

The parameters of interest in the  $E-i$  response curve are the value of  $\tau$ , the shape of the  $E-i$  curve, and their dependencies on the applied current [11]. Less attention has been paid to CP, compared to the alternative techniques, because of the difficulties in determining an accurate transition time [11].

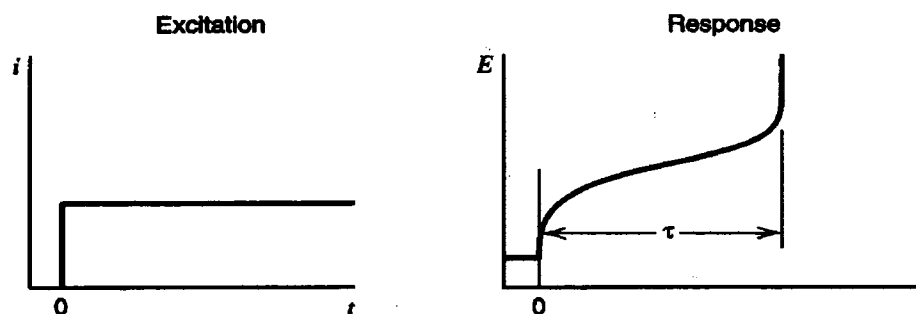


Fig.3.6.9. Variation of potential with time for a step change in applied current [20].

### 3.6.6. Summary of Electrochemical Techniques Employed in this Study

Table 3.6 gives a summary of the electrochemical techniques employed in this study. Also contained in this Table are the references to the relevant equations used in the analysis, together with a summary of the measured parameters (basically current, potential and time) and the calculated electrochemical parameters.

Table. 3.6. Summary of the electrochemical techniques employed together with the relevant equations and the measured and calculated parameters.

Electrochemical Technique	Useful Formula	Measured Parameters			Calculated Parameters				
		<i>i</i>	<i>E</i>	<i>t</i>	<i>n</i>	<i>A</i>	<i>b<sub>a</sub></i>	<i>i<sub>o</sub></i>	<i>k<sub>h</sub></i>
CV	3.6.27	•	•		•				
CA	3.6.29	•		•		•			
CC	3.6.32	•		•					•
RDE/ Tafel Plot	3.6.12	•	•				•	•	
FC		•	•						

### 3.7. References

1. H. Bönneinan, W. Brijoux, R. Brinkmann, E. Dinjus, T. Joußen, B Korall, *Angew. Chem. Int. Engl.*, 30 (10) (1991) 1312-1314.
2. M. Götz and H. Wendt, *Electrochim Acta*, 43, 24 (1998) 3637-3644.
3. R. Richards, R. Mortel, H. Bonnemann, *Fuel Cell Bulletin*, 4, 37 (2001) 7-10.
4. H. Bönneinan, Private Communication, October 16, 2003.
5. H. Bönneinan, U. Endruschat, J. Hormes, G. Kohl, S. Kruse, H. Modrow, R. Mortel, K.S. Nagabhushana, *Fuel Cells*, 4, 3 (2004) 297-308.
6. D. Lewis, E. S. Wheeler, D. O. Northwood, *J. Educational Modules for Materials Science and Engineering*, 4 (4) (1982) 665-700.
7. T. Kovacs, *Principles of X-ray Metallurgy*, Iliffe Book Ltd, London, (1969) 151-152.
8. H. Dohl, J. Mergel, D. Stolen, *J. Power Sources*, 111 (2002) 268-282.
9. A.S. Arico, P. Creti, V. Baglio, E. Modica, V. Antonucci, *J. Power Sources* 91 (2000)
10. J. O'M. Bockris, S. Srivinasan, *Fuel Cells: Their Electrochemistry*, McGraw Hill, NY (1969) 469-486.
11. B. W. Rossiter, J. F. Hamilton, *Physical Methods of Chemistry, Vol. II, Electrochemical Methods*, John Wiley, NY (1986) 191-271, 525-589.
12. K. B. Oldham, J. C. Myland, *Fundamentals of Electrochemical Science*, Academic Press, Inc., NY (1994) 263-303, 179-227.



13. E. Gileadi, E. Kirowa-Eisner, J. Penciner, *Interfacial Electrochemistry An Experimental Approach*, Addison-Wesley Publishing Company, Inc., Massachusetts (1975) 347-430, 179-181.
14. F. C. Anson, *Anal. Chem.*, 38 (1966) 54.
15. R. S. Nicholson, I. Shain, *Analytical Chemistry*, 36, 4 (1964) 706-723.
16. D. Oletcher, F. Walsh, *Industrial Electrochemistry*, Chapman and Hall, New York (1993) 1-38.
17. K. J. Vetter, *Electrochemical Kinetics*, Academic Press, NY (1967) 213-216.
18. A. C. Fisher, *Electrode Dynamics*, Oxford University Press, Oxford (1996) 27-50.
19. S. H. Jordanov, P. Paunovic. O. Popovski, A. Dimitrov, D. Slavkov, *Bull. Chem. Tech. of Macedonia*, 23 (2) (2004) 101-112.
20. A. J. Bard, L. R. Faulkner, *Electrochemical Methods Fundamental and Applications*, 2<sup>nd</sup> Ed., JW, NY (2001) 156-260, 331-348.
21. C. H. Hamann, A. Hamnett, W. Vielstich, *Electrochemistry*, Wielt-VCH, Weinheim (1998) 143-179, 227-234.
22. W. Vielstich, *Handbook of Fuel Cells-Fundamental, Technology, and Applications*, John Wiley, vol. 2 (2003) 153-162.
23. J. Wang, *Analytical Electrochemistry*, John Wiley, NY (2000) 28-59.
24. H. Gerischer, W. Vielstich, *Z. Phys. Chem.*, 3 (16) (1955).
25. W. Vielstich, H. Gerischer, *Z. Phys. Chem.*, 4 (10) (1955).
26. R. Greef, P. Peat, L. Peter, D. Pletcher, J. Robinson, *Instrumental Methods in Electrochemistry*, John Wiley, NY (1985) 113-147, 229-250, 356-364.
27. C. M. A. Brett, A. M. O. Brett, *Electrochemistry Principles, Methods, and Applications*, Oxford University Press, Oxford (1993) 70-102, 174-198.

## CHAPTER 4

### RESULTS AND DISCUSSION

#### 4.1. Osmium and Osmium-Alloys

Prior to this study, there was limited information available in the open literature on methanol oxidation on Os. Kua and Goddard [1], using computational chemistry techniques, presented detailed charts for the heat of formation for both methanol dehydrogenation and water oxidation pathways for *Pt*, *Ir*, *Os*, *Pd*, *Rh* and *Ru*. They confirmed the bifunctional action of *Pt-Ru* towards  $CH_3OH$  and  $H_2O$  oxidation. They also concluded that pure *Os* could favor both the  $CH_3OH$  and  $H_2O$  oxidation recommending therefore the experimental testing of this hypothesis [1]. *Pt-Os* alloys have been experimentally investigated for methanol oxidation largely with negative results [2, 3]. Gökağaç and Kennedy [2] found that for certain *Os* to *Pt* atomic ratios the formation of surface Os-oxide inhibits the methanol oxidation reaction. Moore et al [3] found that the presence of *Os* leads to a lower open-circuit potentials and higher overpotentials as compared to both pure *Pt* and *Pt-Ru*.

##### 4.1.1. Comparative Cyclic Voltammetry of Methanol on Colloidal Os and Os-alloys

Figures 4.1.1 and 4.1.2 show the cyclic voltammograms recorded for  $CH_3OH$  on colloidal 20 %wt Os (20 and 30 %wt) and colloidal 20 %wt (1:1 atomic ratio) Os-Mo, Os-Sn and Os-V, respectively. In both figures the methanol concentration was 1 M in 0.5 M  $H_2SO_4$ , and the potential range of -0.1 to +0.7 V vs. Ag/AgCl,  $KCl_{std}$ . No oxidation peaks were observed, and these findings, are in a good agreement with the negative results that were obtained by previous experimental studies on *Pt-Os* electrocatalysts [2, 3]. However, on the other hand, they contradict the theoretical findings of Kua and Goddard [1], who based on the calculated heats of formation, for *Pt*, *Ir*, *Os*, *Pd*, *Rh* and *Ru*, suggested that *Os* could oxidize both  $CH_3OH$  and  $H_2O$ .

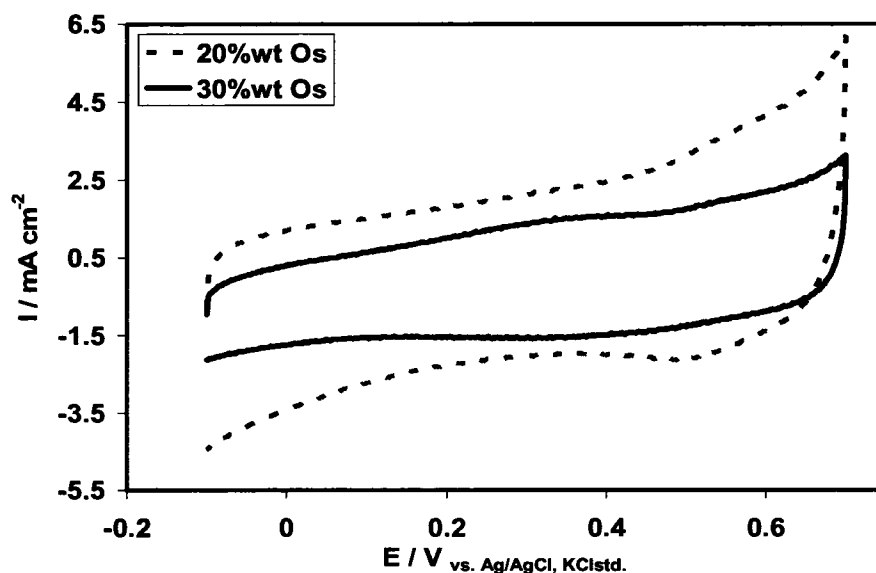


Fig. 4.1.1. Cyclic voltammogram of 1 M methanol in 0.5 M H<sub>2</sub>SO<sub>4</sub> on colloidal Os. Scan rate 50 mV s<sup>-1</sup>, temperature 295 K.

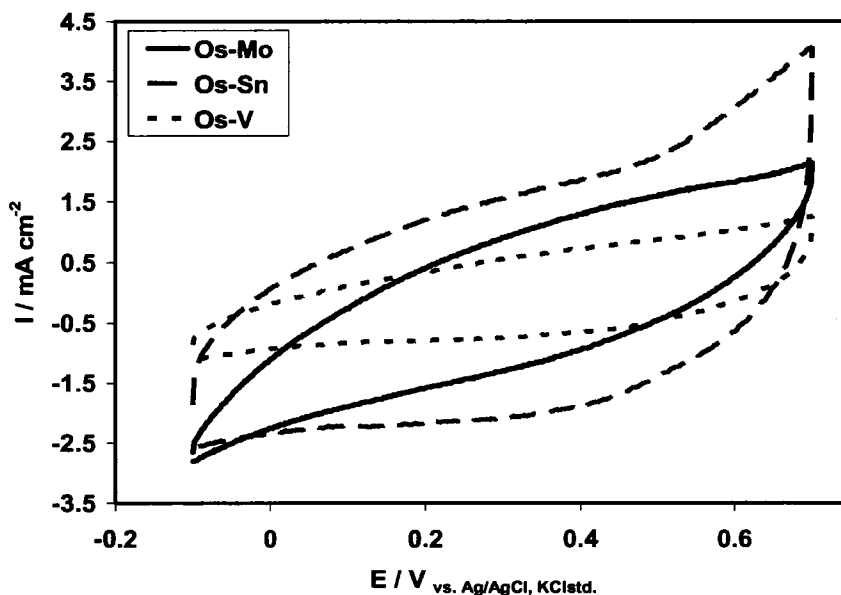


Fig. 4.1.2. Cyclic voltammogram of 1 M methanol in 0.5 M H<sub>2</sub>SO<sub>4</sub> on 20 %wt colloids Os-Mo, Os-Sn and Os-V (1:1 atomic ratio). Scan rate 50 mV s<sup>-1</sup>, temperature 295 K.

#### 4.1.2. Cyclic Voltammetry (CV) of $\text{BH}_4^-$ on Colloidal Os and Os-alloys

Fig. 4.1.3 and 4.1.4 show the cyclic voltammograms of 0.03 M  $\text{BH}_4^-$  on Os and Os-alloys colloids. The potential range was -1.0 to +0.5 V vs. Ag/AgCl,  $\text{KCl}_{\text{std}}$ . Oxidation peaks were observed at 0.187, 0.187 and 0.27 V vs. Ag/AgCl,  $\text{KCl}_{\text{std}}$  on 10%, 20% and 30% Os, respectively. Further investigation is needed to verify that these peaks resulted from borohydride oxidation, since according to the potential-pH graph for Os [4], these peaks could be attributed to Os oxide formation. Alloying Os with Mo, V and Sn would affect the catalytic behaviour toward borohydride oxidation. Figure 4.1.4 compares the cyclic voltammograms of 0.03 M  $\text{NaBH}_4$  in 2 M  $\text{NaOH}$  on the colloidal alloys Os-Mo, Os-V and Os-Sn (1:1 atomic ratio). In the potential range relevant for the direct oxidation of borohydride, i.e. -0.4 to +0.2 V vs. SSCE the cyclic voltammograms show that Os-Sn had a very poor activity characterized by current densities below  $20 \text{ mA cm}^{-2}$ . From a cyclic voltammetry standpoint, Os-Mo and Os-V gave a better response with peak current densities up to  $40 \text{ mA cm}^{-2}$ . The oxidation peaks, on colloidal 20wt% (1:1 atomic ratio) Os-Mo, Os-Sn and Os-V, occur at 0.196, 0.185 and 0.115 V vs. Ag/AgCl,  $\text{KCl}_{\text{std}}$ , respectively.

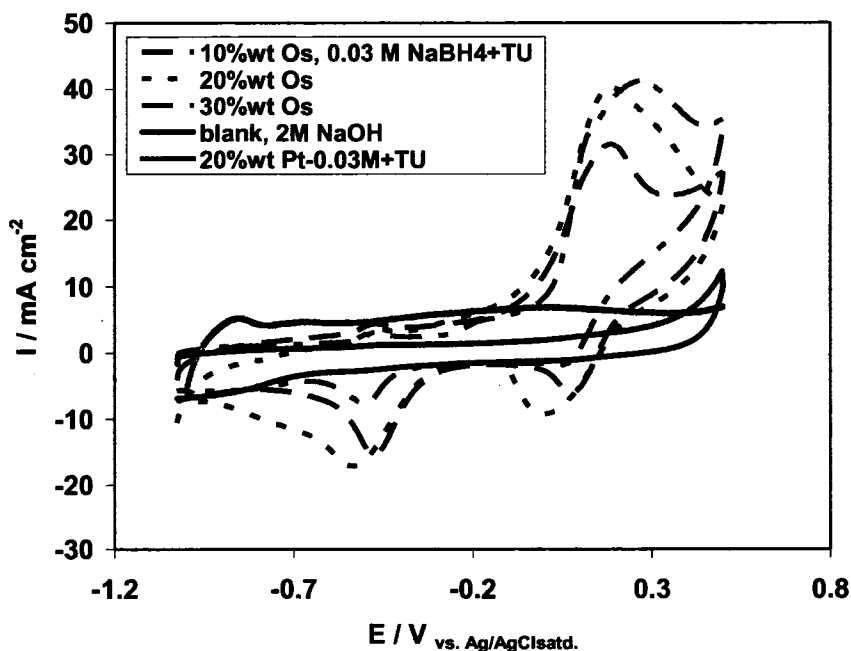


Fig. 4.1.3. Cyclic voltammetry of 0.03 M  $\text{NaBH}_4$  in 2 M  $\text{NaOH}$  on colloid 20%wt Os. Alloy load  $30 \mu\text{g cm}^{-2}$ , and on 20%wt Pt Temperature 295 K.

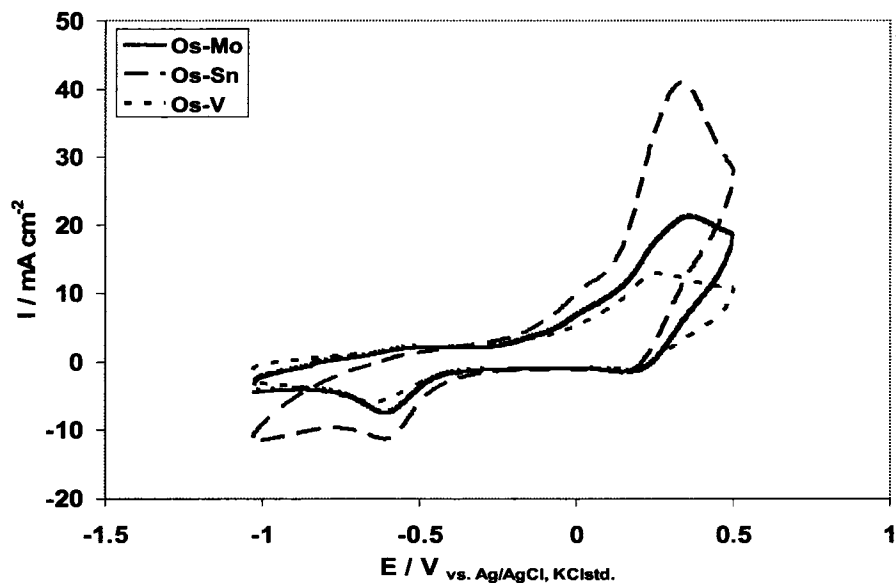


Fig. 4.1.4. Cyclic voltammetry of 0.03 M  $\text{NaBH}_4$  in 2 M NaOH on colloidal 20%wt (1:1 atomic ratio) Os-Mo, Os-V and Os-Sn. Alloy load  $30 \mu\text{g cm}^{-2}$ . Temperature 295 K.

Fig. 4.1.5 shows the  $\text{BH}_4^-$  concentration dependence of  $I_p$  at a constant scan rate of  $100 \text{ mV s}^{-1}$ . The peak current increased sharply with concentration up to 0.1 M, and then leveled off.

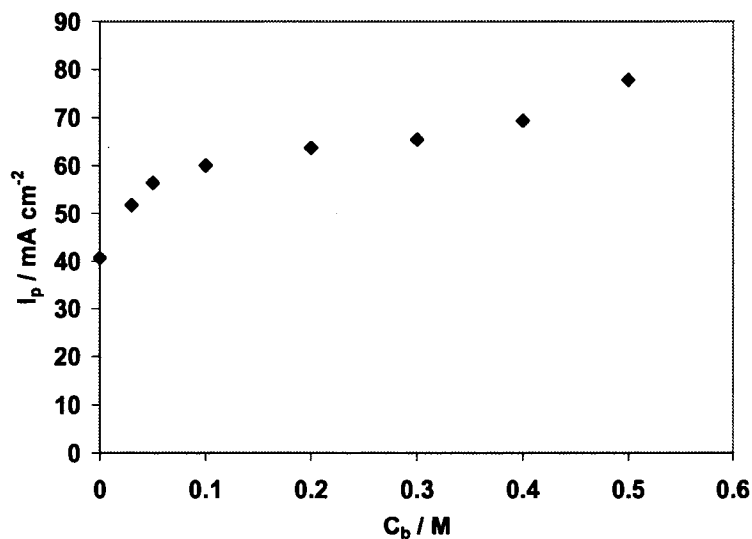


Fig. 4.1.5. Concentration dependence of the peak current  $I_p$  for the oxidation of 0.03 M  $\text{BH}_4^-$  in 2 M NaOH with  $1.5 \times 10^{-3}$  M TU on colloidal 20wt% Os at 298 K.

#### 4.1.3. Effect of Thiourea (TU) on the Electro-oxidation of $BH_4^-$ on Colloidal Os

Thiourea is a well-known corrosion inhibitor for iron in acidic media. It is also known as a hydrogen evolution inhibitor. Thus, it could potentially influence the  $BH_4^-$  oxidation by affecting the hydrolysis and hydrogen evolution reactions.

Fig. 4.1.6 shows the cyclic voltammogram of 2 M NaOH, 2 M NaOH with  $1.5 \times 10^{-3}$  M TU, and 0.03 M  $NaBH_4$  in 2 M NaOH with  $1.5 \times 10^{-3}$  M TU on colloidal 10%wt Os. Oxidation waves recorded for both TU and  $BH_4^-$  were almost at the same potential range (i.e., 0.1-0.3 V vs. Ag/AgCl, KCl<sub>std</sub>) (Fig.4.1.6). Thus, the oxidation peak at 0.2 V could be for both TU and  $BH_4^-$  oxidation. It is worth mentioning that the voltammetric peak current for TU on Pt was found by Yan [5] to be  $35 \text{ mA cm}^{-2}$ , while on the colloidal Os it was  $\sim 10 \text{ mA cm}^{-2}$ . Therefore, Os is less active than Pt in oxidizing thiourea.

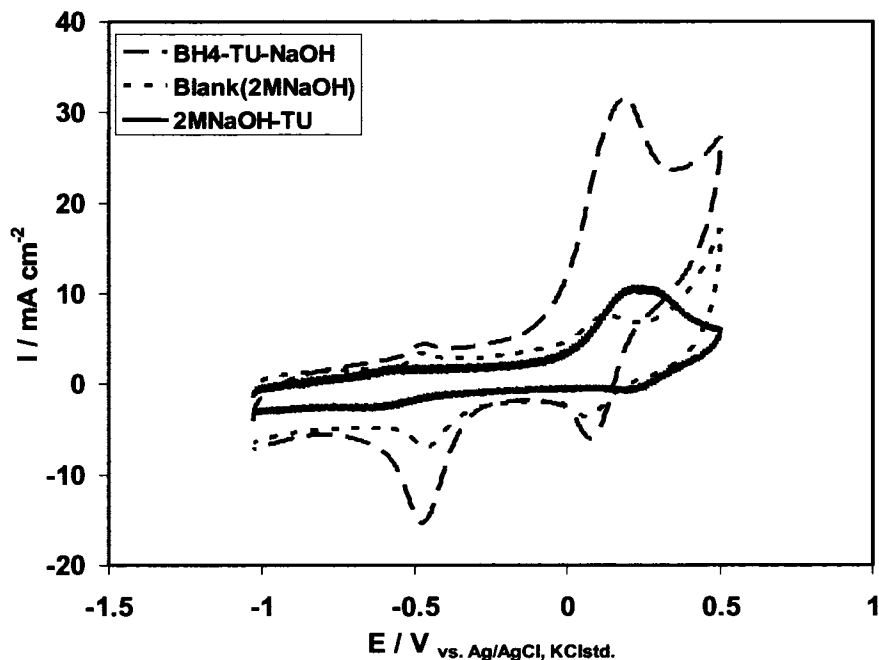


Fig. 4.1.6. Cyclic voltammogram obtained on 10 %wt colloidal Os electrode in 2 M NaOH in the absence and in the presence of 0.03 M  $NaBH_4$  and  $1.5 \times 10^{-3}$  M TU. Scan rate  $100 \text{ mV s}^{-1}$ . Temperature 295 K.

#### 4.1.4. Chronopotentiometry

By analogy with the constant current operation of a direct borohydride fuel cell, chronopotentiometry could provide further relevant information regarding the overpotentials for a step change in the applied current density for Os and Os-alloys catalysts. Fig. 4.1.7 compares the chronopotentiograms of a 0.03 M  $\text{BH}_4^-$  solution in 2 M  $\text{NaOH}$ , obtained on colloidal 10%, 20% and 30% Os in the presence of  $1.5 \times 10^{-3}$  M TU at current density of  $25 \text{ mA cm}^{-2}$ . The operating potential of the 20% Os was more negative, about  $-0.73 \text{ V}$  vs. SSCE, compared to 10%, and 30% Os colloids (Fig. 4.1.7). It can also be seen from Fig. 4.1.7 that the open circuit potential of  $\text{NaBH}_4$  in contact with colloidal Os is between  $-1.03$  and  $-1.06 \text{ V}$  vs. SSCE, i.e. close to the reversible  $\text{H}_2$  electrode potential in the same media (2 M  $\text{NaOH}$ ). This finding is indicative of the catalytic hydrolysis of  $\text{BH}_4^-$  generating  $\text{H}_2$  at open circuit conditions according to equation (2.10.1) [6].

Figure 4.1.8, on the other hand, shows that the Os-Sn alloy operated at a very high overpotential associated with a current step of  $25 \text{ mA cm}^{-2}$ . Generally, all three investigated Os-alloys performed poorly compared to the pure Os colloid (Figs. 4.1.7).

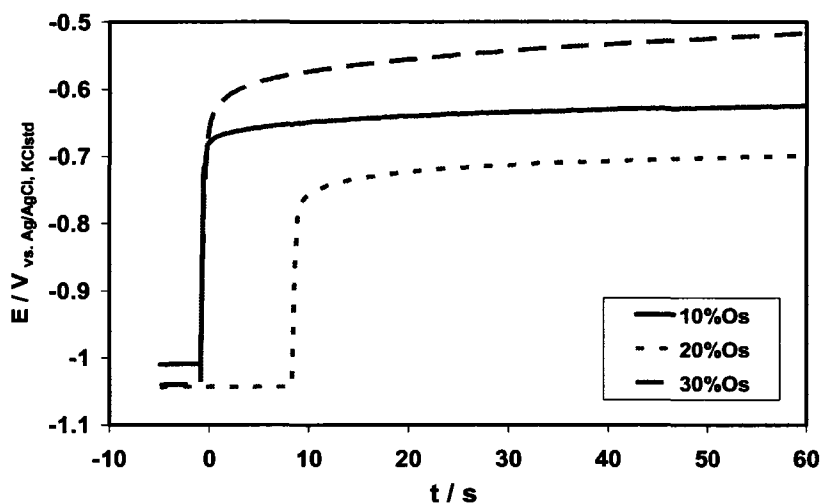


Fig. 4.1.7. Chronopotentiogram of 0.03 M  $\text{NaBH}_4$  in 2 M  $\text{NaOH}$  on 10, 20 and 30%wt colloidal Os electrodes with a  $30 \mu\text{g cm}^{-2}$  Os load. Current density step was from 0 to  $25 \text{ mA cm}^{-2}$ . Temperature 298 K.

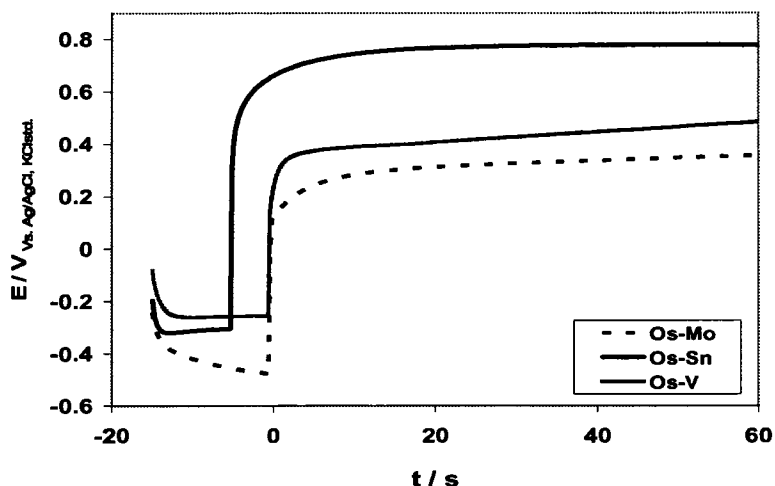


Fig. 4.1.8. Chronopotentiometry of 0.03 M  $\text{NaBH}_4$  in 2 M NaOH on colloidal 20%wt Os-Mo, Os-V and Os-Sn. Metal load of  $30 \mu\text{g cm}^{-2}$ . Current density step: from 0 to  $25 \text{ mA cm}^{-2}$ . Temperature 295 K.

#### 4.1.5. Chronoamperometry

Figs. 4.1.9 and 10 show the chronoamperometric response, potential step from -0.8 to +0.3 V vs.  $\text{Ag/AgCl, KCl}_{\text{std}}$ , of 0.1 M  $\text{NaBH}_4$  on both colloidal Os and Os-alloys in the presence of  $1.5 \times 10^{-3}$  M TU. The currents were higher on colloidal 20% and 30% Os compared to the colloidal 10% Os and Os-alloys colloids. The concentration dependence of the current decay is shown in Fig. 4.1.11. The peak current was about 2.5 times higher for 1.0 M compared to 0.1 M  $\text{NaBH}_4$  concentration.

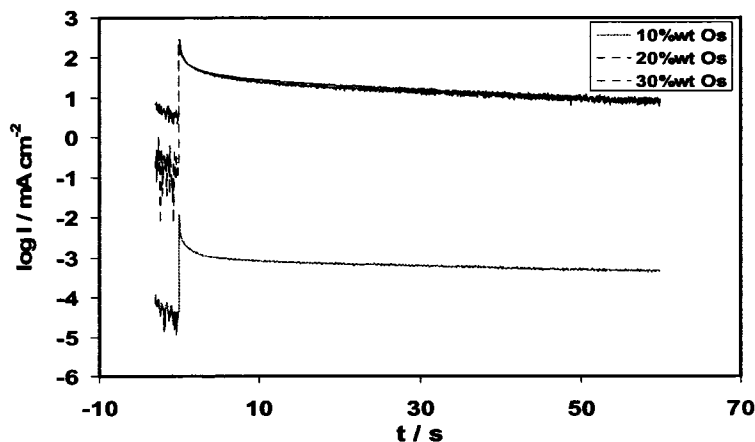


Fig. 4.1.9. Chronoamperometry of 0.1 M  $\text{BH}_4^-$  in 2M NaOH with  $1.5 \times 10^{-3}$  M TU on colloidal 10wt%, 20wt% and 30wt% Os, potential step from -0.8 to 0.3 V vs.  $\text{Ag/AgCl, KCl}_{\text{std}}$ , at 298 K.



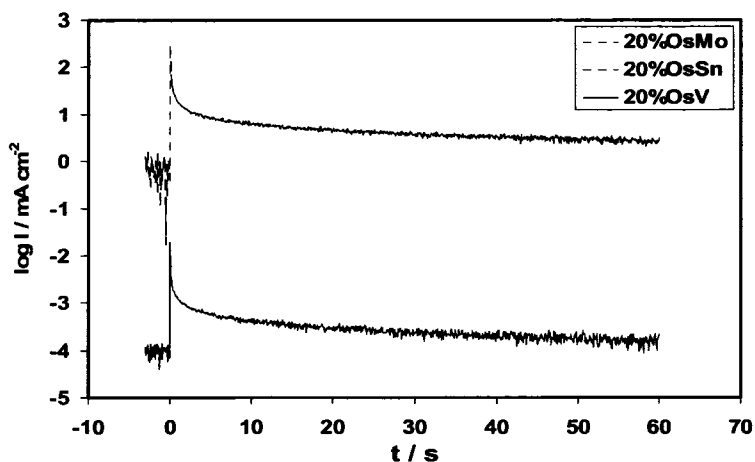


Fig. 4.1.10. Chronoamperometry of 0.1 M  $BH_4^-$  in 2 M NaOH with  $1.5 \times 10^{-3}$  M TU on colloidal 20wt% (50/50atomic) OsMo, OsSn and OsV, potential step from -0.8 to 0.3 V vs. Ag/AgCl,  $KCl_{std}$ , at 298 K.

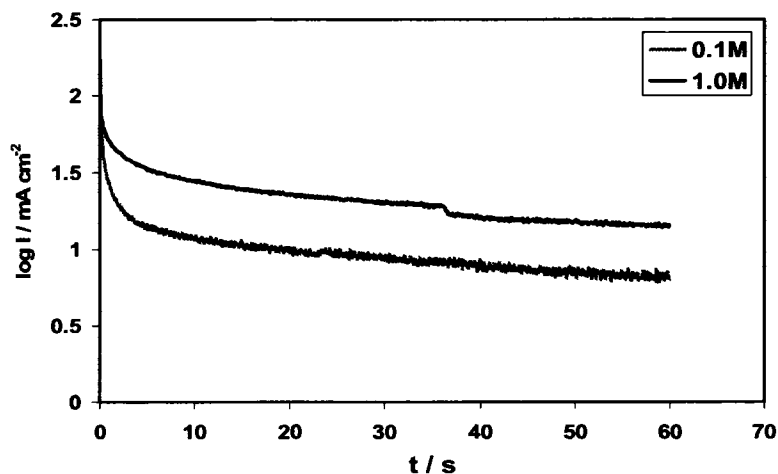


Fig. 4.1.11. Chronoamperometry response on colloidal 20%wt Os as a function of  $NaBH_4$  concentration in 2 M NaOH. Potential step from - 0.8 to + 0.3 V vs. Ag/AgCl,  $KCl_{std}$ . Temperature 295 K.

#### 4.1.6. Summary

In conclusion, voltammetry results showed that the investigated supported colloidal Os and Os-alloys were catalytically inactive with respect to methanol oxidation. On the other hand, the cyclic voltammograms on both colloidal Os and Os-alloys suggest the possibility of  $BH_4^-$  oxidation. The oxidation peak potentials between 0.1 and 0.3 V were a mix of  $BH_4^-$  and TU oxidation for all the supported colloidal Os and Os-alloys.

## 4.2. Platinum and Platinum Alloys

### 4.2.1. Voltammetry of borohydride oxidation on static electrodes

The linear voltammograms on static electrodes for colloidal Pt, Pt-Au, Pt-Ni, Pt-Ir, and Pt-Ag shown in Figures 4.2.1 to 4.2.5, were recorded at a scan rate of  $100 \text{ mV s}^{-1}$  as a function of increasing  $\text{NaBH}_4$  concentration (between 0.03 and 1 M).

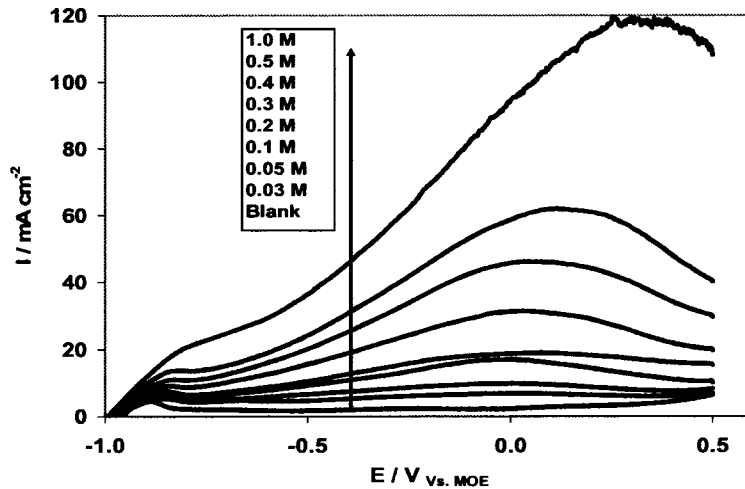


Fig. 4.2.1. Linear voltammogram of  $\text{BH}_4^-$  oxidation on colloidal Pt catalyst using a static electrode showing the effect of  $\text{BH}_4^-$  concentration. Scan rate  $100 \text{ mV s}^{-1}$ , 298 K. Inset legend indicates the  $\text{NaBH}_4$  concentration in 2 M NaOH.

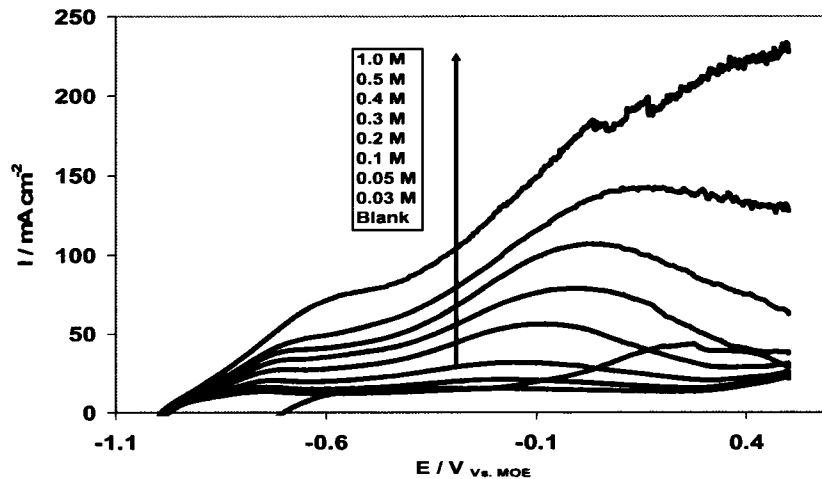


Fig. 4.2.2. Linear voltammogram of  $\text{BH}_4^-$  oxidation on colloidal Pt-Au catalyst using a static electrode showing the effect of  $\text{BH}_4^-$  concentration. Scan rate  $100 \text{ mV s}^{-1}$ , 298 K. Inset legend indicates the  $\text{NaBH}_4$  concentration in 2 M NaOH.

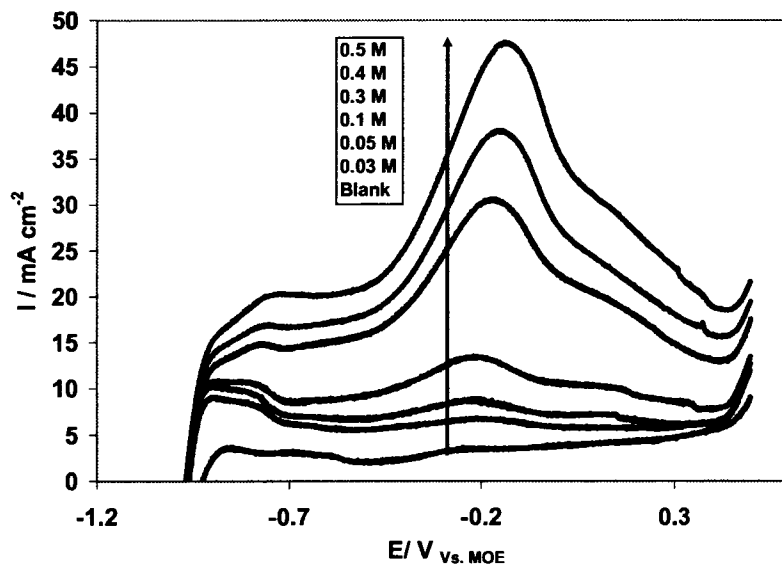


Fig. 4.2.3. Linear voltammogram of  $\text{BH}_4^-$  oxidation on colloidal Pt-Ni catalyst using a static electrode showing the effect of  $\text{BH}_4^-$  concentration. Scan rate  $100 \text{ mV s}^{-1}$ , 298 K. Inset legend indicates the  $\text{NaBH}_4$  concentration in 2 M NaOH.

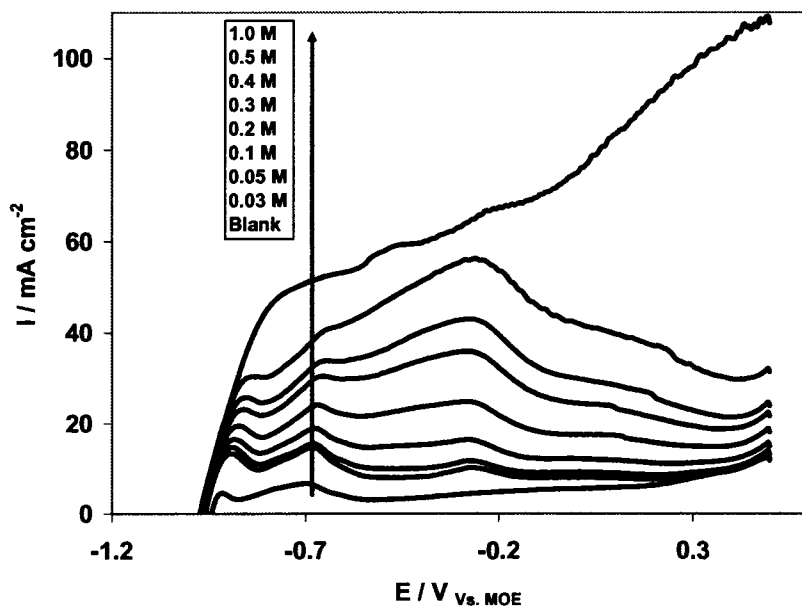


Fig. 4.2.4. Linear voltammogram of  $\text{BH}_4^-$  oxidation on colloidal Pt-Ir catalyst using a static electrode showing the effect of  $\text{BH}_4^-$  concentration. Scan rate  $100 \text{ mV s}^{-1}$ , 298 K. Inset legend indicates the  $\text{NaBH}_4$  concentration in 2 M NaOH.

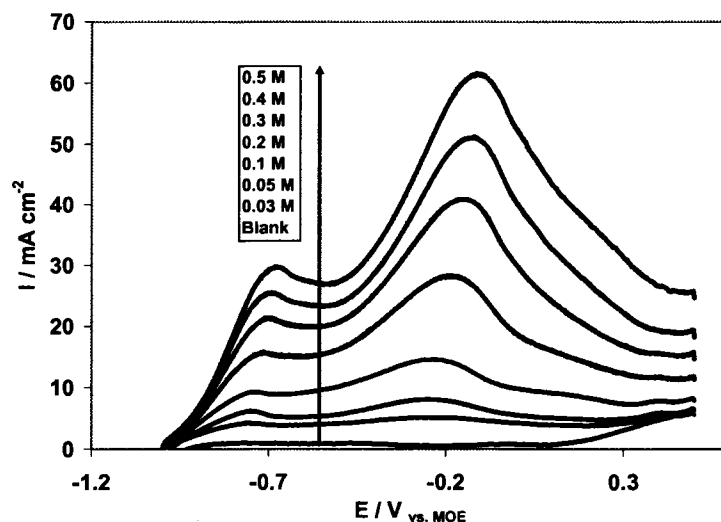
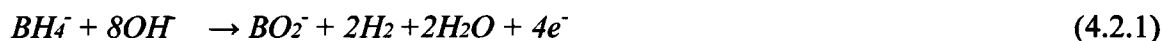


Fig. 4.2.5. Linear voltammogram of  $BH_4^-$  oxidation on colloidal Pt-Ag catalyst using a static electrode showing the effect of  $BH_4^-$  concentration. Scan rate  $100 \text{ mV s}^{-1}$ , 298 K. Inset legend indicates the  $NaBH_4$  concentration in 2 M NaOH.

Two peaks were identified on colloidal Pt (Fig. 4.2.1), one around  $-0.85 \text{ V}$  vs. MOE, and the other between 0 and  $+0.3 \text{ V}$  as a function of  $BH_4^-$  concentration, which shifts slightly toward more positive values with increasing  $NaBH_4$  concentration (Fig. 4.2.8). These peaks were in a good agreement with Gyenge's findings [6]. The first peak (at  $-0.85 \text{ V}$ ), is due to the oxidation of  $H_2$  generated by the catalytic hydrolysis of  $BH_4^-$  (eq. 2.10.1), while the peak around 0 and  $+0.3 \text{ V}$  results from the direct oxidation of  $BH_4^-$  on Pt (eq. 4.2.1).

Liu et al [7] have shown that on carbon-supported Pt and Pd catalysts, hydrogen evolution is decreased, compared to their planar surfaces, and can also be halted under certain conditions. It was also shown that the addition of thiourea (TU) increases the oxidation peak ratio of the borohydride and hydrolysis (eq. 2.10.2), resulting hydrogen oxidation on Pt for borohydride concentrations of 0.5 to 1 M [6].



It was of interest to alloy Pt, well known active surface for complete oxidation and hydrogenation-dehydrogenation processes, with same family elements, Pd, Ni, Ir, and with elements that are considered virtually inert for the hydrogenation-dehydrogenation processes, Ag and Au [8], in attempt to combine the higher kinetics of Pt with the higher coulombic efficiency of Au, for complete borohydride oxidation (eq. 2.10.3) [6].

The effect of alloying on Pt-Au catalysts activity can be seen clearly through the comparison of Figs. 4.2.1 and the CV data for Au (in section 4.3) with Fig. 4.2.2. The large direct  $BH_4^-$  oxidation wave for Pt-Au peaked at more negative potentials compared to pure Pt and pure Au, i.e. between  $-0.1$  and  $0.05$  V vs. MOE is recorded.

The activity of Pt-Ni, Pt-Ir, and Pt-Ag colloidal catalysts for borohydride oxidation was also tested. On Pt-Ni, (no oxidation peaks were recorded on a pure Ni colloid, Fig. 4.2.6), the oxidation peak occurred at  $-0.2$  V vs. MOE at a potential which is almost independent of  $BH_4^-$  concentration (Fig. 4.2.3). Multiple peaks at negative potentials, at about  $-0.85$  V,  $-0.65$  V and  $-0.27$  V, were recorded on colloidal Pt-Ir, and they show a slight concentration dependence. Comparing Fig. 4.2.1 and the CV data for Ir (in section 4.4) with Fig. 4.2.4, the existence of the third peak and the effect of such alloying on Pt electroactivity, can be explained as the effect of the Ir or, alternately on the effect of an intermediate species such as  $BH_3OH$  [9].

With Ag present, (colloidal Ag shows one peak at around  $+0.4$  V vs. MOE, Fig. 4.2.7), two oxidation peaks occurred are at  $-0.7$  V vs. MOE and the second between  $-0.24$  and  $-0.1$  V vs. MOE as a function of  $NaBH_4$  concentration (Fig. 4.2.5). Thus, amongst the investigated alloy catalysts, Pt-Ir showed oxidation peaks at the most negative potentials, indicating potentially favorable kinetics on such a catalyst. Whereas, the peak at  $-0.85$  V was due to  $H_2$  oxidation and the one at  $-0.27$  V corresponded to direct  $BH_4^-$  oxidation, the peak at  $-0.65$  V seems to be characteristic of alloying effects [10, 11, 12, 13, 14] such as geometric and surface electronic structure changes, or the close proximity effect.

Elder and Hickling in their study, using smooth Pt, Platinized Pt, and gray platinum electrode surfaces, concluded that the competition between the borohydride oxidation and corresponding hydrolysis is different on different surfaces, and this accounts for their different activities [15]. Liu et al [7] concluded that the anodic oxidation of borohydride (eq.2.10.3) has to compete with the hydrolysis reaction (eq.2.10.2). They also proposed an equation for the overall actual anodic reaction (eq. 2.10.13). Therefore, the different behaviour of the colloids under investigation is expected according to Elder's [15] and Liu's [7] findings. It can be concluded that Pt-Ir among the investigated colloidal catalysts showed the highest peak current at more negative potential, in a the domain that is of interest for borohydride fuel cells, i.e., more negative than  $-0.2$  V vs. MOE.

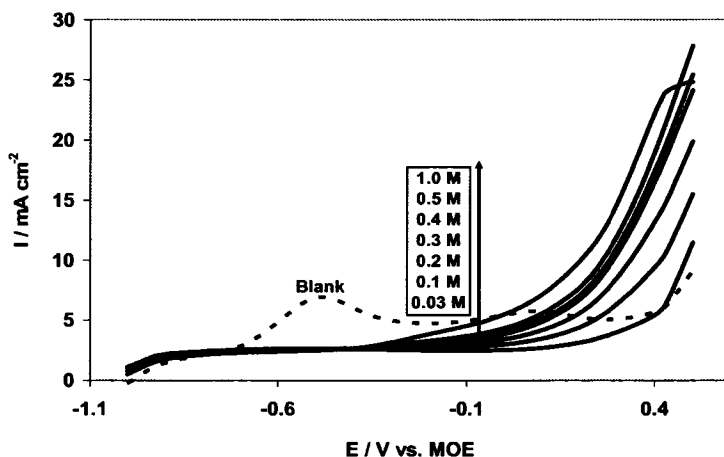


Fig. 4.2.6. Linear voltammogram of  $\text{BH}_4^-$  oxidation on colloidal Ni catalyst using a static electrode showing the effect of  $\text{BH}_4^-$  concentration. Scan rate  $100 \text{ mV s}^{-1}$ , 298 K. Inset legend indicates the  $\text{NaBH}_4$  concentration in 2 M NaOH.

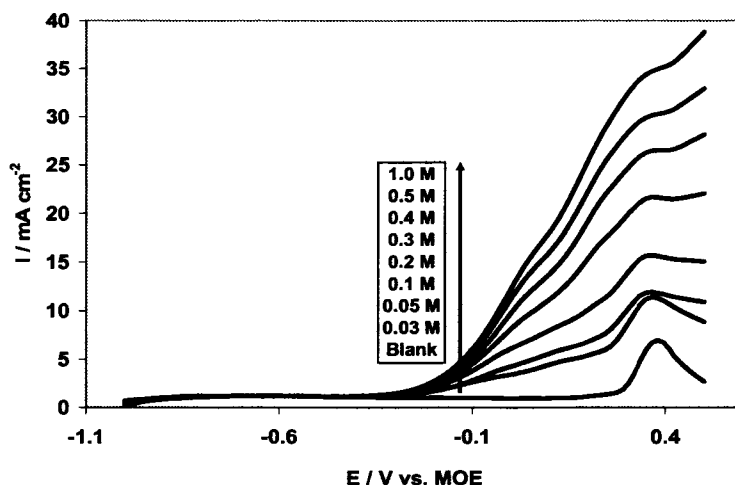


Fig. 4.2.7. Linear voltammogram of  $\text{BH}_4^-$  oxidation on colloidal Ag catalyst using a static electrode showing the effect of  $\text{BH}_4^-$  concentration. Scan rate  $100 \text{ mV s}^{-1}$ , 298 K. Inset legend indicates the  $\text{NaBH}_4$  concentration in 2 M NaOH.

The peak current density increases linearly with concentration for all investigated colloids for the peak potential ranges; Pt (0.088 to 0.256 V), Pt-Au (-0.2 to 0.15 V), Pt-Ni (-0.227 to -0.13 V), Pt-Ir (-0.68 to -0.264 V), and Pt-Ag (-0.237 to 0.01 V). The higher peak current density was recorded on colloidal Pt-Au (Fig. 4.2.8). This indicates that the oxidation of  $\text{BH}_4^-$  is a diffusion controlled process [16, 6, 17].

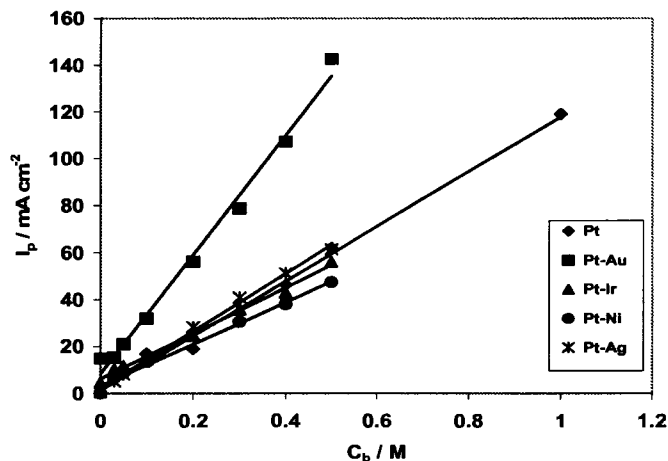


Fig. 4.2.8. The concentration dependence of the peak current density on colloidal Pt and Pt-alloys. Scan rate  $100 \text{ mV s}^{-1}$ , 298 K.

The scan rate dependence of linear voltammograms, in the range between 5 to  $500 \text{ mV s}^{-1}$  at a  $0.03 \text{ M NaBH}_4$  concentration, on static electrodes for Pt, Pt-Au, Pt-Ni, Pt-Ir, and Pt-Ag have been recorded (Figures 4.2.9-4.2.13 respectively). It can be seen that the oxidation peak potentials, for Pt, Pt-Ni, and Pt-Ag, are only slightly affected by the scan rate, while they are significantly affected in the cases of Pt-Au and Pt-Ir.

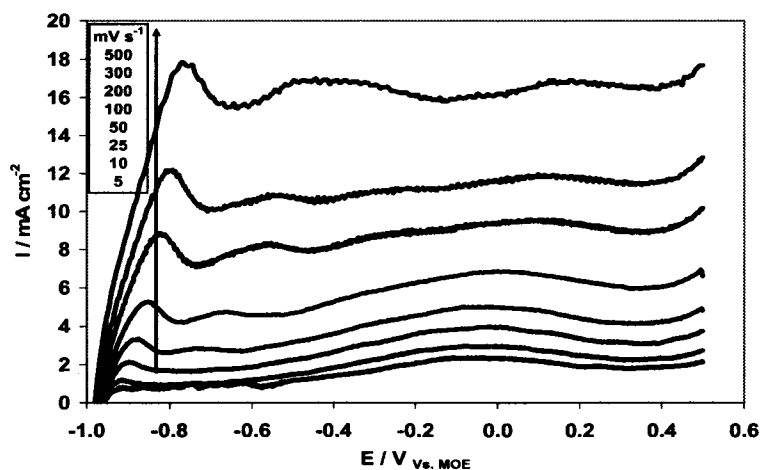


Fig. 4.2.9. Linear voltammogram of  $\text{BH}_4^-$  oxidation on colloidal Pt catalyst using a static electrode showing the effect of scan rate.  $\text{NaBH}_4$  concentration  $0.03 \text{ M}$ , 298 K. Inset legend indicates the scan rate.

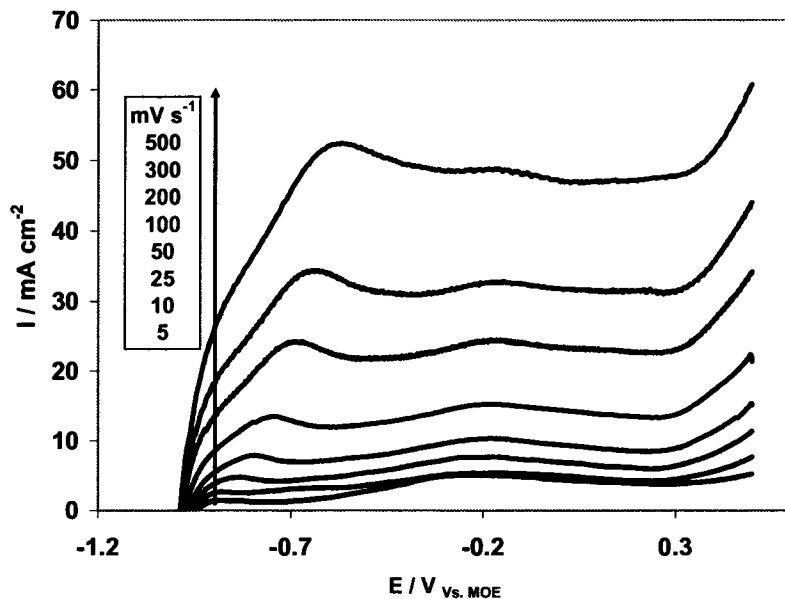


Figure 4.2.10. Linear voltammogram of  $\text{BH}_4^-$  oxidation on colloidal Pt-Au catalyst using a static electrode showing the effect of scan rate.  $\text{NaBH}_4$  concentration 0.03 M, 298 K. Inset legend indicates the scan rate.

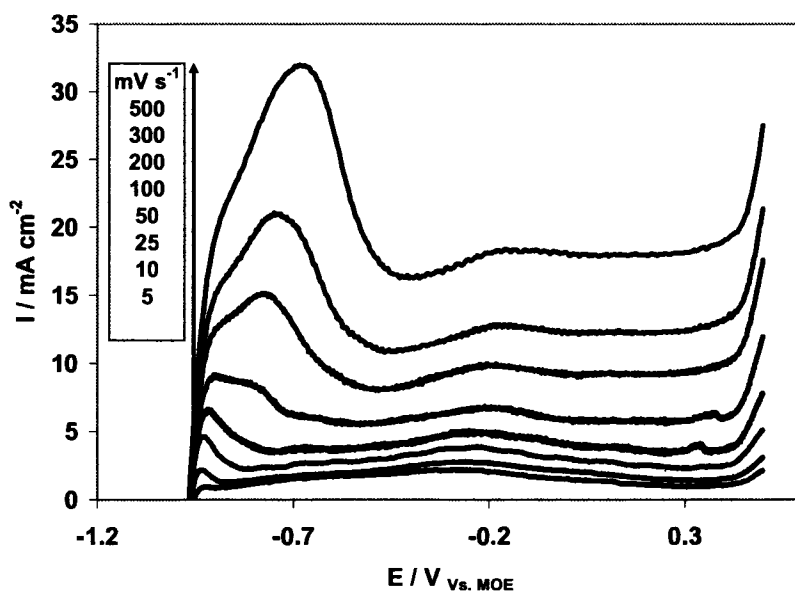


Fig. 4.2.11. Linear voltammogram of  $\text{BH}_4^-$  oxidation on colloidal Pt-Ni catalyst using a static electrode showing the effect of scan rate.  $\text{NaBH}_4$  concentration 0.03 M, 298 K. Inset legend indicates the scan rate.



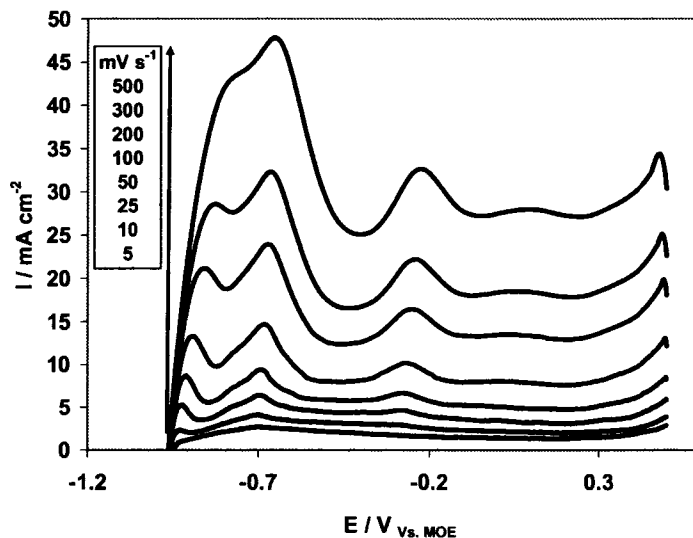


Fig. 4.2.12. Linear voltammogram of  $BH_4^-$  oxidation on colloidal Pt-Ir catalyst using a static electrode showing the effect of scan rate.  $NaBH_4$  concentration 0.03 M, 298 K. Inset legend indicates the scan rate.

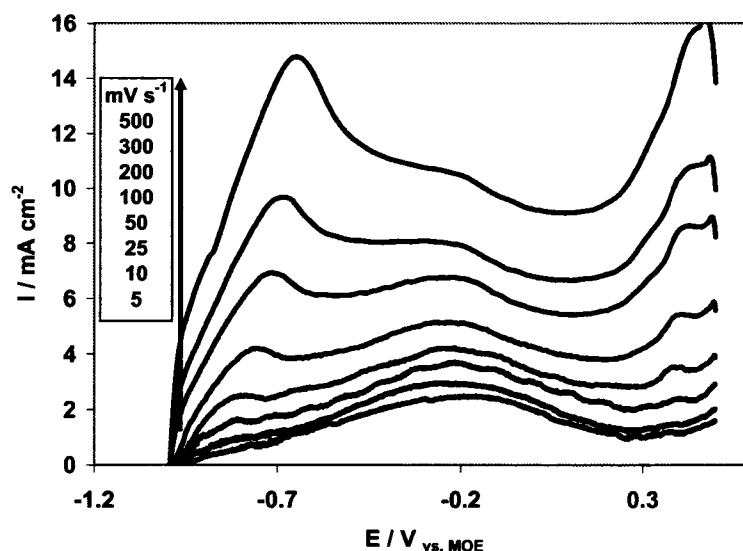


Fig. 4.2.13. Linear voltammogram of  $BH_4^-$  oxidation on colloidal Pt-Ag catalyst using a static electrode showing the effect of scan rate.  $NaBH_4$  concentration 0.03 M, 298 K. Inset legend indicates the scan rate.

Fig. 4.2.14 shows that the peak current density increased linearly with the square root of scan rate for all the investigated catalysts for the peak potential ranges; Pt (0.08 to 0.185), Pt-Au (-0.26 to -0.15), Pt-Ni (-0.312 to -0.13), Pt-Ir (-0.70 to -0.22), and Pt-Ag (-0.195 to -0.16 V). This indicates that the oxidation of  $BH_4^-$  is a diffusion controlled process. Pt-Ir and Pt-Au show a special behaviour, in that their slopes have deviated from

linearity at a scan rate of  $100 \text{ mV s}^{-1}$ , and thus such a deviation suggests an adsorption effect on the voltammetry response [16, 17-22].

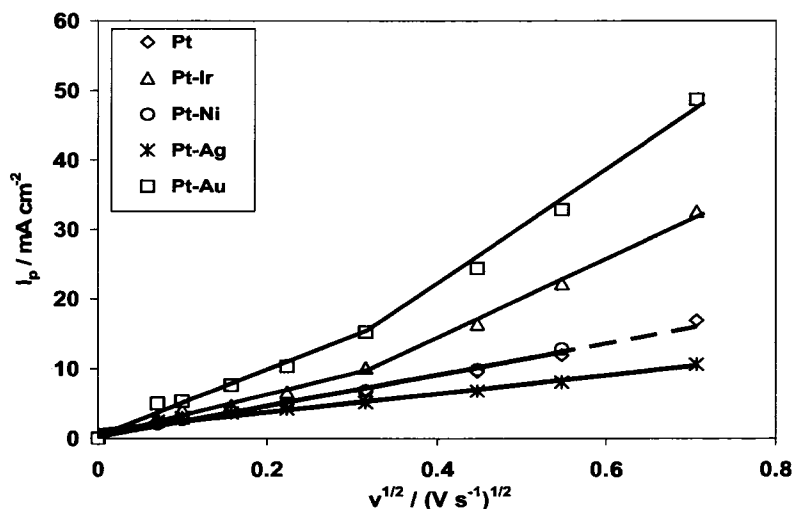


Fig. 4.2.14. The scan rate dependence of the peak current densities obtained on the colloidal Pt and Pt-alloys catalysts:  $\text{NaBH}_4$  concentration 0.03 M, 298 K.

#### 4.2.2. Voltammetry of borohydride oxidation on rotating electrodes

Voltammetry on rotating disc electrode (RDE) can be used to simulate the operation of the fuel cell anode catalyst. RDE voltammograms were recorded for Pt, Pt-Au, Pt-Ni, Pt-Ir, and Pt-Ag, and are shown in Figs. 4.2.15-4.2.19, respectively. These experiments were performed at a constant  $\text{NaBH}_4$  concentration of 0.3 M and a rotation per minute (rpm) ranging between 500 and 3,000 rpm. The strong temperature and the weak rotation speed effects can be seen clearly from these figures. The weak rotation speed effect is an indication of the surface-reaction-limited rather than transport-limited. The bell-shaped suggesting that at potentials more positive than the peak potential, is depleted inside the porous electrode structure and it is not replenished by the external convective flow imparted by the rotating electrode.

The peak potential on Pt was around  $-0.18$  and  $-0.15$  V at 298 K, and  $-0.12$  and  $-0.10$  V at 313 K, and was just slightly a function of the rotation speed (Fig. 4.2.15). On Pt-Au the peak occurred at more positive potentials, between  $-0.08$  and  $-0.04$  V (Fig. 4.2.16). Pt-Ni (Fig. 4.2.17), on the other hand, gave a peak exactly in the same range as pure Pt, whilst the presence of Ir shifted the potential to more negative values, i.e.  $-0.25$ ,

-0.3 V (Fig. 4.2.18). On Pt-Ag the peak occurred at more negative potentials, between -0.05 for rpm range of 500-1000 and -0.15 V for 3000 rpm at 298 K, and in the same range at 313 K (Fig. 4.2.19)

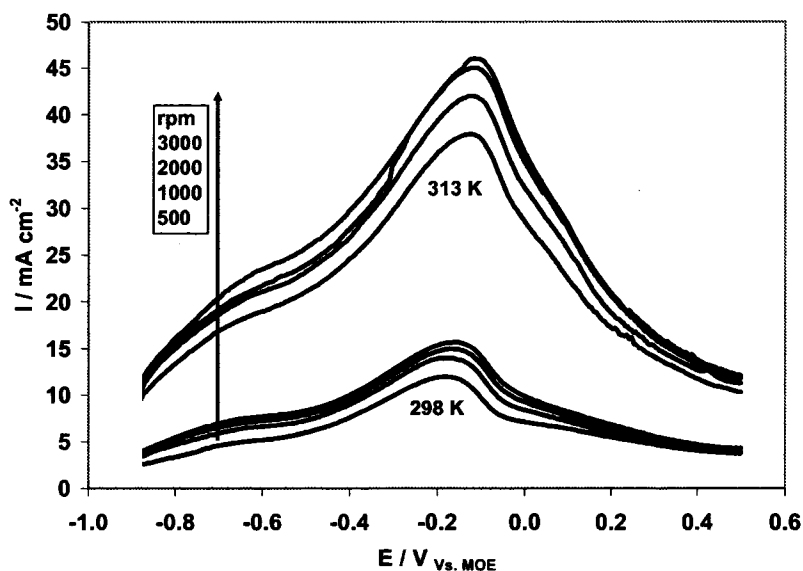


Fig. 4.2.15. Linear voltammetry of  $\text{BH}_4^-$  oxidation on colloidal Pt catalysts using a rotating electrode showing the effects of rotation speed and temperature. Scan rate  $5 \text{ mV s}^{-1}$ , 298 K and 313 K.  $\text{NaBH}_4$  concentration 0.3 M in 2 M NaOH. Inset legend indicates the rotation speed per minute.

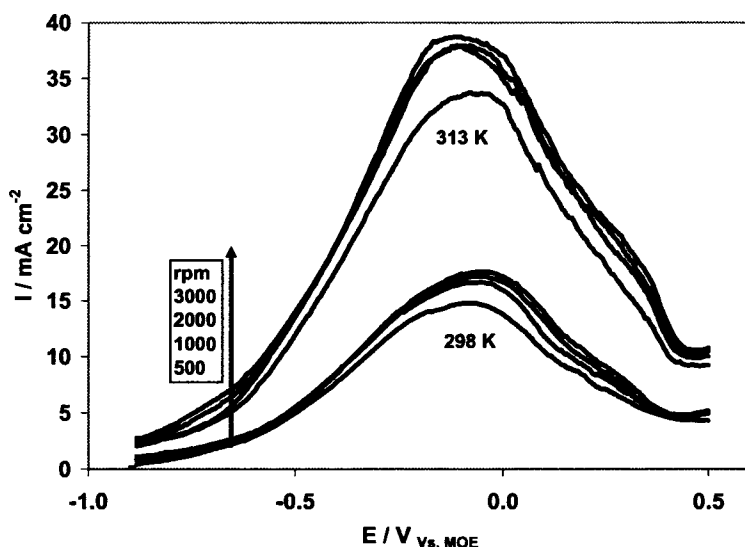


Fig. 4.2.16. Linear voltammetry of  $\text{BH}_4^-$  oxidation on colloidal Pt-Au catalysts using a rotating electrode showing the effects of rotation speed and temperature. Scan rate  $5 \text{ mV s}^{-1}$ , 298 K and 313 K.  $\text{NaBH}_4$  concentration 0.3 M in 2 M NaOH. Inset legend indicates the rotation speed per minute.

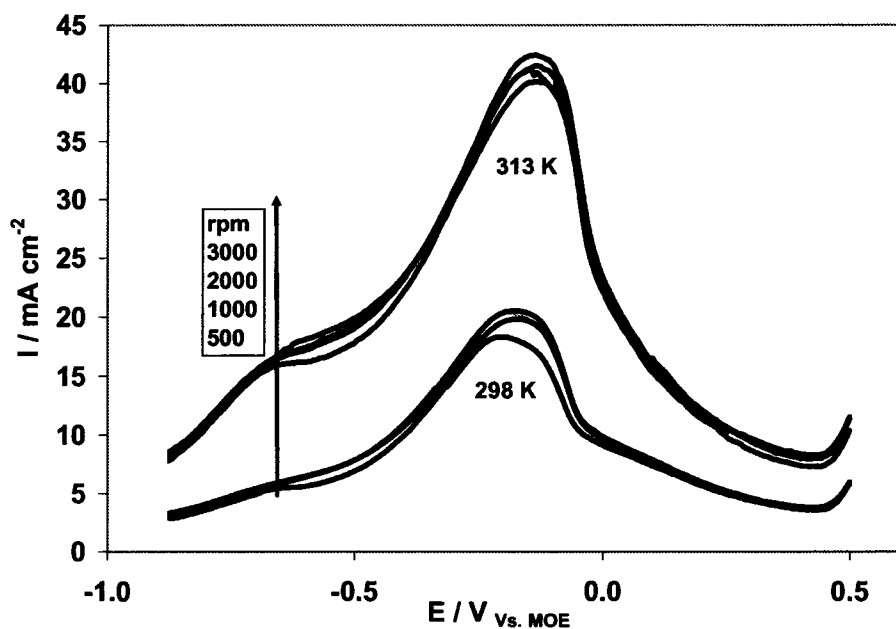
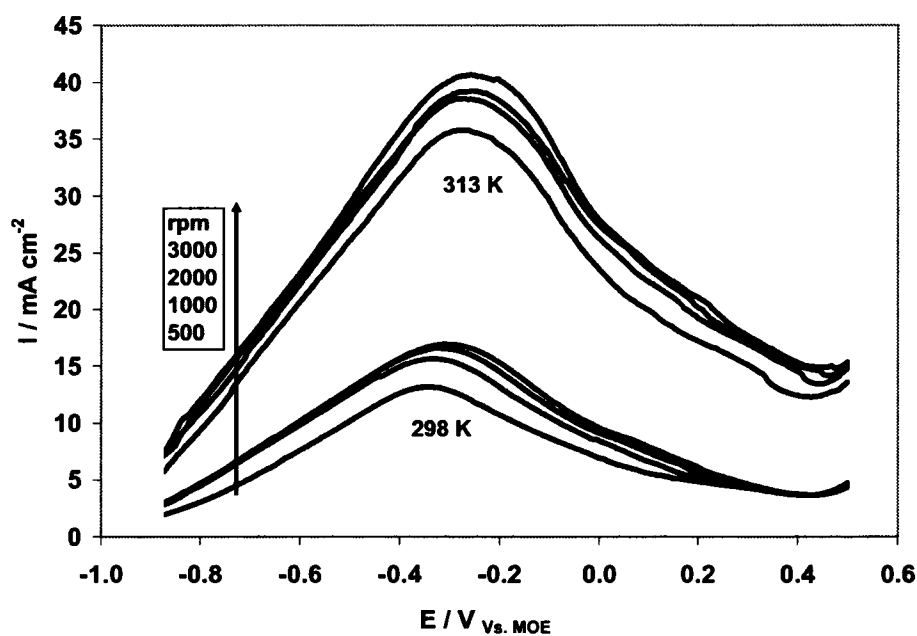
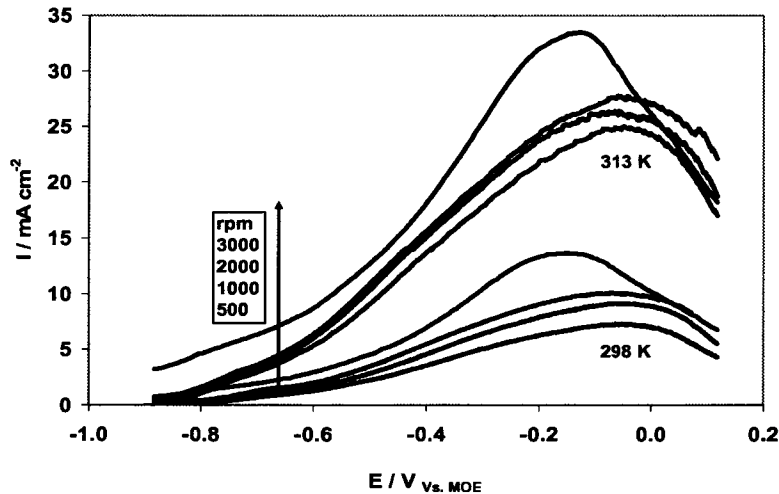


Fig. 4.2.17. Linear voltammetry of  $\text{BH}_4^-$  oxidation on colloidal Pt-Ni catalysts using a rotating electrode showing the effects of rotation speed and temperature. Scan rate  $5 \text{ mV s}^{-1}$ , 298 K and 313 K.  $\text{NaBH}_4$  concentration 0.3 M in 2 M NaOH. Inset legend indicates the rotation speed per minute.



4.2.18. Linear voltammetry of  $\text{BH}_4^-$  oxidation on colloidal Pt-Ir catalysts using a rotating electrode showing the effects of rotation speed and temperature. Scan rate  $5 \text{ mV s}^{-1}$ , 298 K and 313 K.  $\text{NaBH}_4$  concentration 0.3 M in 2 M NaOH. Inset legend indicates the rotation speed per minute.



4.2.19. Linear voltammetry of  $\text{BH}_4^-$  oxidation on colloidal Pt-Ag catalysts using a rotating electrode showing the effects of rotation speed and temperature. Scan rate  $5 \text{ mV s}^{-1}$ , 298 K and 313 K.  $\text{NaBH}_4$  concentration 0.3 M in 2 M NaOH. Inset legend indicates the rotation speed per minute.

#### *Tafel slopes and the exchange current densities*

According to the Tafel equation, eq. (eq. 3.6.12), a plot of  $\log i$  vs.  $\eta (= E - E_{oc})$  was made, using the exponential increase domain of Figs. 4.2.15-4.2.19, were about 400-800 actual experimental points recorded, in order to calculate the apparent Tafel slopes and the exchange current densities (Fig. 4.2.20).

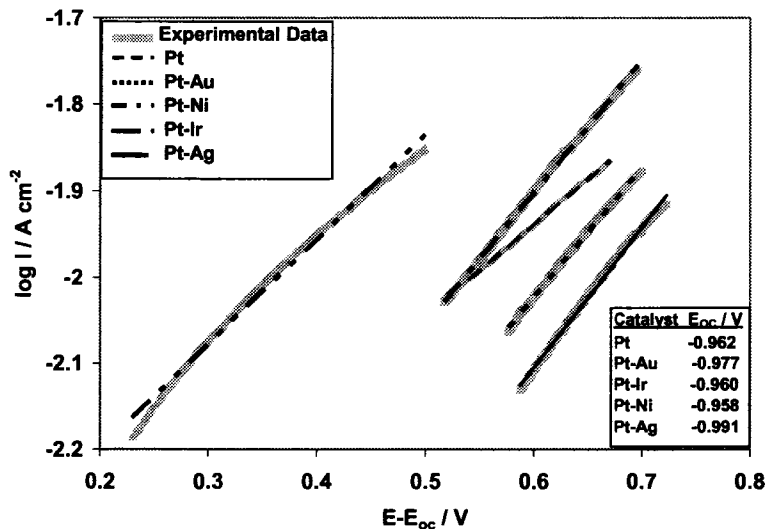


Fig. 4.2.20. Tafel plots for the supported colloidal Pt and Pt-alloys catalysts generated from the rotating disk electrode data. 298 K.

Table 4.2.1 shows that the apparent Tafel slopes  $b_a$  exchange current densities. High apparent Tafel slopes were determined in this study. They were at least four times higher than the values found by Gyenge [6], based on pure electrode kinetics, i.e.,  $b_a$  value of 0.18 V for Pt. Perry et al. [23] proposed that the ionic conductivity, and mass transfer limitations coupled with the electrode kinetics, are the reasons behind the large Tafel slopes. Furthermore, adsorption can also increase the Tafel slope of porous electrodes [24]. Nafion<sup>®</sup> was used as a binder to support the catalysts on the glassy carbon electrode (Experimental Methods Section), which acts as an ionic conductor within the catalysts pores and might thus suppress intra-catalyst layer mass transfer of both  $BH_4^-$  and  $OH^-$  to the active sites of the catalyst. This idea is supported by the weak rotation speed effect seen in the polarization curves (Figs. 4.2.15-4.2.19).

Lowering the Tafel slope,  $b_a$ , for an electrocatalyst is a crucial step in enhancing its activity towards electro-oxidation or electroreduction processes, since lower values will lead to higher exchange current densities and lower overpotentials (eq. 3.6.28 and Fig. 3.6.10) [25, 26]. Alloying Pt with Au, Ni, Ir and Ag decreased the apparent Tafel slope while also decreasing the exchange current density for all catalysts except Pt-Ir (Table 4.2.1). The Pt-Ag catalyst had the lowest exchange current density,  $0.83 \times 10^{-3} \text{ A cm}^{-2}$ , indicating the kinetic sluggishness of borohydride oxidation on Ag. Pt-Ir on the other hand, gave the highest exchange current density of  $3.62 \times 10^{-3} \text{ A cm}^{-2}$ .

To calculate the number of electrons transferred, the voltammetry governing equation for an irreversible system [16], eq. 3.6.27, was used in a modified form. The ratio of the number of electrons transferred between Pt-alloys and Pt can be calculated from the respective slope ratios (eq. 4.2.2).

$$\frac{n_{Pt-X}}{n_{Pt}} \cdot \left( \frac{b_{a,Pt}}{b_{a,Pt-X}} \right)^{1/2} = \frac{\beta_{Pt-X}}{\beta_{Pt}}, \quad (4.2.2)$$

where  $X = \text{Au, Ir, Ni, Ag}$  and  $\beta$  is the slope of the  $i_p$  vs.  $C_b$  linear function from Fig. 4.2.8.

Substituting the  $b_a$  values from Table 4.2.1 into eq. (4.2.2), and using  $n = 4$  for Pt [5, 15], gives the numbers of electrons transferred in the borohydride oxidation process for Pt and its alloys (Table 4.2.1). On Pt-Au, almost eight electrons are transferred in the  $BH_4^-$  oxidation process ( $n = 7.67$ ). This shows the beneficial effect of the Au add atom, and is in good agreement with the findings of Mirkin et al. [27] for flat Au micro-electrodes ( $n$

= 7.9). For Pt-Ni, Pt-Ir and Pt-Ag, on the other hand, there is incomplete oxidation as characterized by  $n < 8$  (Table 4.2.1).

Table 4.2.1. Apparent Tafel slopes,  $b_a$ , exchange current densities,  $i_{0,a}$ , and total number of electrons exchanged,  $n$ , determined from RDE data using supported colloidal Pt and Pt-alloys catalysts with Nafion 117 polymer electrolyte. Eq. (4.2.2) was used to calculate  $n$ .

Catalysts	$b_a$ (V dec <sup>-1</sup> ) 298 K	$i_{0,a}$ (A cm <sup>-2</sup> ) 298 K	$n$
Pt	0.939	$2.64 \times 10^{-3}$	4
Pt-Au	0.662	$1.18 \times 10^{-3}$	7.7
Pt-Ni	0.651	$1.50 \times 10^{-3}$	2.5
Pt-Ir	0.823	$3.62 \times 10^{-3}$	3.2
Pt-Ag	0.615	$0.83 \times 10^{-3}$	3.4

#### 4.2.3. Chronopotentiometry

In order to simulate the constant current operation of a fuel cell, chronopotentiometry experiments were performed for the investigated catalysts at an applied current density step of  $10 \text{ mA cm}^{-2}$  to the electrode for 60 s, in a solution of  $0.5 \text{ M NaBH}_4$  concentration. It can be clearly seen from Fig. 4.2.21 that the anode potential was the most negative on Pt-Ir, followed by Pt-Ag, Pt-Au, Pt-Ni, and lastly Pt, where the potential was up to 460 mV higher. Furthermore, the open circuit potential could serve as an indication of hydrolysis activity. The more negative the open circuit potential of the anode, the lower is the hydrolysis activity for the catalyst [7].

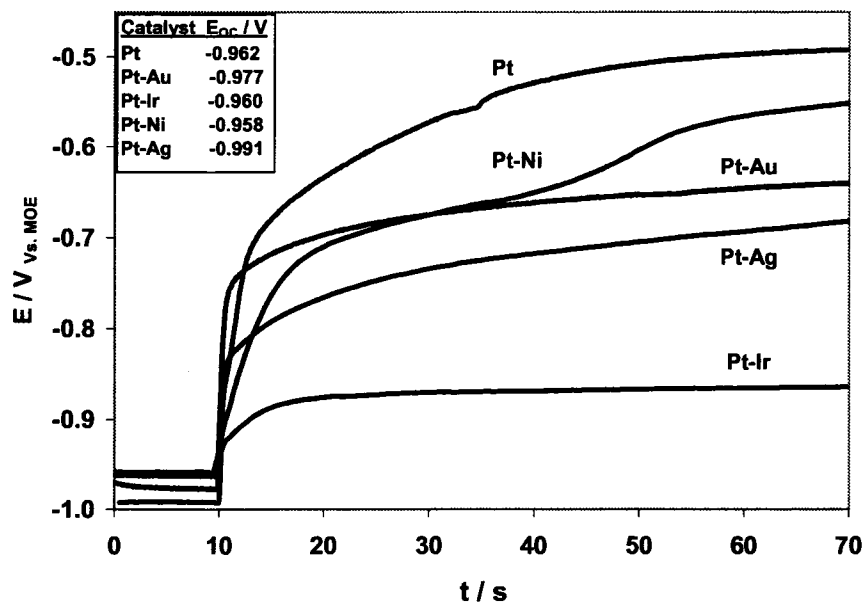


Fig. 4.2.21. Chronopotentiometry of  $\text{BH}_4^-$  oxidation on colloidal Pt and Pt-alloys catalysts. Current step from 0 to  $10 \text{ mA cm}^{-2}$ .  $0.5 \text{ M Na BH}_4$  in  $2 \text{ M NaOH}$ .  $298 \text{ K}$ .

#### 4.2.4. Chronoamperometry and chronocoulometry

Based on voltammograms shown by Figs. 4.2.17-19, three potential steps were chosen from the rising, the middle and close to the peak zones, ( $-0.6$ ,  $-0.4$  and  $-0.2 \text{ V vs. MOE}$ ) to perform the chronoamperometry experiments. The potential steps were started from  $-0.9 \text{ V vs. MOE}$ .

Figures 4.2.22-4.2.26 show the superficial current density transients on Pt, Pt-Au, Pt-Ni, Pt-Ir, and Pt-Ag, respectively. The highest anodic current densities at the  $-0.2 \text{ V}$  and  $-0.4 \text{ V}$  potential steps were recorded on Pt-Ir, i.e. about  $0.03 \text{ A cm}^{-2}$  and  $0.04 \text{ A cm}^{-2}$  after 60 s, respectively (Fig. 4.2.25). Thus, in the negative potential range of  $-0.9 \text{ V}$  and  $-0.4 \text{ V}$ , the domain of interest for practical fuel cell anodes, Pt-Ir was the most active catalyst, and the other electrocatalysts showed lower current densities. At the  $-0.2 \text{ V}$  step change, the highest current density was recorded on Pt-Au, e.g.  $0.07 \text{ A cm}^{-2}$  (Fig. 4.2.23). The overlapping in the case of Pt-Ir at  $-0.2 \text{ V}$  with the one obtained at  $-0.4 \text{ V}$  can be attributed to intra-catalyst layer diffusion which becomes rate limiting in addition to kinetics (mixed control) at  $-0.2 \text{ V}$ , while at  $-0.4 \text{ V}$  the oxidation is still under pure electrode kinetics control (Fig. 4.2.18).



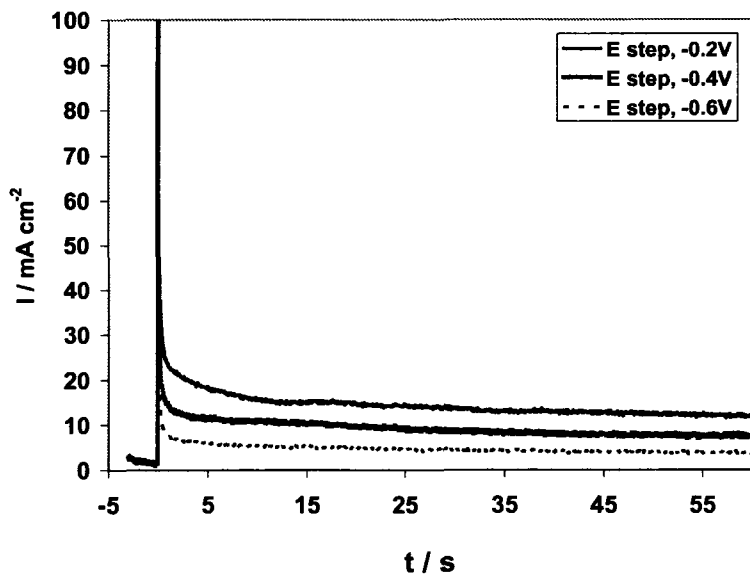


Fig. 4.2.22. Chronoamperometry of  $\text{BH}_4^-$  oxidation on a colloidal Pt catalyst. Potential steps from  $-0.9 \text{ V vs. MOE}$  to  $-0.6$ ,  $-0.4$  and  $-0.2 \text{ V vs. MOE}$ , respectively.  $0.5 \text{ M NaBH}_4$  in  $2 \text{ M NaOH}$ .  $298 \text{ K}$ .

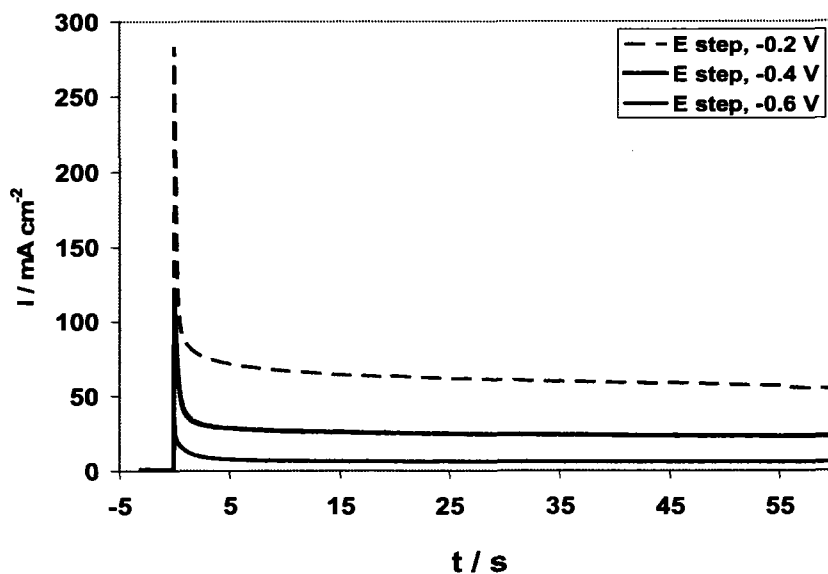


Fig. 4.2.23. Chronoamperometry of  $\text{BH}_4^-$  oxidation on a colloidal Pt-Au catalyst. Potential steps from  $-0.9 \text{ V vs. MOE}$  to  $-0.6$ ,  $-0.4$  and  $-0.2 \text{ V vs. MOE}$ , respectively.  $0.5 \text{ M NaBH}_4$  in  $2 \text{ M NaOH}$ .  $298 \text{ K}$ .

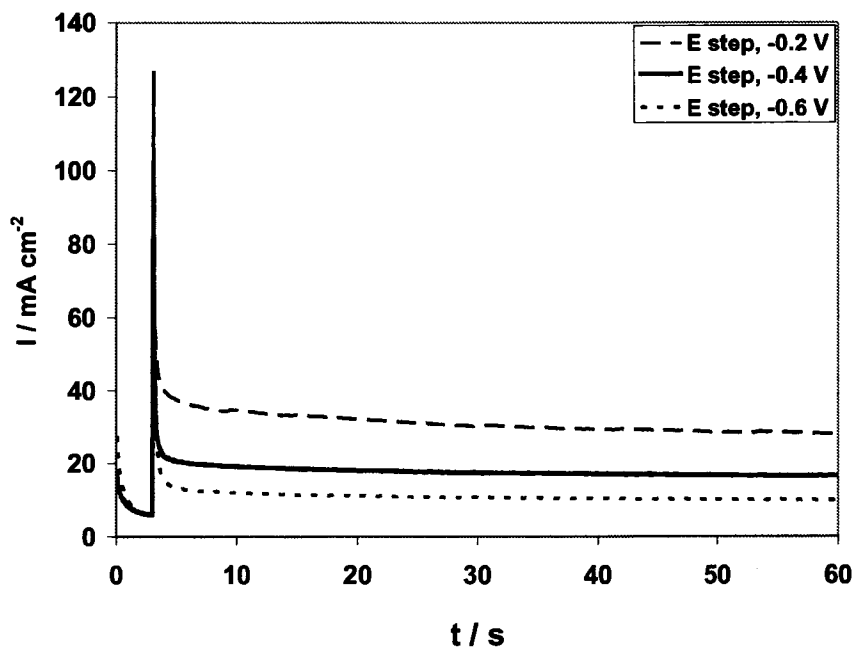


Fig. 4.2.24. Chronoamperometry of  $\text{BH}_4^-$  oxidation on a colloidal Pt-Ni catalyst. Potential steps from  $-0.9$  V vs. MOE to  $-0.6$ ,  $-0.4$  and  $-0.2$  V vs. MOE, respectively.  $0.5$  M  $\text{NaBH}_4$  in  $2$  M  $\text{NaOH}$ .

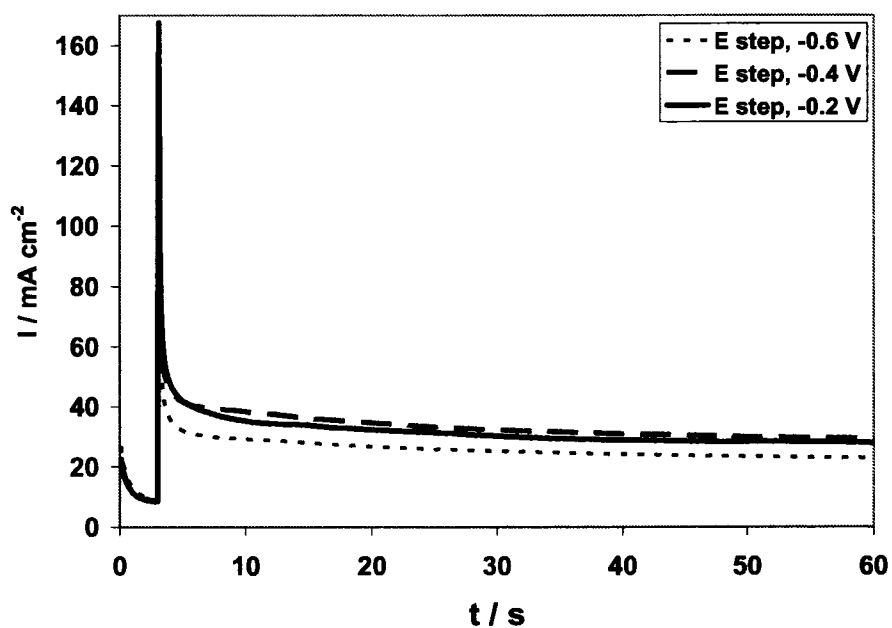


Fig. 4.2.25. Chronoamperometry of  $\text{BH}_4^-$  oxidation on a colloidal Pt-Ir catalyst. Potential steps from  $-0.9$  V vs. MOE to  $-0.6$ ,  $-0.4$  and  $-0.2$  V vs. MOE, respectively.  $0.5$  M  $\text{NaBH}_4$  in  $2$  M  $\text{NaOH}$ .  $298$  K.

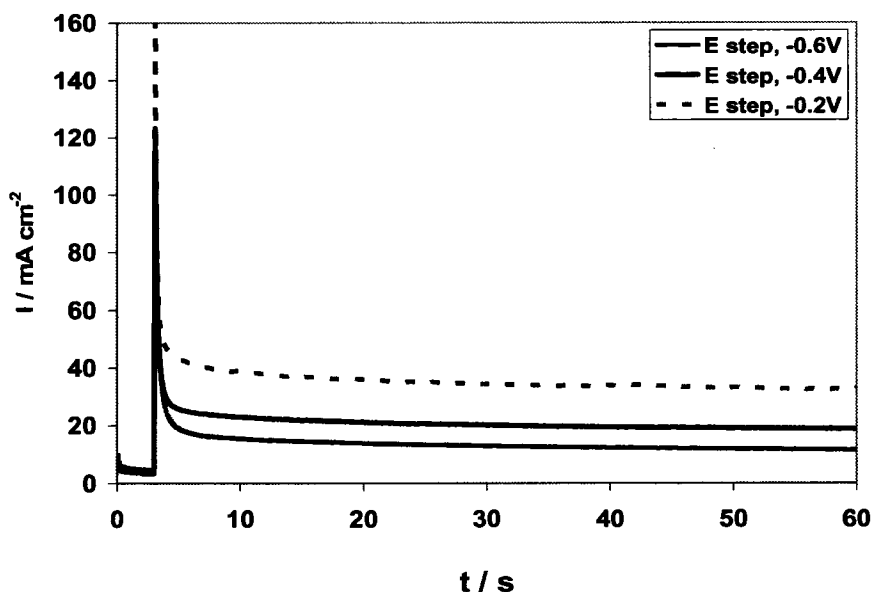


Fig. 4.2.26. Chronoamperometry of  $\text{BH}_4^-$  oxidation on a colloidal Pt-Ag catalyst. Potential steps from  $-0.9$  V vs. MOE to  $-0.6$ ,  $-0.4$  and  $-0.2$  V vs. MOE, respectively.  $0.5$  M  $\text{NaBH}_4$  in  $2$  M  $\text{NaOH}$ .  $298$  K.

### Cottrell Plot

$i \cdot \sqrt{t}$  vs.  $t$  were constructed using the chronoamperometry data to study the interplay of the electrode kinetics and mass transfer.

In attempt to calculate the effective surface area to be used in calculating the heterogeneous rate constant, the  $i \cdot \sqrt{t}$  value of colloidal pure Pt can be assumed almost constant after about  $30$  s. Thus, after a longer exposure time on colloidal Pt electrode, intra-catalyst layer diffusion becomes rate determining. Therefore, the rearranged Cottrell equation (eq. 3.6.29) can be applied (eq. 4.2.3). The effective  $\text{BH}_4^-$  diffusion coefficient in the catalyst layer,  $D$ , estimated with a Bruggeman-type relationship (eq. 4.2.4) [28, 29, 30, 31, 32]:

$$i\sqrt{t} = \frac{nFAC_b\sqrt{D_R}}{A_s\sqrt{t}} \left[1 - \exp\left(\frac{nF\eta_c}{RT}\right)\right] \quad (2.4.3)$$

$$D = D_0\varepsilon^{1.5} \quad (4.2.4)$$

where,  $A$  is the effective (electrochemically active) electrode area,  $A_s$  the superficial (i.e. geometric) electrode area ( $= 0.0706 \text{ cm}^2$ ),  $n = 4$  for Pt,  $D_0$  the borohydride diffusion

coefficient in the bulk alkaline solution ( $= 1 \times 10^{-5} \text{ cm}^2$  in 2 M NaOH [5]),  $\varepsilon$  is the porosity which is estimated as approximately equals to 0.3 based on the employed catalyst layer preparation method,  $i$  and  $i_L$  (for  $\eta_c$  calculation) values were taken from Fig. 4.2.22 at -0.4 V ( $= 7$  and  $25 \text{ mA cm}^{-2}$ , respectively), since the potential step method is widely used in determining  $i_L$  for an electrochemical process by applying a sufficiently positive potential value [33], and  $s$  (in eq. 3.6.17 which used to calculate  $\eta_c$ ) is the stoichiometric coefficient of  $\text{BH}_4^-$  ( $= -1$ ) according to the following equation:



Substituting the numerical values of  $I\sqrt{t}$  for Pt at  $t = 60 \text{ s}$  ( $= 59 \times 10^{-3} \text{ A cm}^{-2} \text{ s}^{1/2}$ ) from Fig. 4.2.28,  $D$  ( $= 1.643 \times 10^{-6} \text{ cm}^2 \text{ s}^{-1}$ ),  $\eta_c$  ( $= 0.0021 \text{ V}$ ),  $C_b$  ( $= 0.5 \times 10^{-3} \text{ mol cm}^{-3}$ ),  $F$  ( $= 96485 \text{ C mol}^{-1}$ ) into eq. (4.2.3) gives  $A = 0.106 \text{ cm}^2$ , the effective area  $A/A_s = 1.51 \text{ cm}^{-2} \text{ eff. / cm}^2 \text{ geom.}$ , and the effective Pt electrode area is about  $10.8 \text{ cm}^2 \text{ mg}^{-1}$  (based on a load of  $0.14 \text{ mg cm}^{-2}$ ). Given the similar preparation method (Bonnemann Method) used for all colloids, this electrochemically active area for Pt, can be applied to the rest of colloids, in order to calculate the apparent heterogeneous rate constant  $k_h$  using eq. 3.6.32. It is well known that determining the electrochemically active electrode area is not an easy task [28].

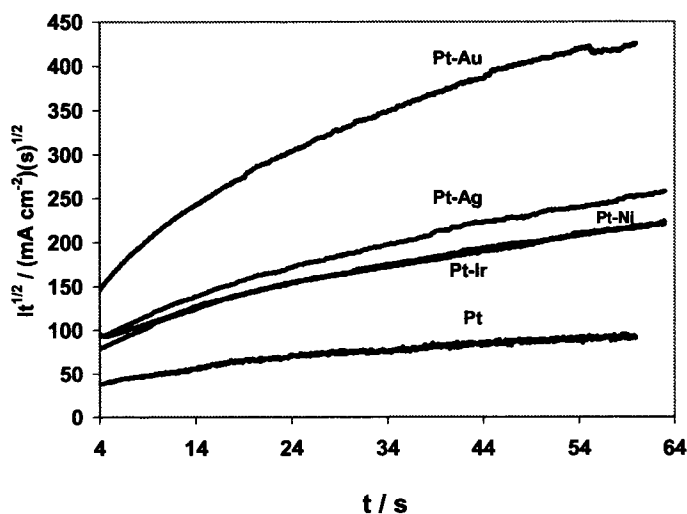


Fig. 4.2.27. Cottrell plot generated from the chronoamperometry data with a potential step from -0.9 V to -0.2 V vs. MOE.

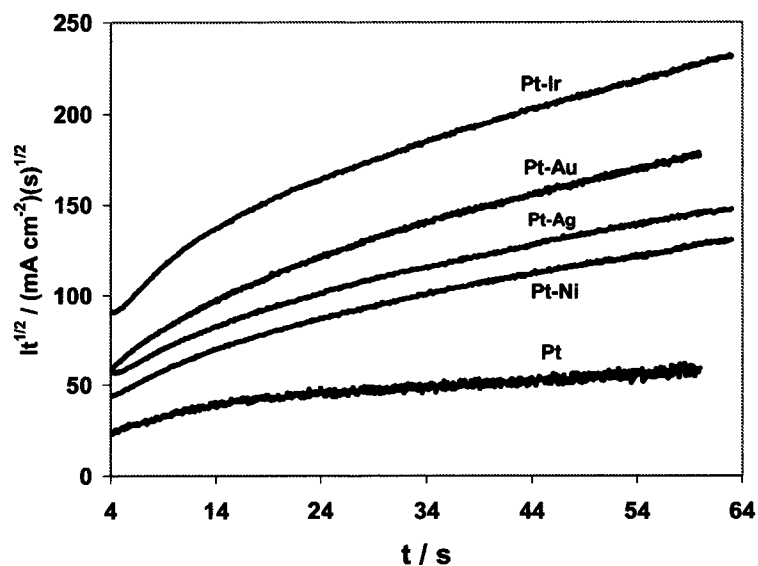


Fig. 4.2.28. Cottrell plot generated from the chronoamperometry data with a potential step from  $-0.9$  V to  $-0.4$  V vs. MOE.

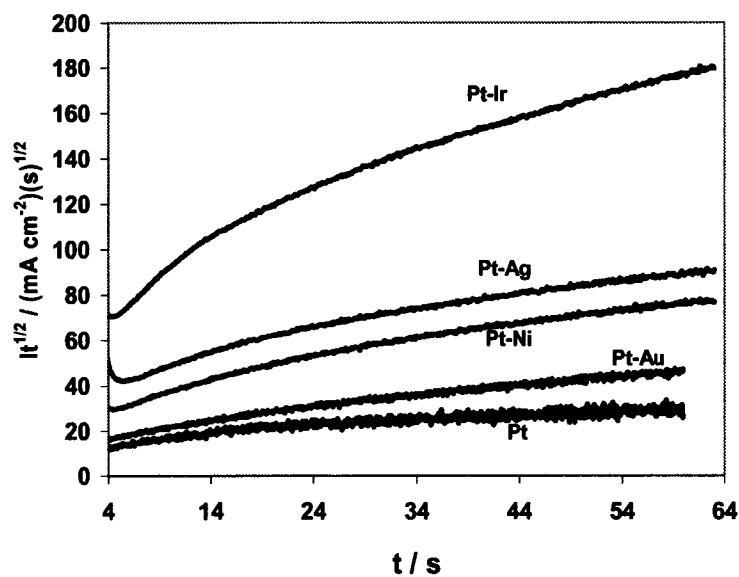


Fig. 4.2.29. Cottrell plot generated from the chronoamperometry data with a potential step from  $-0.9$  V to  $-0.6$  V vs. MOE.

### Chronocoulometry

Another useful way used to look at the superficial current density transients is by plotting the cumulative charge density  $Q$  vs.  $\sqrt{t}$  (Anson plot), and this is called chronocoulometry. Figures 4.2.30-4.2.32 are the Anson plots for the Au and Au-alloy catalysts obtained for potential steps from  $-0.9$  V to  $-0.2$  V,  $-0.4$  V, and  $-0.6$  V vs. MOE.

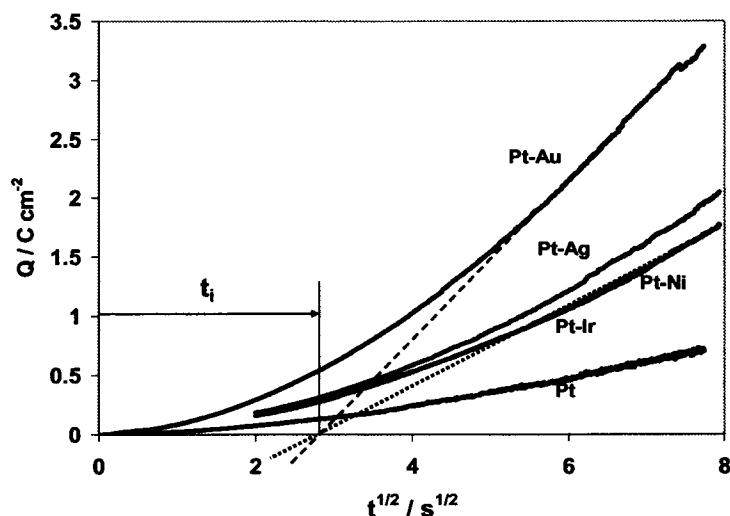


Fig. 4.2.30. Cumulative charge density as a function of square root of time (Anson plot) generated from the chronoamperometry data for a potential step from  $-0.9$  V to  $-0.2$  V vs. MOE.

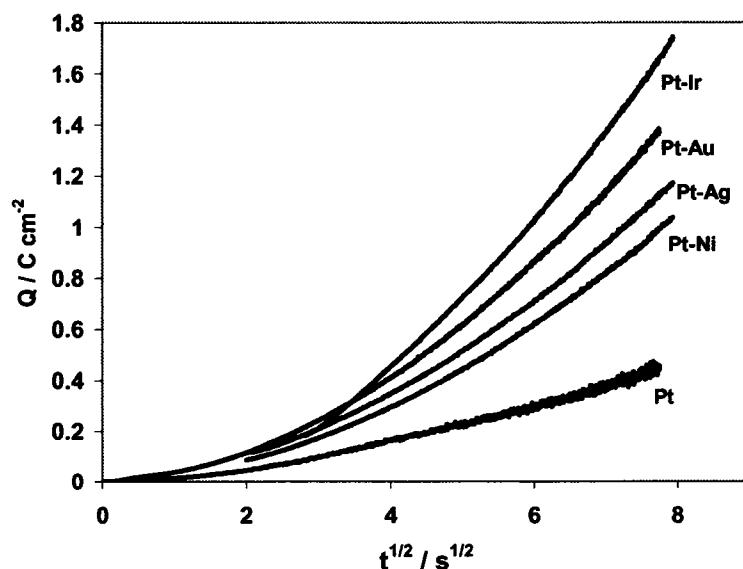


Fig. 4.2.31. Cumulative charge density as a function of square root of time (Anson plot) generated from the chronoamperometry data for a potential step from  $-0.9$  V to  $-0.4$  V vs. MOE.

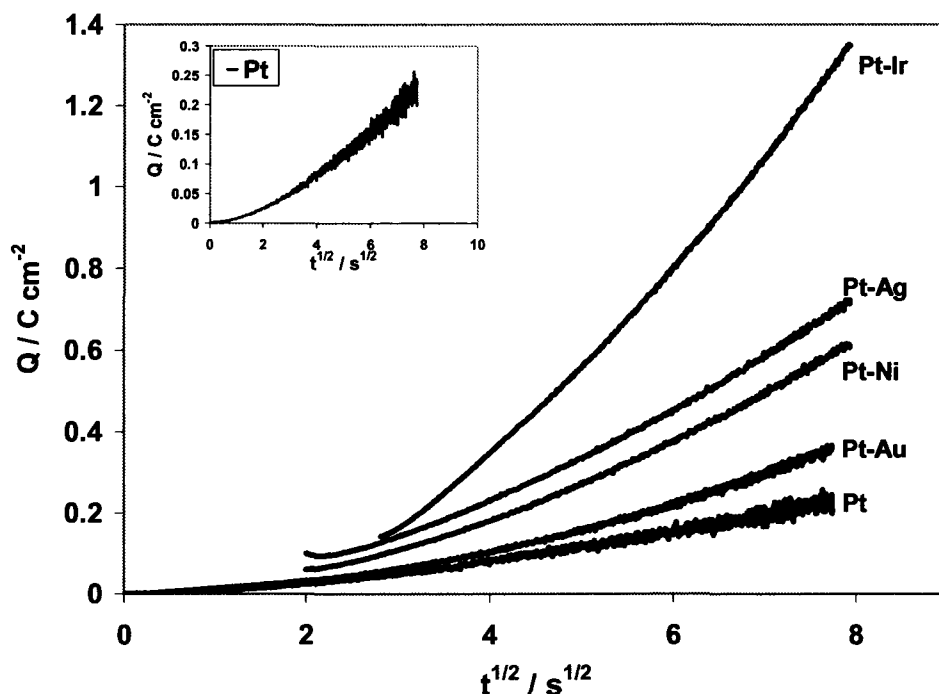


Fig. 4.2.32. Cumulative charge density as a function of square root of time (Anson plot) generated from the chronoamperometry data for a potential step from  $-0.9$  V to  $-0.6$  V vs. MOE.

These plots,  $Q$  vs.  $\sqrt{t}$ , are characterized by a negative intercept on the  $Q$  axis and a positive intercept on the  $\sqrt{t}$ -axis [16]. From the slope of the linear domain,  $2nF\left(\frac{A}{A_s}\right)k_a C_b / (H\pi^{1/2})$  of eq. 3.6.32, for the curves shown Figure 4.2.31, the apparent heterogeneous rate constant  $k_h$  at  $-0.4$  V can be determined [16]. For  $k_h$  the apparent heterogeneous rate constant (in  $\text{cm s}^{-1}$ ),  $Q$  is the superficial charge density (in  $\text{C cm}^{-2}$ ), and  $t_i$  is determined from the intercept of  $Q$  vs.  $\sqrt{t}$  at  $Q = 0$  (Fig. 4.2.31),  $n$  is the calculated number of electrons transferred,  $F$  is the Faraday constant ( $96485 \text{ C mol}^{-1}$ ),  $A_s$  is the geometrical surface area ( $= 0.0706 \text{ cm}^2$ ),  $C_b$  is bulk concentration ( $= 0.5 \times 10^{-3} \text{ mol cm}^{-3}$ ), and  $H$  is taken from eq. 4.6.33. Table 4.2.2 summarizes the  $k_h$  values at  $-0.4$  at 298 K obtained from the slope of eq. (3.6.32) corresponding to the data from Fig. 4.2.31. The apparent heterogeneous rate constants for  $-0.4$  V potential step show the following order of electrocatalytic activity: Pt-Ir > Pt-Ag > Pt-Ni > Pt-Au > Pt, with  $k_h$  between  $28.7 \times 10^{-6} \text{ cm s}^{-1}$  for Pt-Ir and  $5.84 \times 10^{-6} \text{ cm s}^{-1}$  for Pt.

Table 4.2.2. Apparent heterogeneous rate constants for  $BH_4^-$  oxidation at  $-0.4$  V vs. MOE and 298 K calculated from chronocoulometry.

Catalyst	Pt	Pt-Au	Pt-Ni	Pt-Ir	Pt-Ag
$k_h$ (cm s <sup>-1</sup> )	$5.84 \times 10^{-6}$	$6.26 \times 10^{-6}$	$12.6 \times 10^{-6}$	$28.7 \times 10^{-6}$	$13.9 \times 10^{-6}$

The observed catalytic effect of Pt-Ir on the electro-oxidation of borohydride can either be explained based on the change in the surface electronic structure due to the alloying [10, 11, 12, 13, 14], or by a bifunctional model of Kua and Goddard [1], where  $OH^-$  is preferentially adsorbed on the Ir active sites forming  $OH_{ad}$ , while the  $BH_4^-$  is adsorbed and oxidized on Pt generating, initially,  $BH_{3,ad}$  [15]. The reaction is likely to further proceed according to the Langmuir-Hinshelwood [8] kinetics between two different surface adsorbed species. The differences in the electrocatalyst activity can be attributed to differences in the reaction paths for each catalyst: mainly the competition between hydrolysis, direct oxidation, intermediates and hydrogen oxidation [7]. Therefore, further fundamental studies are needed to further elucidate the multi-electron multi-step borohydride mechanism and the associated catalytic effects of the various materials.

#### 4.2.5. Fuel cell performance

Figures 4.2.33-4.2.36 show the temperature and fuel flow rates effects on the polarization curves obtained using the colloidal Pt, Pt-Au, Pt-Ni and Pt-Ir catalysts respectively. Increasing the temperature from 298 K to 333 K, significantly improved the borohydride fuel cell performance. At 298 K, the flow rate had a very small effect on the fuel cell performance in all cases. This is in good agreement with the RDE results. At 333 K, the flow rate had a very small effect on the fuel cell performance only in the cases of Pt-Ni and Pt-Ir, while for Pt-Au flow rate showed a significant effect as flow rate increases. For Pt at 333 K showed unexpected behaviour, where as the flow rate increases the fuel cell performance decreases.



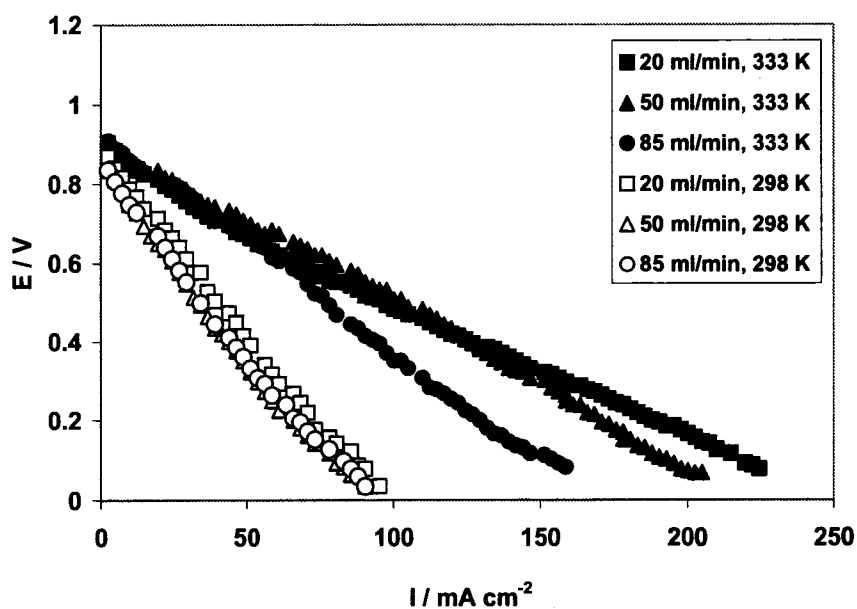


Fig. 4.2.33. Direct borohydride fuel cell polarization curves at 298 K and 333 K: Anode catalyst (Pt) load  $5 \text{ mg cm}^{-2}$ .  $2 \text{ M NaBH}_4 - 2 \text{ M NaOH}$ . Cathode catalyst (Pt) load  $4 \text{ mg cm}^{-2}$ .  $\text{O}_2$  flow rate  $200 \text{ ml min}^{-1}$  at 2.7 atm.

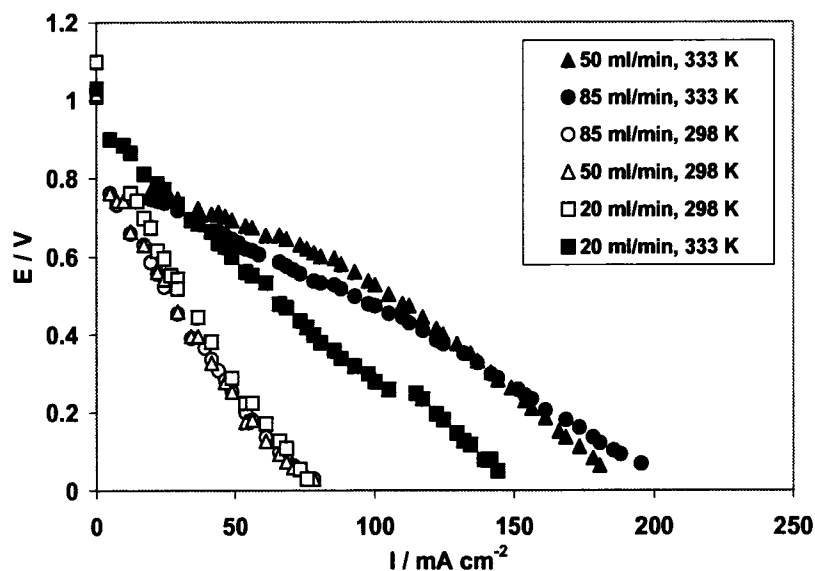


Fig. 4.2.34. Direct borohydride fuel cell polarization curves at 298 K and 333 K: Anode catalyst (Pt-Au) load  $5 \text{ mg cm}^{-2}$ .  $2 \text{ M NaBH}_4 - 2 \text{ M NaOH}$ . Cathode catalyst (Pt) load  $4 \text{ mg cm}^{-2}$ .  $\text{O}_2$  flow rate  $200 \text{ ml min}^{-1}$  at 2.7 atm.

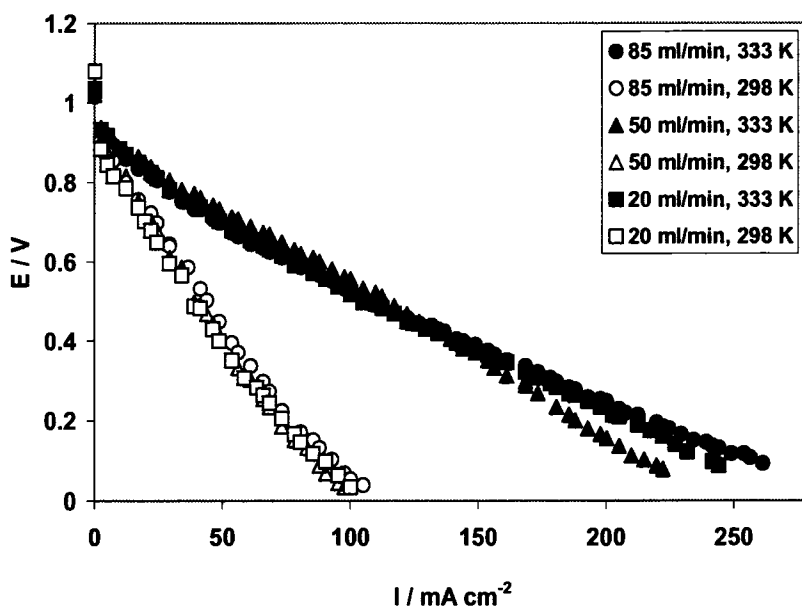


Fig. 4.2.35. Direct borohydride fuel cell polarization curves at 298 K and 333 K: Anode catalyst (Pt-Ni) load  $5 \text{ mg cm}^{-2}$ .  $2 \text{ M NaBH}_4 - 2 \text{ M NaOH}$ . Cathode catalyst (Pt) load  $4 \text{ mg cm}^{-2}$ .  $\text{O}_2$  flow rate  $200 \text{ ml min}^{-1}$  at  $2.7 \text{ atm}$ .

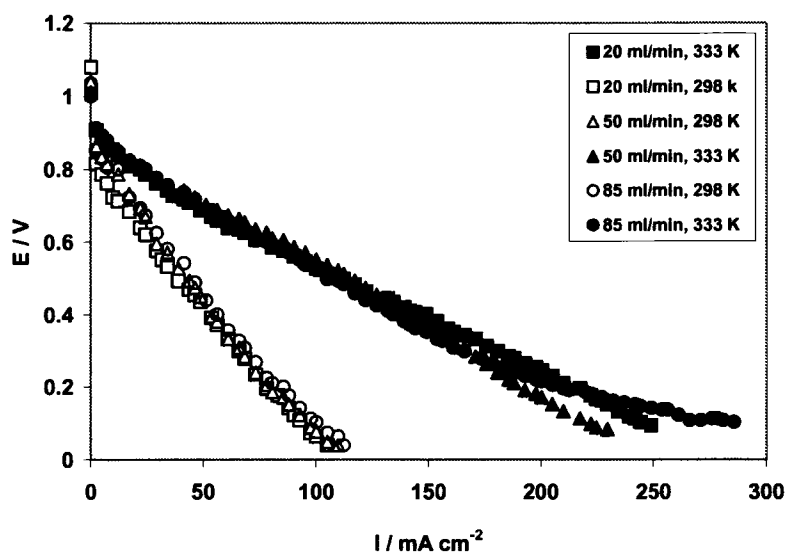


Fig. 4.2.36. Direct borohydride fuel cell polarization curves at 298 K and 333 K: Anode catalyst (Pt-Ir) load  $5 \text{ mg cm}^{-2}$ .  $2 \text{ M NaBH}_4 - 2 \text{ M NaOH}$ . Cathode catalyst (Pt) load  $4 \text{ mg cm}^{-2}$ .  $\text{O}_2$  flow rate  $200 \text{ ml min}^{-1}$  at  $2.7 \text{ atm}$ .

A comparison of the colloidal Pt, Pt-Au, Pt- Ni and Pt-Ir catalysts' performance can be seen in Fig. 4.2.37. Pt-Ir has the best performance, and a fuel cell with Pt-Ir as the anode catalyst, operating at a cell voltage of 0.5 V, can give a current of 46 mA cm<sup>-2</sup> and 105 mA cm<sup>-2</sup> at 298 K and 333 K, respectively.

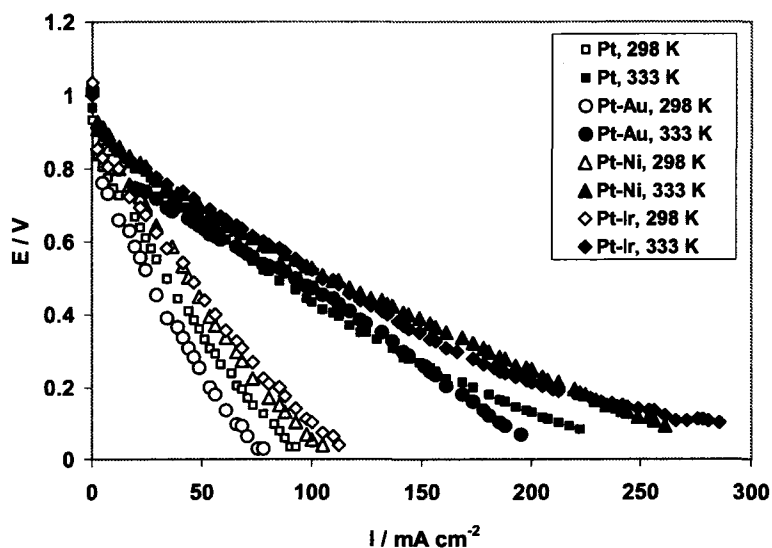


Fig. 4.2.37. Direct borohydride fuel cell polarization curves at 298 K and 333 K: Comparison between the colloidal catalysts prepared in the present work (Pt, Pt-Au, Pt-Ni and Pt-Ir). Anode catalyst load 5 mg cm<sup>-2</sup>. 50 ml min<sup>-1</sup> 2 M NaBH<sub>4</sub> – 2 M NaOH. Cathode catalyst (Pt) load 4 mg cm<sup>-2</sup>. O<sub>2</sub> flow rate 200 ml min<sup>-1</sup> at 2.7 atm.

It is of interest to compare the performance of these colloidal Pt, Pt-Au, Pt- Ni and Pt-Ir catalysts with a commercial Pt-Ru catalyst (1:1 atomic ratio, 20 %wt on Vulcan XC-72, ETEK Inc.) as an anode electrocatalyst for DBFC. A load of 5 mg cm<sup>-2</sup> was used for all catalysts and they were prepared using the same preparation method. Figure 4.2.38 shows that for the conditions investigated, all the laboratory-made catalysts showed superior performance to the commercial Pt-Ru catalyst. Employing Pt-Ir, for example, can give a current density which is 2.11 times higher than that for the commercial Pt-Ru at a cell voltage of 0.5 V and 298 K.

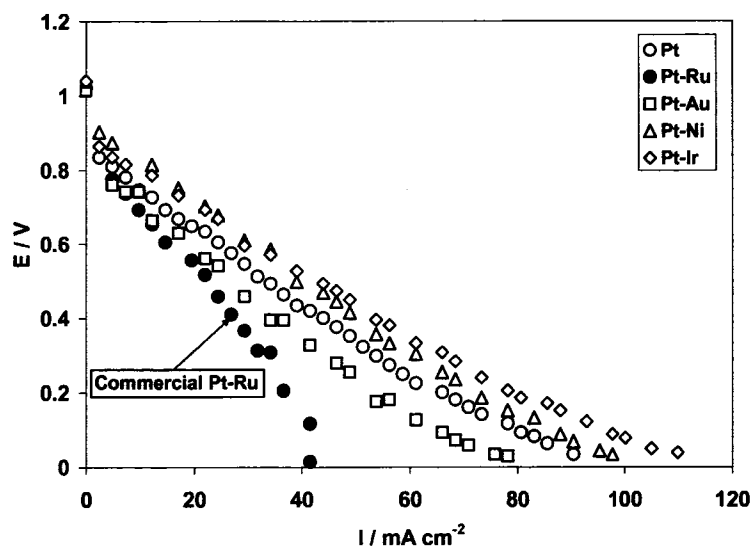


Fig. 4.2.38. Direct borohydride fuel cell polarization curve at 298 K: Comparison between commercial Pt-Ru and the colloidal catalysts prepared in the present work (Pt, Pt-Au, Pt-Ni and Pt-Ir). Anode catalyst load  $5 \text{ mg cm}^{-2}$ .  $50 \text{ ml min}^{-1}$   $2 \text{ M NaBH}_4$ -  $2 \text{ M NaOH}$ . Cathode catalyst (Pt) load  $4 \text{ mg cm}^{-2}$ .  $\text{O}_2$  flow rate  $200 \text{ ml min}^{-1}$  at 2.7 atm.

#### 4.2.6. Summary

In summary, the most active catalysts among the Pt-group were Pt-Ni and Pt-Ir. The lowest Tafel slope  $b_a$  was for Pt-Ni, and the highest exchange current density  $i_o$  and heterogeneous rate constant,  $k_h$ , was for Pt-Ir. The best fuel cell performance at 298 K was for Pt-Ir, while at 333 K it was for Pt-Ni. The fuel cell performance (as measured by current density) for the Pt-group catalysts were about 2.11 times higher than that for Pt-Ru, the most popular commercial catalyst.

### 4.3. Gold and Gold Alloys

#### 4.3.1. Voltammetry of borohydride oxidation on static electrodes

The linear voltammograms on static electrodes for colloidal Au, Au-Pt, Au-Pd, Au-Ni, and Au-Ag catalysts are shown in Figs. 4.3.1-4.3.4 and 4.2.2. They were recorded at scan rate of  $100 \text{ mV s}^{-1}$  as a function of increasing  $\text{NaBH}_4$  concentration (between 0.03 and 1 M).

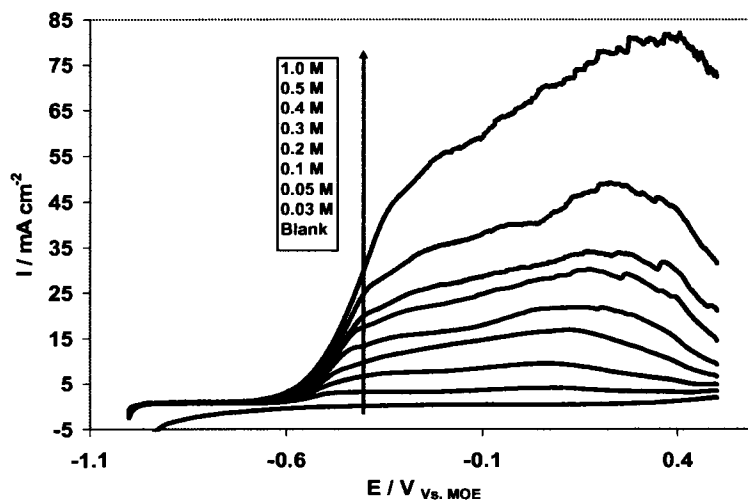


Fig. 4.3.1. Linear voltammogram of  $\text{BH}_4^-$  oxidation on colloidal Au catalyst using a static electrode showing the effect of  $\text{BH}_4^-$  concentration. Scan rate  $100 \text{ mV s}^{-1}$ , 298 K. Inset legend indicates the  $\text{NaBH}_4$  concentration in 2 M NaOH.

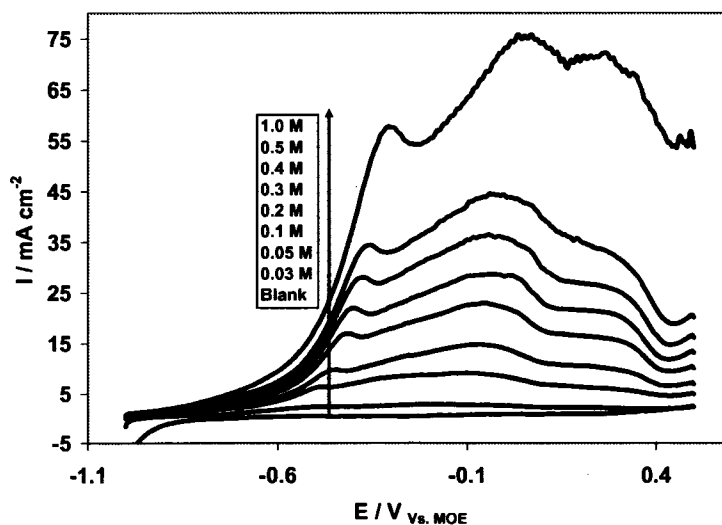


Fig. 4.3.2. Linear voltammogram of  $\text{BH}_4^-$  oxidation on colloidal Au-Pd catalyst using a static electrode showing the effect of  $\text{BH}_4^-$  concentration. Scan rate  $100 \text{ mV s}^{-1}$ , 298 K. Inset legend indicates the  $\text{NaBH}_4$  concentration in 2 M NaOH.

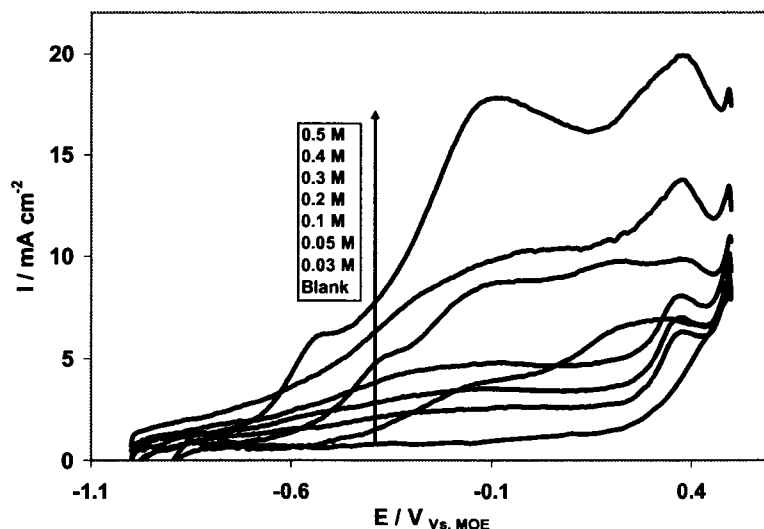


Fig. 4.3.3. Linear voltammogram of  $\text{BH}_4^-$  oxidation on colloidal Au-Ni catalyst using a static electrode showing the effect of  $\text{BH}_4^-$  concentration. Scan rate  $100 \text{ mV s}^{-1}$ , 298 K. Inset legend indicates the  $\text{NaBH}_4$  concentration in 2 M NaOH.

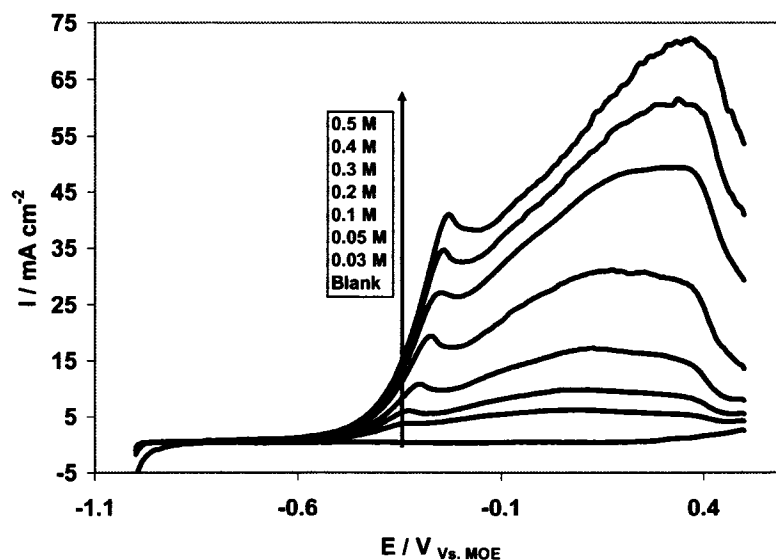


Fig. 4.3.4. Linear voltammogram of  $\text{BH}_4^-$  oxidation on colloidal Au-Ag catalyst using a static electrode showing the effect of  $\text{BH}_4^-$  concentration. Scan rate  $100 \text{ mV s}^{-1}$ , 298 K. Inset legend indicates the  $\text{NaBH}_4$  concentration in 2 M NaOH.

On the colloidal Au catalyst, only one wide oxidation peak was identified. This peak ranged between  $-0.4$  and  $+0.3 \text{ V vs. MOE}$  and was a function of the borohydride concentration. This peak potential shifts slightly toward more positive values with increasing  $\text{NaBH}_4$  concentration (Fig. 4.3.5). This is generally consistent with the

findings of Mirkin and Bard [34] and Gyenge [6] for a planar gold surface, with a single peak between  $-0.12$  and  $+0.38$   $V_{\text{SHE}}$  or ( $-0.249$  to  $0.251$  V vs. MOE) for the oxidation of  $3.2$  mM  $\text{BH}_4^-$  in  $0.2$ - $1$  M  $\text{NaOH}$ , and  $-0.2$  to  $-0.4$   $V_{\text{Ag/AgCl, KClstd}}$  for the oxidation of  $0.03$  M  $\text{BH}_4^-$  in  $2$  M  $\text{NaOH}$ . It has been demonstrated that this peak is a result of the direct oxidation of  $\text{BH}_4^-$  on Au with eight electrons transferred (eq. 2.10.3) [6, 35].

Alloying gold, which has a fairly inert surface, at least for dehydrogenation [8], with metals that are being widely used for complete oxidation and hydrogenation/dehydrogenation processes, (e.g., Pt, Pd, and Ni) is of interest in order to see their effects on Au's catalytic activity to  $\text{NaBH}_4$  oxidation [8, 36-43]. On Au-Pt, a large oxidation wave was recorded at more negative peak potentials than Au, i.e., between  $-0.1$  and  $0.05$  V vs. MOE. A comparison of Figs. 4.2.1, 4.3.1 and 4.2.2 shows the effect of Pt as an add atom. The oxidation wave has widened and peaks at a more negative potential compared to both pure Au and pure Pt.

Colloidal, Au-Pd, Au-Ni, and Au-Ag catalysts were also tested as anode electrocatalyst for borohydride oxidation (Figs. 4.3.2, 4.3.3 and 4.3.4, respectively). With Pd as an add atom, two oxidation peaks were present. The first occurred between  $-0.5$  and  $-0.1$  V vs. MOE, and the other between  $-0.1$  and  $0$  V vs. MOE, and was a function of the borohydride concentration. The peak potentials shifted towards more negative values compared to pure Au. Again, by comparing Figs. 4.3.1 and the CV data for Pd (section 4.5) with 4.3.2, the effect of the Pd add atom in enhancing the Au electroactivity can be clearly seen.

Although the pure Ni catalyst did not show any peaks (Fig. 4.2.6), on alloying Au with Ni, there were multiple peaks, at  $-0.5$ ,  $0$ , and  $+0.4$  V vs. MOE respectively, and these showed a slight dependence on concentration (Fig. 4.3.3). The peaks were clearer at high  $\text{NaBH}_4$  concentrations. This might be due to the changes in structure and surface electronic structure of the bimetallic Au-Ni, which led to the activation of the Ni and/or Au surfaces [10, 11, 12, 13, 14]. For Ag-Au (only one peak at a more positive potential was recorded on pure Ag, Fig. 4.2.7), two oxidation peaks occurred. One was around  $-0.30$  V vs. MOE and showed a slight dependence on concentration. The second was between  $0.15$  and  $0.37$  V vs. MOE and varied with  $\text{NaBH}_4$  concentration (Fig. 4.3.4). By knowing that the pure Ni did not show any oxidation peak, and that pure Ag showed an

oxidation peak at a very positive potential, around +0.4 V vs. MOE, and by recalling Figs. 4.3.3 and 4.3.4, the effect of these add atoms on the electroactivity of Au can be explained by the presence of the new oxidation peaks at more negative potentials compared to pure Ni and Pure Ag.

The Au-Pt catalyst gave the largest voltammetric  $BH_4^-$  oxidation current densities at potentials which were more negative than the rest of the Au-based catalysts. Au-Pd also exhibited comparable negative peak potentials to Au-Pt, but had lower peak current densities.

The linear relationship between the peak current density and  $NaBH_4$  concentration for the peak potential ranges; Au (0.01 to 0.30 V), Au-Pt (-0.2 to 0.15 V), Au-Pd (-0.075 to -0.185 V), Au-Ni (~-0.4 V), and Au-Ag (0.077 to 0.366 V) can be seen in Fig. 4.3.5. The highest slope of the  $I_p$  vs.  $C_b$  plot was found for Au-Pt.

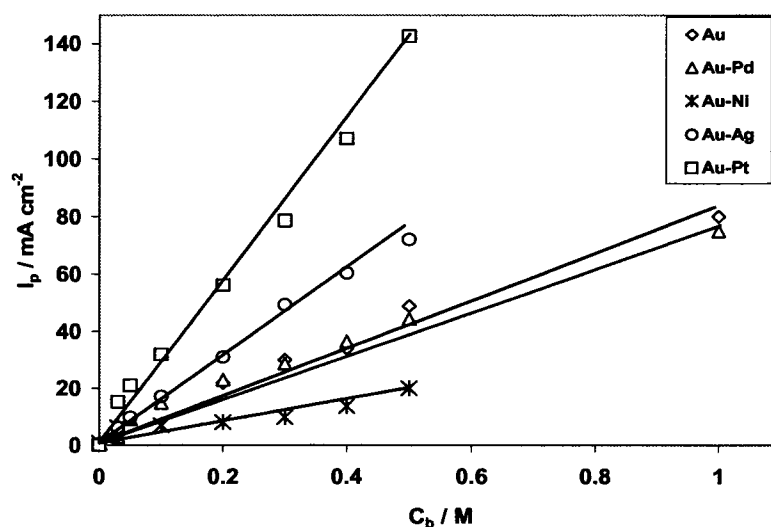


Fig. 4.3.5. The concentration dependence of the peak current density for colloidal Au and Au-alloys. Scan rate  $100 \text{ mV s}^{-1}$ , 298 K.

The scan rate dependence of linear voltammograms, in the range between 5 to 500  $\text{mV s}^{-1}$  at 0.03 M  $NaBH_4$  concentration, on static electrodes for colloidal Au, Au-Pd, Au-Ni, Au-Ag and Au-Pt have been recorded (Figures 4.3.6-4.3.9 and 4.2.10, respectively). It is obvious that the oxidation peak potentials are very slightly dependent on the scan rate for most of the investigated catalysts.



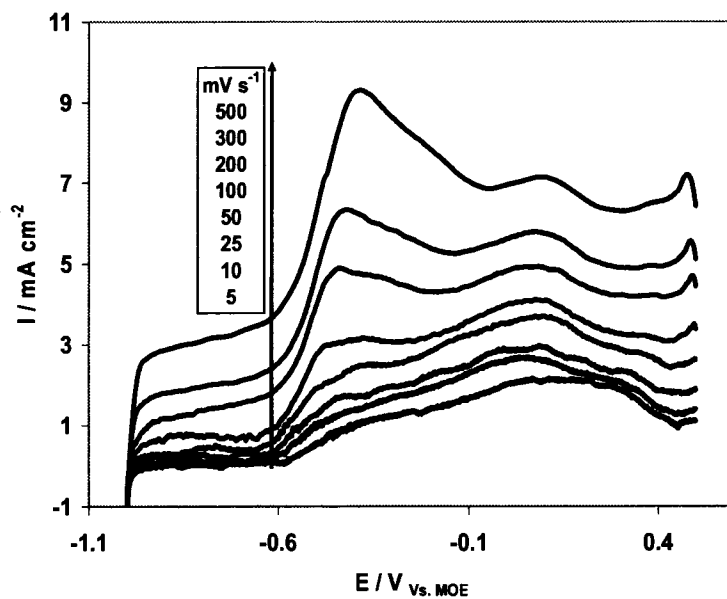


Fig. 4.3.6. Linear voltammogram of  $\text{BH}_4^-$  oxidation on colloidal Au catalyst using a static electrode showing the effect of scan rate.  $\text{NaBH}_4$  concentration 0.03 M, 298 K. Inset legend indicates the scan rate.

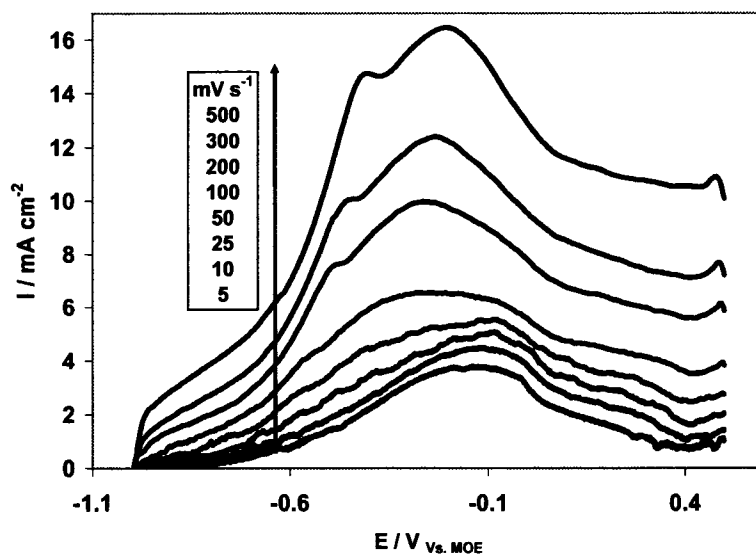


Fig. 4.3.7. Linear voltammogram of  $\text{BH}_4^-$  oxidation on colloidal Au-Pd catalyst using a static electrode showing the effect of scan rate.  $\text{NaBH}_4$  concentration 0.03 M, 298 K. Inset legend indicates the scan rate.

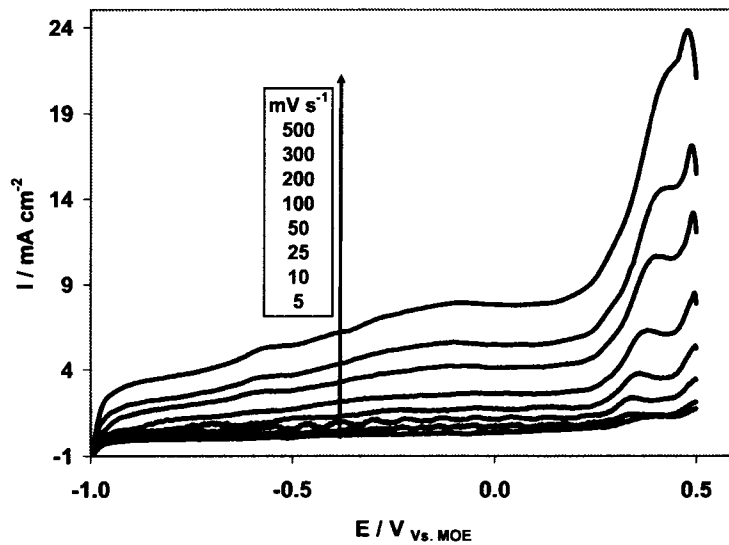


Fig. 4.3.8. Linear voltammogram of  $\text{BH}_4^-$  oxidation on colloidal Au-Ni catalyst using a static electrode showing the effect of scan rate.  $\text{NaBH}_4$  concentration 0.03 M, 298 K. Inset legend indicates the scan rate.

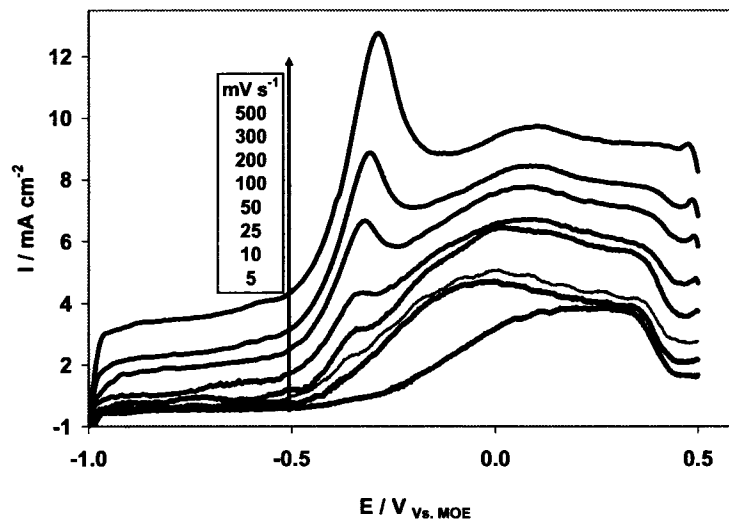


Fig. 4.3.9. Linear voltammogram of  $\text{BH}_4^-$  oxidation on colloidal Au-Ag catalyst using a static electrode showing the effect of scan rate.  $\text{NaBH}_4$  concentration 0.03 M, 298 K. Inset legend indicates the scan rate.

Fig. 4.3.10 is a plot the peak current density versus the square root of scan rate at a constant  $\text{NaBH}_4$  concentration of 0.03 M for the peak potential ranges; Au (0.01 to 0.140 V), Au-Pt (-0.2 to 0.15 V), Au-Pd (-0.14 to -0.20 V), Au-Ni (0.4 to 0.5 V), and Au-Ag (0.127 to 0.214 V). A linear increase of peak current density with the square root of scan rate is expected for diffusion controlled processes, in which adsorption effects are

negligible [6, 16, 17-22]. The peak current density of Au-Pt is the most influenced by the scan rate and there is a change at  $100 \text{ mV s}^{-1}$ . Similarly, for Au-Ni and Au-Pd, there is a slope change at  $50 \text{ mV s}^{-1}$ , but the peak current density is dependent on the scan rate compared to Au-Pt. Au and Au-Ag, on the other hand, are the least dependent on the scan rate, and the  $I_p$  vs.  $v^{1/2}$  plots level off at scan rates  $> 50 \text{ mV s}^{-1}$ , indicating slow kinetics for the catalytic process [20].

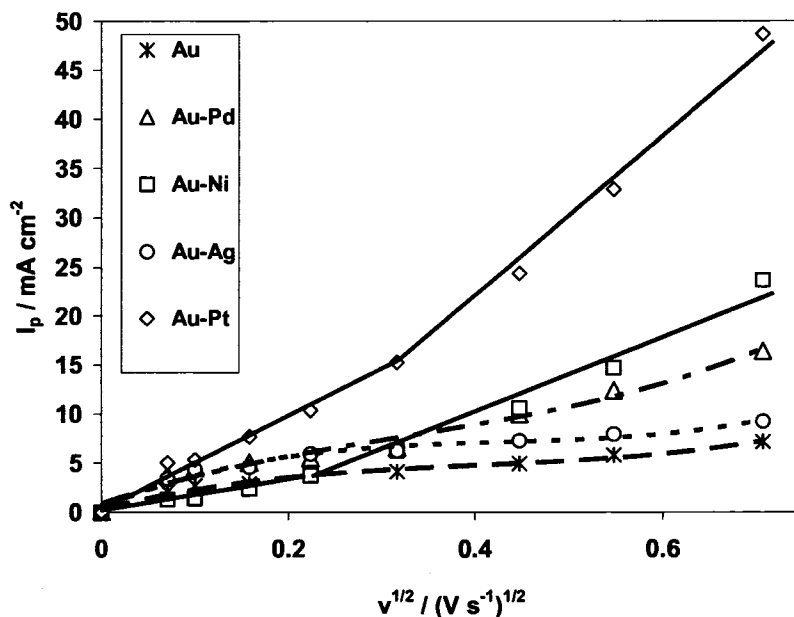


Fig. 4.3.10. The scan rate dependence of the peak current densities obtained on the colloidal Au and Au-alloys catalysts:  $\text{NaBH}_4$  concentration  $0.03 \text{ M}$ ,  $298 \text{ K}$ .

#### 4.3.2. Voltammetry of borohydride oxidation on rotating electrodes

RDE experiments were performed for the colloidal Au, Au-Pd, Au-Ni, Au-Ag and Au-Pt catalysts, and the results are shown in Figures 4.3.11-4.3.14 and 4.2.16, respectively. As in the case of Pt-based catalysts (section 4.2), a strong temperature effect and a weak rotation speed effect can be clearly seen, and their bell-shape type curve was explained in section 4.2.2 for the Pt-alloys.

The peak potential for Au was around  $+0.3 \text{ V}$  vs. MOE, at both  $298 \text{ K}$ ,  $313 \text{ K}$ , and for all rotation speeds (Fig. 4.3.11). On Au-Pt the peak occurred at more negative potentials, around  $0 \text{ V}$  vs. MOE, at both  $298 \text{ K}$  and  $313 \text{ K}$ , and for all rotation speeds (Fig. 4.2.16).

Au-Pd (Fig. 4.3.12) exhibited a peak in the same range as Au-Pt, whilst the presence of Ni gave rise to a peak in the same range as for pure Au (Fig. 4.3.13). On Au-Ag the peak occurred at more positive potentials, between 0.25 V to 0.35 V vs. MOE at 298 K, and around 0.4 V vs. MOE, at 313 K, and for all rotation speeds (Fig. 4.3.14).

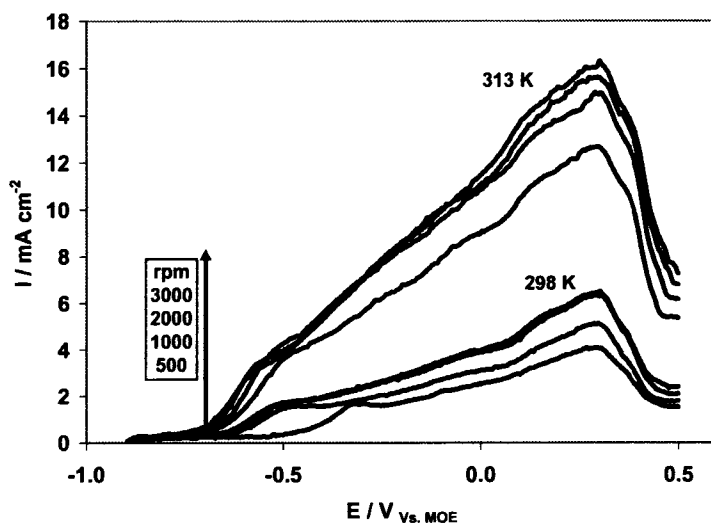


Fig. 4.3.11. Linear voltammetry of  $\text{BH}_4^-$  oxidation on a colloidal Au catalyst using a rotating electrode showing the effects of rotation speed and temperature. Scan rate  $5 \text{ mV s}^{-1}$ , 298 K and 313 K.  $\text{NaBH}_4$  concentration 0.3 M in 2 M NaOH. Inset legend indicates the rotation speed per minute.

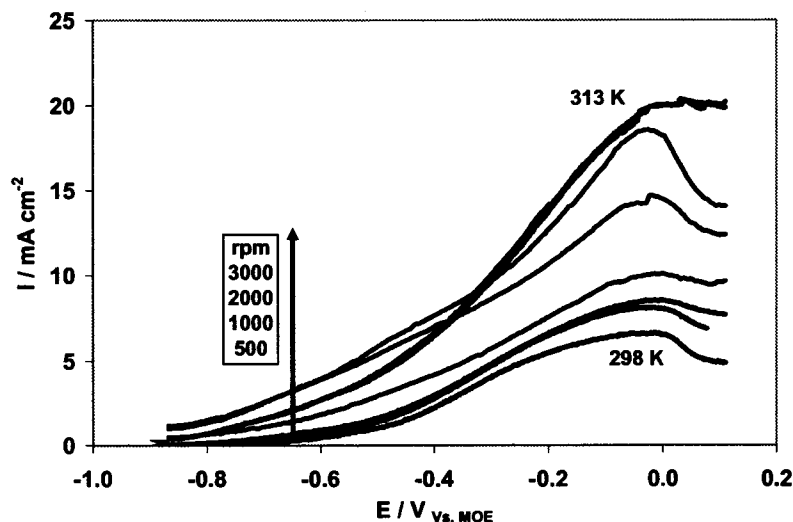


Fig. 4.3.12. Linear voltammetry of  $\text{BH}_4^-$  oxidation on a colloidal Au-Pd catalyst using rotating electrode showing the effects of rotation speed and temperature. Scan rate  $5 \text{ mV s}^{-1}$ , 298 K and 313 K.  $\text{NaBH}_4$  concentration 0.3 M in 2 M NaOH. Inset legend indicates the rotation speed per minute.

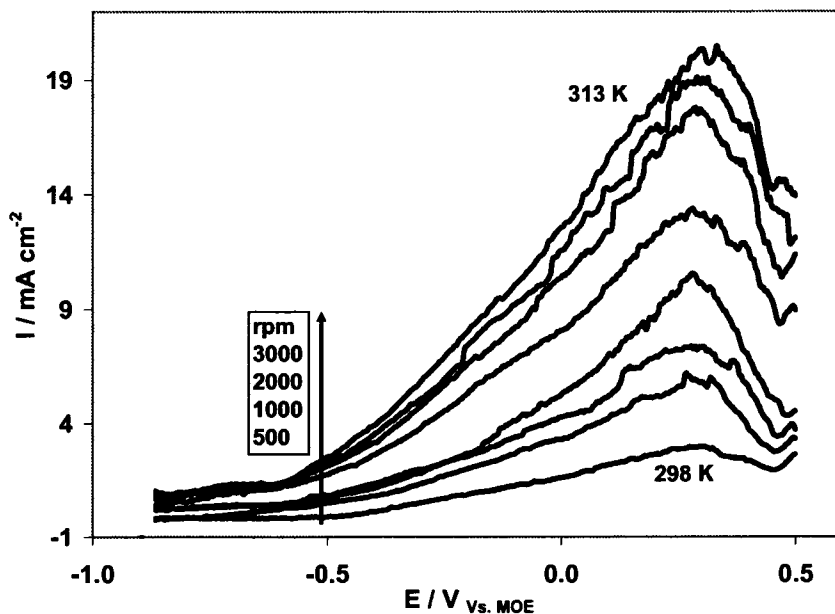


Fig. 4.3.13. Linear voltammetry of  $\text{BH}_4^-$  oxidation on a colloidal Au-Ni catalyst using a rotating electrode showing the effects of rotation speed and temperature. Scan rate  $5 \text{ mV s}^{-1}$ , 298 K and 313 K.  $\text{NaBH}_4$  concentration 0.3 M in 2 M NaOH. Inset legend indicates the rotation speed per minute.

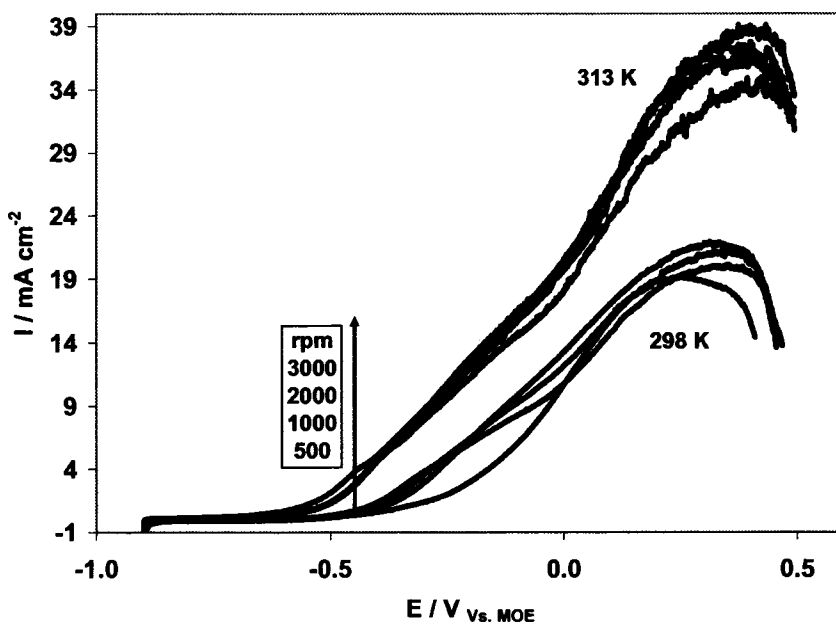


Fig. 4.3.14. Linear voltammetry of  $\text{BH}_4^-$  oxidation on a colloidal Au-Ag catalyst using a rotating electrode showing the effects of rotation speed and temperature. Scan rate  $5 \text{ mV s}^{-1}$ , 298 K and 313 K.  $\text{NaBH}_4$  concentration 0.3 M in 2 M NaOH. Inset legend indicates the rotation speed per minute.

### Tafel slopes and the exchange current densities

Similarly as in the case of Pt-based catalysts (section 4.2.2), a plot of  $\log i$  vs.  $\eta (= E - E_{oc})$  was made as per the Tafel eq. 3.6.12, using the rising domain of Figs. 4.3.11-4.3.14 and 4.2.16. This enabled the calculation of both the apparent Tafel slopes and the exchange current densities (Fig. 4.3.15).

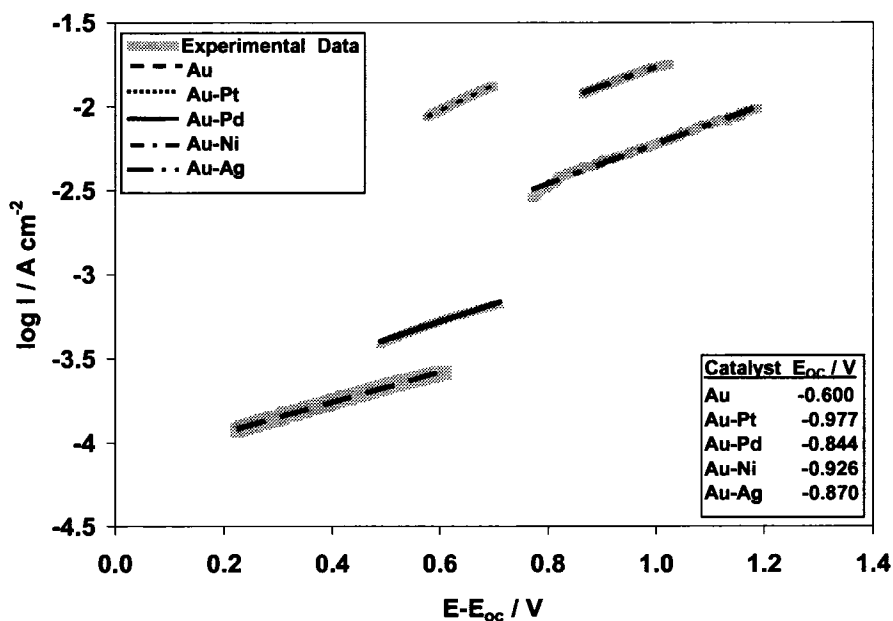


Fig. 4.3.15. Tafel plots for the supported colloidal Au and Au-alloys catalysts generated from the rotating disk electrode data. 298 K.

Table 4.3.1 shows that the apparent Tafel slopes  $b_a$  were in the range of about 0.723 to 1.121 V at 298 K, and are higher by a factor of three to five than the value found for a planar gold surface, i.e., 0.19 V [6]. Alloying Au with Pt, Pd, Ni, and Ag has decreased the apparent Tafel slope at 298 K, which is advantageous from a practical point of view [25, 26]. Also, the exchange current density is increased by alloying Au with Pt, Pd, Ni, and Ag (Table 4.3.1). At 298 K, the Pt-Au catalyst had the highest exchange current density,  $1.4 \times 10^{-3} \text{ A cm}^{-2}$ . Au and Au-Pd on the other hand, gave the lowest exchange current densities of  $0.076 \times 10^{-3}$  at 298 K, indicating the slowest kinetics of borohydride oxidation on Au.

Similarly, as in section 4.2.2, using the  $b_a$  values from Table 4.3.1 in conjunction with eq. 4.3.1 which is similar to eq. (4.2.2), the number of electrons involved in the borohydride oxidation can be calculated taking into account that  $n$  is equal to 8 for pure Au [6, 26, 34, 35]:

$$\frac{n_{Au-X}}{n_{Au}} \cdot \left( \frac{b_{a,Au}}{b_{a,Au-X}} \right)^{1/2} = \frac{\beta_{Au-X}}{\beta_{Au}} \quad (4.3.1)$$

Table 4.3.1 summarizes the number of electrons involved in the oxidation of borohydride on Au and its alloys. The oxidation of  $BH_4^-$  on Au-based catalysts leads to an incomplete oxidation (i.e.,  $n < 8$ ) except for Au-Ag. For Au-Pd  $n = 6.21$ , and for Au-Ni  $n = 2.51$ . Au-Ag, on the other hand, showed an unexpected number of electrons transferred, i.e.  $n \sim 12$ , which is more than that could be gained by the complete oxidation described by eq. 2.10.3 ( $n = 8$ ).

Table 4.3.1. Apparent Tafel slopes,  $b_a$ , exchange current densities,  $i_{0,a}$ , total number of electrons exchanged,  $n$ , determined from RDE data using supported colloidal Au and Au-alloys catalysts with Nafion 117 polymer electrolyte. Eq. (4.3.1) was used for the calculation of  $n$ .

Catalysts	$b_a$ (V dec <sup>-1</sup> ) 298 K	$i_{0,a}$ (A cm <sup>-2</sup> ) 298 K	n
Au	1.121	0.076x10 <sup>-3</sup>	8
Au-Pt	0.723	1.4x10 <sup>-3</sup>	7.8
Au-Pd	0.938	0.120x10 <sup>-3</sup>	6.2
Au-Ni	0.851	0.399x10 <sup>-3</sup>	2.5
Au-Ag	0.888	1.285x10 <sup>-3</sup>	12

### 4.3.3. Chronopotentiometry

The overpotential,  $\eta (= E - E_{oc})$ , was the smallest on Au-Pt, about 325 mV, followed by Au-Ag (422 mV), Au-Pd (553 mV), Au (576 mV) and lastly Au-Ni, where the overpotential was 895 mV. Au-Pt is the most active among the investigated Au-alloys, since it shows a lower overpotential [16]. The more negative the open circuit potential of the anode, the lower hydrolysis activity of the catalyst [7].

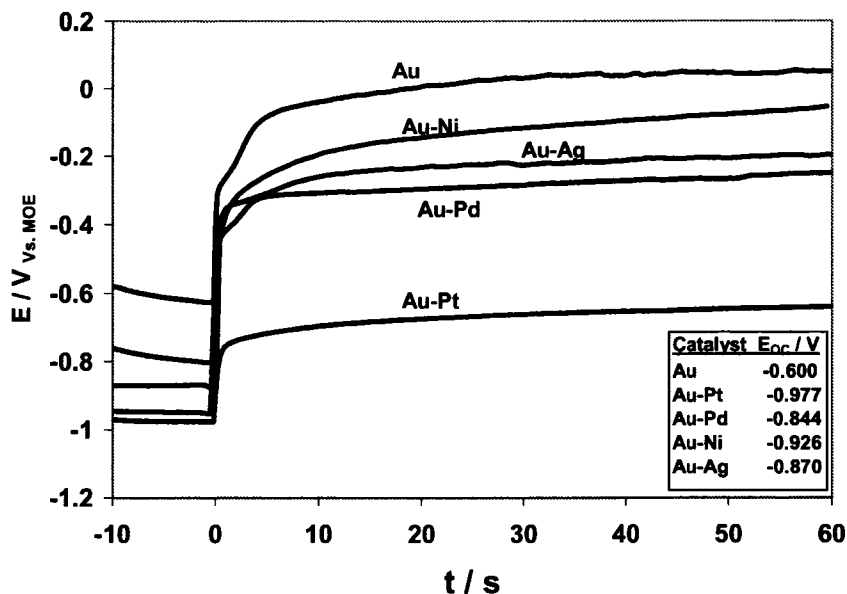


Fig. 4.3.16. Chronopotentiometry of  $\text{BH}_4^-$  oxidation on colloidal Au and Au-alloys catalysts. Current step: from 0 to  $10 \text{ mA cm}^{-2}$ .  $0.5 \text{ M Na BH}_4$  in  $2 \text{ M NaOH}$ .  $298 \text{ K}$ .

#### 4.3.4. Chronoamperometry and chronocoulometry

Figures 4.3.17-4.3.20 and 4.2.23 show the current density transients responses on Au, Au-Pd, Au-Ni, Au-Ag and Au-Pt, respectively. The highest anodic current densities, for the  $-0.6 \text{ V}$ ,  $-0.4 \text{ V}$  and  $-0.2 \text{ V}$  potential steps, were measured on Au-Pt, at about  $0.06$ ,  $0.024$ , and  $0.006 \text{ A cm}^{-2}$  respectively (Fig. 4.2.23). Lower current densities than for Au-Pt were recorded on the rest of the colloidal catalysts in the following order,  $\text{Au-Pd} > \text{Au-Ag} > \text{Au-Ni}$  under similar conditions. Therefore, Au-Pt was the most active catalyst among the colloidal Au-alloys in the negative potential range of  $-0.9 \text{ V}$  and  $-0.4 \text{ V}$ , the domain of interest for practical fuel cell anodes.



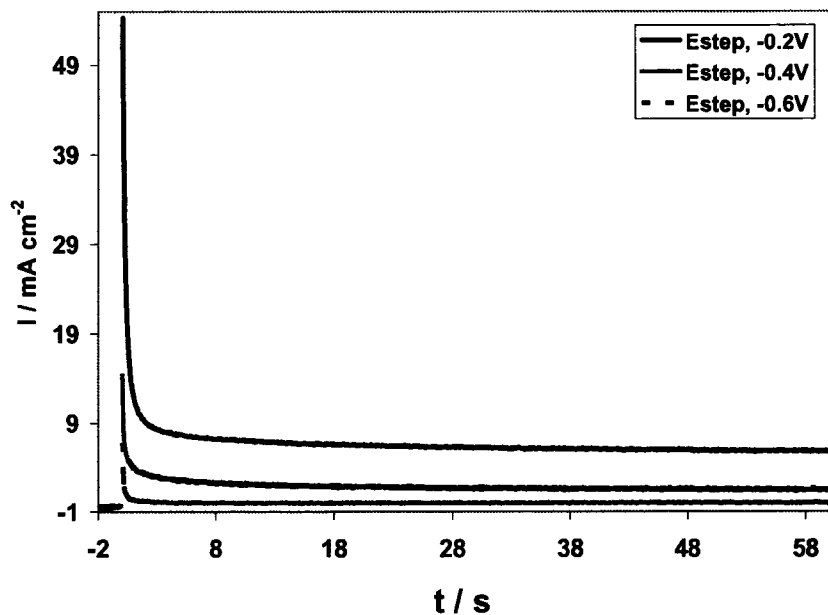


Fig. 4.3.17. Chronoamperometry of  $\text{BH}_4^-$  oxidation on colloidal Au catalyst. Potential steps from  $-0.9 \text{ V}$  vs. MOE to  $-0.6$ ,  $-0.4$  and  $-0.2 \text{ V}$  vs. MOE, respectively  $0.5 \text{ M}$   $\text{NaBH}_4$  in  $2 \text{ M}$   $\text{NaOH}$ .  $298 \text{ K}$ .

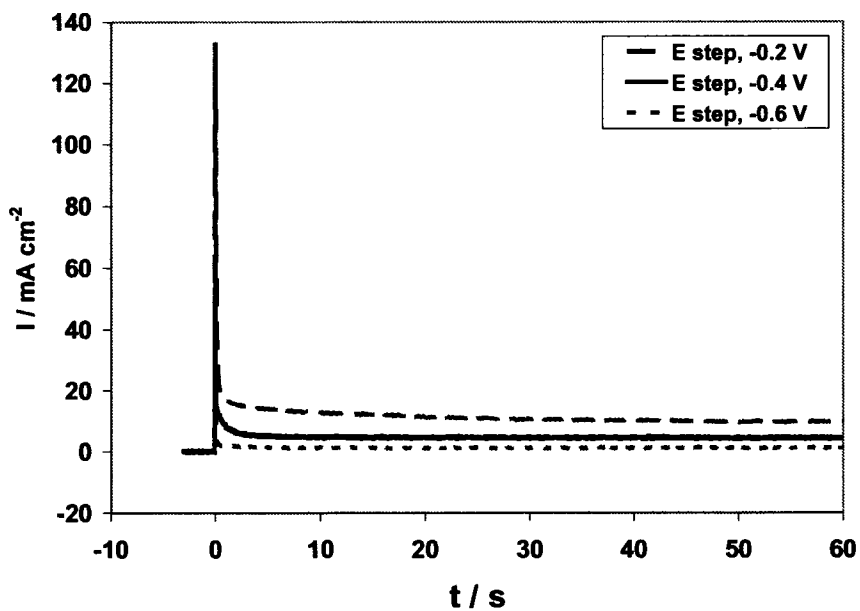


Fig. 4.3.18. Chronoamperometry of  $\text{BH}_4^-$  oxidation on colloidal Au-Pd catalyst. Potential steps from  $-0.9 \text{ V}$  vs. MOE to  $-0.6$ ,  $-0.4$  and  $-0.2 \text{ V}$  vs. MOE, respectively  $0.5 \text{ M}$   $\text{NaBH}_4$  in  $2 \text{ M}$   $\text{NaOH}$ .

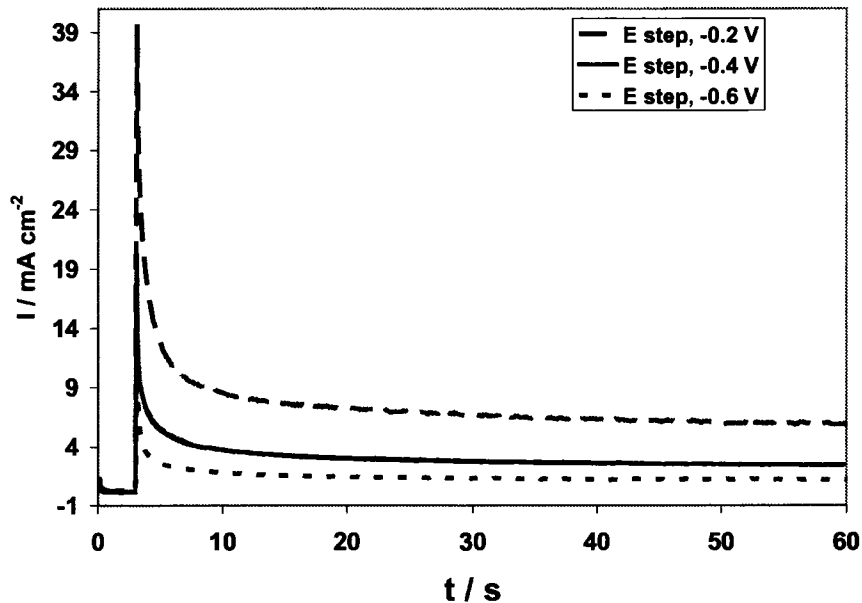


Fig. 4.3.19. Chronoamperometry of  $\text{BH}_4^-$  oxidation on colloidal Au-Ni catalyst. Potential steps from  $-0.9$  V vs. MOE to  $-0.6$ ,  $-0.4$  and  $-0.2$  V vs. MOE, respectively  $0.5$  M  $\text{NaBH}_4$  in  $2$  M  $\text{NaOH}$ .  $298$  K.

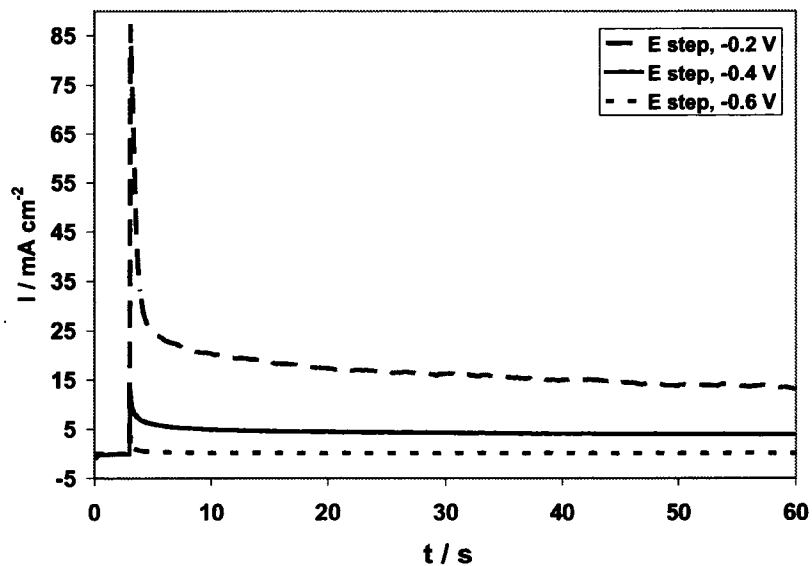


Fig. 4.3.20. Chronoamperometry of  $\text{BH}_4^-$  oxidation on colloidal Au-Ag catalyst. Potential steps from  $-0.9$  V vs. MOE to  $-0.6$ ,  $-0.4$  and  $-0.2$  V vs. MOE, respectively  $0.5$  M  $\text{NaBH}_4$  in  $2$  M  $\text{NaOH}$ .  $298$  K.

### Cottrell Plot

An almost Cottrellian response, i.e., purely diffusion controlled, is shown by the  $i \cdot \sqrt{t}$  vs.  $t$  plots where  $i \cdot \sqrt{t}$  is approximately constant, for all the investigated Au and Au-alloys catalysts for all step changes, except for Au-Pt (Figs. 4.3.21-4.3.23).

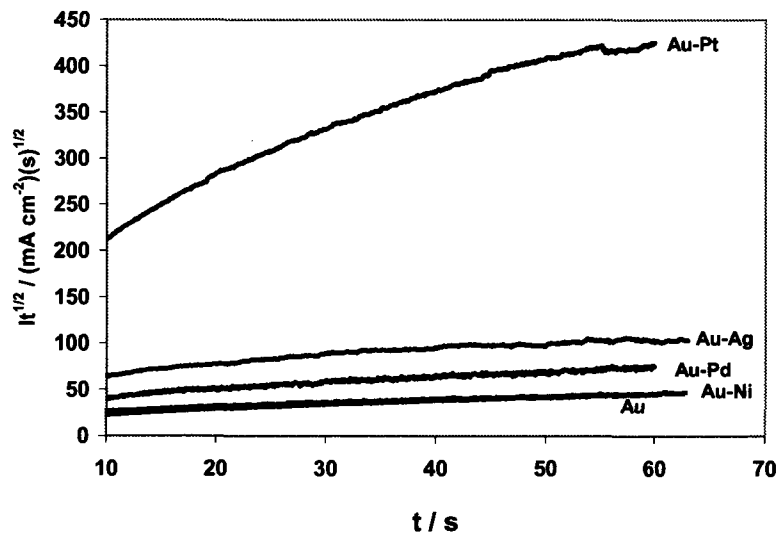


Fig. 4.3.21. Cottrell plots generated from the chronoamperometry data for potential step from  $-0.9 \text{ V}$  to  $-0.2 \text{ V}$  vs. MOE.

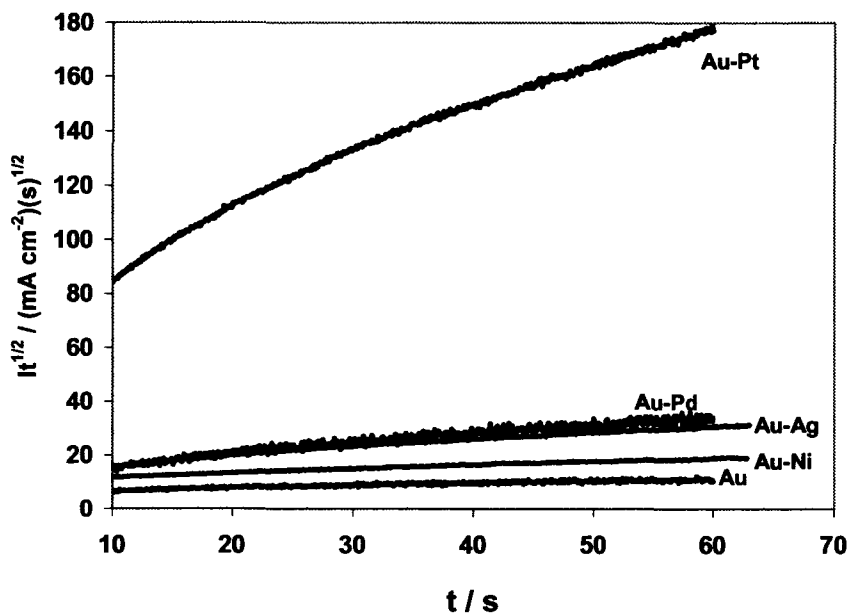


Fig. 4.3.22. Cottrell plots generated from the chronoamperometry data for potential step from  $-0.9 \text{ V}$  to  $-0.4 \text{ V}$  vs. MOE.

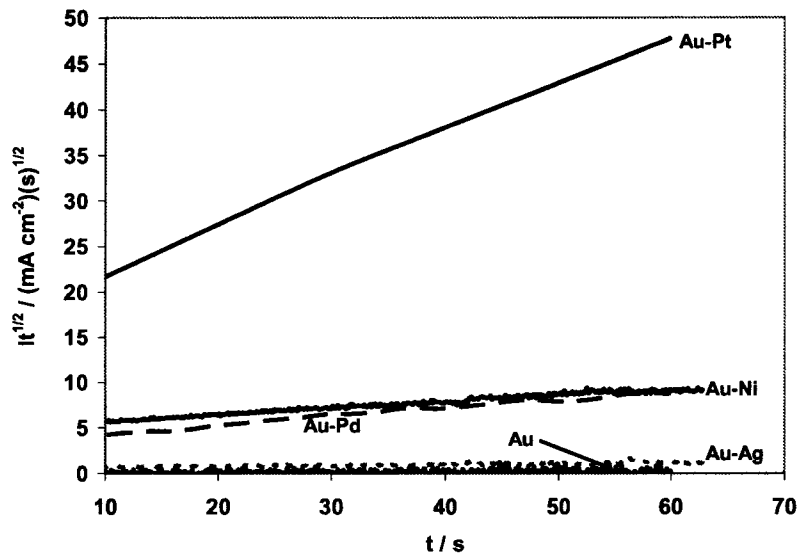


Fig. 4.3.23. Cottrell plots generated from the chronoamperometry data for potential step from  $-0.9 \text{ V}$  to  $-0.6 \text{ V}$  vs. MOE.

### Chronocoulometry

Figures 4.3.28-4.3.30 are Anson plots for Au and its alloy catalysts obtained for potential steps from  $-0.9 \text{ V}$  to  $-0.2 \text{ V}$ ,  $-0.4 \text{ V}$ , and  $-0.6 \text{ V}$  vs. MOE.

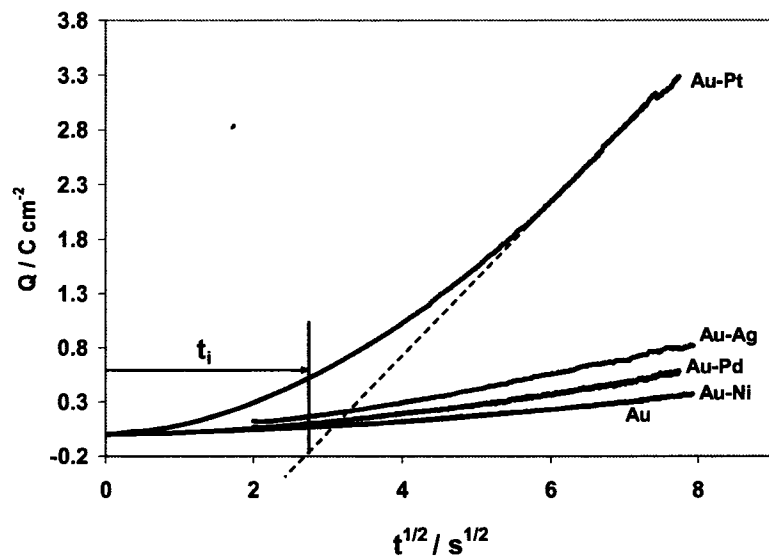


Fig. 4.3.24. Cumulative charge density as a function of square root of time (Anson plot) generated from the chronoamperometry data for a potential step from  $-0.9 \text{ V}$  to  $-0.2 \text{ V}$  vs. MOE.

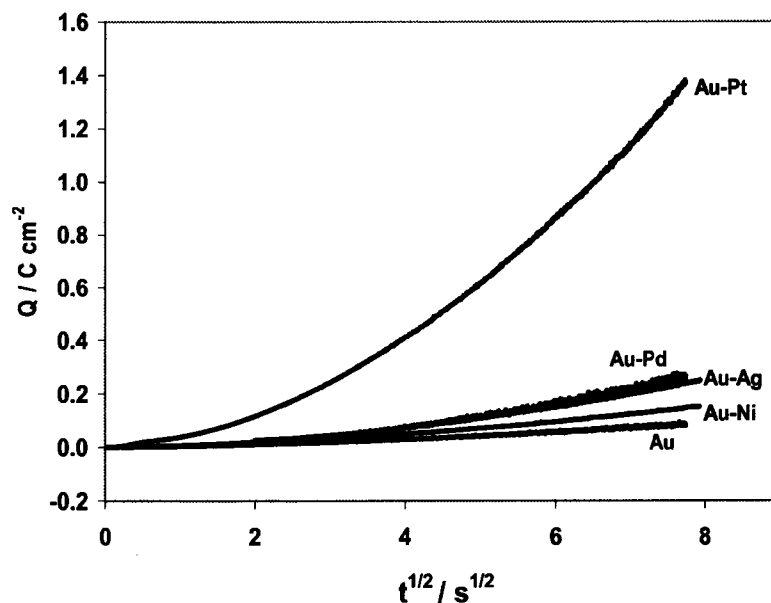


Fig. 4.3.25. Cumulative charge density as a function for square root of time (Anson plot) generated from the chronoamperometry data for a potential step from  $-0.9 \text{ V}$  to  $-0.4 \text{ V}$  vs. MOE.

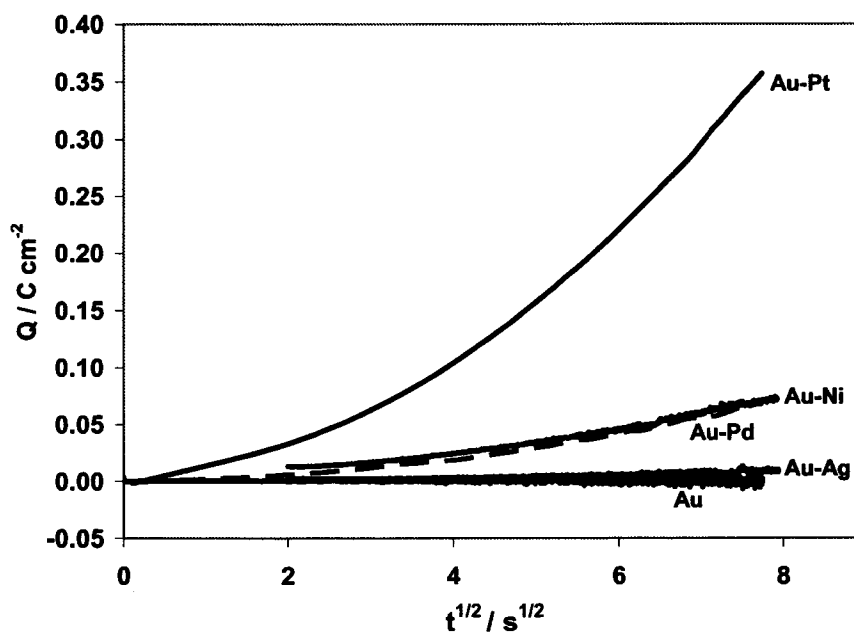


Fig. 4.3.26. Cumulative charge density as a function of square root of time (Anson plot) generated from the chronoamperometry data for a potential step from  $-0.9 \text{ V}$  to  $-0.6 \text{ V}$  vs. MOE.

Figures 4.3.28-4.3.30 show that the plot for Au-Pt highly deviates from linearity, while, the rest of Au-alloys only show a slight deviation. Again, by employing eqs. 3.6.32 and 3.6.33 in conjunction with the extrapolation of the linear domain of these curves shown Figure 4.3.29 to  $Q = 0$ , the apparent heterogeneous rate constant  $k_h$  at  $-0.4$  V can be determined [16].

Table 4.3.2 summarizes the  $k_h$  values at  $-0.4$  V at 298 K obtained from the slope of eq. (3.6.32) corresponding to the data from Fig. 4.3.29. The apparent heterogeneous rate constants for the  $-0.4$  V potential step show the following order of electrocatalytic activity; Au-Pt > Au-Pd > Au-Ni > Au-Ag > Au, with  $k_h$  between  $6.26 \times 10^{-6} \text{ cm s}^{-1}$  for Au-Pt and  $0.559 \times 10^{-6} \text{ cm s}^{-1}$  for pure Au. The high electrocatalytic activity of Au-Pt can be attributed to the addition of Pt, which has a higher activity compared to Au, in addition to, the surface changes due to alloying.

Table 4.3.2. Apparent heterogeneous rate constants for  $\text{BH}_4^-$  oxidation at  $-0.4$  V vs. MOE at 298 K calculated from chronocoulometry.

Catalyst	Au	Au-Pt	Au-Pd	Au-Ni	Au-Ag
$k_h \text{ (cm s}^{-1}\text{)}$	$0.559 \times 10^{-6}$	$6.26 \times 10^{-6}$	$4.08 \times 10^{-6}$	$1.40 \times 10^{-6}$	$1.01 \times 10^{-6}$

#### 4.3.5. Fuel cell performance

Figures 4.3.27-4.3.30 show the effects of temperature and fuel flow rates on the polarization curves obtained using the colloidal Au, Au-Pt, and Au-Pd catalysts. As was the case for the Pt-group, temperature has a significant impact on the fuel cell performance for all alloys, while the flow rate has no significant effect on the fuel cell performance. This could be attributed, at specific temperature, to the intrinsic activity of the catalysts. Accordingly, at all the investigated flow rates, enough fuel is available at the catalyst surface to react. In another words, the flow rate was high enough that the reaction was surface-reaction-limited rather than transport-limited.

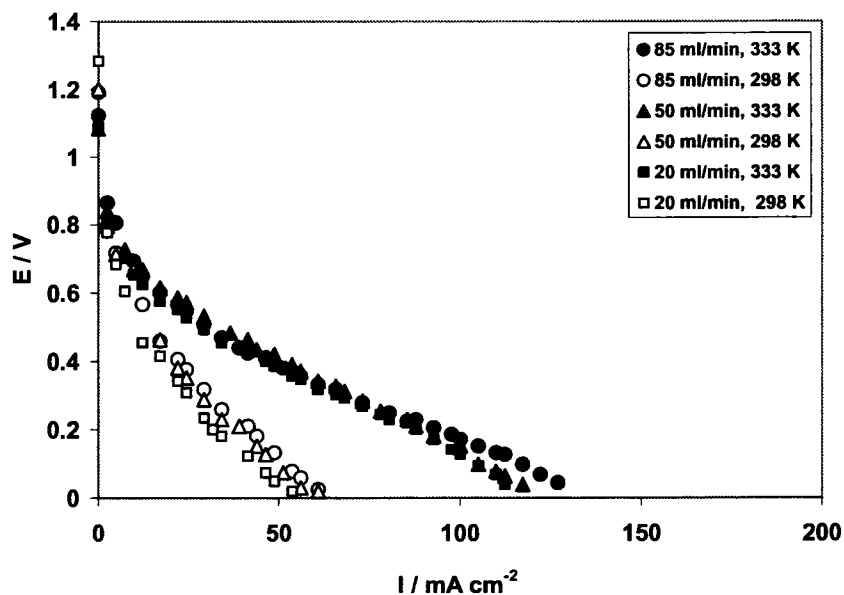


Fig. 4.3.27. Direct borohydride fuel cell polarization curves at 298 K and 333 K: Anode catalyst (Au) load  $5 \text{ mg cm}^{-2}$ .  $2 \text{ M NaBH}_4 - 2 \text{ M NaOH}$ . Cathode catalyst (Pt) load  $4 \text{ mg cm}^{-2}$ .  $\text{O}_2$  flow rate  $200 \text{ ml min}^{-1}$  at  $2.7 \text{ atm}$ .

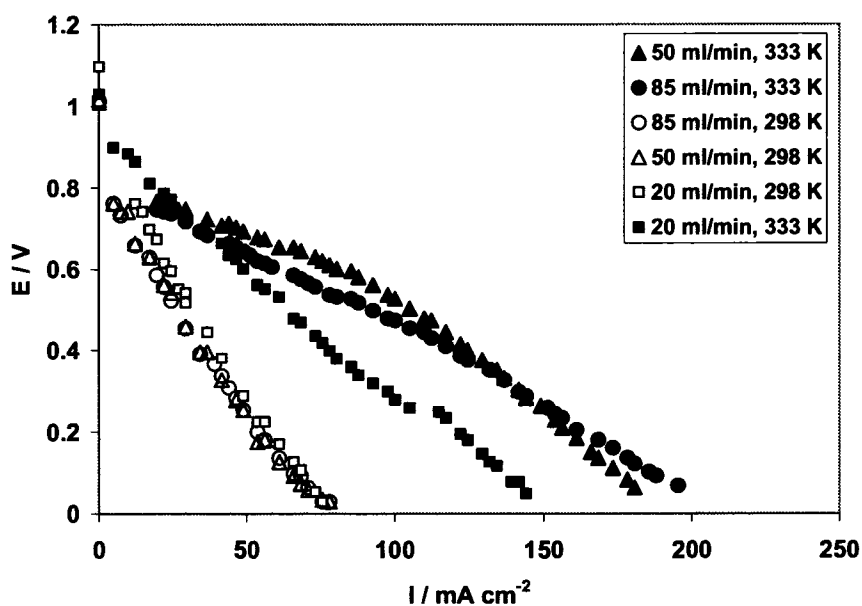


Fig. 4.3.28. Direct borohydride fuel cell polarization curves at 298 K and 333 K: Anode catalyst (Au-Pt) load  $5 \text{ mg cm}^{-2}$ .  $2 \text{ M NaBH}_4 - 2 \text{ M NaOH}$ . Cathode catalyst (Pt) load  $4 \text{ mg cm}^{-2}$ .  $\text{O}_2$  flow rate  $200 \text{ ml min}^{-1}$  at  $2.7 \text{ atm}$ .

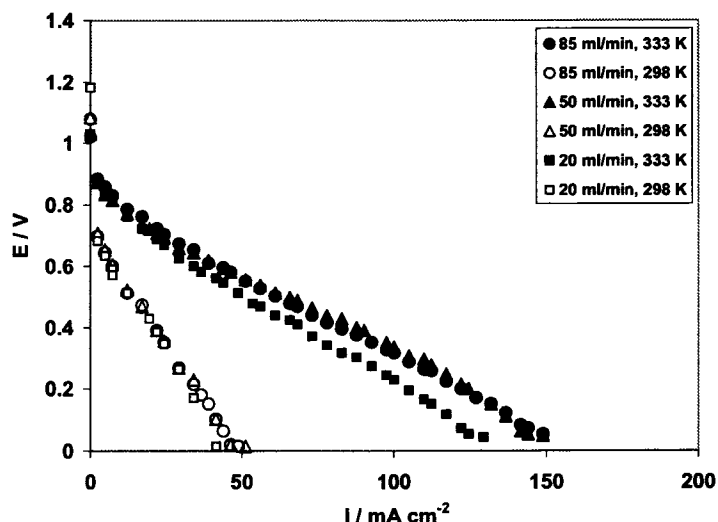


Fig. 4.3.29. Direct borohydride fuel cell polarization curves at 298 K and 333 K: Anode catalyst (Au-Pd) load  $5 \text{ mg cm}^{-2}$ .  $2 \text{ M NaBH}_4 - 2 \text{ M NaOH}$ . Cathode catalyst (Pt) load  $4 \text{ mg cm}^{-2}$ .  $\text{O}_2$  flow rate  $200 \text{ ml min}^{-1}$  at  $2.7 \text{ atm}$ .

The fuel cell performance of the Au, Au-Pt, and Au-Pd catalysts are compared in Fig. 4.3.34. At both 298 K and 333 K, Au-Pt showed the best performance followed by Au-Pd and then Au. A fuel cell with Au-Pt as the anode catalyst, operating at a cell voltage of  $0.5 \text{ V}$  can give a current of  $27 \text{ mA cm}^{-2}$ , while at  $333 \text{ K}$ , the same catalyst can give a current of  $93 \text{ mA cm}^{-2}$  at the same  $0.5 \text{ V}$  cell voltage.

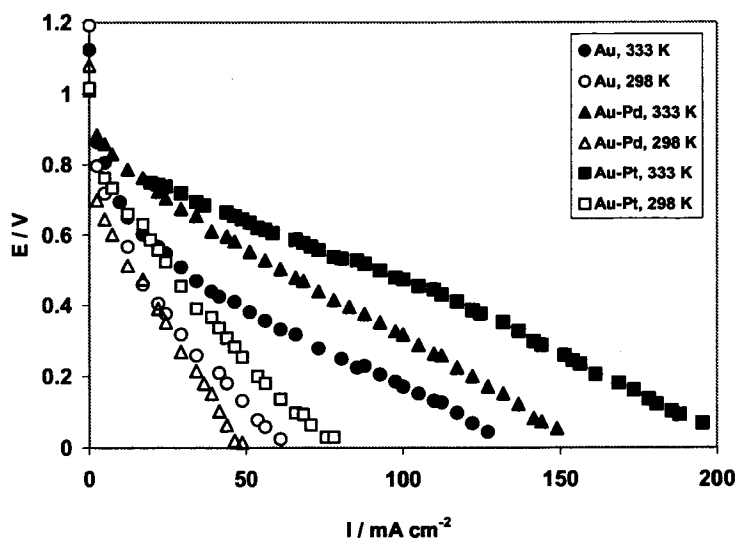


Fig. 4.3.30. Direct borohydride fuel cell polarization curves at 298 K and 333 K: Comparison between the colloidal Au and Au-alloys catalysts prepared. Anode catalyst load  $5 \text{ mg cm}^{-2}$ .  $85 \text{ ml min}^{-1} 2 \text{ M NaBH}_4 - 2 \text{ M NaOH}$ . Cathode catalyst (Pt) load  $4 \text{ mg cm}^{-2}$ .  $\text{O}_2$  flow rate  $200 \text{ ml min}^{-1}$  at  $2.7 \text{ atm}$ .



#### 4.3.6. Summary

In summary, the most active electrocatalyst was Au-Pt catalyst. Au-Pt exhibited the lowest  $b_a$ , and the highest  $i_o$  and heterogeneous rate constant,  $k_h$ , all of which are characteristics of a good electrocatalyst. These fundamental studies have been supported by the fuel cell tests where Au-Pt showed superior performance compared to the Au and Au-Pd catalysts.

## 4.4. Iridium and Iridium Alloys

### 4.4.1. Voltammetry of borohydride oxidation on static electrodes

The linear voltammograms for a static electrode for colloidal Ir, Ir-Ni, Ir-Pd, Ir-Ag and Ir-Pt are shown in Figures 4.4.1-4.4.4 and 4.2.4, respectively.

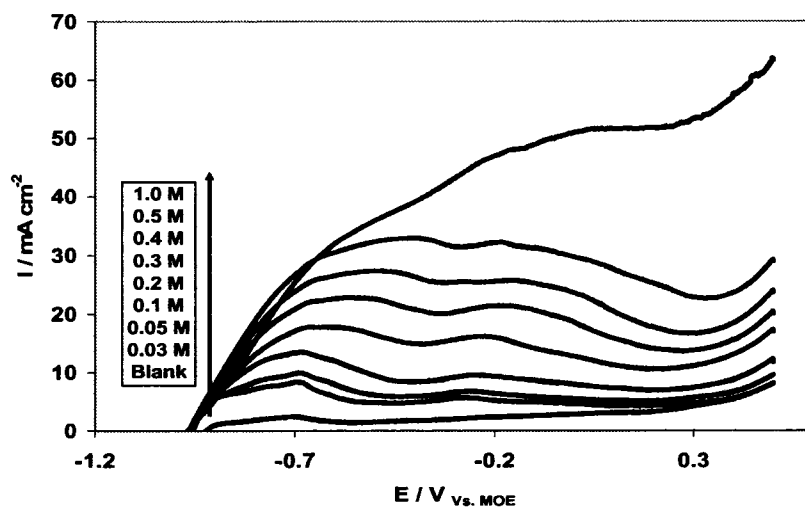


Fig. 4.4.1. Linear voltammogram of  $\text{BH}_4^-$  oxidation on colloidal Ir catalyst using a static electrode showing the effect of  $\text{BH}_4^-$  concentration. Scan rate  $100 \text{ mV s}^{-1}$ , 298 K. Inset legend indicates the  $\text{NaBH}_4$  concentration in 2 M NaOH.

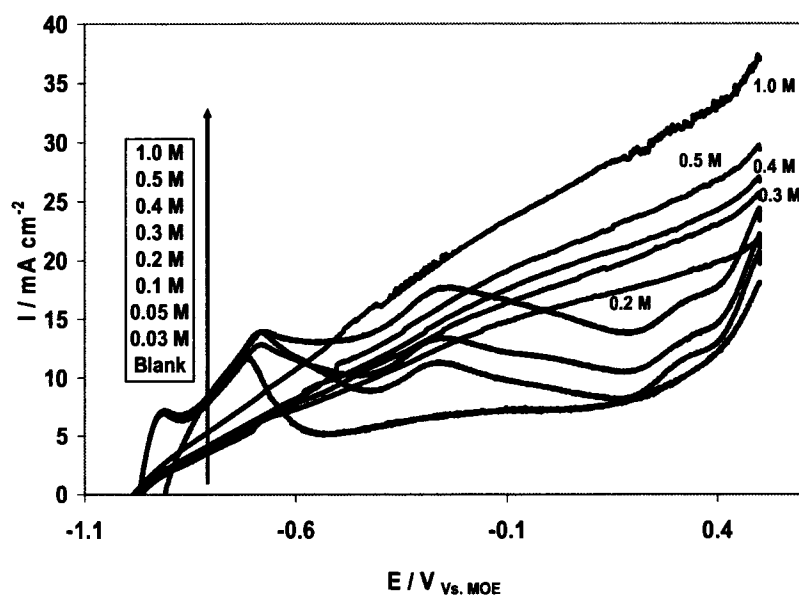


Fig. 4.4.2. Linear voltammogram of  $\text{BH}_4^-$  oxidation on colloidal Ir-Ni catalyst using a static electrode showing the effect of  $\text{BH}_4^-$  concentration. Scan rate  $100 \text{ mV s}^{-1}$ , 298 K. Inset legend indicates the  $\text{NaBH}_4$  concentration in 2 M NaOH.

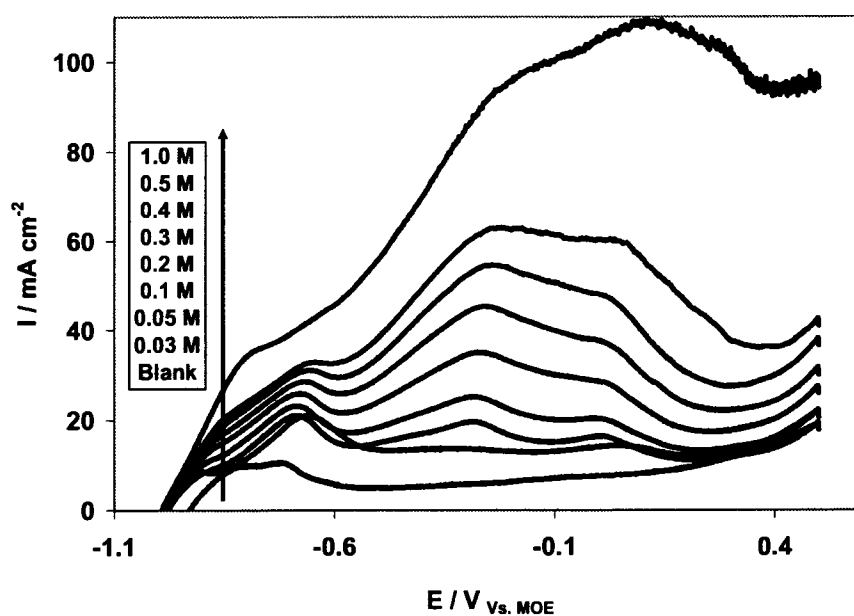


Fig. 4.4.3. Linear voltammogram of  $\text{BH}_4^-$  oxidation on colloidal Ir-Pd catalyst using a static electrode showing the effect of  $\text{BH}_4^-$  concentration. Scan rate  $100 \text{ mV s}^{-1}$ , 298 K. Inset legend indicates the  $\text{NaBH}_4$  concentration in 2 M NaOH.

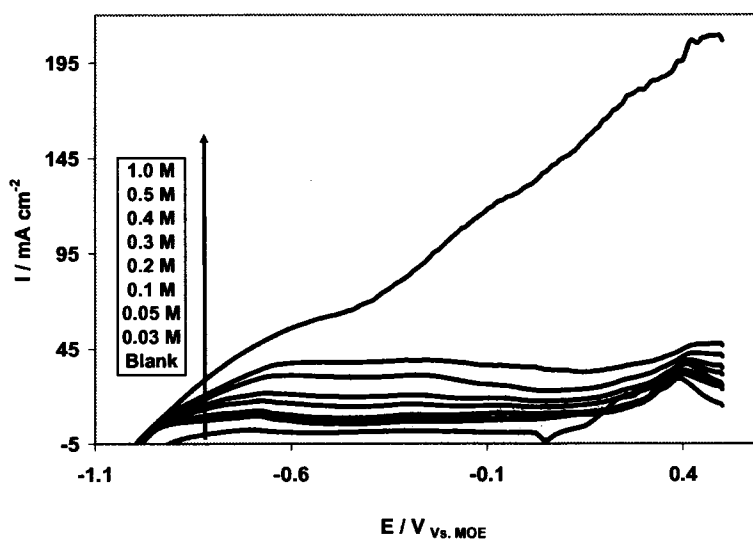


Fig. 4.4.4. Linear voltammogram of  $\text{BH}_4^-$  oxidation on colloidal Ir-Ag catalyst using a static electrode showing the effect of  $\text{BH}_4^-$  concentration. Scan rate  $100 \text{ mV s}^{-1}$ , 298 K. Inset legend indicates the  $\text{NaBH}_4$  concentration in 2 M NaOH.

For colloidal Ir, two oxidation peaks were identified at between  $-0.68$  V and  $-0.40$  V vs. MOE, and between  $-0.27$  V and  $0$  V vs. MOE, respectively. Both peak potentials shifted significantly towards more positive values with increasing  $\text{NaBH}_4$  concentration.

Although pure Ni did not show any oxidation peak (Fig. 4.2.5), on alloying Ir with Ni multiple oxidation peaks occurred at around  $-0.9$ ,  $-0.7$ , and  $-0.26$  V vs. MOE for  $\text{NaBH}_4$  concentrations between  $0.03$  and  $0.1$  M. However, at higher  $\text{NaBH}_4$  concentrations no oxidation peaks were observed within the investigated potential range (Fig. 4.4.2). This is interesting from a practical point of view since it shows a wide negative potential range before getting into the mass transfer region. Comparing Figs. 4.4.1 and 4.4.2 shows the alloying effects.

On alloying with Pd, on the other hand, multiple oxidation peaks occurred at around  $-0.65$ ,  $-0.25$ , and between  $0$  and  $0.1$  V vs. MOE, with a slight dependence on concentration (Fig. 4.4.3). Comparing Figs. 4.4.1 and the CV data for Pd (section 4.5) with 4.4.3, one can clearly see that the first and second peaks were due to the catalytic action of Ir, while the third peak is due to the catalytic action of the add atom, Pd.

With Ag as an add atom, one oxidation peak was observed at around  $+0.4$  V vs. MOE, same as for blank solution, for the concentration range of  $0.03$  to  $0.5$  M  $\text{NaBH}_4$ , while for  $1$  M  $\text{NaBH}_4$  there was no oxidation peak recorded (Fig. 4.4.4). This can be ascribed to the Ag catalytic action since the pure Ag colloid shows only one peak at around  $+0.4$  V vs. MOE (Fig. 4.2.7). This is an indicative of the Ag atoms catalytic activity at the colloidal Ir-Ag surface. This must, however, be verified. The EDS powder analysis, Fig. 3.1.8, showed the existence of both Ir and Ag. Again, more detailed materials characterization is needed.

Ir-Pd, Ir-Pt, and Ir-Ni showed oxidation peaks at the most negative potentials. The peaks at  $-0.65$ ,  $-0.85$ , and  $-0.912$  V, respectively, are due to  $\text{H}_2$  oxidation as per the reaction shown in eq. 2.10.1. The peaks at  $-0.25$ ,  $-0.27$ , and  $-0.27$  V, respectively, correspond to direct  $\text{BH}_4^-$  oxidation. The peaks at  $-0.65$  V on Ir-Pt, and  $-0.7$  on Ir-Ni, seem to be characteristic of the alloy's catalytic activities.

Thus, it can be concluded that amongst the investigated catalysts, the Ir-Pd, the Ir-Pt, and the Ir-Ni alloys gave the largest voltammetric  $\text{BH}_4^-$  oxidation current densities at

more negative potentials, in the domain that is of interest for borohydride fuel cells, i.e., more negative than -0.2 V vs. MOE.

Figure 4.4.5 shows that the peak current density increases linearly with concentration for Ir, Ir-Pt, Ir-Ni, and Ir-Ag. For Ir-Pd the slopes have changed at 0.05 M. The peak potential ranges were; Ir (-0.3 to -0.188 V), Ir-Ni (-0.65 to -0.225 V), Ir-Pt (-0.68 to -0.264 V), Ir-Pd (-0.30 to 0.1 V), and Ir-Ag (-0.70 to -0.5 V). Such a change in slope with concentration could be attributed to the change in the number of electrons transferred during the process according to eq. 3.6.27. The highest slope of  $I_p$  vs.  $C_b$  was for colloidal Ir-Pd. The peak current densities at a scan rate of  $100 \text{ mV s}^{-1}$  were higher on Ir-Pd followed by Ir-Pt and then Ir-Ni for the entire range of borohydride concentrations. The slopes of the linear portions of the peak current density vs. concentration plots for Ir-Pd, Ir-Pt, and Ir-Ni were about 2 times the value obtained for pure Ir.

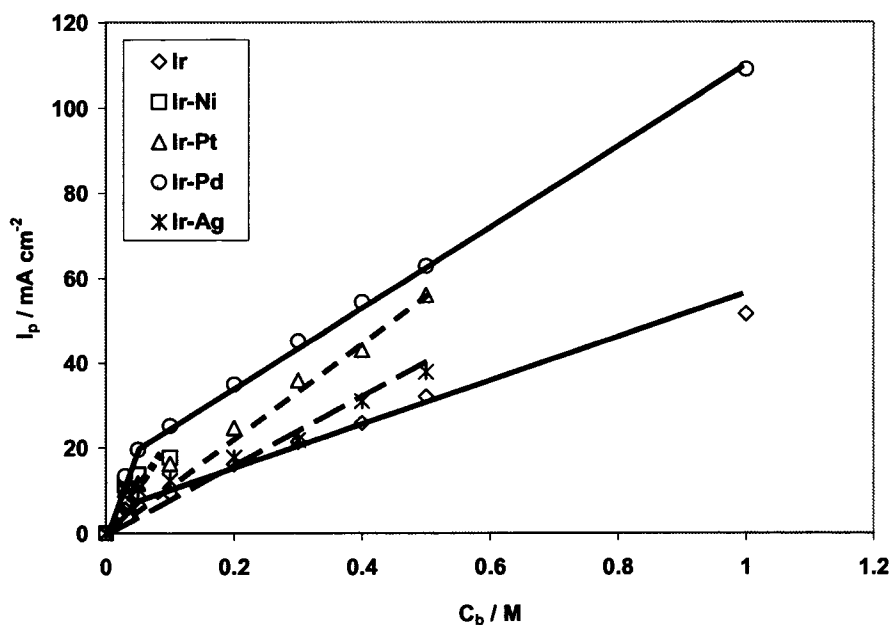


Fig. 4.4.5. The concentration dependence of the peak current density on colloidal Ir and Ir-alloys. Scan rate  $100 \text{ mV s}^{-1}$ , 298 K.

The scan rate dependence of the linear voltammograms for Ir, Ir-Ni, Ir-Pd, Ir-Ag and Ir-Pt are shown in Figures 4.4.6-4.4.9 and 4.2.12. It can be clearly seen from these figures that the oxidation peak potentials are almost independent of the scan rate for most of the investigated catalysts.

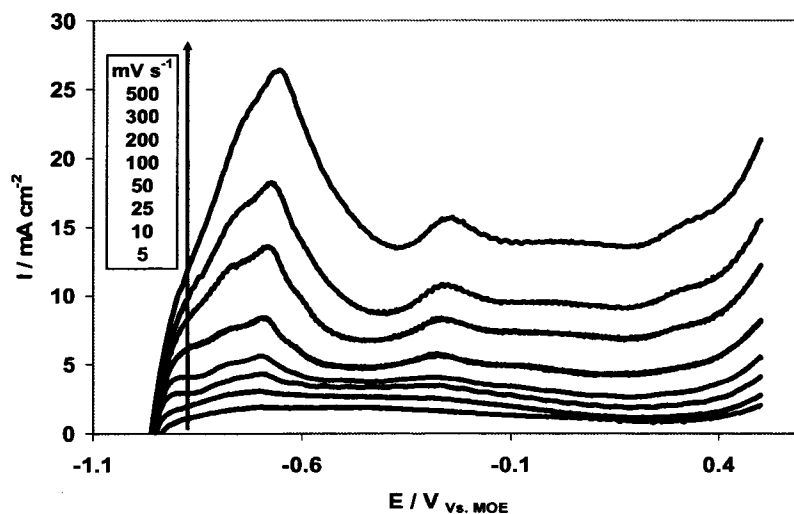


Fig. 4.4.6. Linear voltammogram of  $\text{BH}_4^-$  oxidation on colloidal Ir catalyst using a static electrode showing the effect of scan rate.  $\text{NaBH}_4$  concentration 0.03 M, 298 K. Inset legend indicates the scan rate.

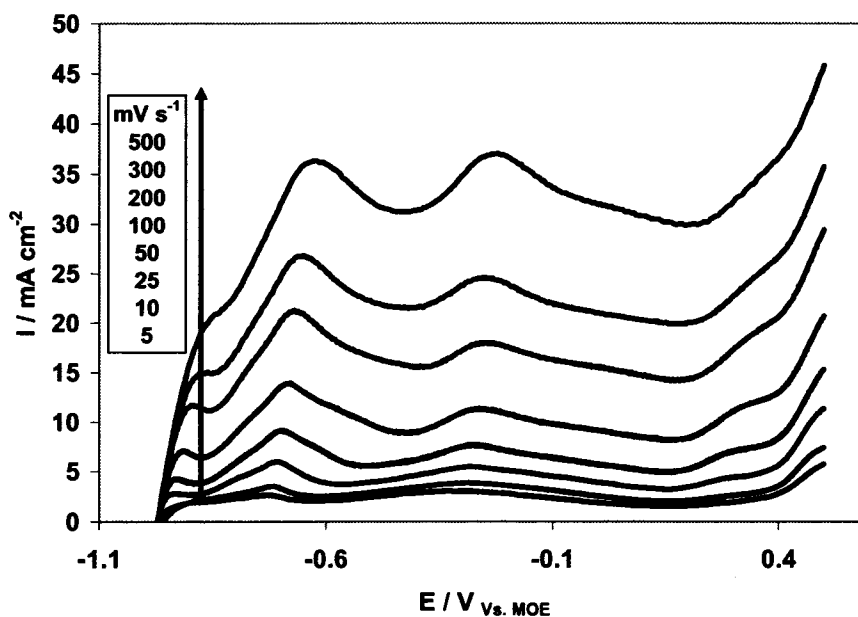


Fig. 4.4.7. Linear voltammogram of  $\text{BH}_4^-$  oxidation on colloidal Ir-Ni catalyst using a static electrode showing the effect of scan rate.  $\text{NaBH}_4$  concentration 0.03 M, 298 K. Inset legend indicates the scan rate.

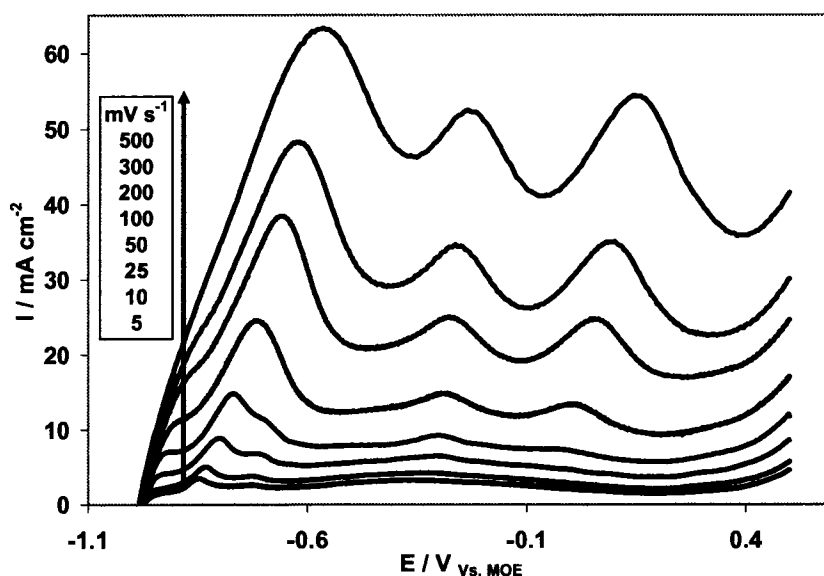


Fig. 4.4.8. Linear voltammogram of  $\text{BH}_4^-$  oxidation on colloidal Ir-Pd catalyst using a static electrode showing the effect of scan rate.  $\text{NaBH}_4$  concentration 0.03 M, 298 K. Inset legend indicates the scan rate.

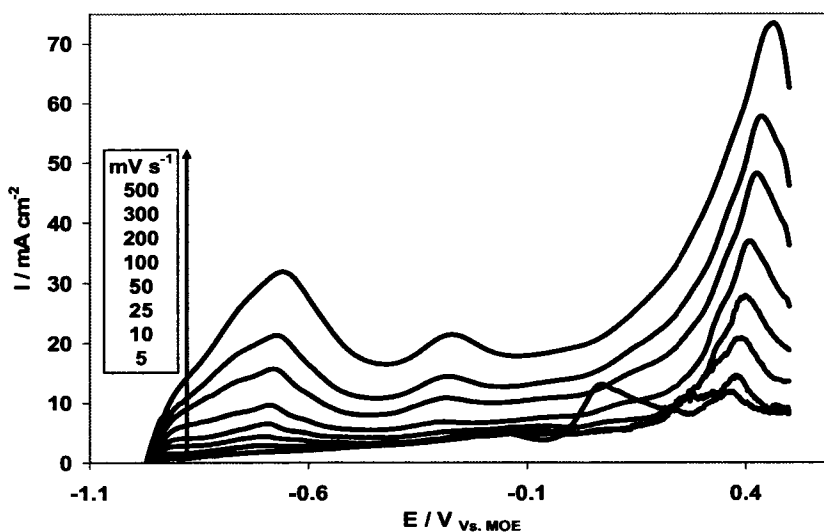


Fig. 4.4.9. Linear voltammogram of  $\text{BH}_4^-$  oxidation on colloidal Ir-Ag catalyst using a static electrode showing the effect of scan rate.  $\text{NaBH}_4$  concentration 0.03 M, 298 K. Inset legend indicates the scan rate.

Figure 4.4.10 shows that the peak current density increased linearly with the square root of scan rate for Ir and Ir-Ag catalysts at a constant  $\text{NaBH}_4$  concentration of 0.03 M. The peak potential ranges were; Ir (-0.4 to -0.235 V), Ir-Ni (-0.311 to -0.220 V), Ir-Pt (-0.70

to -0.22 V), Ir-Pd (-0.38 to -0.215 V), and Ir-Ag (0.35 to 0.465 V). Ir-Ag is the most influenced by the scan rate. For Ir-Pt, Ir-Ni, and Ir-Pd, a change in slope was observed at a scan rate of  $50 \text{ mV s}^{-1}$ , and a deviation from linearity of the increasing slope at high scan rates suggests an adsorption effect on the voltammetry response [6, 16, 17-22].

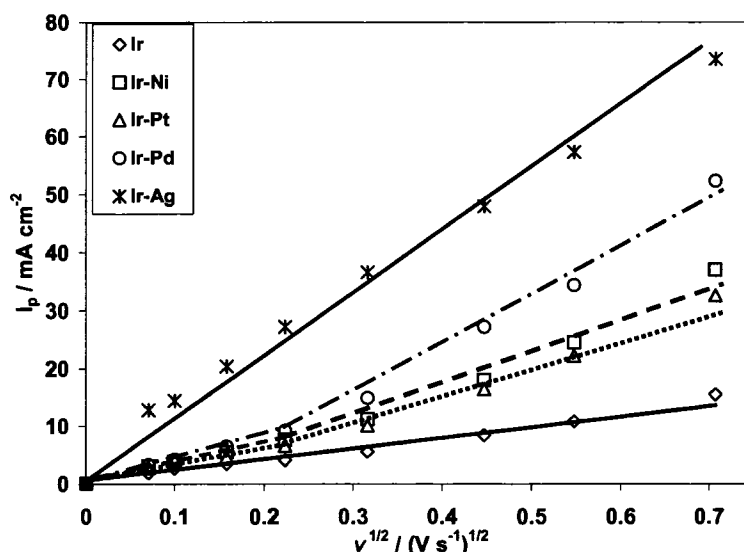


Fig. 4.4.10. The scan rate dependence of the peak current densities obtained on the colloidal Ir and Ir-alloys catalysts:  $\text{NaBH}_4$  concentration 0.03 M, 298 K.

#### 4.4.2. Voltammetry of borohydride oxidation on rotating electrodes

The RDE voltammograms recorded for colloidal Ir, Ir-Ni Ir-Pd, Ir-Ag and Ir-Pt are shown in Figs. 4.4.11-4.4.14 and 4.2.18, respectively. As was the case for both the Pt- and Au-alloys, a strong temperature effect was seen and only a fairly weak effect of the rotation speed.

The peak potential for Ir was around  $-0.5 \text{ V}$  vs. MOE at both 298 K and 313 K (Fig. 4.4.11). Ir-Ni (Fig. 4.2.12), on the other hand, exhibited a peak in the same range as pure Ir at 298 K, but less negative at 313 K, i.e.,  $-0.4 \text{ V}$ . Ir-Pd, showed a peak at around  $-0.4 \text{ V}$  at both 298 K and 313 K (Fig. 4.4.13). On Ir-Ag the peak occurred in the same range as for Ir-Ni at both 298 K and 313 K (Fig. 4.4.14). The highest peak current was for Ir-Pd.



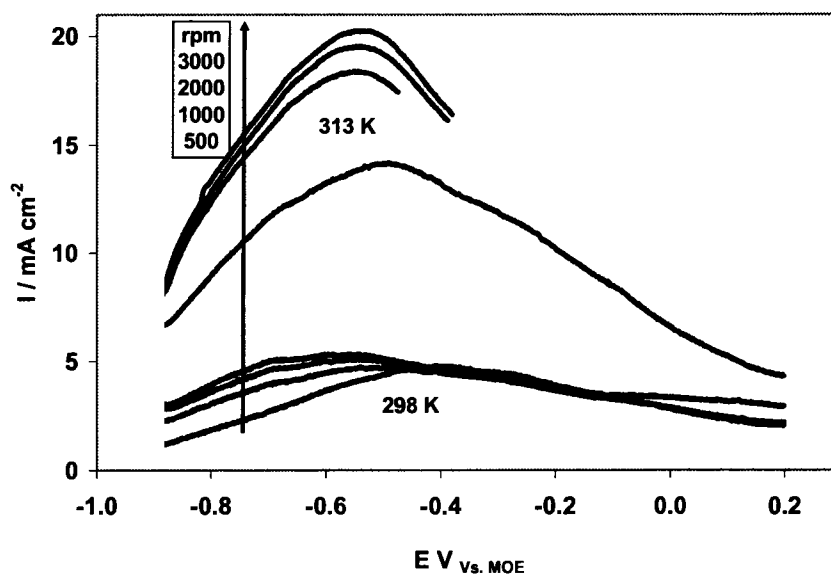


Fig. 4.4.11. Linear voltammetry of  $\text{BH}_4^-$  oxidation on colloidal Ir catalysts using a rotating electrode showing the effect of rotation speed and temperature. Scan rate  $5 \text{ mV s}^{-1}$ , 298 K and 313 K.  $\text{NaBH}_4$  concentration 0.3 M in 2 M NaOH. Inset legend indicates the rotation speed per minute.

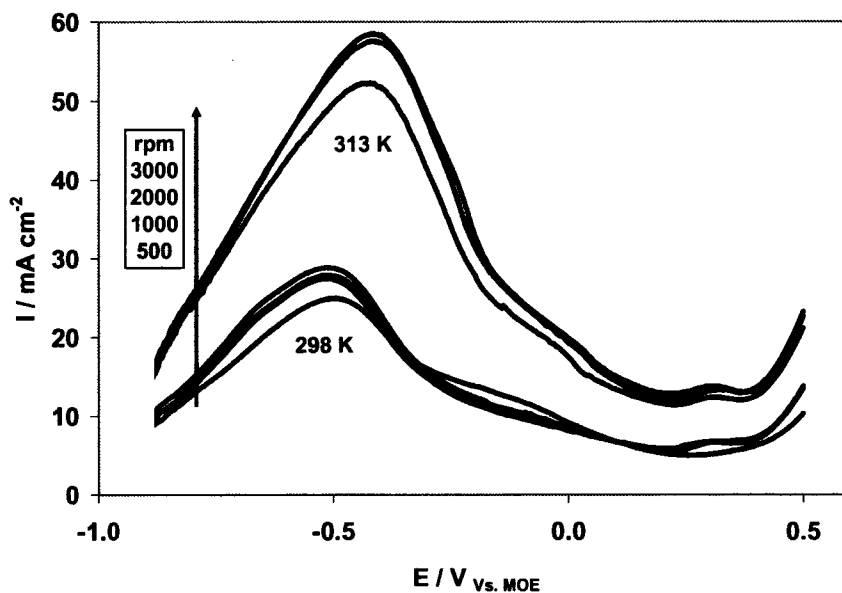


Fig. 4.4.12. Linear voltammetry of  $\text{BH}_4^-$  oxidation on colloidal Ir-Ni catalysts using a rotating electrode showing the effect of rotation speed and temperature. Scan rate  $5 \text{ mV s}^{-1}$ , 298 K and 313 K.  $\text{NaBH}_4$  concentration 0.3 M in 2 M NaOH. Inset legend indicates the rotation speed per minute.

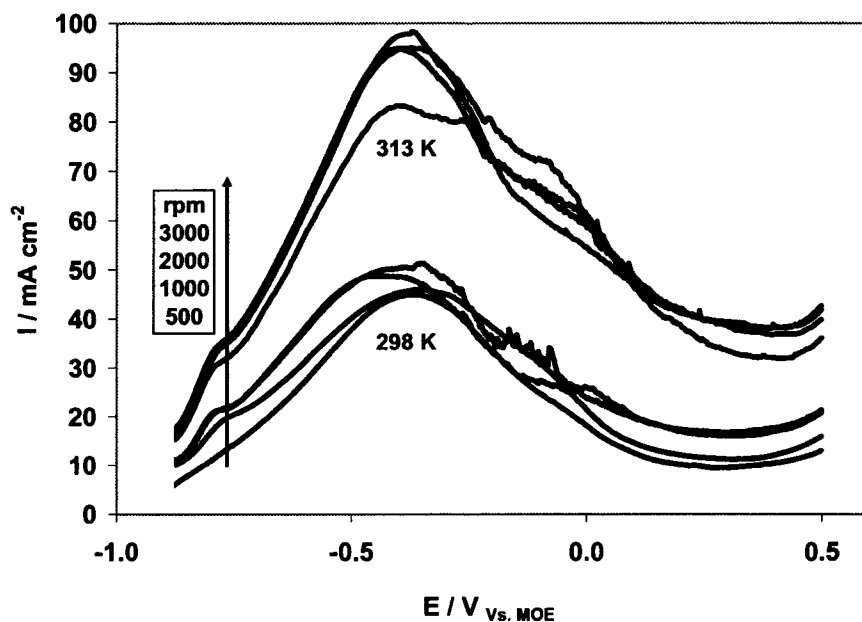


Fig. 4.4.13. Linear voltammetry of  $\text{BH}_4^-$  oxidation on colloidal Ir-Pd catalysts using a rotating electrode showing the effect of rotation speed and temperature. Scan rate  $5 \text{ mV s}^{-1}$ , 298 K and 313 K.  $\text{NaBH}_4$  concentration 0.3 M in 2 M NaOH. Inset legend indicates the rotation speed per minute.

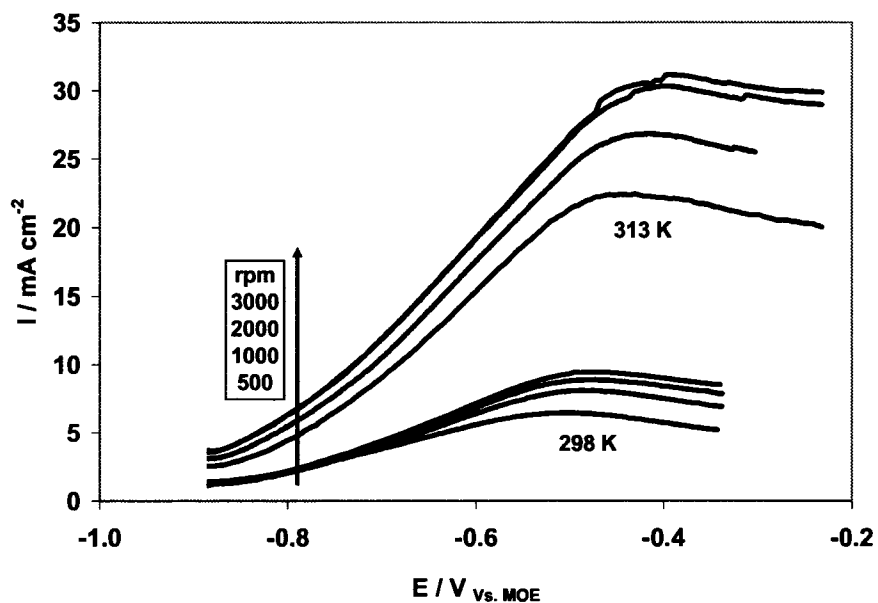


Fig. 4.4.14. Linear voltammetry of  $\text{BH}_4^-$  oxidation on colloidal Ir-Ag catalysts using a rotating electrode showing the effect of rotation speed and temperature. Scan rate  $5 \text{ mV s}^{-1}$ , 298 K and 313 K.  $\text{NaBH}_4$  concentration 0.3 M in 2 M NaOH. Inset legend indicates the rotation speed per minute.

### Tafel slopes and the exchange current densities

As for the other groups, Tafel plots of  $\log i$  vs.  $\eta (= E - E_{oc})$  were made, using the exponential increase domain of Figs. 4.4.11-4.4.14 and 4.2.18, were about 300-800 actual experimental points recorded, in order to calculate the apparent Tafel slopes and exchange current densities (Fig. 4.2.15).

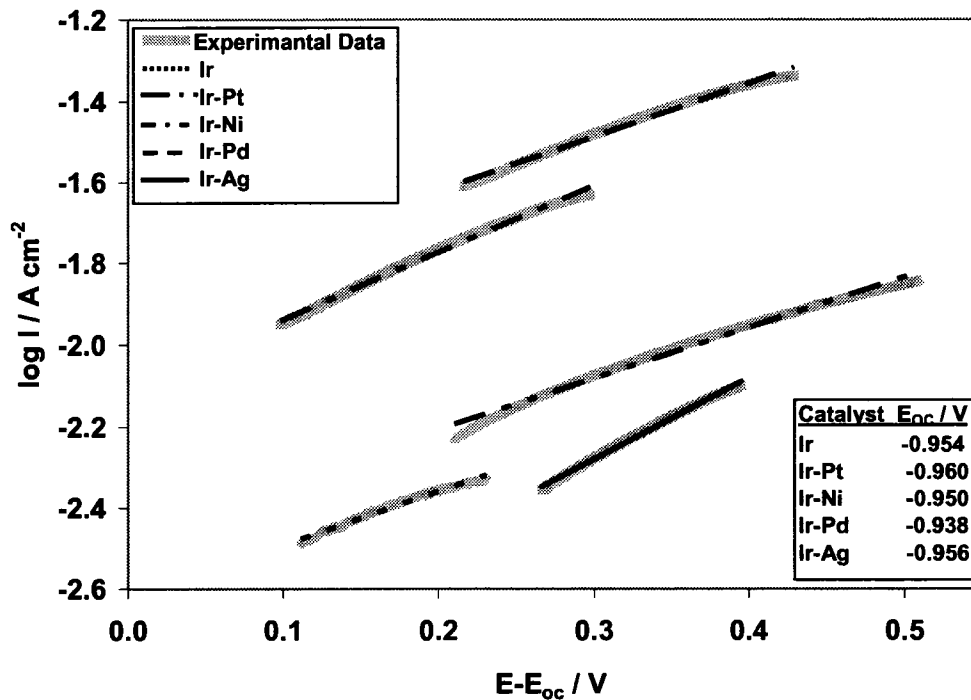


Fig. 4.4.15. Tafel plots for the supported colloidal Ir and Ir-alloys catalysts generated from the rotating disk electrode data at 298 K.

Table 4.4.1 shows that the apparent Tafel slopes,  $b_a$ , were in the range of about 0.498 to 0.815V at 298 K. Alloying Ir with Pt and Pd increases the apparent Tafel slope at 298 K, but it is decreased by alloying with Ni and Ag. The exchange current density, on the other hand, increased in all cases with the exception of Ir-Ag. As mentioned before, lowering the  $b_a$  values and increasing the  $i_{0,a}$  values is crucial issue in developing the electrocatalysts [25, 26].

Table 4.4.1 summarizes the number of electrons involved in the oxidation of borohydride by the Ir-based alloys. The oxidation of  $BH_4^-$  on Ir and Ir-alloys is, in all cases, an incomplete oxidation process, i.e.,  $n < 8$ . On Ir-Pt, Ir-Pd, and Ir-Ni,  $n = 3$ , while, on Ir and Ir-Ag,  $n = 1.5$  (Table 4.4.1). Based on eq. 2.10.13, the following equation is representative of a three electron process:

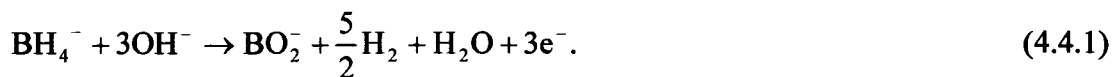


Table 4.4.1. Apparent Tafel slopes,  $b_a$ , exchange current densities,  $i_{0,a}$ , total number of electrons exchanged,  $n$ , determined from RDE data using supported colloidal Ir and Ir-alloys catalysts with a Nafion 117 polymer electrolyte. Eq. (4.2.2) is used for the calculation of  $n$ .

Catalysts	$b_a$ (V dec <sup>-1</sup> ) 298 K	$i_{0,a}$ (A cm <sup>-2</sup> ) 298 K	$n$
Ir	0.755	$2.37 \times 10^{-3}$	1.5
Ir-Pt	0.815	$3.62 \times 10^{-3}$	3.2
Ir-Ni	0.607	$7.90 \times 10^{-3}$	2.8
Ir-Pd	0.757	$13.06 \times 10^{-3}$	2.9
Ir-Ag	0.498	$1.31 \times 10^{-3}$	1.5

#### 4.4.3. Chronopotentiometry

The results of the chronopotentiometry experiments are given in Figure 4.4.16. It can be clearly seen that the overpotential ( $=E-E_{oc}$ ) was smallest for Ir-Pt, about 80 mV, followed by Ir (125 mV), Ir-Ag (173 mV), Ir-Pd (295 mV), and lastly Ir-Ni, where the overpotential was about 330 mV. Therefore, colloidal Ir-Pt is the most active catalyst, due to its lower overpotential [26]. The more negative the open circuit potential of the anode, the less the hydrolysis activity of the catalyst [7].

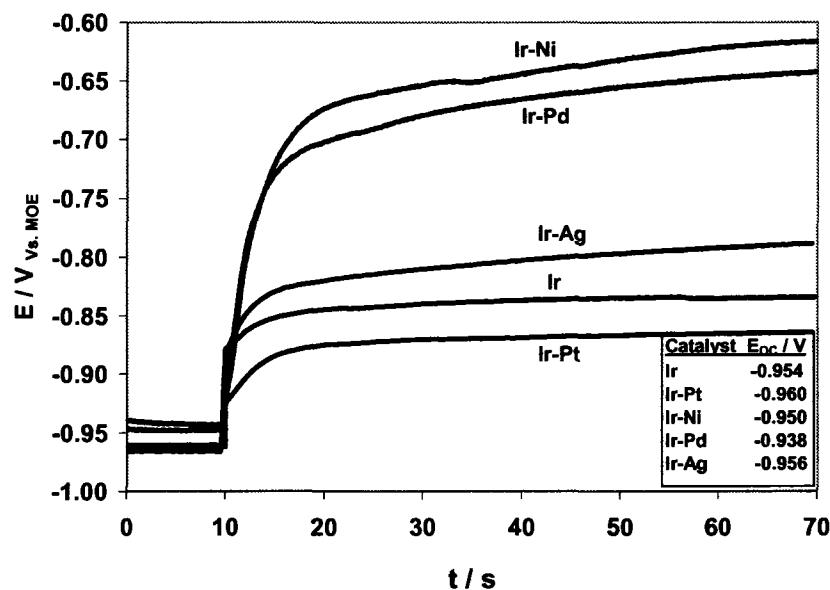


Fig. 4.4.16. Chronopotentiometry of  $\text{BH}_4^-$  oxidation on colloidal Ir and Ir-alloys catalysts. Current step: from 0 to  $10 \text{ mA cm}^{-2}$ .  $0.5 \text{ M Na BH}_4$  in  $2 \text{ M NaOH}$ .  $298 \text{ K}$ .

#### 4.4.4. Chronoamperometry and chronocoulometry

Figures 4.4.17-4.4.20 and 4.2.25 show the superficial current density transients for Ir, Ir-Ni, Ir-Pd, Ir-Ag, and Ir-Pt, respectively. For the cases of  $-0.6 \text{ V}$ ,  $-0.4 \text{ V}$  and  $-0.2 \text{ V}$  potential steps, the highest anodic current densities were recorded on Ir-Pt (i.e. about  $0.029$ ,  $0.032$ , and  $0.025 \text{ A cm}^{-2}$  respectively, after  $60 \text{ s}$ , Fig.4.2.25), while the other electrodes exhibited current densities smaller than for Ir-Pt, in the following order, Ir-Pd > Ir > Ir-Ag > Ir-Ni. Thus, in the negative potential range of  $-0.9 \text{ V}$  and  $-0.4 \text{ V}$ , which is the domain of interest for practical fuel cell anodes, Ir-Pt was the most active catalyst.

The highest anodic current at  $-0.2 \text{ V}$  was measured on Ir-Pt followed by Ir-Pd, e.g.  $0.029$ , and  $0.026 \text{ A cm}^{-2}$  after  $60 \text{ s}$  respectively (Figs. 4.2.25 and 4.4.19).

By knowing that the intra-catalyst layer diffusion becomes rate limiting in addition to kinetics at  $-0.2 \text{ V}$ , while at  $-0.4 \text{ V}$  the oxidation is under pure electrode kinetic control (Figs. 4.4.17-4.4.20, and 4.2.25), the independence of the chronoamperometric response on the size of the potential step is indicative of a slow heterogeneous chemical reaction preceding the electrochemical step. This supports the proposed chemical-electrochemical mechanism for borohydride oxidation.

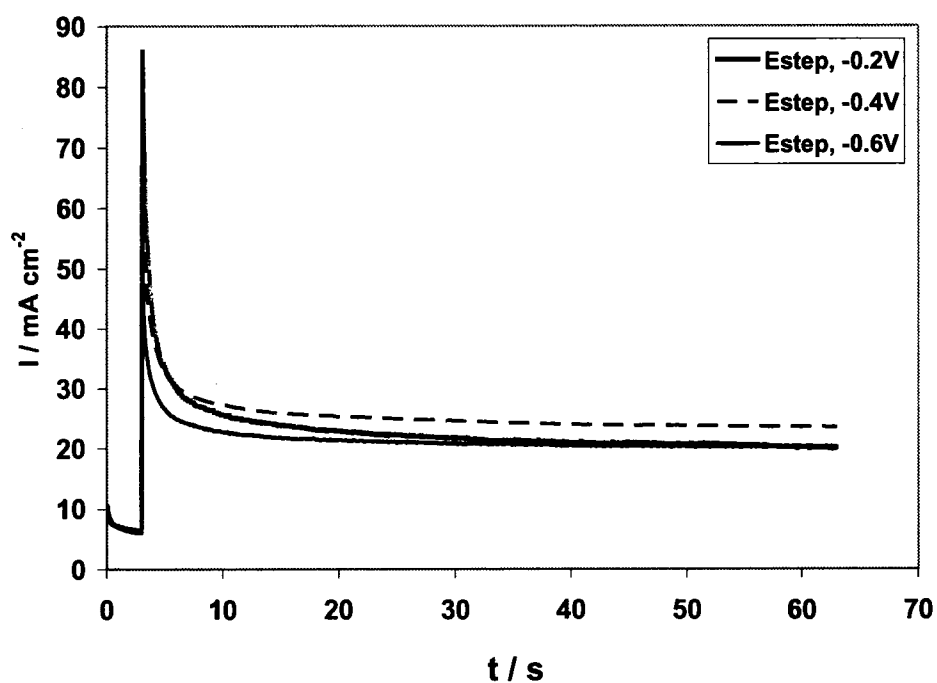


Fig. 4.4.17. Chronoamperometry of  $\text{BH}_4^-$  oxidation on a colloidal Ir catalyst. Potential steps from  $-0.9$  V vs. MOE to  $-0.6$ ,  $-0.4$  and  $-0.2$  V vs. MOE, respectively  $0.5$  M  $\text{NaBH}_4$  in  $2$  M  $\text{NaOH}$ .  $298$  K.

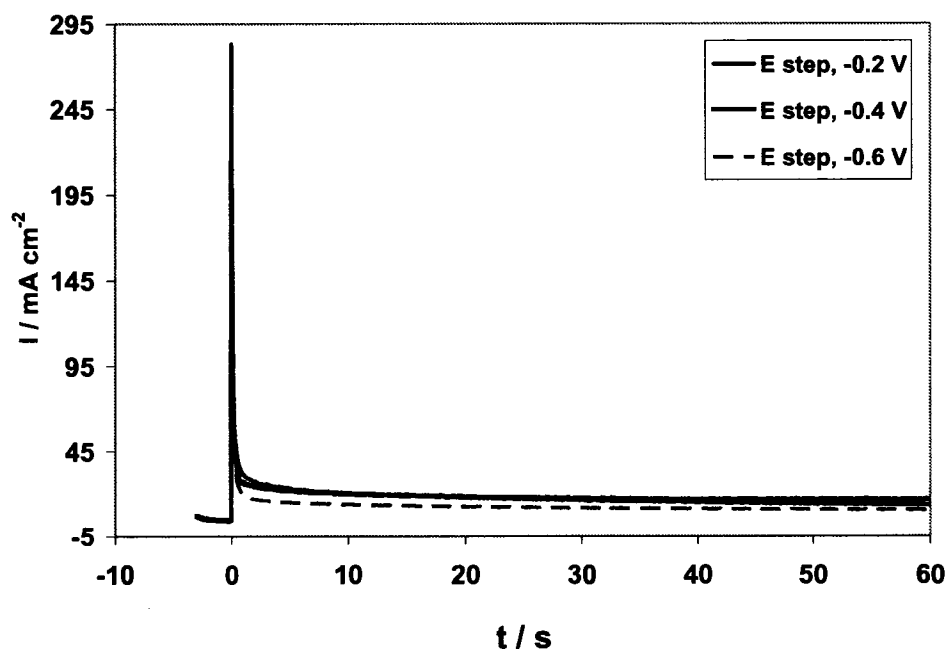


Fig. 4.4.18. Chronoamperometry of  $\text{BH}_4^-$  oxidation on a colloidal Ir-Ni catalyst. Potential steps from  $-0.9$  V vs. MOE to  $-0.6$ ,  $-0.4$  and  $-0.2$  V vs. MOE, respectively  $0.5$  M  $\text{NaBH}_4$  in  $2$  M  $\text{NaOH}$ .

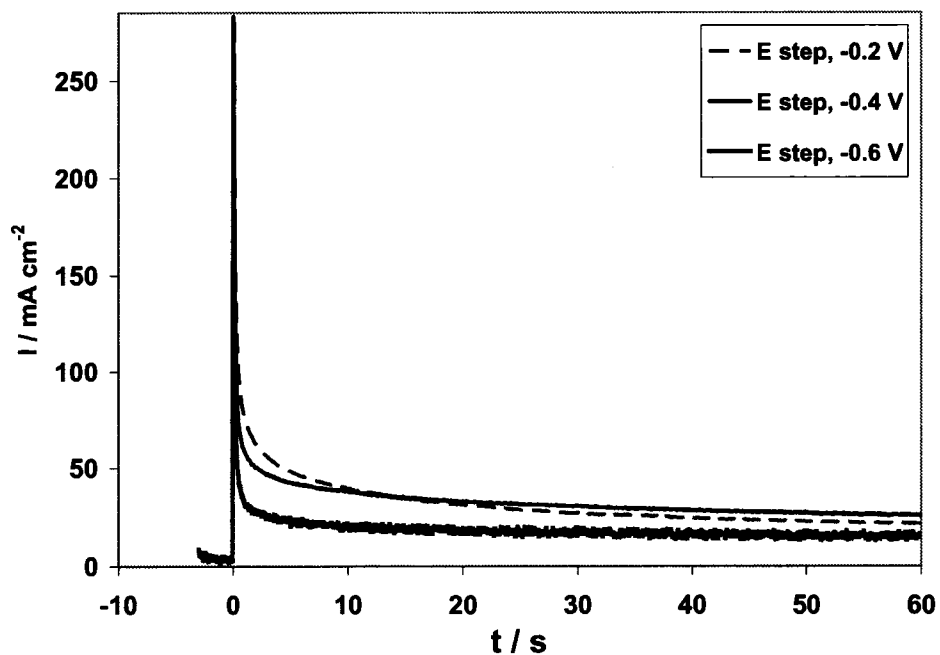


Fig. 4.4.19. Chronoamperometry of  $\text{BH}_4^-$  oxidation on a colloidal Ir-Pd catalyst. Potential steps from  $-0.9 \text{ V}$  vs. MOE to  $-0.6$ ,  $-0.4$  and  $-0.2 \text{ V}$  vs. MOE, respectively  $0.5 \text{ M NaBH}_4$  in  $2 \text{ M NaOH}$ .  $298 \text{ K}$ .

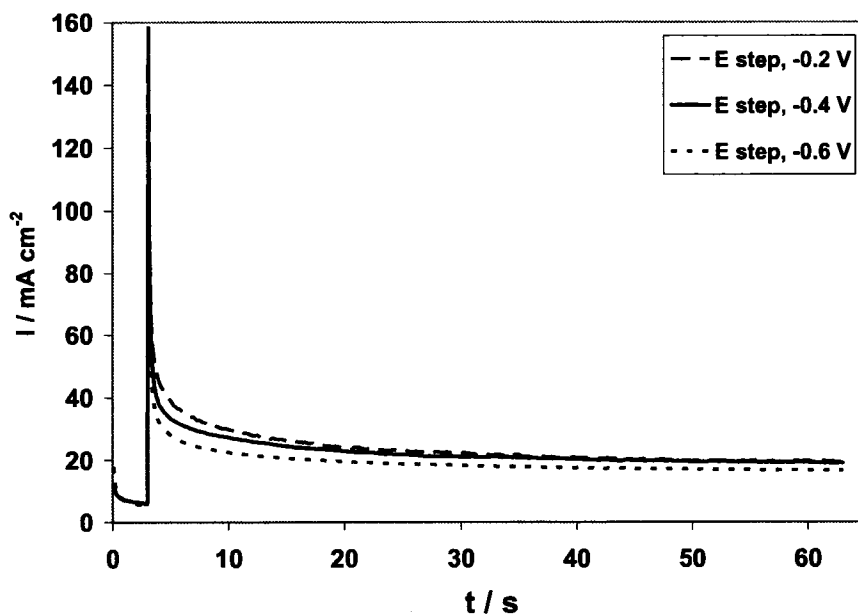


Fig. 4.4.20. Chronoamperometry of  $\text{BH}_4^-$  oxidation on a colloidal Ir-Ag catalyst. Potential steps from  $-0.9 \text{ V}$  vs. MOE to  $-0.6$ ,  $-0.4$  and  $-0.2 \text{ V}$  vs. MOE, respectively  $0.5 \text{ M NaBH}_4$  in  $2 \text{ M NaOH}$ .  $298 \text{ K}$ .

### Cottrell Plot

A non-Cottrellian response, i.e., not purely diffusion controlled, is shown in the  $i \cdot \sqrt{t}$  vs.  $t$  plots for all the investigated Ir and Ir-alloy catalysts (Figs. 4.4.21-4.4.23).

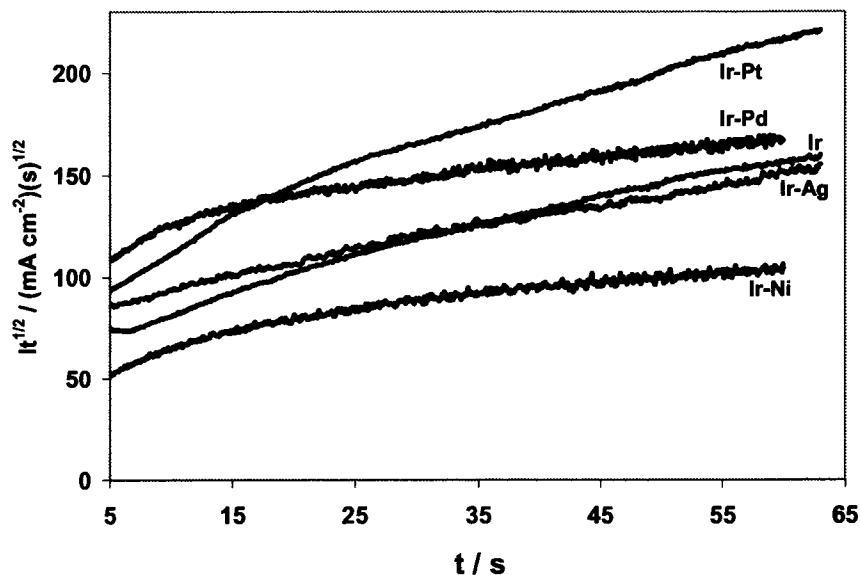


Fig. 4.4.21. Cottrell plot generated from the chronoamperometry data for potential step from  $-0.9$  V to  $-0.2$  V vs. MOE.

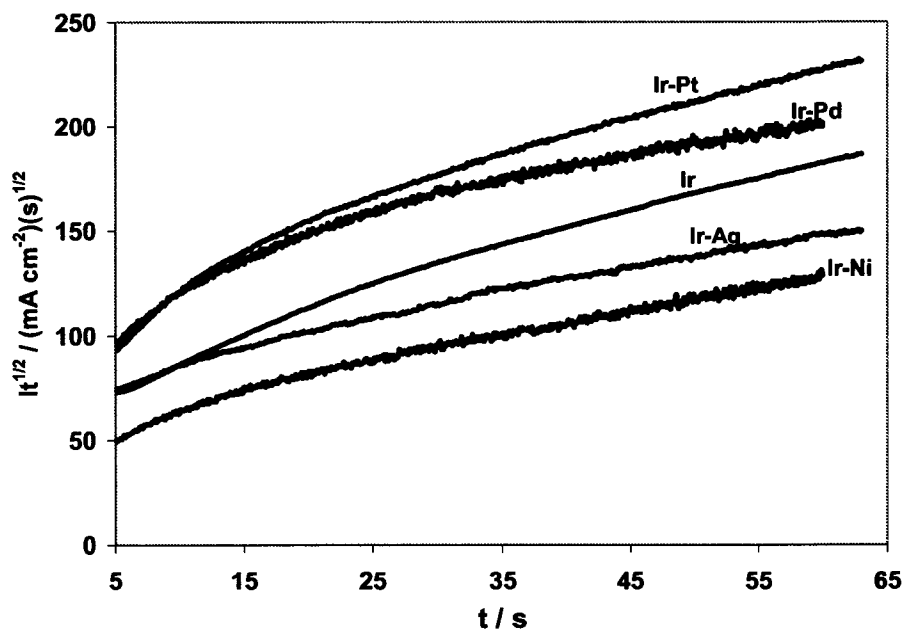


Fig. 4.4.22. Cottrell plot generated from the chronoamperometry data for potential step from  $-0.9$  V to  $-0.4$  V vs. MOE.



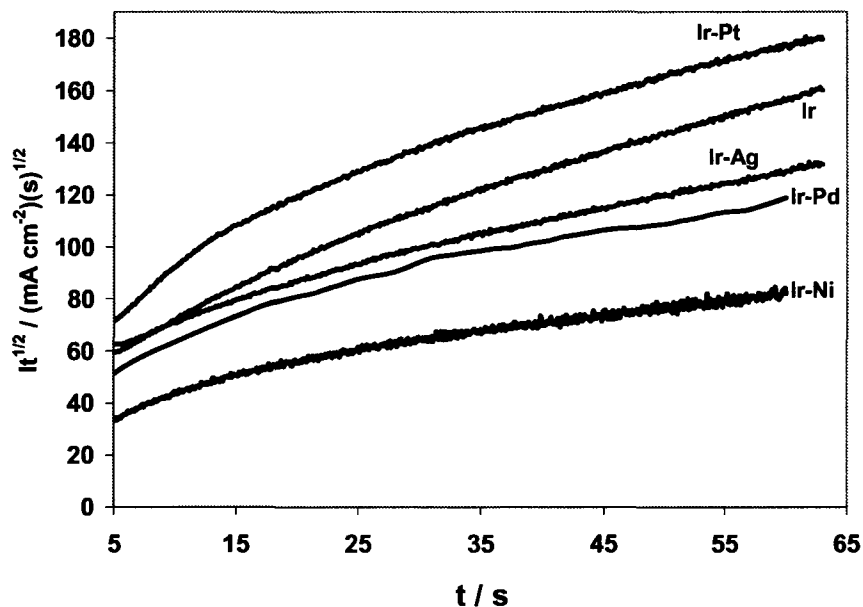


Fig. 4.4.23. Cottrell plot generated from the chronoamperometry data for potential step from  $-0.9$  V to  $-0.6$  V vs. MOE.

### Chronocoulometry

Figures 4.4.24-4.4.26 show the Anson plots for Ir and Ir-alloys catalysts obtained for potential steps from  $-0.9$  V to  $-0.2$  V,  $-0.4$  V, and  $-0.6$  V vs. MOE.

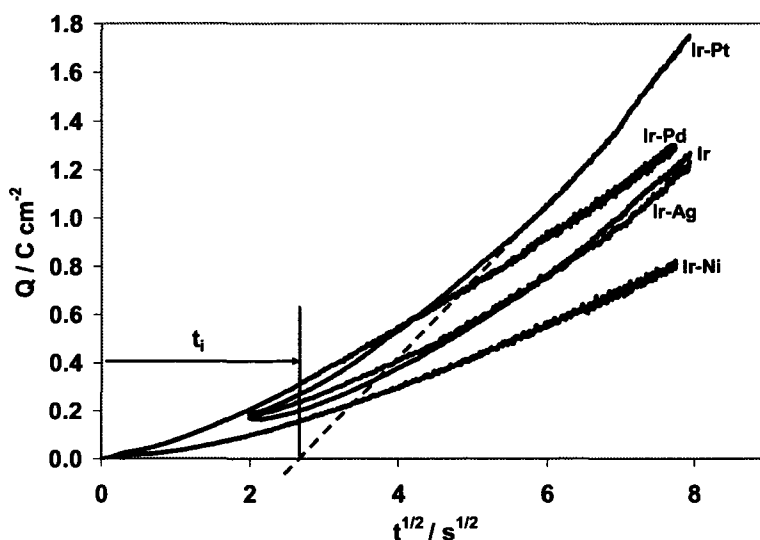


Fig. 4.4.24. Cumulative charge density as a function of square root of time (Anson plot) generated from the chronoamperometry data for a potential step from  $-0.9$  V to  $-0.2$  V vs. MOE.

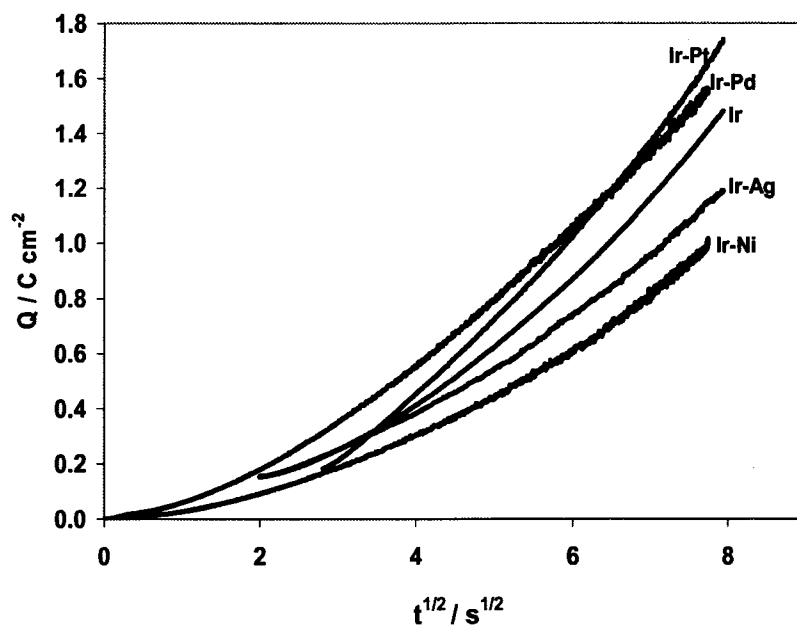


Fig. 4.4.25. Cumulative charge density as a function of square root of time (Anson plot) generated from the chronoamperometry data for a potential step from  $-0.9$  V to  $-0.4$  V vs. MOE.

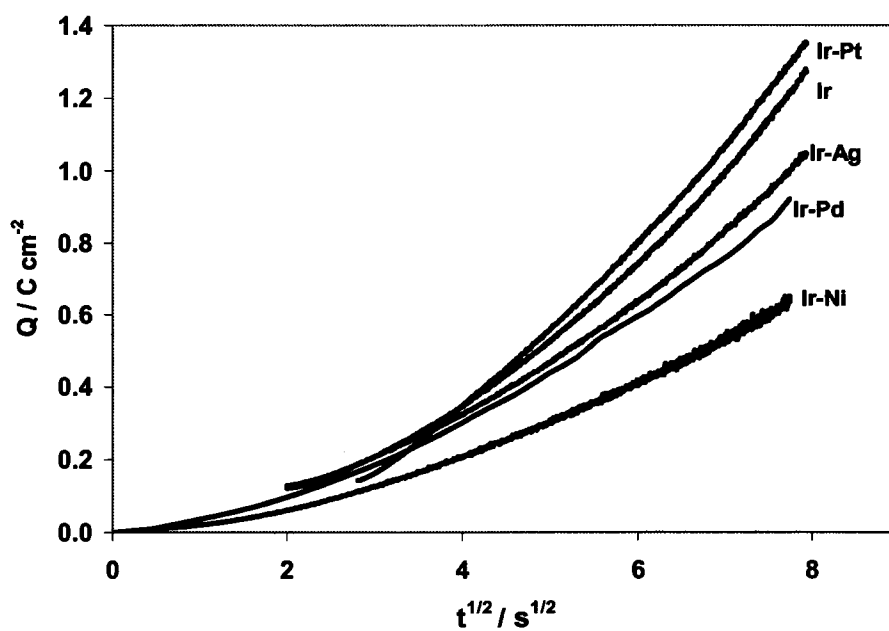


Fig. 4.4.26. Cumulative charge density as a function of square root of time (Anson plot) generated from the chronoamperometry data for a potential step from  $-0.9$  V to  $-0.6$  V vs. MOE.

Figures 4.4.24-26 show a deviation from linearity of the  $Q$  vs.  $\sqrt{t}$  dependence for all the catalysts investigated. A negative intercept on the  $Q$  axis and a positive intercept on the  $\sqrt{t}$  -axis are indicative of electrode kinetic effects on the chronocoulometry response [16]. Once again, employing equations 3.6.32 and 3.6.33 in conjunction with extrapolating the linear domain of these curves shown in Figure 4.4.25 to  $Q = 0$ , the apparent heterogeneous rate constant  $k_h$  at  $-0.4$  V can be determined [16]. Table 4.4.2 summarizes the  $k_h$  values at  $-0.4$  V at 298 K obtained from the slope of eq. (3.6.32) corresponding to the data from Fig. 4.2.25. The apparent heterogeneous rate constants for  $-0.4$  V potential step show the following order of electrocatalytic activity: Ir > Ir-Ag > Ir-Pt > Ir-Pd > Ir-Ni, with  $k_h$  between  $35.5 \times 10^{-6} \text{ cm s}^{-1}$  for Ir and  $11.5 \times 10^{-6} \text{ cm s}^{-1}$  for Ir-Ni. The differences in the activity might be due to the changes in the surface electronic structure in addition to the bifunctional ability due to the alloying.

Table 4.4.2. Apparent heterogeneous rate constants for  $\text{BH}_4^-$  oxidation at  $-0.4$  V vs. MOE and 298 K calculated from chronocoulometry.

Catalyst	Ir	Ir-Pt	Ir-Ni	Ir-Pd	Ir-Ag
$k_h$ ( $\text{cm s}^{-1}$ )	$35.5 \times 10^{-6}$	$28.7 \times 10^{-6}$	$11.5 \times 10^{-6}$	$25 \times 10^{-6}$	$30 \times 10^{-6}$

#### 4.4.5. Fuel cell performance

Figures 4.4.26-4.4.27 show the temperature and fuel flow rate effects on the polarization curves obtained using the colloidal Ir-Pt, Ir-Ni, and Ir-Pd catalysts, respectively. As for Pt- and Au-alloys, the temperature has a significant impact on the fuel cell performance in all cases, while the flow rate has no significant effect on the fuel cell performance.

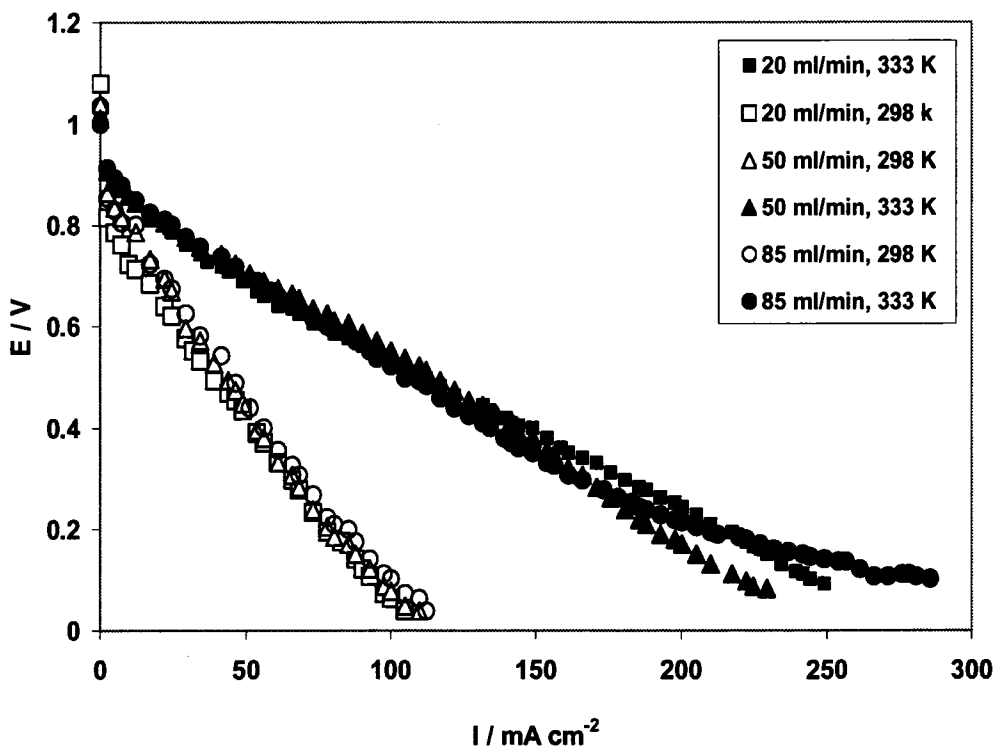


Fig. 4.4.27. Direct borohydride fuel cell polarization curves at 298 K and 333 K: Anode catalyst (Ir-Pt) load  $5 \text{ mg cm}^{-2}$ .  $2 \text{ M NaBH}_4 - 2 \text{ M NaOH}$ . Cathode catalyst (Pt) load  $4 \text{ mg cm}^{-2}$ .  $\text{O}_2$  flow rate  $200 \text{ ml min}^{-1}$  at 2.7 atm.

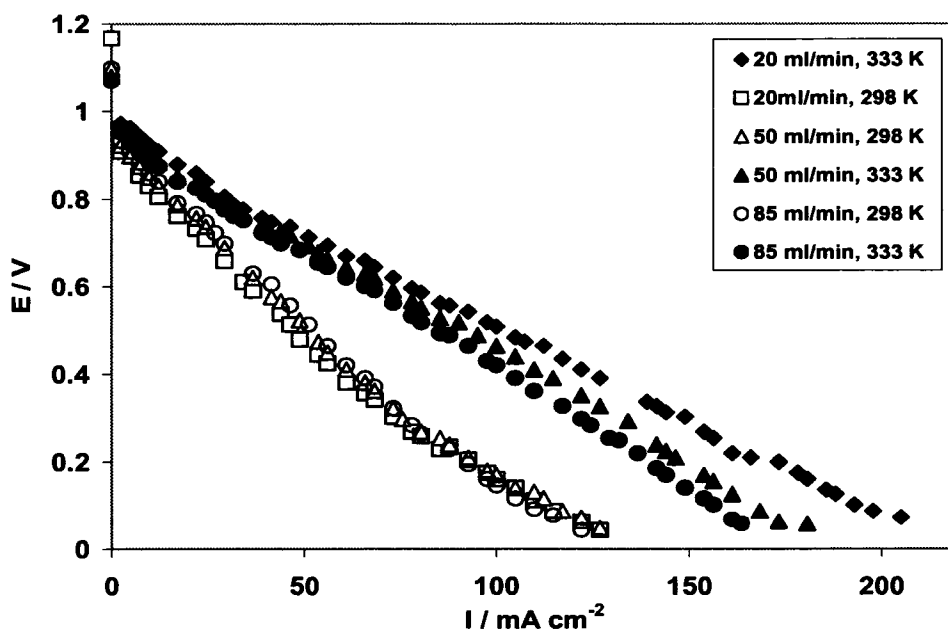


Fig. 4.4.28. Direct borohydride fuel cell polarization curves at 298 K and 333 K: Anode catalyst (Ir-Ni) load  $5 \text{ mg cm}^{-2}$ .  $2 \text{ M NaBH}_4 - 2 \text{ M NaOH}$ . Cathode catalyst (Pt) load  $4 \text{ mg cm}^{-2}$ .  $\text{O}_2$  flow rate  $200 \text{ ml min}^{-1}$  at 2.7 atm.

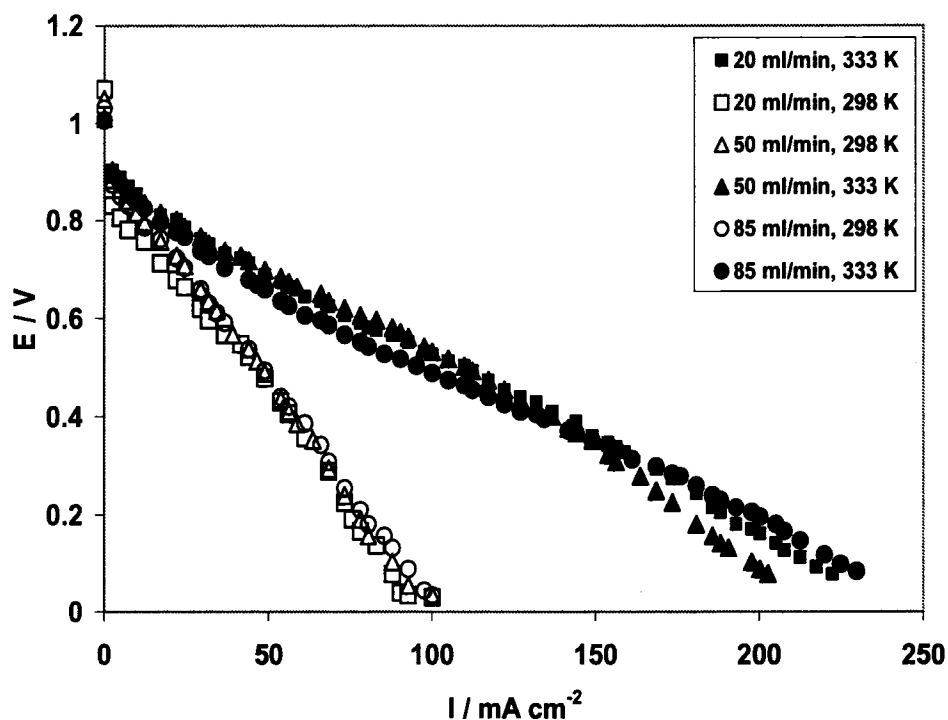


Fig. 4.4.29. Direct borohydride fuel cell polarization curves at 298 K and 333 K: Anode catalyst (Ir-Pd) load  $5 \text{ mg cm}^{-2}$ .  $2 \text{ M NaBH}_4 - 2 \text{ M NaOH}$ . Cathode catalyst (Pt) load  $4 \text{ mg cm}^{-2}$ .  $\text{O}_2$  flow rate  $200 \text{ ml min}^{-1}$  at  $2.7 \text{ atm}$ .

Figure 4.4.29 compares the fuel cell performance using colloidal Ir-Pt, Ir-Ni, and Ir-Pd as the anode electrocatalysts. At 298 K, almost the same performance was recorded for all catalysts. However, at 333 K, Ir-Pd and Ir-Pt were the most active catalysts. With Ir-Pt or Ir-Pd a cell operating at a voltage of  $0.5 \text{ V}$  can give a current of about  $46$  and  $49 \text{ mA cm}^{-2}$  at 298 K, respectively, while at 333 K, the same catalyst can give  $105$  and  $95 \text{ mA cm}^{-2}$ , respectively at the same  $0.5 \text{ V}$  cell voltage.

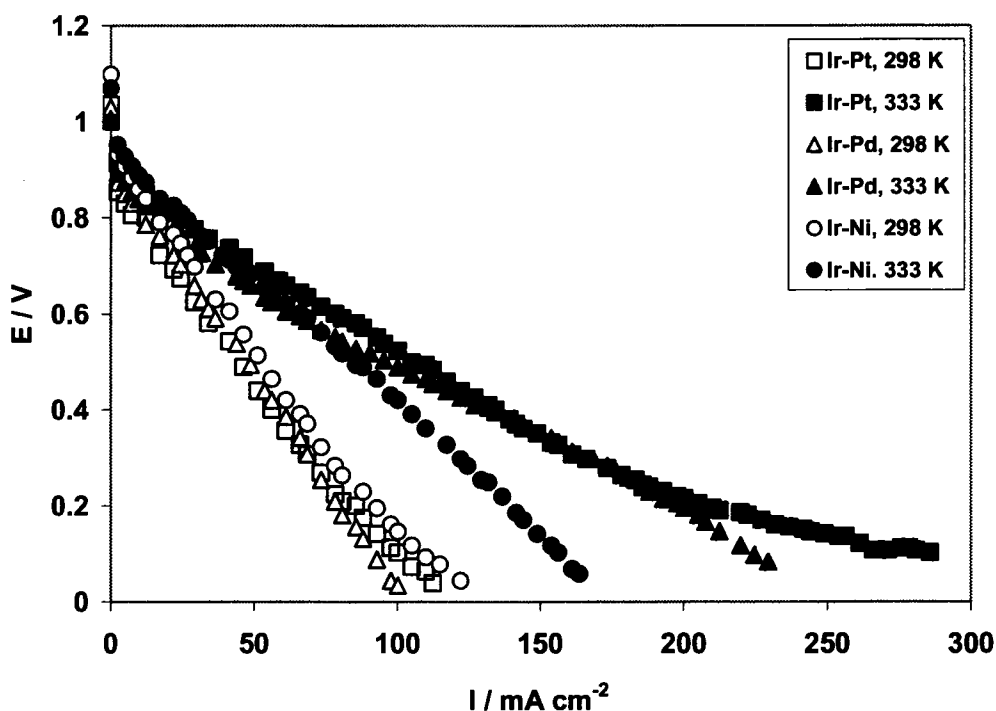


Fig. 4.4.30. Direct borohydride fuel cell polarization curves at 298 K and 333 K: Comparison between the colloidal catalysts prepared in the present work (Ir-Pt, Ir-Ni and Ir-Pd). Anode catalyst load  $5 \text{ mg cm}^{-2}$ .  $50 \text{ ml min}^{-1}$   $2 \text{ M NaBH}_4 - 2 \text{ M NaOH}$ . Cathode catalyst (Pt) load  $4 \text{ mg cm}^{-2}$ .  $\text{O}_2$  flow rate  $200 \text{ ml min}^{-1}$  at  $2.7 \text{ atm}$ .

#### 4.4.6. Summary

In summary, the highest electrocatalytic activity amongst the Ir-group was for the Ir-Ni catalyst. Ir-Ni showed a relatively low  $b_a$  and the second highest  $i_o$ . The heterogeneous rate constant,  $k_h$ , for Ir-Ni was found to be three times lower than that of pure Ir. Fuel cell tests at 298 K, showed that Ir-Ni has the highest performance compared to the other Ir-group members.

## 4.5. Palladium and Palladium Alloys

### 4.5.1. Voltammetry of borohydride oxidation on static electrodes

The linear voltammograms on static electrodes for colloidal Pd, Pd-Ni, Pd-Ag, and Pd-Au, Pd-Ir catalysts are shown in Figs. 4.5.1-4.5.3, 4.3.2 and 4.4.3, respectively.

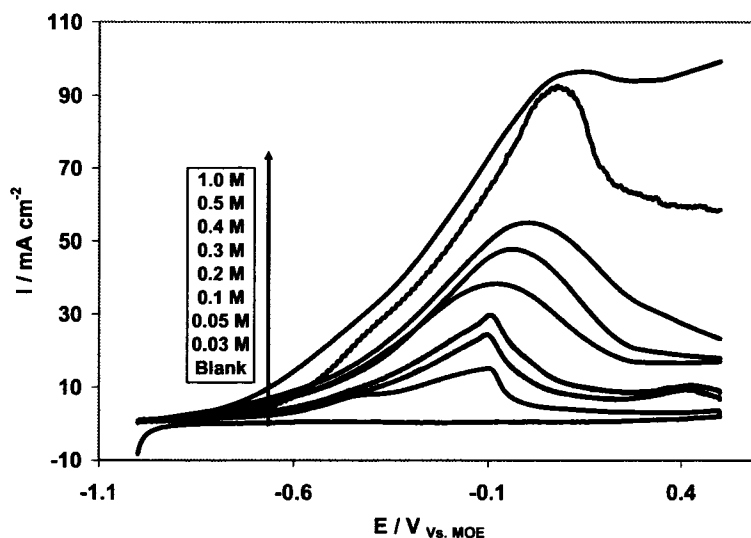


Fig. 4.5.1. Linear voltammogram of  $\text{BH}_4^-$  oxidation on colloidal Pd catalyst using a static electrode showing the effect of  $\text{BH}_4^-$  concentration. Scan rate  $100 \text{ mV s}^{-1}$ , 298 K. Inset legend indicates the  $\text{NaBH}_4$  concentration in 2 M NaOH.

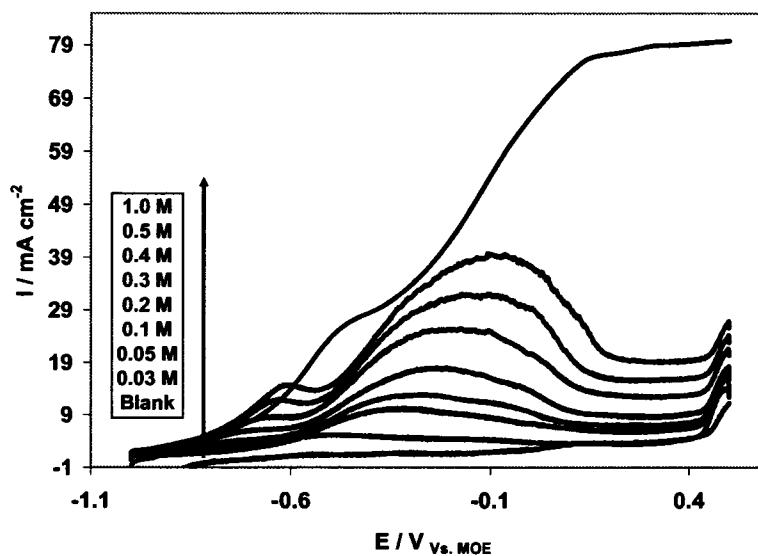


Fig. 4.5.2. Linear voltammogram of  $\text{BH}_4^-$  oxidation on colloidal Pd-Ni catalyst using a static electrode showing the effect of  $\text{BH}_4^-$  concentration. Scan rate  $100 \text{ mV s}^{-1}$ , 298 K. Inset legend indicates the  $\text{NaBH}_4$  concentration in 2 M NaOH.

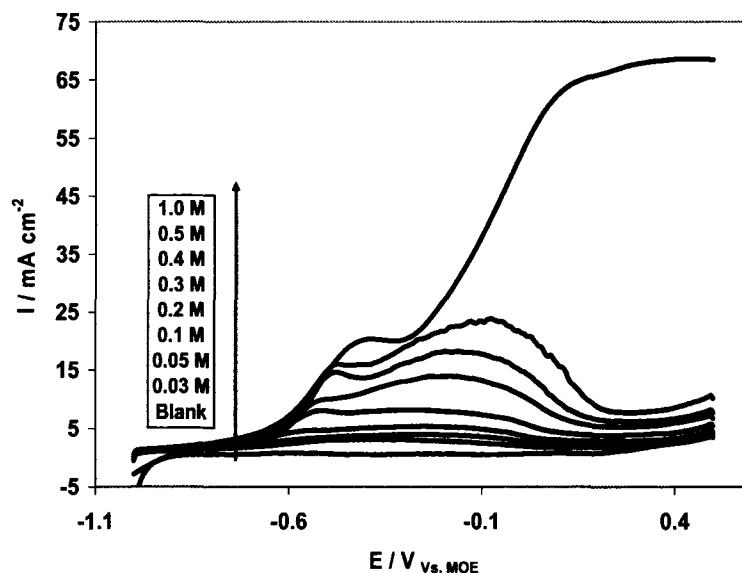


Fig. 4.5.3. Linear voltammogram of  $\text{BH}_4^-$  oxidation on colloidal Pd-Ag catalyst using a static electrode showing the effect of  $\text{BH}_4^-$  concentration. Scan rate  $100 \text{ mV s}^{-1}$ , 298 K. Inset legend indicates the  $\text{NaBH}_4$  concentration in 2 M NaOH.

For colloidal Pd, only one oxidation peak could be identified between  $-0.1$  and  $+0.1$  V vs. MOE (Fig. 4.5.1). The peak potential shifted slightly towards more positive values with increasing  $\text{NaBH}_4$  concentration.

Therefore, it was interest to alloy it with a similar element, Ni, with a metal that has many free electrons, Ir, and with elements that are considered to be virtually inert for the hydrogenation-dehydrogenation processes, such as Au and Ag [8].

For Pd-Ni, two oxidation peaks were observed, one between  $-0.7$  to  $-0.6$  V vs. MOE which is considered to be due alloying catalytic action, and the second between  $-0.25$  to  $0.1$  V vs. MOE (Figs. 4.5.1, 4.2.6, and 4.5.2). The peak potential shifts slightly toward more positive values with increasing  $\text{NaBH}_4$  concentration. It is worth mentioning that Kinjo [44], in his study of the oxidation of  $0.1 \text{ M KBH}_4$  in  $0.1 \text{ M KOH}$  on Pd deposited on porous sintered Ni, recorded three peaks at  $-0.3$ ,  $-0.07$ , and  $0.1$  V vs. MOE. He proposed that  $\text{H}_2$  gas evolution was due to  $\text{BH}_3\text{OH}$  oxidization in a three electron process. With Au present (Figs. 4.3.2), two oxidation peaks were observed, one between  $-0.5$  to  $-0.3$  V vs. MOE, with a significant potential shift towards more positive values with increasing  $\text{NaBH}_4$  concentration, and the other around  $0$  V vs. MOE, with slight dependence on  $\text{NaBH}_4$  concentration. The add atom effect can be clearly shown by



comparing Figs. 4.5.1 and 4.3.1 with 4.3.2. The presence of a new first peak at a more negative potential and the second wide-wave peaks at a more negative potential compared to that of pure Au (Fig. 4.3.1) can be attributed to the alloying effects. On Pd-Ag, on the other hand, two oxidation peaks were again observed, one between -0.55 to -0.4 V vs. MOE, and the other between -0.2 to 0 V vs. MOE with a slight dependence on  $\text{NaBH}_4$  concentration. Again, by comparing Figs. 4.5.1 and 4.2.7 with 4.5.3, the effect of the add atom, Ag, can be clearly seen through diminishing the more positive peak (around +0.4 V) for pure Ag and shifting and widening the negative peak (between -0.1 to +0.1 V) for pure Pd.

Figure 4.5.4 shows that the peak current density increases linearly with concentration for Pd-Ni, Pd-Au, and Pd-Ag, while for Pd and Pd-Ir the slopes have changed at 0.05 M. For the peak potential ranges were; Pd (-0.1 to 0.125 V), Pd-Ir (-0.3 to -0.1 V), Pd-Ni (-0.50 to 0.30 V), Pd-Au (-0.185 to -0.075 V), and Pd-Ag (-0.44 to 0.265 V). The slope of the linear dependence between peak current density and concentration on Pd was about 3 times the values obtained on Pd-Ni and Pd-Ag, double the value obtained on Pd-Au, and 1.5 times the value obtained on Ir-Pd.

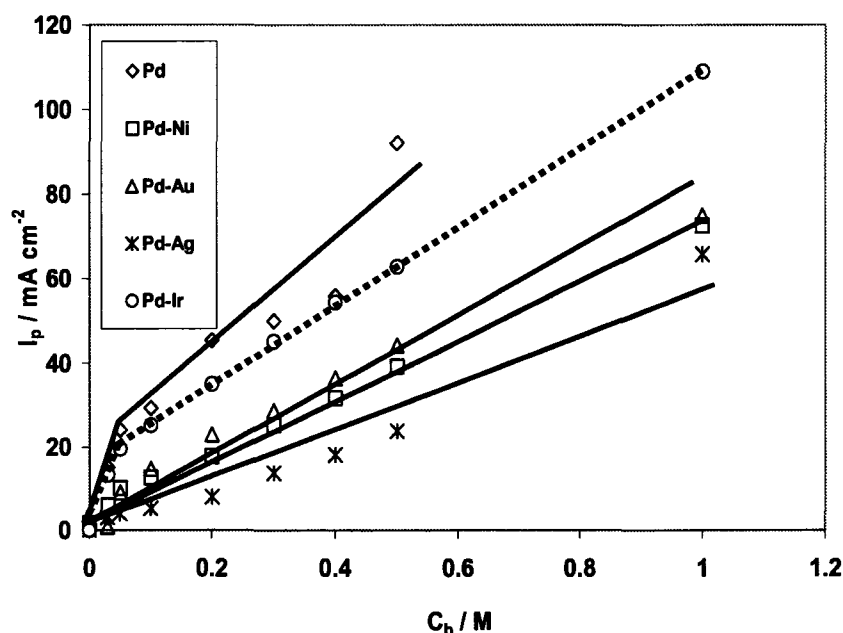


Fig. 4.5.4. The concentration dependence of the peak current density on colloidal Pd and Pd-alloys catalysts. Scan rate  $100 \text{ mV s}^{-1}$ , 298 K.

The scan rate dependence of linear voltammograms, are shown in Figs. 4.5.5-4.5.7. It is obvious that the oxidation peak potentials are only slightly dependent on the scan rate for most of the Pd-based catalysts.

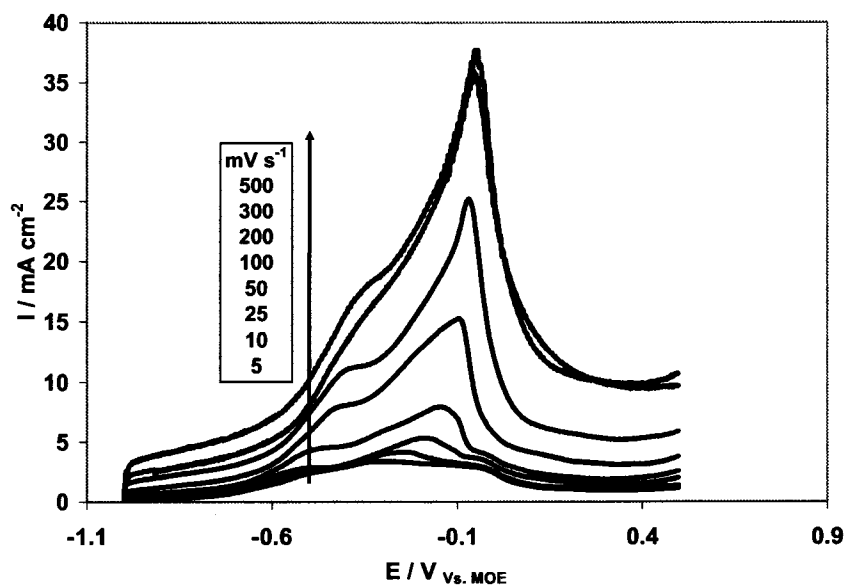


Fig. 4.5.5. Linear voltammogram of  $\text{BH}_4^-$  oxidation on colloidal Pd catalyst using a static electrode showing the effect of scan rate.  $\text{NaBH}_4$  concentration 0.03 M, 298 K. Inset legend indicates the scan rate.

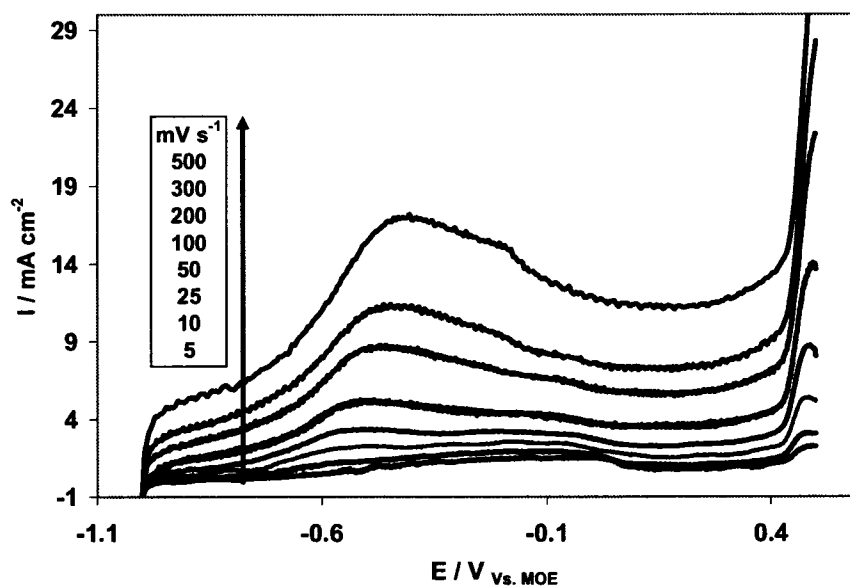


Fig. 4.5.6. Linear voltammogram of  $\text{BH}_4^-$  oxidation on colloidal Pd-Ni catalyst using a static electrode showing the effect of scan rate.  $\text{NaBH}_4$  concentration 0.03 M, 298 K. Inset legend indicates the scan rate

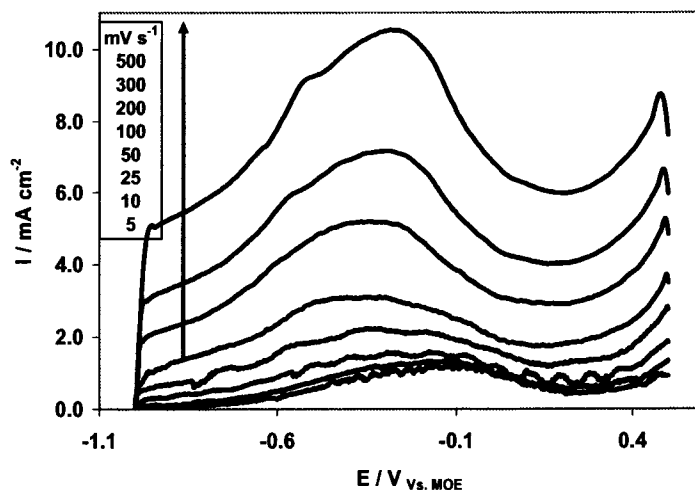


Fig. 4.5.7. Linear voltammogram of  $\text{BH}_4^-$  oxidation on colloidal Pd-Ag catalyst using a static electrode showing the effect of scan rate.  $\text{NaBH}_4$  concentration 0.03 M, 298 K. Inset legend indicates the scan rate.

Fig. 4.5.8 shows the peak current density versus square root of scan rate at a constant  $\text{NaBH}_4$  concentration of 0.03 M. The peak potential ranges were; Pd (-0.3 to -0.045 V), Pd-Ir (-0.38 to -0.215 V), Pd-Ni (-0.40 to 0.07 V), Pd-Au (-0.20 to -0.14 V), and Pd-Ag (-0.26 to -0.10 V). In the case of Pd and Pd-Ir a change in their slopes has been observed at a scan rate of  $50 \text{ mV s}^{-1}$ . Such an increase at high scan rates suggesting that adsorption has an effect on the voltammetry response [6, 16, 17-22].

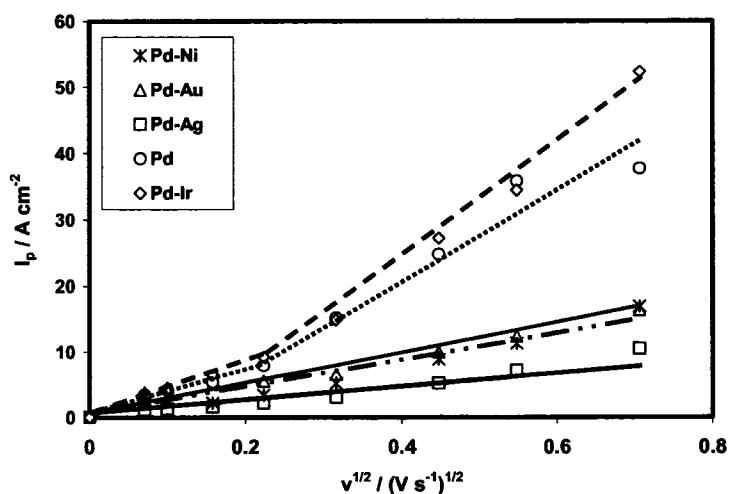


Fig. 4.5.8. The scan rate dependence of the peak current densities obtained on the colloidal Pd and Pd-alloys catalysts:  $\text{NaBH}_4$  concentration 0.03 M, 298 K.

#### 4.5.2. Voltammetry of borohydride oxidation on rotating electrodes

The RDE results for the colloidal Pd, Pd-Ni, Pd-Ag, and Pd-Au, Pd-Ir catalysts are shown in Figures 4.5.9-4.5.11, 4.3.12, and 4.4.13, respectively. As was the case for Pt-, Au-, and Ir-alloys, a strong temperature dependence and a weak rotation speed effect can be clearly seen.

The peak potential on Pd was around 0 V at both 298 K and 313 K, Fig. 4.5.9. On Pd-Ir the peak occurred at more negative potentials, around 0 V, at both 298 K and 313 K (Fig. 4.4.13). For Pd-Ni, Pd-Au and Pd-Ag (Figs. 4.5.10, 4.3.12, and 4.5.11, respectively) on the peak was in the same range as for pure Pd.

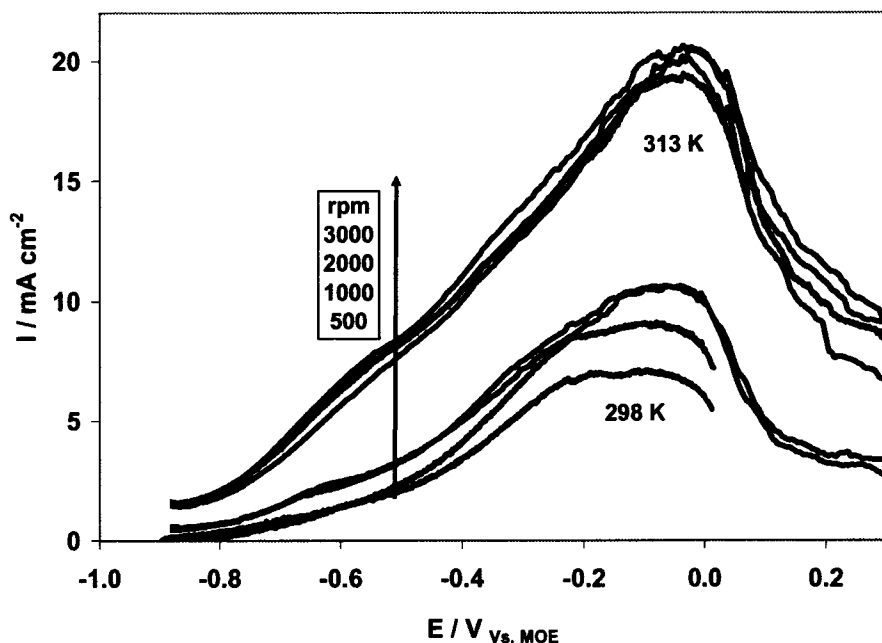


Fig. 4.5.9. Linear voltammetry of  $\text{BH}_4^-$  oxidation on colloidal Pd catalysts using a rotating electrode showing the effect of rotation speed and temperature. Scan rate  $5 \text{ mV s}^{-1}$ , 298 K and 313 K.  $\text{NaBH}_4$  concentration 0.3 M in 2 M NaOH. Inset legend indicates the rotation speed per minute.

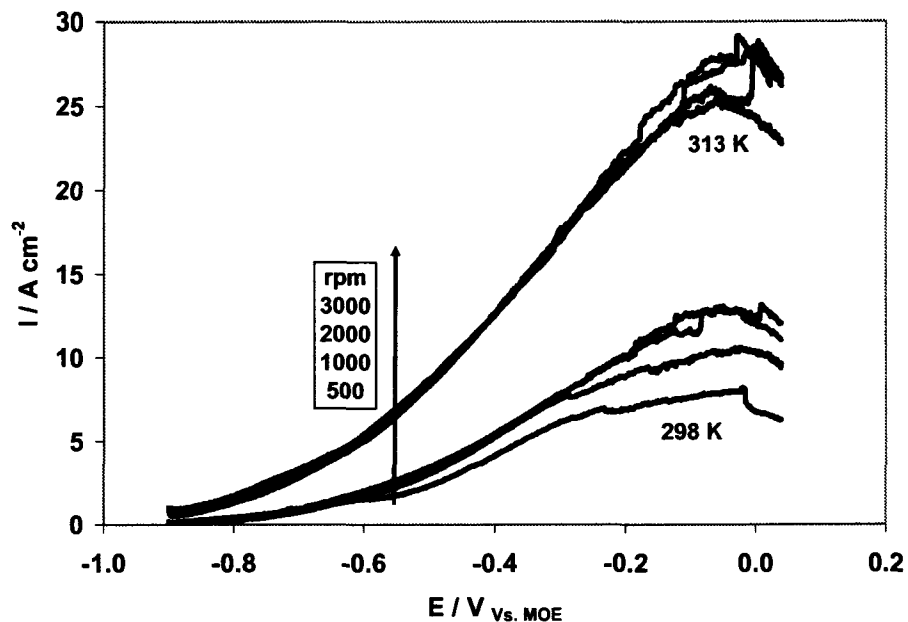


Fig. 4.5.10. Linear voltammetry of  $\text{BH}_4^-$  oxidation on colloidal Pd-Ni catalysts using a rotating electrode showing the effect of rotation speed and temperature. Scan rate  $5 \text{ mV s}^{-1}$ , 298 K and 313 K.  $\text{NaBH}_4$  concentration 0.3 M in 2 M NaOH. Inset legend indicates the rotation speed per minute.

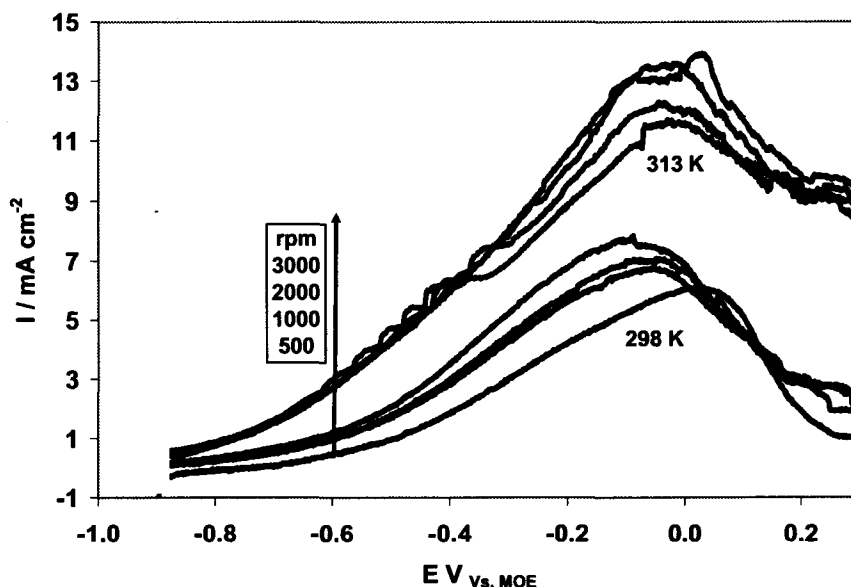


Fig. 4.5.11. Linear voltammetry of  $\text{BH}_4^-$  oxidation on colloidal Pd-Ag catalysts using a rotating electrode showing the effect of rotation speed and temperature. Scan rate  $5 \text{ mV s}^{-1}$ , 298 K and 313 K.  $\text{NaBH}_4$  concentration 0.3 M in 2 M NaOH. Inset legend indicates the rotation speed per minute.

### Tafel slopes and the exchange current densities

Tafel plots of  $\log i$  vs.  $\eta (= E - E_{oc})$  made using the rising domain of Figs. 4.5.9-4.5.11, 4.3.12, and 4.4.13, were about 300-460 actual experimental points recorded, are shown in Fig. 4.5.18.

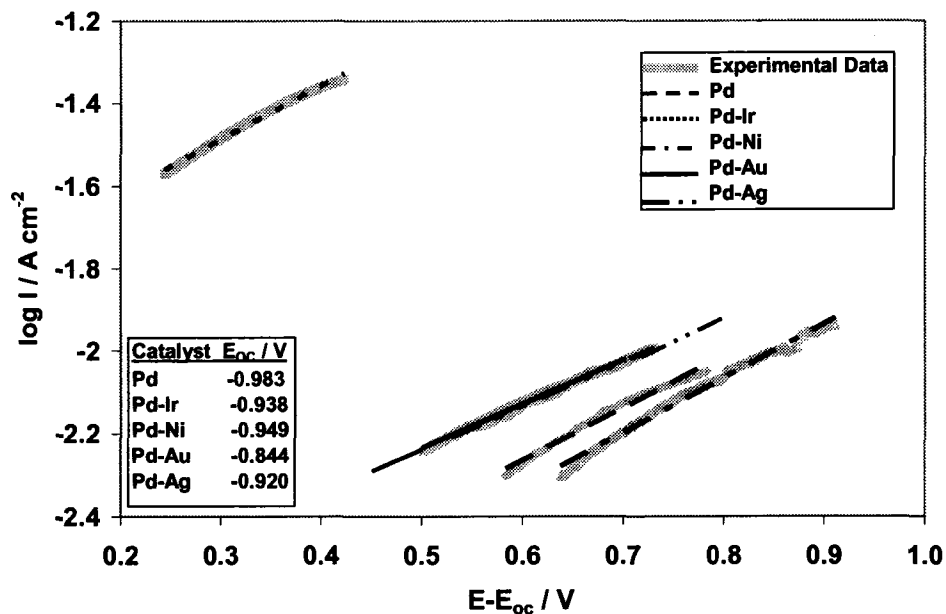


Fig. 4.5.12. Tafel plots for the supported colloidal Pd and Pd-alloys catalysts generated from the rotating disk electrode data at 298 K.

The apparent Tafel slopes ( $b_a$ ) are given in Table 4.5.1. The minimum and maximum values were 0.761 and 0.938 V for Pd-Ni and Pd-Au, respectively at 298 K. As mentioned previously, porous electrodes are characterized by so called multiple Tafel slopes due to ionic conductivity and/or mass transfer limitations coupled with electrode kinetics [25].

Alloying Pd with either Au or Ag increases the apparent Tafel slope. It is decreased at 298 K when it is alloyed with Ni and Ir. The exchange current density, on the other hand, increased by 13 times at 298 K when alloyed with Ir (Table 4.5.1). Thus, alloying with Ir enhances the activity, since it slightly lowers the Tafel slope and significantly increases the exchange current density [25, 26].

Table 4.5.1 summarizes the number of electrons involved in the oxidation of borohydride. The oxidation of  $BH_4^-$  on Pd and Pd-alloys is an incomplete oxidation process, i.e.,  $n < 8$ : On Pd-Au ( $n = 6.2$ ), on Pd ( $n = 4.4$ ) (Kinjo [44] found  $n = 3$  for Pd deposited on sintered Ni), on Pd-Ir ( $n \sim 3$ ), and on Pd-Ni and Pd-Ag ( $n = 2$ ).

Table 4.5.1. Apparent Tafel slopes,  $b_a$ , exchange current densities,  $i_{0,a}$ , total number of electrons exchanged,  $n$ , determined from RDE data using supported colloidal Pd and Pd-alloys catalysts with Nafion 117 polymer electrolyte. Eq. (4.2.2) is used to calculate  $n$ .

Catalysts	$b_a$ (V dec <sup>-1</sup> ) 298 K	$i_{0,a}$ (A cm <sup>-2</sup> ) 298 K	n
<b>Pd</b>	0.787	$0.939 \times 10^{-3}$	4.5
<b>Pd-Ir</b>	0.757	$13.06 \times 10^{-3}$	2.9
<b>Pd-Ni</b>	0.761	$0.765 \times 10^{-3}$	2.0
<b>Pd-Au</b>	0.938	$0.120 \times 10^{-3}$	6.2
<b>Pd-Ag</b>	0.934	$1.67 \times 10^{-3}$	2.0

#### 4.5.3. Chronopotentiometry

It can be clearly seen from Fig. 4.5.13 that the overpotential ( $=E-E_{oc}$ ) was the smallest on Pd-Ir, about 295 mV, followed by Pd (467 mV), Pd-Au (553 mV), Pd-Ni (690 mV), and lastly Pd-Ag, where the overpotential was about 760 mV. Pd-Ir is the most active among the investigated catalysts, since it shows a lower overpotential [26]. The more negative the open circuit potential of the anode, the less is the hydrolysis activity of the catalyst [7].

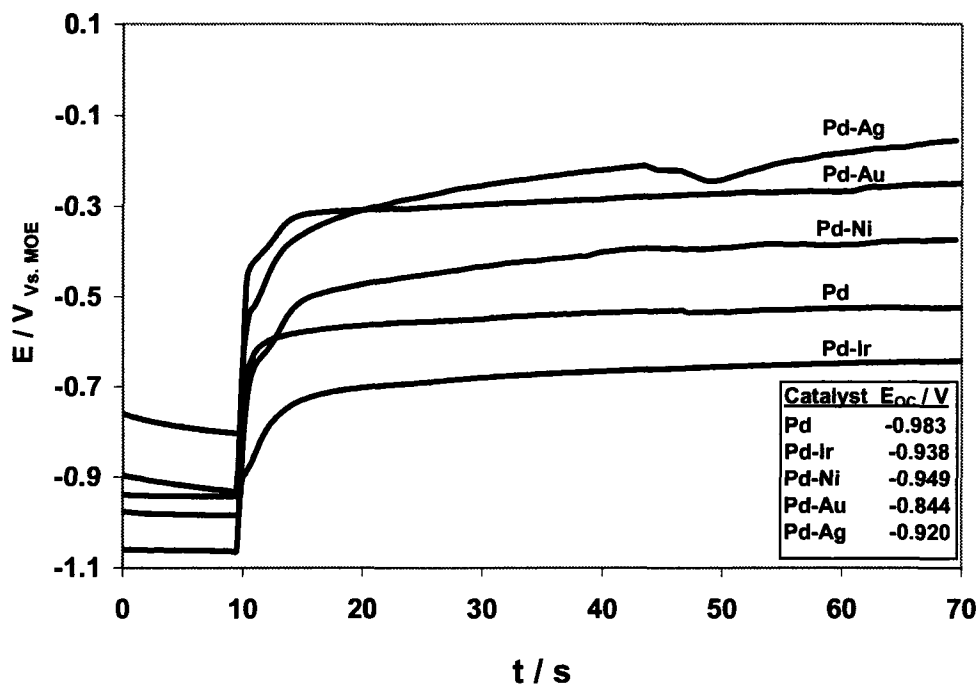


Fig. 4.5.13. Chronopotentiometry of  $\text{BH}_4^-$  oxidation on colloidal Pd and Pd-alloys catalysts. Current step: from 0 to  $10 \text{ mA cm}^{-2}$ .  $0.5 \text{ M Na BH}_4$  in  $2 \text{ M NaOH}$ .  $298 \text{ K}$ .

#### 4.5.4. Chronoamperometry and chronocoulometry

The chronoamperometry results for the colloidal Pd, Pd-Ni, Pd-Ag, and Pd-Au, Pd-Ir catalysts are shown in Figs. 4.5.14-4.5.16, 4.3.18, and 4.4.19, respectively.

For the  $-0.6 \text{ V}$ ,  $-0.4 \text{ V}$  and  $-0.2 \text{ V}$  potential steps, the highest anodic current densities were measured on Pd-Ir (i.e. about  $0.026$ ,  $0.017$ , and  $0.015 \text{ A cm}^{-2}$  respectively, after  $60 \text{ s}$ , (Fig.4.4.19). The rest of the electrodes gave current densities less than Pd-Ir in the following order,  $\text{Pd} > \text{Pd-Ni} > \text{Pd-Au} > \text{Pd-Ag}$  under similar conditions.

For both the  $-0.6 \text{ V}$  and  $-0.4 \text{ V}$  potential steps, the highest anodic current densities were measured on Pd-Ir (i.e. about  $0.03 \text{ A cm}^{-2}$  after  $60 \text{ s}$  at the former and  $0.04 \text{ A cm}^{-2}$ . Thus, in the negative potential range of  $-0.9 \text{ V}$  and  $-0.4 \text{ V}$ , which is the domain of interest for practical fuel cell anodes, Pd-Ir was the most active catalyst.



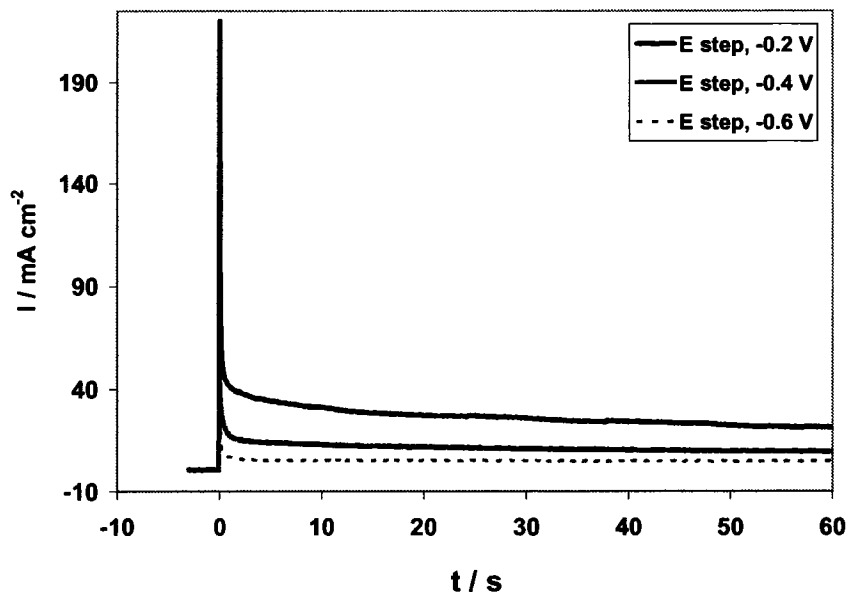


Fig. 4.5.14. Chronoamperometry of  $\text{BH}_4^-$  oxidation on a colloidal Pd catalyst. Potential steps from  $-0.9 \text{ V}$  vs. MOE to  $-0.6$ ,  $-0.4$  and  $-0.2 \text{ V}$  vs. MOE, respectively  $0.5 \text{ M}$   $\text{NaBH}_4$  in  $2 \text{ M}$   $\text{NaOH}$ .  $298 \text{ K}$ .

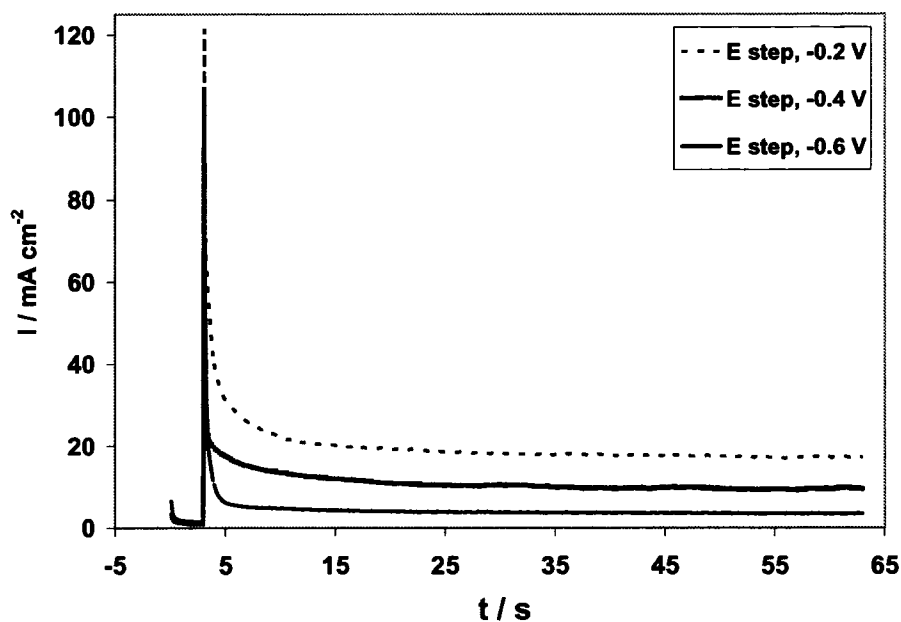


Fig. 4.5.15. Chronoamperometry of  $\text{BH}_4^-$  oxidation on a colloidal Pd-Ni catalyst. Potential steps from  $-0.9 \text{ V}$  vs. MOE to  $-0.6$ ,  $-0.4$  and  $-0.2 \text{ V}$  vs. MOE, respectively  $0.5 \text{ M}$   $\text{NaBH}_4$  in  $2 \text{ M}$   $\text{NaOH}$ .  $298 \text{ K}$ .

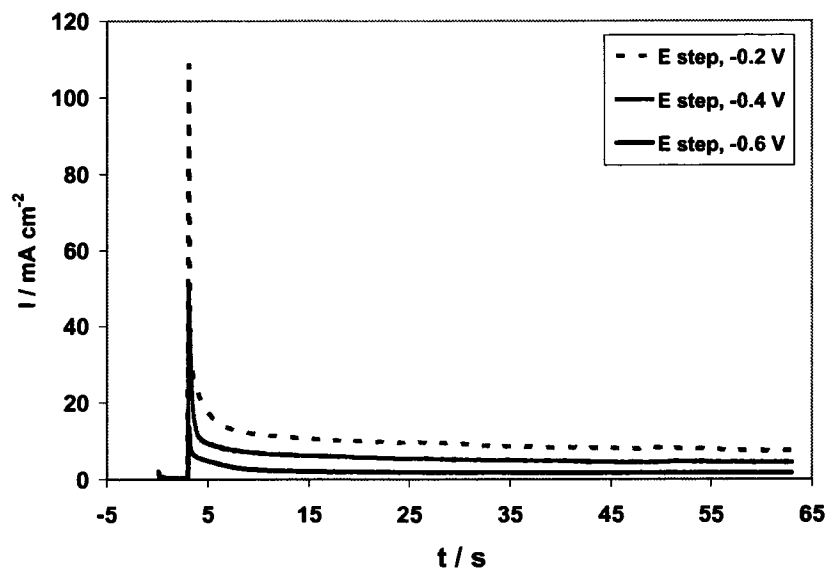


Fig. 4.5.16. Chronoamperometry of  $\text{BH}_4^-$  oxidation on a colloidal Pd-Ag catalyst. Potential steps from  $-0.9$  V vs. MOE to  $-0.6$ ,  $-0.4$  and  $-0.2$  V vs. MOE, respectively  $0.5$  M  $\text{NaBH}_4$  in  $2$  M  $\text{NaOH}$ .  $298$  K.

### Cottrell Plot

A non Cottrellian response as shown in the  $i \cdot \sqrt{t}$  vs.  $t$  plots was exhibited for all Pd and Pd-alloys catalysts, except for Pd-Au and Pd-Ag at both the  $-0.4$  and the  $-0.6$  V step changes (Figs. 4.5.17-4.5.18).

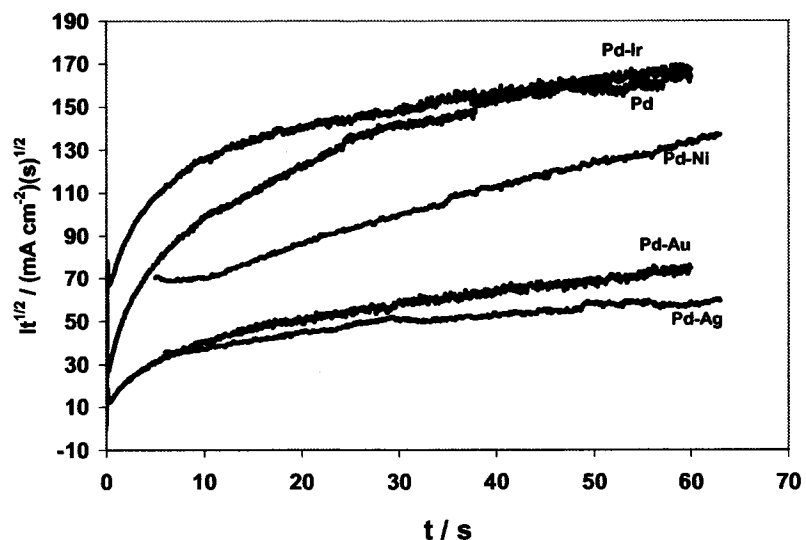


Fig. 4.5.17. Cottrell plot generated from the chronoamperometry data for potential step from  $-0.9$  V to  $-0.2$  V vs. MOE.

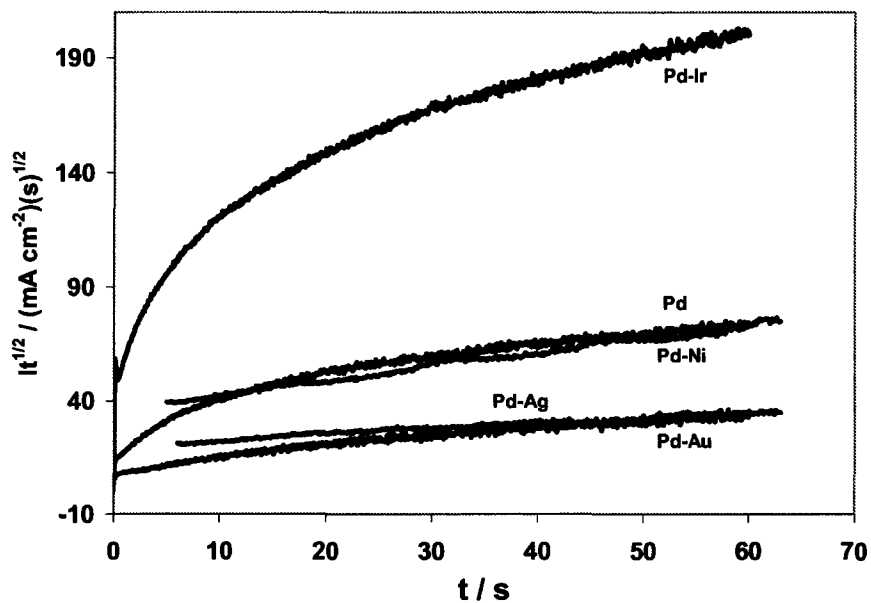


Fig. 4.5.18. Cottrell plot generated from the chronoamperometry data for potential step from  $-0.9 \text{ V}$  to  $-0.4 \text{ V}$  vs. MOE.

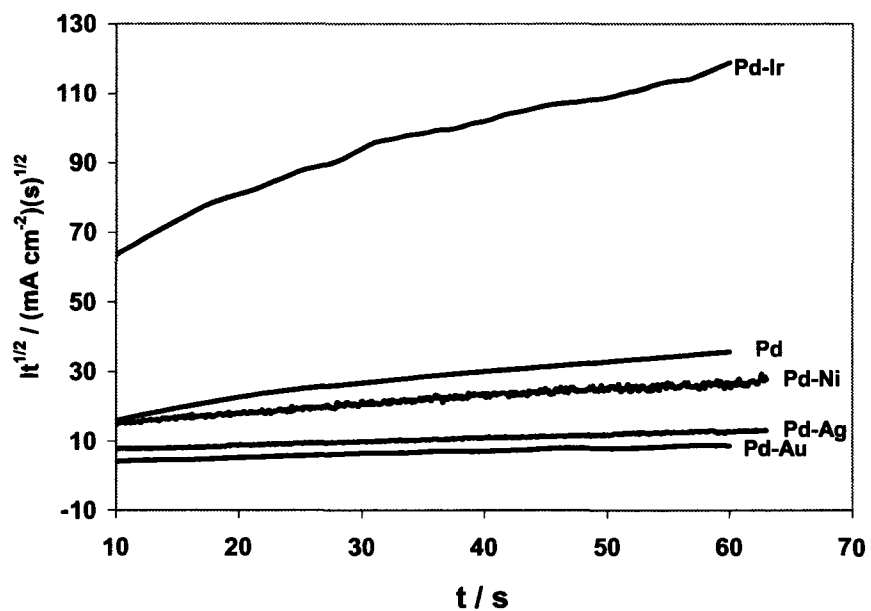


Fig. 4.5.19. Cottrell plot generated from the chronoamperometry data for potential step from  $-0.9 \text{ V}$  to  $-0.6 \text{ V}$  vs. MOE.

## Chronocoulometry

Figures 4.5.20-4.5.22 show Anson plots for the Pd and Pd-alloy catalysts obtained for potential steps from  $-0.9$  V to  $-0.2$  V,  $-0.4$  V, and  $-0.6$  V vs. MOE.

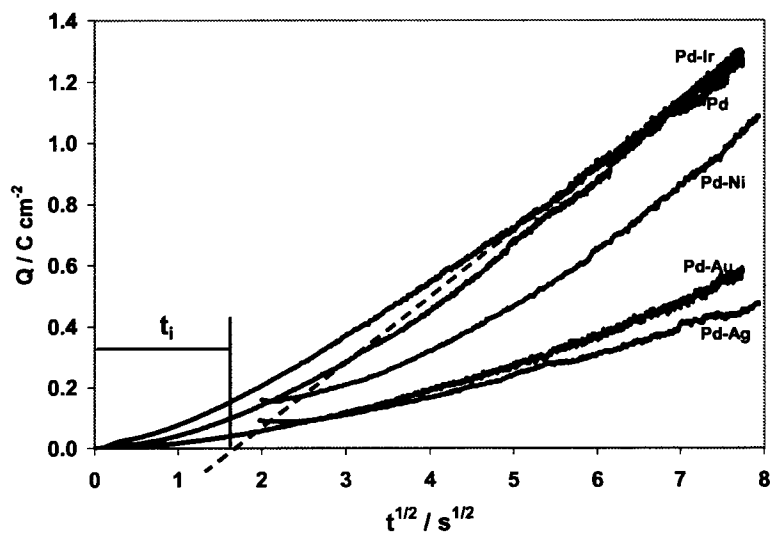


Fig. 4.5.20. Cumulative charge density as a function of square root of time (Anson plot) generated from the chronoamperometry data for potential step from  $-0.9$  V to  $-0.2$  V vs. MOE.

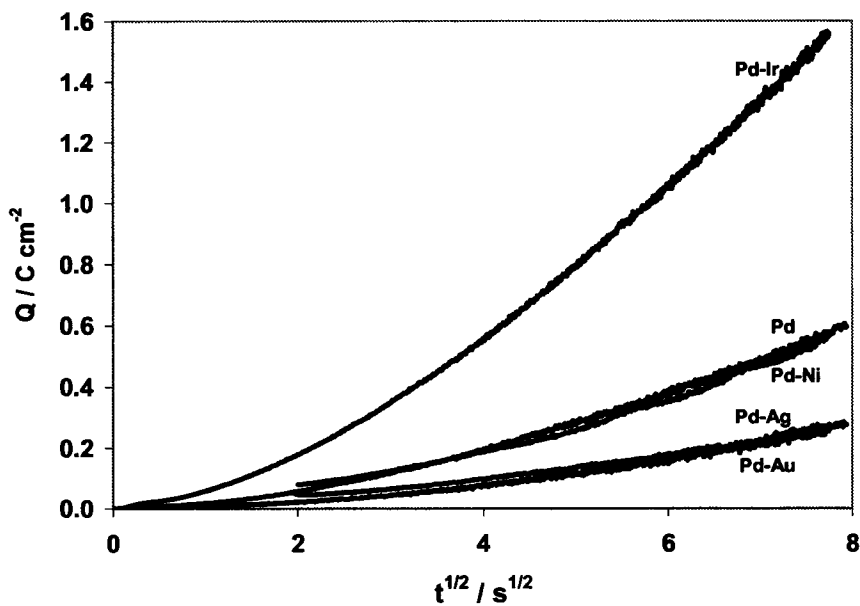


Fig. 4.5.21. Cumulative charge density as a function of square root of time (Anson plot) generated from the chronoamperometry data for potential step from  $-0.9$  V to  $-0.4$  V vs. MOE.

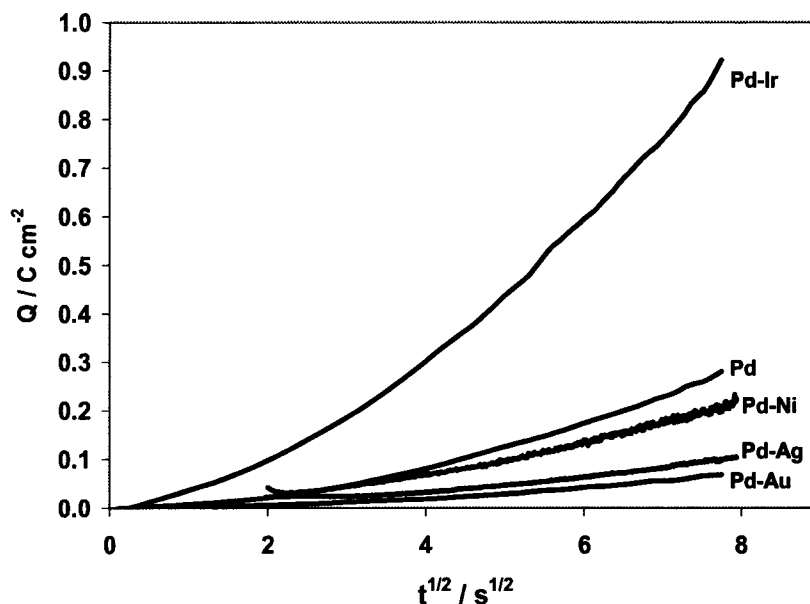


Fig. 4.5.22. Cumulative charge density as a function of square root of time (Anson plot) generated from the chronoamperometry data for potential step from  $-0.9$  V to  $-0.6$  V vs. MOE.

Table 4.5.2 summarizes the  $k_h$  values at  $-0.4$  V and 298 K obtained from the slope of eq. (3.6.32) corresponding to the data from Fig. 4.2.29.

Table 4.5.2. Apparent heterogeneous rate constants for  $\text{BH}_4^-$  oxidation at  $-0.4$  V vs. MOE and 298 K calculated from chronocoulometry.

Catalyst	Pd	Pd-Au	Pd-Ni	Pd-Ir	Pd-Ag
$k_h$ ( $\text{cm s}^{-1}$ )	$6.72 \times 10^{-6}$	$4.08 \times 10^{-6}$	$10.8 \times 10^{-6}$	$25 \times 10^{-6}$	$7.35 \times 10^{-6}$

The apparent heterogeneous rate constants for  $-0.4$  V potential step show the following order of electrocatalytic activity: Pd-Ir > Pd-Ni > Pd-Ag > Pd > Pd-Au, with  $k_h$  between  $25 \times 10^{-6} \text{ cm s}^{-1}$  for Pd-Ir and  $4.08 \times 10^{-6} \text{ cm s}^{-1}$  for Pd-Au.

#### 4.5.5. Fuel cell performance

Figures 4.5.23-25 show the temperature and fuel flow rates effects on the polarization curves obtained using the colloidal Pd, Pd-Ir, and Pd-Au catalysts respectively. The temperature has a significant impact on the fuel cell performance for all investigated cases, while, the flow rate has no significant effect on the fuel cell performance.

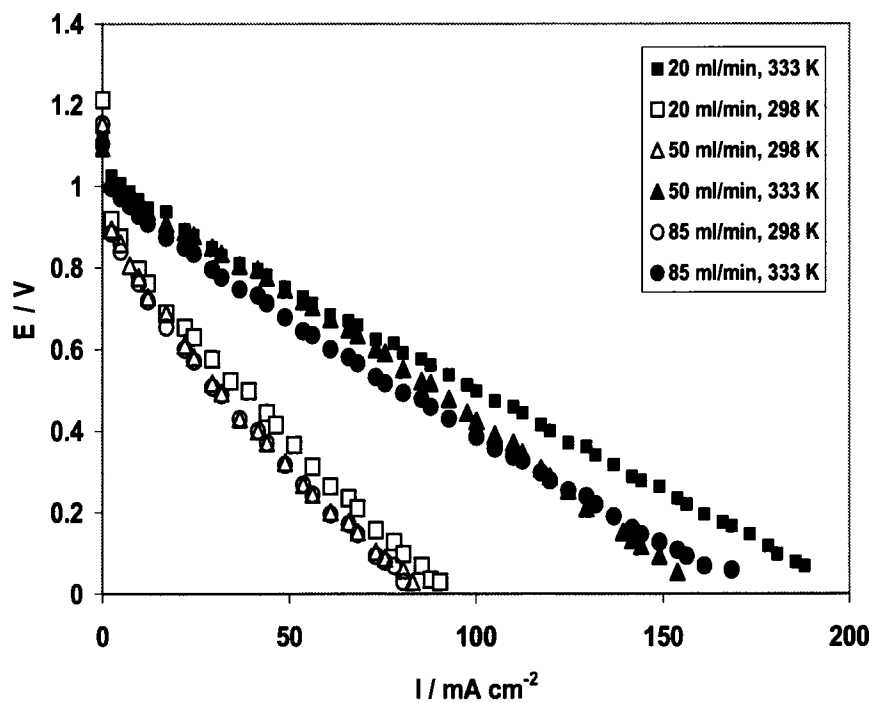


Fig. 4.5.23. Direct borohydride fuel cell polarization curves at 298 K and 333 K: Anode catalyst (Pd) load  $5 \text{ mg cm}^{-2}$ .  $2 \text{ M NaBH}_4 - 2 \text{ M NaOH}$ . Cathode catalyst (Pt) load  $4 \text{ mg cm}^{-2}$ .  $\text{O}_2$  flow rate  $200 \text{ ml min}^{-1}$  at  $2.7 \text{ atm}$ .

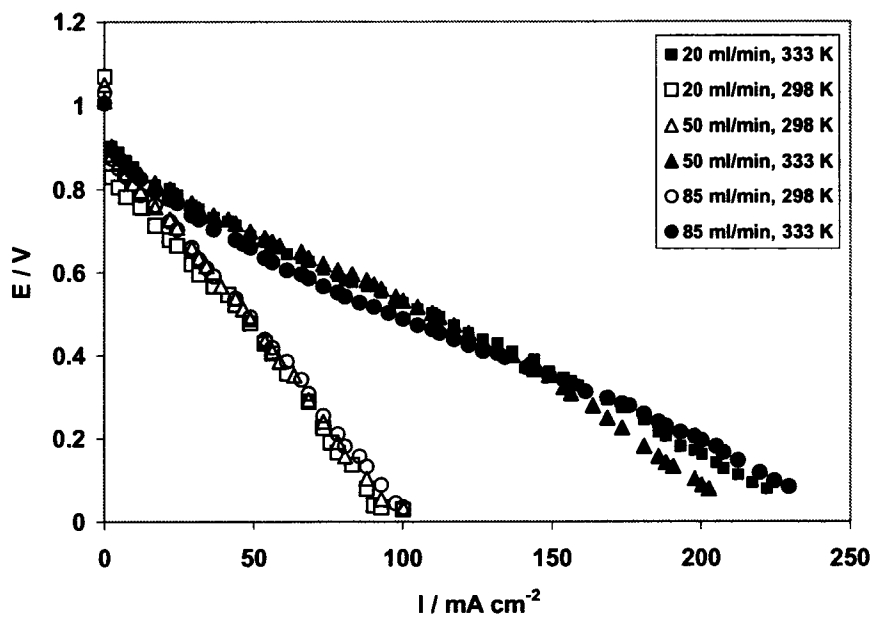


Fig. 4.5.24. Direct borohydride fuel cell polarization curves at 298 K and 333 K: Anode catalyst (Pd-Ir) load  $5 \text{ mg cm}^{-2}$ .  $2 \text{ M NaBH}_4 - 2 \text{ M NaOH}$ . Cathode catalyst (Pt) load  $4 \text{ mg cm}^{-2}$ .  $\text{O}_2$  flow rate  $200 \text{ ml min}^{-1}$  at  $2.7 \text{ atm}$ .

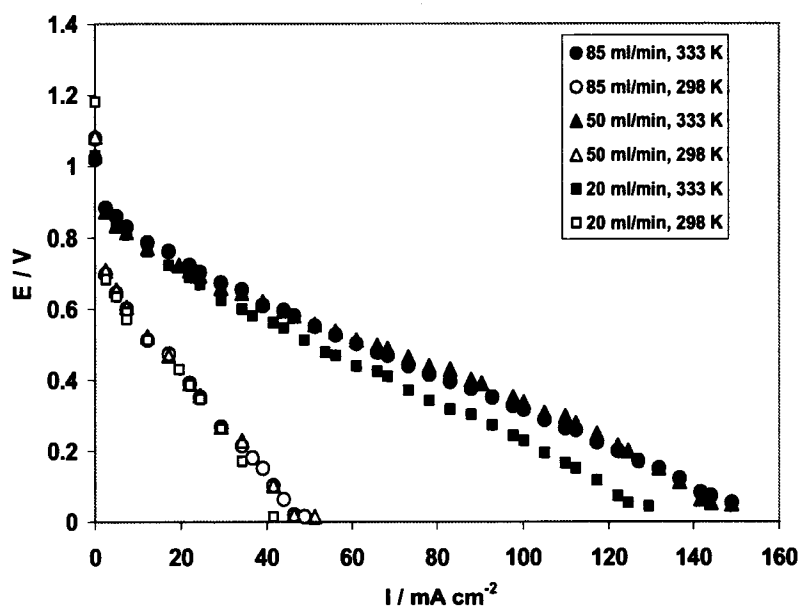


Fig. 4.5.25. Direct borohydride fuel cell polarization curves at 298 K and 333 K: Anode catalyst (Pd-Au) load  $5 \text{ mg cm}^{-2}$ .  $2 \text{ M NaBH}_4 - 2 \text{ M NaOH}$ . Cathode catalyst (Pt) load  $4 \text{ mg cm}^{-2}$ .  $\text{O}_2$  flow rate  $200 \text{ ml min}^{-1}$  at  $2.7 \text{ atm}$ .

Figure 4.5.26 shows a comparison between the fuel cell performances using colloidal Pd, Pd-Au, and Pd-Ir as anode catalyst. Pd-Ir is the most active, and fuel cell employing such anode catalyst and operate at a cell voltage of 0.5 V can give a current of 48.84 mA cm<sup>-2</sup>, while at 333 K, same catalyst, can give 95.23 mA cm<sup>-2</sup> at 0.5 V cell voltage.

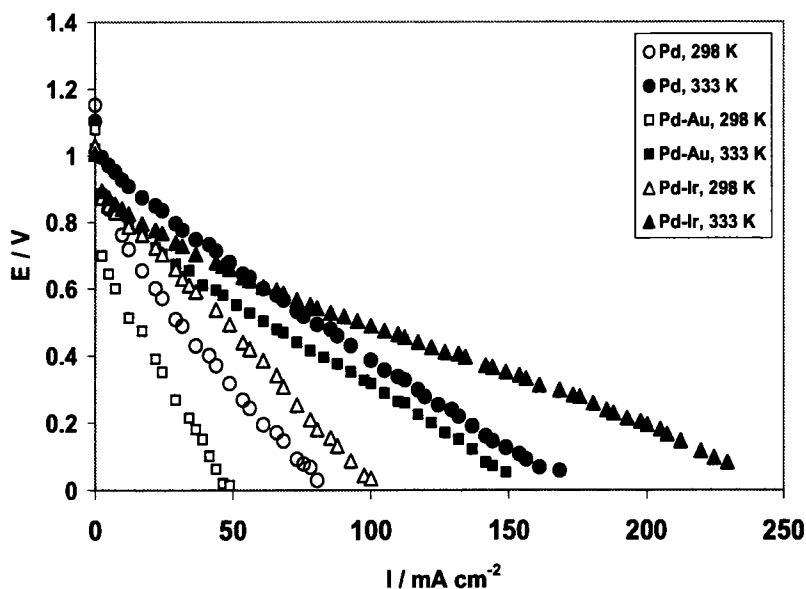


Fig. 4.5.26. Direct borohydride fuel cell polarization curves at 298 K and 333 K: Comparison between the colloidal catalysts prepared in the present work (Pd, Pd-Ir, and Pd- Au). Anode catalyst load 5 mg cm<sup>-2</sup>. 50 ml min<sup>-1</sup> 2 M NaBH<sub>4</sub> – 2 M NaOH. Cathode catalyst (Pt) load 4 mg cm<sup>-2</sup>. O<sub>2</sub> flow rate 200 ml min<sup>-1</sup> at 2.7 atm.

#### 4.5.6. Summary

In summary, Pd-Ir was the most active electrocatalyst amongst the Pd-group, with the lowest  $b_a$  and the highest  $i_o$  and heterogeneous rate constant,  $k_h$ . The fuel cell test performance (as measured by current density) of Pd-Ir was 1.66 times higher than for pure Pd and 3.32 higher than for Pd-Au.



## 4.6. Overall Comparison of the Best of the Catalyst Groups

### 4.6.1. Voltammetry of borohydride oxidation on static electrodes

Linear voltammograms on static electrodes for the colloidal Pt, Pt-Au, Pt-Ir, Pt-Ni, Pd, Pd-Ir, and Ir-Ni catalysts, recorded at 298 K and a constant scan rate of  $100 \text{ mV s}^{-1}$ , for 0.03 M and 0.1  $\text{NaBH}_4$  concentrations are shown in Figures 4.6.1 and 4.6.2, respectively. The most negative oxidation peaks were obtained on Pt-Ir, Pt-Ni, and Pd-Ir, while the highest peak current was recorded on Pd-Ir at the low  $\text{NaBH}_4$  concentration and on Pt-Au at the higher  $\text{NaBH}_4$  concentration. The most positive oxidation potentials were obtained on Pd and Pt-Au respectively. The oxidation peaks shift slightly to a more positive value with an increase in  $\text{NaBH}_4$  concentration (Figs. 4.6.1 and 4.6.2).

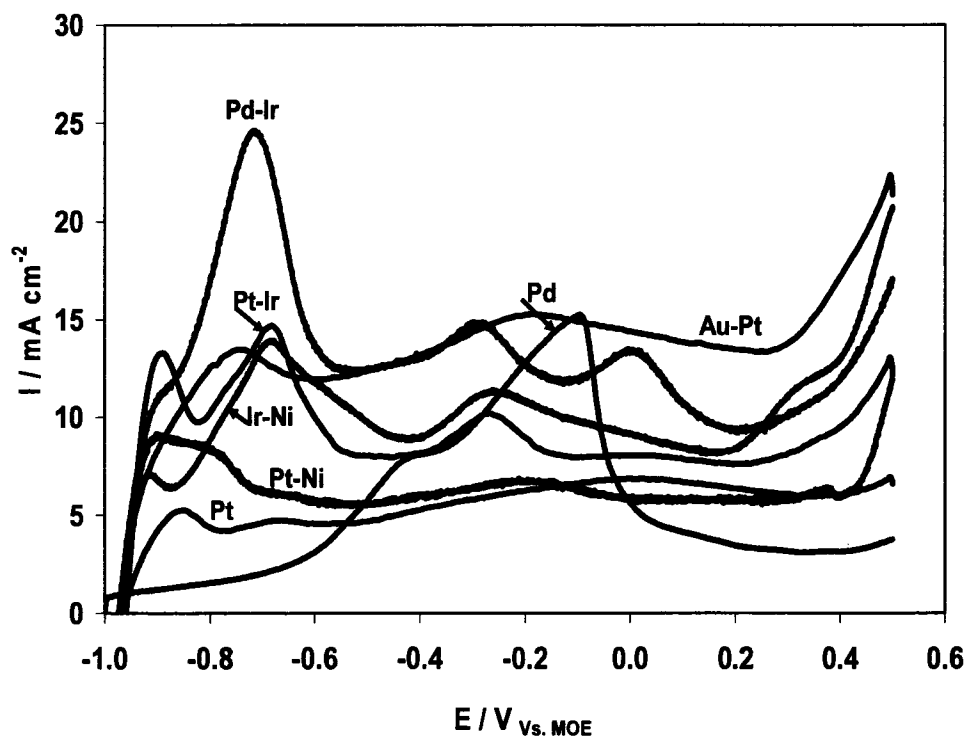


Fig. 4.6.1. Linear voltammogram of  $\text{BH}_4^-$  oxidation on colloidal catalysts using static electrode.  $\text{NaBH}_4$  concentration 0.03 M  $\text{BH}_4^-$  in 2 M NaOH. Scan rate  $100 \text{ mV s}^{-1}$ , 298 K.

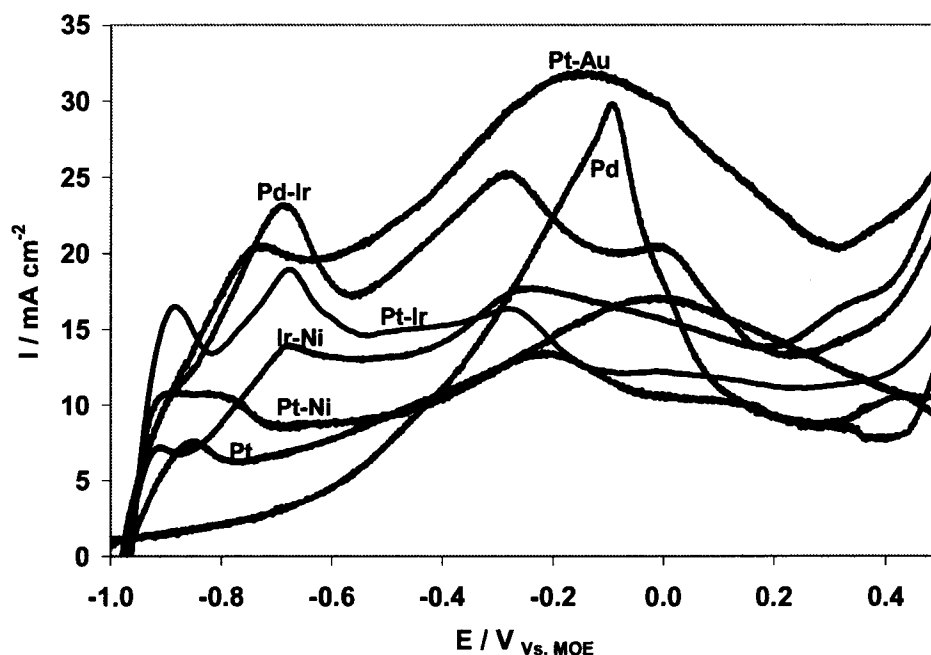


Fig. 4.6.2. Linear voltammogram of  $\text{BH}_4^-$  oxidation on colloidal catalysts using static electrode.  $\text{NaBH}_4$  concentration 0.1 M in 2 M NaOH. Scan rate  $100 \text{ mV s}^{-1}$ , 298 K.

Table 4.6.1 summarizes the peak currents and potentials of the best of the catalysts group. It can be clearly seen that the highest first peak current was recorded for Pd, while the most negative first peak potential was recorded for Ir-Ni followed by Pt-Ni. The highest second peak current was recorded for Pt-Au followed by Pd-Ir, while the most negative second peak potential was recorded for Ir-Ni followed by Pt-Ni. The third peak was only present for Pt-Ir, Pd-Ir, and Ir-Ni. The highest third peak current was for Pd-Ir, while the most negative third peak potential was for Pt-Ir.

Table 4.6.1. Summary of peaks current and potential of the best of the catalysts group at 0.1 M  $\text{NaBH}_4$  and  $100 \text{ mV s}^{-1}$ .

Catalyst	First Peak		Second Peak		Third Peak	
	Current ( $\text{mA cm}^{-2}$ )	Potential (V)	Current ( $\text{mA cm}^{-2}$ )	Potential (V)	Current ( $\text{mA cm}^{-2}$ )	Potential (V)
Pt	7.62	-0.849	16.97	-0.014		
Pt-Au	20.65	-0.736	31.67	-0.14		
Pt-Ni	10.74	-0.903	13.36	-0.206		
Pt-Ir	16.48	-0.883	18.91	-0.673	16.32	-0.271
Pd	29.72	-0.089				
Pd-Ir	23.14	-0.682	25.22	-0.281	20.5	0.0
Ir-Ni	7.07	-0.905	14.0	-0.676	17.71	-0.24

#### 4.6.2. Voltammetry of borohydride oxidation on rotating electrodes

Figure 4.6.3 compares the polarization curves for a RDE for Pt, Pd, Pd-Ir, Pt-Ni, Pt-Au, Pt-Ir and Ir-Ni as recorded at a scan rate was  $5 \text{ mV s}^{-1}$ , and a rotation speed of 500 rpm and  $0.3 \text{ M BH}_4^-$  concentration. It can be clearly seen that for Ir-Pd the highest peak current can be obtained at a potential of  $-0.36 \text{ V}$  vs. MOE. For Pd, on the other hand, the lowest peak current was recorded at potential of  $-0.125 \text{ V}$  vs. MOE. It is worth mentioning that the second highest peak current was on Ir-Ni, but at the most negative oxidation potential, i.e.,  $-0.5 \text{ V}$  vs. MOE (Fig. 4.6.3).

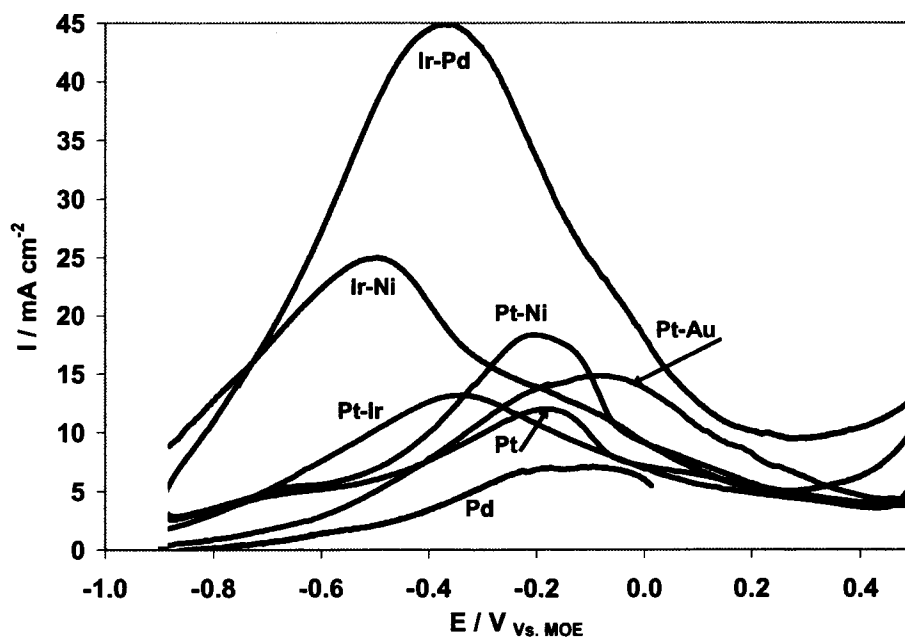


Fig. 4.6.3. Linear voltammetry of  $\text{BH}_4^-$  oxidation on colloidal catalysts using rotating electrodes: Rotation per minute 500. Scan rate  $5 \text{ mV s}^{-1}$ , 298.  $\text{NaBH}_4$  concentration  $0.3 \text{ M}$  in  $2 \text{ M NaOH}$ .

Table 4.6.2 summarizes the apparent Tafel slopes,  $b_a$ , as reported in the previous sections. The Tafel slopes range between  $0.607$  to  $0.939 \text{ V decade}^{-1}$  at  $298 \text{ K}$ . The highest exchange current densities, at  $298 \text{ K}$ , were recorded on Pd-Ir, followed by Ir-Ni, Pt-Ir, Pt, Pt-Ni, Pt-Au and Pd, respectively.

Table 4.6.2. Apparent Tafel slopes,  $b_a$ , exchange current densities,  $i_{0,a}$ , and the total number of electrons exchanged,  $n$ , at 298 K determined from RDE data using supported colloidal catalysts with Nafion 117 polymer electrolyte. Eq. (4.2.2) was used to calculate  $n$ .

Catalysts	$b_a$ (V dec <sup>-1</sup> ) 298 K	$i_{0,a}$ (A cm <sup>-2</sup> ) 298 K	$n$
Pd	0.787	$0.939 \times 10^{-3}$	4.5
Pt	0.939	$2.648 \times 10^{-3}$	4
Pd-Ir	0.757	$13.06 \times 10^{-3}$	3.0
Pt-Au	0.662	$1.180 \times 10^{-3}$	7.7
Pt-Ni	0.651	$1.506 \times 10^{-3}$	2.5
Pt-Ir	0.823	$3.622 \times 10^{-3}$	3.2
Ir-Ni	0.607	$7.906 \times 10^{-3}$	2.9

### 4.6.3. Chronopotentiometry

Figure 4.6.4 shows the anode potentials and the open circuit values for the Pt, Pt-Au, Pt-Ni, Pt-Ir, Pd, Pd-Ir, and Ir-Ni catalysts operating at  $10 \text{ mA cm}^{-2}$ .

The overpotential ( $= E - E_{oc}$ ) was the smallest on Pt-Ir, about 100 mV, followed by Ir-Pd, Pt-Au, Ir-Ni, Pt-Ni, Pd, and lastly Pt, where the overpotential was about 630 mV. The more negative the open circuit potential of the anode, the less is the hydrolysis activity of the catalyst [7].

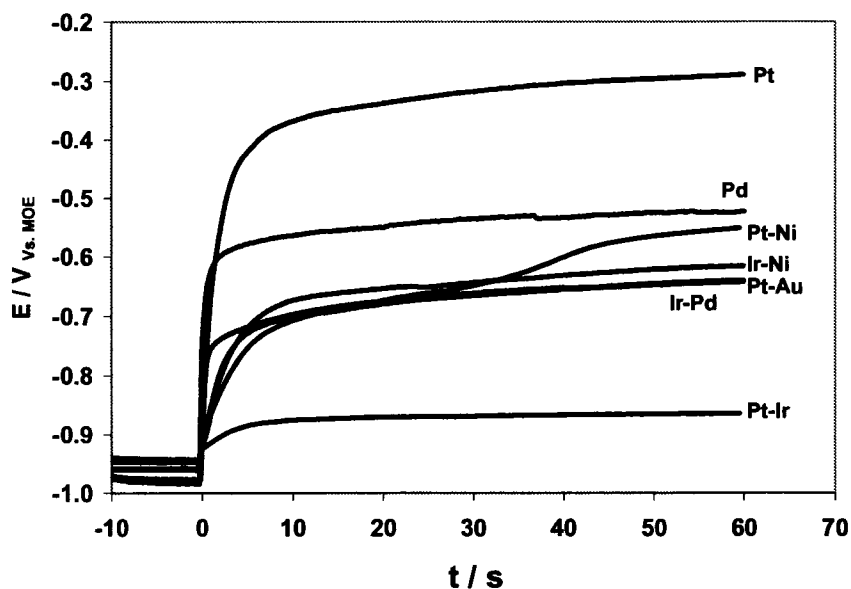


Fig. 4.6.4. Chronopotentiometry of  $\text{BH}_4^-$  oxidation on colloidal catalysts. Current step: from 0 to  $10 \text{ mA cm}^{-2}$ .  $0.5 \text{ M Na BH}_4$  in  $2 \text{ M NaOH}$ . 298 K.

#### 4.6.4. Chronoamperometry and chronocoulometry

The chronoamperometry results for colloidal Pd, Pt, Pt-Au, Pt-Ni, Pt-Ir, Pd, Pd-Ir, Ir-Ni, Catalysts for a potential step change of  $-0.9$  V to  $-0.4$  V vs. MOE are shown in Fig. 4.6.5. The highest superficial current density transient was recorded on Pt-Au, while the least was on Pt. The remainder gave current densities less than for Pt-Au in the following order, Pd-Ir > Pt-Ir > Pt-Ni > Pd > Ir-Ni.

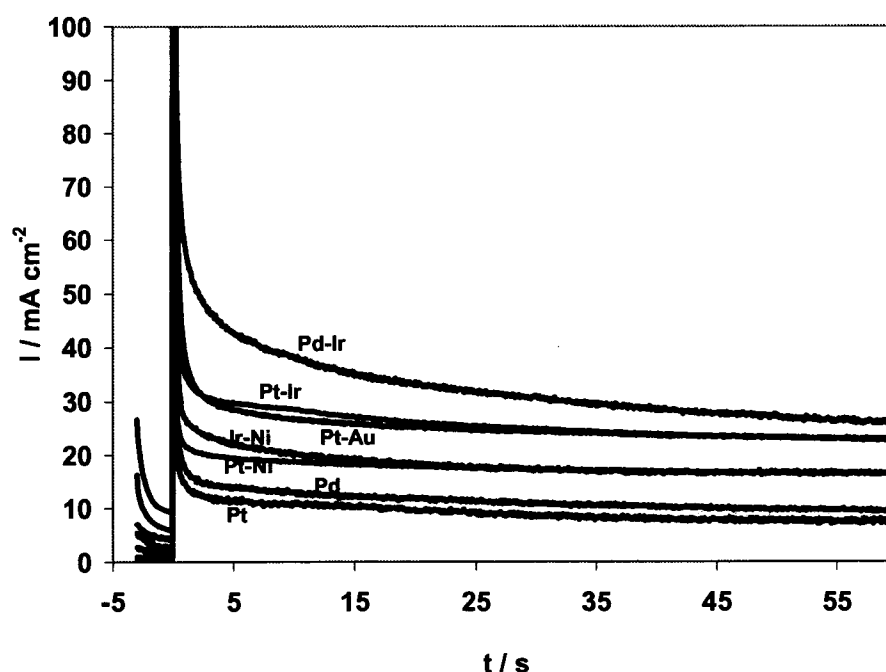


Fig. 4.6.5. Chronoamperometry of  $\text{BH}_4^-$  oxidation on colloidal catalysts. Potential steps from  $-0.9$  V to  $-0.4$  V vs. MOE, respectively  $0.5$  M  $\text{NaBH}_4$  in  $2$  M  $\text{NaOH}$ .  $298$  K.

Table 4.6.3 summarizes the  $k_h$  values at  $298$  K for a potential step of  $-0.4$  V vs. MOE. The apparent heterogeneous rate constants show the following order of electrocatalytic activity: Pt-Ir > Pd-Ir > Pt-Ni > Ir-Ni > Pd > Pt-Au > Pt.

Table 4.6.3. Apparent heterogeneous rate constants for  $\text{BH}_4^-$  oxidation at  $-0.4$  V vs. MOE and  $298$  K calculated from chronocoulometry.

Catalyst	Pt	Pt-Au	Pt-Ni	Pt-Ir	Pd	Pd-Ir	Ir-Ni
$k_h$ ( $\text{cm s}^{-1}$ )	$5.8 \times 10^{-6}$	$6.26 \times 10^{-6}$	$12 \times 10^{-6}$	$28 \times 10^{-6}$	$6.7 \times 10^{-6}$	$25 \times 10^{-6}$	$11 \times 10^{-6}$

The apparent heterogeneous rate constant differences could be attributed to the hydrogen (generated by the hydrolysis process) adsorption rate, the strength of hydrogen-metal bond and how this affects the competition between hydrogen and borohydride on these surfaces [45], in addition to their intrinsic catalytic activity and the differences in hydrolysis reaction rates on these catalysts (eq. 2.10.2). Moreover, by knowing the precise borohydride oxidation mechanisms, (see Fig. 2.9.4), a better explanation can be put forward for the differences in the oxidation activities. For example, if the borohydride oxidation mechanism follows the Langmuir-Henshelwood type (Fig. 2.9.4), the competition between  $\text{BH}_4^-$  and  $\text{OH}^-$ , and the adsorption bond strength on these mono- and bi-metallic catalysts, could be attributed to their activity differences. It has been postulated that a good electrocatalyst is one which strongly adsorbs the reactant, but not too strongly [8].

#### 4.6.5. Fuel cell performance

Figures 4.6.6 and 4.6.7 show the temperature effect on the polarization curves obtained using the colloidal Pt, Pt-Au, Pt-Ni, Pt-Ir, Pd, Pd-Ir, and Ir-Ni catalysts. Increasing the temperature from 298 K to 333 K, improved dramatically the borohydride fuel cell performance. With Pt, Pt-Au, Pt-Ni, Pt-Ir, Pd, Pd-Ir, and Ir-Ni catalysts, a fuel cell operating at a cell voltage of 0.5 V gives current densities of 34, 26, 44, 46, 29, 49, and 51  $\text{mA cm}^{-2}$ , respectively at 298 K. At 333 K, the current densities were 85, 93, 105, 105, 78, 95, and 83  $\text{mA cm}^{-2}$ , respectively. Thus Ir-Ni and Pd-Ir followed by Pt-Ni, and Pt-Ir are the most active catalysts at 298 K. At 333 K on other hand, the order of the catalysts' activity is Pt-Ir, Pt-Ni, Pd-Ir, Pt-Au and Ir-Ni.

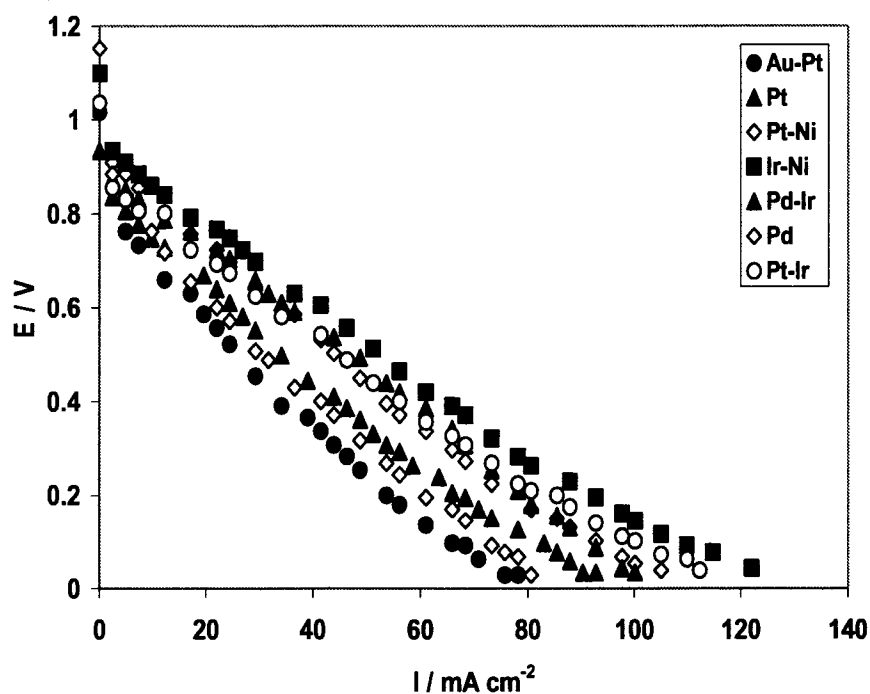


Fig. 4.6.6. Direct borohydride fuel cell polarization curves at 298 K: Comparison between the colloidal catalysts. Anode catalyst load  $5 \text{ mg cm}^{-2}$ .  $85 \text{ ml min}^{-1}$   $2 \text{ M NaBH}_4 - 2 \text{ M NaOH}$ . Cathode catalyst (Pt) load  $4 \text{ mg cm}^{-2}$ .  $\text{O}_2$  flow rate  $200 \text{ ml min}^{-1}$  at  $2.7 \text{ atm}$ .

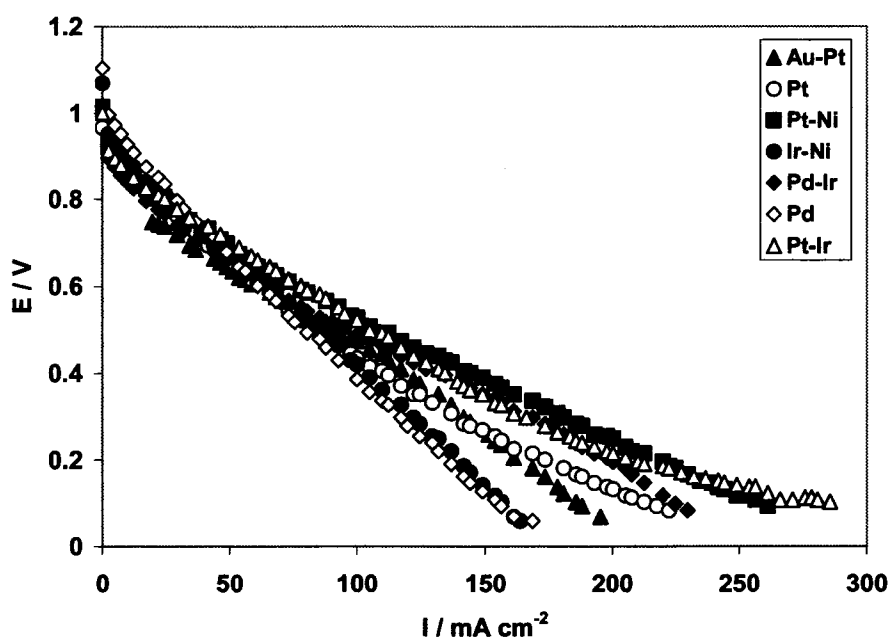


Fig. 4.6.7. Direct borohydride fuel cell polarization curves at 333 K: Comparison between the colloidal catalysts. Anode catalyst load  $5 \text{ mg cm}^{-2}$ .  $85 \text{ ml min}^{-1}$   $2 \text{ M NaBH}_4 - 2 \text{ M NaOH}$ . Cathode catalyst (Pt) load  $4 \text{ mg cm}^{-2}$ .  $\text{O}_2$  flow rate  $200 \text{ ml min}^{-1}$  at  $2.7 \text{ atm}$ .

#### 4.6.6. Summary

In summary, Ir-Ni and Pd-Ir showed the highest electroactivity. The optimum Tafel slope ranking for the best four catalysts was Ir-Ni < Pt-Ni < Ir-Pd < Pt-Ir, while the exchange current densities ranking was Pd-Ir > Ir-Ni > Pt-Ir > Pt-Ni. This supports the idea that a lower Tafel slope and a higher exchange current density are required for an electrocatalyst to show a good activity for a specific reaction. The heterogeneous rate constant was found to be the highest for Pt-Ir and Ir-Pd followed by Pt-Ni and Ir-Ni. The difference in their rate constants, (assuming a constant particle size), is due to the interactions between both the supported alloying elements themselves and with the conductive support that can lead to changes in the metal-metal distance (i.e, decreasing the distance leads to an enhanced close proximity catalyst action), changes in the surface structure, and changes in the surface electronic structure (i.e., an increase in the metal(s) d-electron vacancies is favorable for adsorption controlled processes). Fuel cell tests showed that they almost had comparable performance characteristics. All these anode electrocatalysts showed superior performance compared to the commercial Pt-Ru catalyst.



## 4.7. Effect of Titanium Dioxide Addition

In attempt to see the effect of a promoter such as  $TiO_2$  on the reactivity of Pt, Pd, and Ir toward the oxidation of  $NaBH_4$ , a laboratory-made support of 10wt%  $TiO_2$ -90% C-black was prepared and the performance compared to the standard C-black support.

### 4.7.1. Voltammetry of borohydride oxidation on static electrodes

Figures 4.7.1-4.7.3, 4.2.1, 4.5.1, and 4.4.1 compare the linear voltammograms for static electrodes for colloidal Pt/(C+ $TiO_2$ ), Pd/(C+ $TiO_2$ ), Ir/(C+ $TiO_2$ ), Pt/(C), Pd/(C), and Ir/(C), respectively. In all cases the voltammograms have been recorded at a constant scan rate of  $100 \text{ mV s}^{-1}$  as a function of increasing  $NaBH_4$  concentration (between 0.03 and 1 M).

On Pt, the addition of  $TiO_2$  shifts the second oxidation potential to a more negative value, i.e., from between 0 and +0.3 V to between -0.25 and 0 V vs. MOE. The addition of  $TiO_2$  has no influence on first oxidation potential peak, around -0.85 V vs. MOE (Fig. 4.7.1). The peak current is increased by around 15% in the case of Pt.

Similarly for Pd, the presence of  $TiO_2$  shifts the oxidation potential to a more negative value, i.e., from around 0 V to between -0.14 and 0 V vs. MOE (Fig. 4.7.2), while the peak current remains almost the same as for Pd/C.

On the other hand for Ir, there is a negative effect when  $TiO_2$  is added to the C-Black support. Although the second oxidation peak is shifted to a more negative value (from between -0.25 and -0.1 to around -0.3 V vs. MOE), the peak current drops dramatically by a factor of 3.2 (Fig. 4.7.3). These effects could be attributed to the change in the surface electronic structure due to the addition of the promoter  $TiO_2$  [10, 11, 46-49].

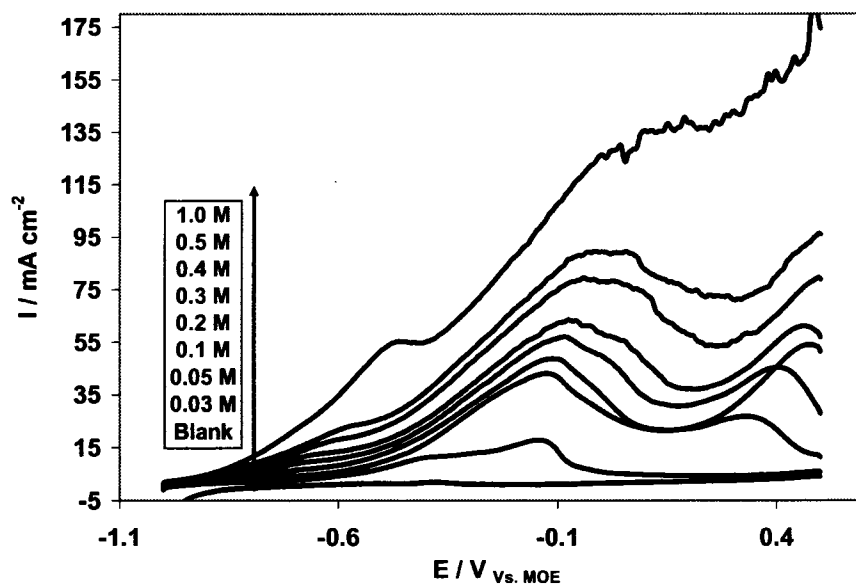


Fig. 4.7.1. Linear voltammogram of  $\text{BH}_4^-$  oxidation on colloidal Pt catalyst using a static electrode showing the effect of  $\text{BH}_4^-$  concentration: The colloidal supported on 90wt% C-Black and 10wt%  $\text{TiO}_2$ . Scan rate  $100 \text{ mV s}^{-1}$ , 298 K. Inset legend indicates the  $\text{NaBH}_4$  concentration in 2 M NaOH.

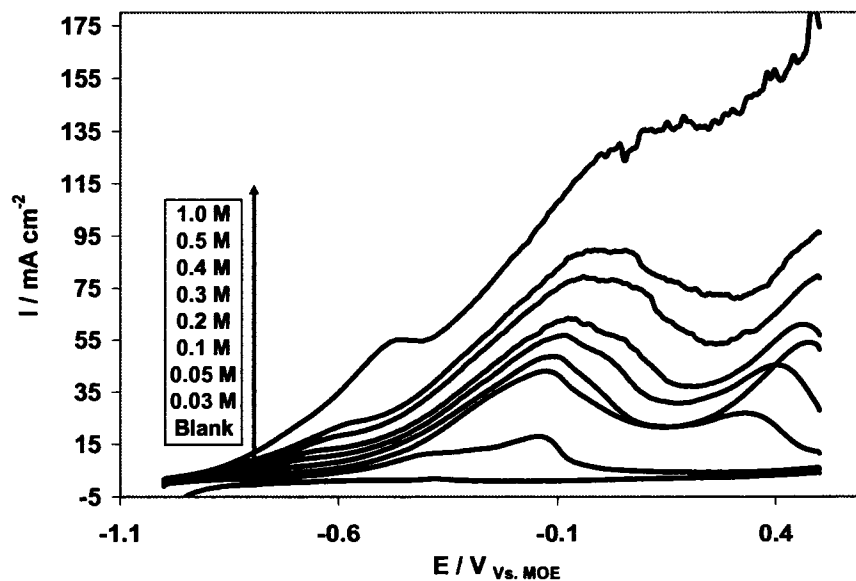


Fig. 4.7.2. Linear voltammogram of  $\text{BH}_4^-$  oxidation on colloidal Pd catalyst using a static electrode showing the effect of  $\text{BH}_4^-$  concentration: The colloidal supported on 90wt% C-Black and 10wt%  $\text{TiO}_2$ . Scan rate  $100 \text{ mV s}^{-1}$ , 298 K. Inset legend indicates the  $\text{NaBH}_4$  concentration in 2 M NaOH.

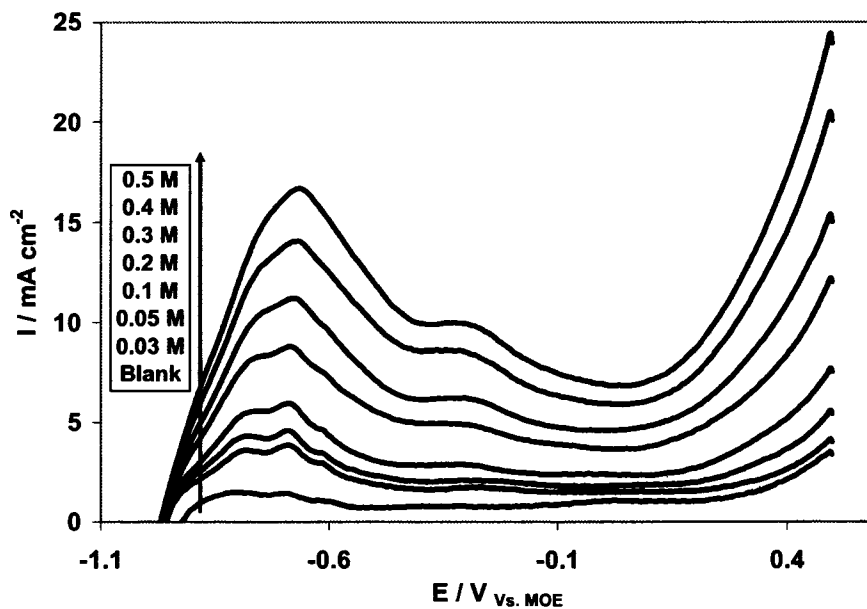


Fig. 4.7.3. Linear voltammogram of  $\text{BH}_4^-$  oxidation on colloidal Ir catalyst using a static electrode showing the effect of  $\text{BH}_4^-$  concentration: The colloidal supported on 90wt% C-Black and 10wt%  $\text{TiO}_2$ . Scan rate  $100 \text{ mV s}^{-1}$ , 298 K. Inset legend indicates the  $\text{NaBH}_4$  concentration in 2 M NaOH.

Figures 4.7.4-4.7.6 show the concentration dependence of the peak current density of Pt/(C-Black) and Pt/(C-Black+ $\text{TiO}_2$ ), Pd/(C-Black) and Pd/(C-Black+ $\text{TiO}_2$ ), and Ir/(C-Black) and Ir/(C-Black+ $\text{TiO}_2$ ) catalysts, respectively. The peak potential ranges were; Pt/(C-Black+ $\text{TiO}_2$ ) (-0.255 to 0.03 V), Pd/(C-Black+ $\text{TiO}_2$ ) (-0.14 to 0.15 V), and Ir/(C-Black+ $\text{TiO}_2$ ) (-0.7 to -0.63 V). It can be clearly seen that the peak current density increases linearly with concentration regardless of whether the support is (C-Black) or (C-Black+ $\text{TiO}_2$ ).

The slope of the linear dependence between peak current density and concentration on Pt/(C-Black+ $\text{TiO}_2$ ) was slightly higher than the values obtained on Pt/(C-Black). On Pd/(C-Black+ $\text{TiO}_2$ ) the trend of the curve was almost same as that of Pd/(C-Black) in that there was a change in slope at about 0.05 M  $\text{NaBH}_4$  concentration. This could be due to the change in the number of the electrons transferred during the oxidation process. On Ir/(C-Black+ $\text{TiO}_2$ ), on other hand, the value has dropped by half compared to that on Ir/(C-Black). Thus, according to eq. 4.2.2, it is expected that the number of electrons transferred will be affected.

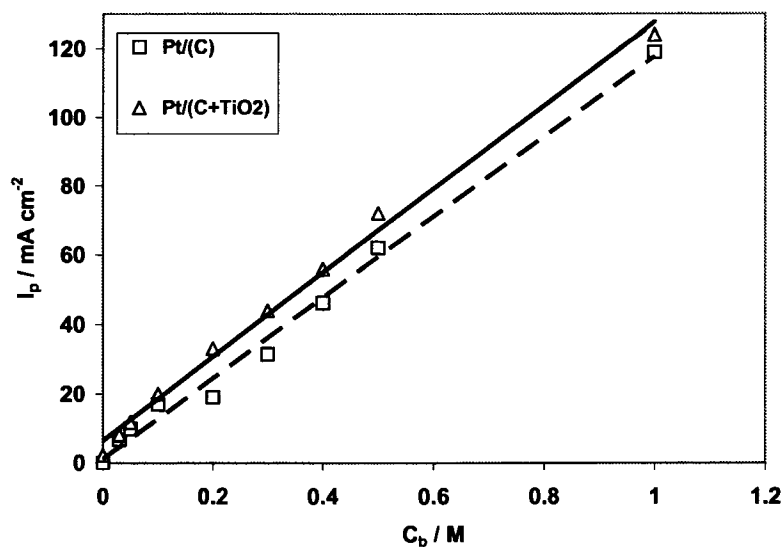


Fig. 4.7.4. The concentration dependence of the peak current density on colloidal Pt/(C-Black) and Pt/(C-Black+TiO<sub>2</sub>) catalysts. Scan rate 100 mV s<sup>-1</sup>, 298 K.

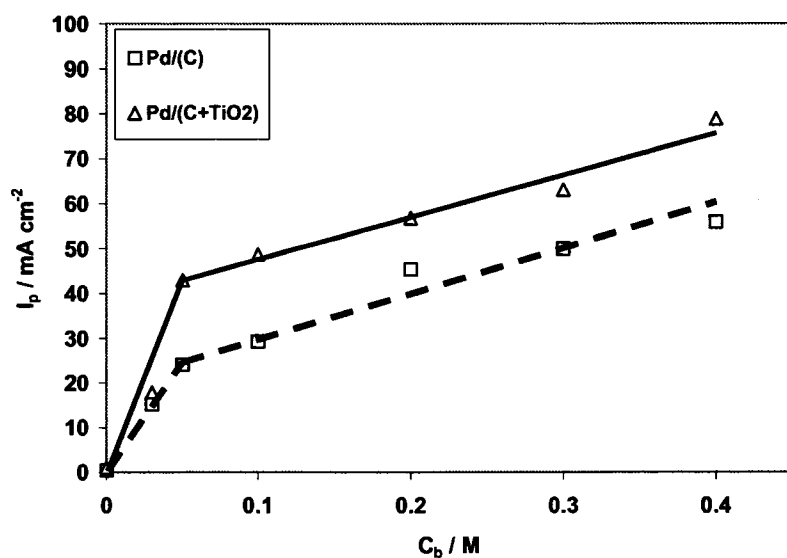


Fig. 4.7.5. The concentration dependence of the peak current density on colloidal Pd/(C-Black) and Pd/(C-Black+TiO<sub>2</sub>) catalysts. Scan rate 100 mV s<sup>-1</sup>, 298 K.

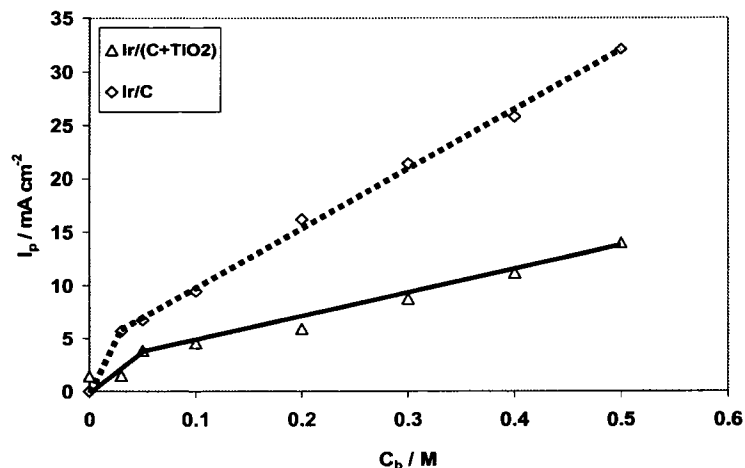


Fig. 4.7.6. The concentration dependence of the peak current density on colloidal Ir/(C-Black) and Ir/(C-Black+TiO<sub>2</sub>) catalysts. Scan rate 100 mV s<sup>-1</sup>, 298 K.

The scan rate dependence of linear voltammograms, in the range between 5 to 500 mV s<sup>-1</sup> at 0.03 M NaBH<sub>4</sub> concentration, on static electrodes for colloidal Pt/(C-Black+TiO<sub>2</sub>), Pd/(C-Black+TiO<sub>2</sub>), Ir/(C-Black+TiO<sub>2</sub>), Pt/(C-Black), Pd/(C-Black), and Ir/(C-Black) catalysts is shown in Figures 4.7.7-4.7.9, 4.2.9, 4.5.5, and 4.4.6, respectively. It is obvious from these figures that the oxidation peak potentials are slightly shifted to a more positive value with scan rate due to the TiO<sub>2</sub> addition.

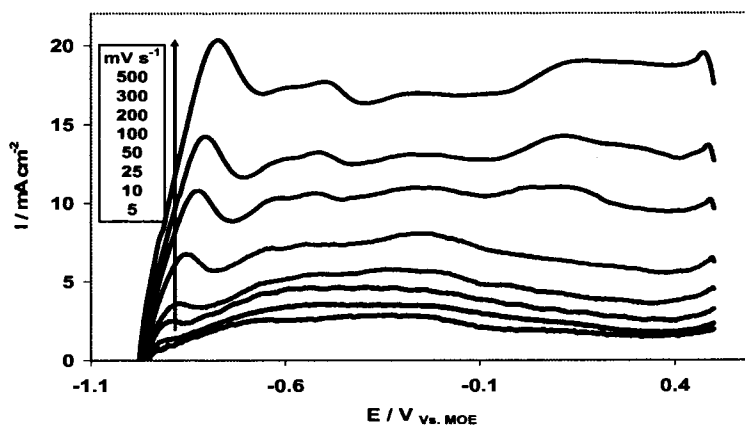


Fig. 4.7.7. Linear voltammogram of BH<sub>4</sub><sup>-</sup> oxidation on colloidal Pt catalyst using a static electrode showing the effect of scan rate: The colloidal supported on 90wt% C-Black and 10wt% TiO<sub>2</sub>. NaBH<sub>4</sub> concentration 0.03 M, 298 K. Inset legend indicates the scan rate.

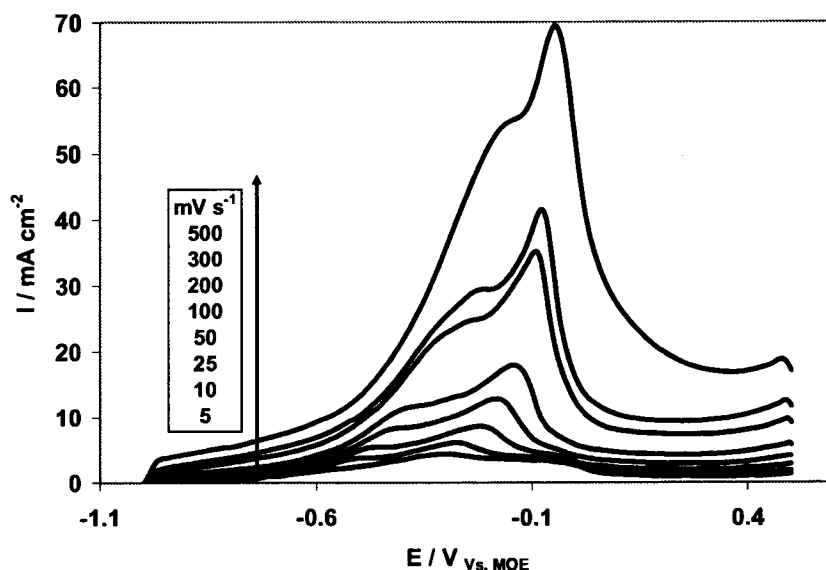


Fig. 4.7.8. Linear voltammogram of  $\text{BH}_4^-$  oxidation on colloidal Pd catalyst using a static electrode showing the effect of scan rate: The colloidal supported on 90wt% C-Black and 10wt%  $\text{TiO}_2$ .  $\text{NaBH}_4$  concentration 0.03 M, 298 K. Inset legend indicates the scan rate.

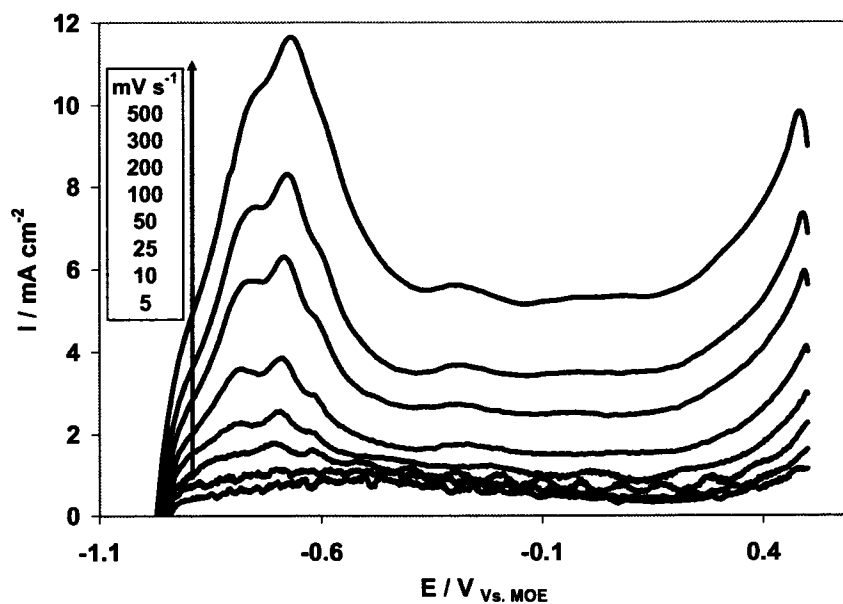


Fig. 4.7.9. Linear voltammogram of  $\text{BH}_4^-$  oxidation on colloidal Ir catalyst using a static electrode showing the effect of scan rate: The colloidal supported on 90wt% C-Black and 10wt%  $\text{TiO}_2$ .  $\text{NaBH}_4$  concentration 0.03 M, 298 K. Inset legend indicates the scan rate.

Figs. 4.7.10-4.7.12 show that the peak current density increased linearly with the square root of scan rate for all the investigated catalysts at a constant  $\text{NaBH}_4$  concentration of 0.03 M. The peak potential ranges were; Pt/(C-Black+ $\text{TiO}_2$ ) (-0.40 to -0.18 V), Pd/(C-Black+ $\text{TiO}_2$ ) (-0.30 to -0.4 V), and Ir/(C-Black+ $\text{TiO}_2$ ) ( $\sim$  -0.70 V). The  $I_p$  vs.  $v^{1/2}$  slope has increased due to the  $\text{TiO}_2$  addition in the case of both Pt and Pd, while it has decreased in case of Ir. Moreover, in the case of Pd, the change in slope of the  $I_p$  vs.  $v^{1/2}$  plot has shifted from the 50 to the 100 to  $\text{mV s}^{-1}$  scan rate, due to the  $\text{TiO}_2$  addition. Accordingly, the adsorption effect has shifted. Such an increase at high scan rates indicates that adsorption has an effect on the voltammetry response [6, 16, 17-22].

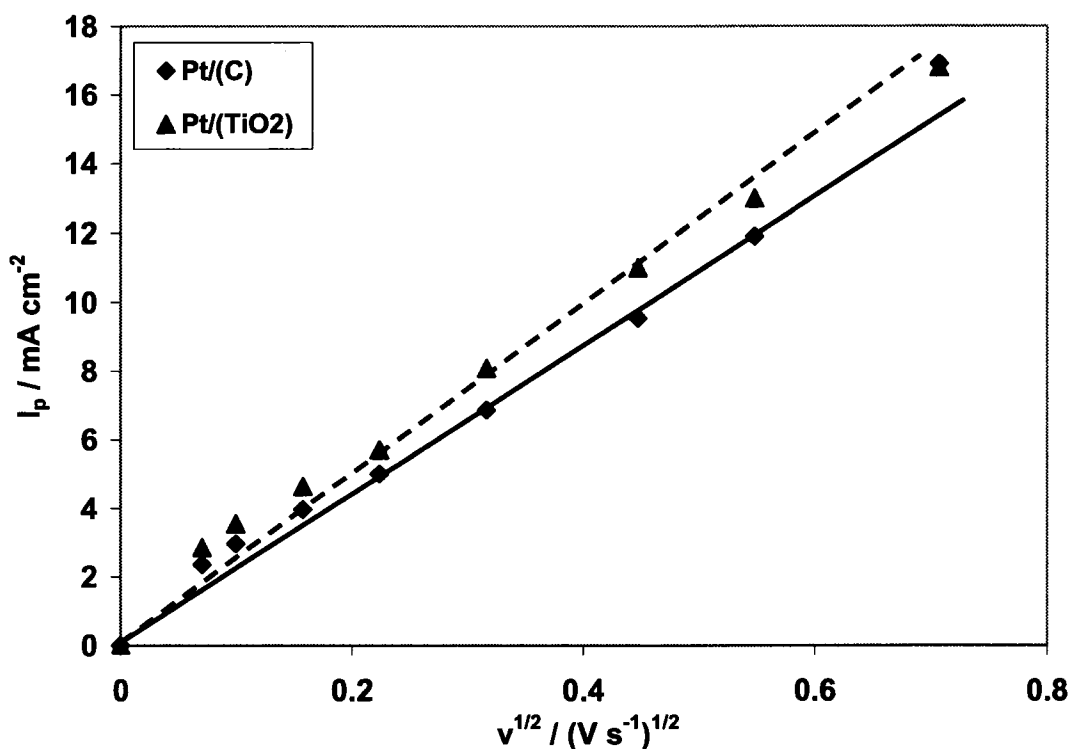


Fig. 4.7.10. The scan rate dependence of the peak current densities obtained on the colloidal Pt/(C-Black) and Pt/(C-Black+  $\text{TiO}_2$ ) catalysts:  $\text{NaBH}_4$  concentration 0.03 M, 298 K.

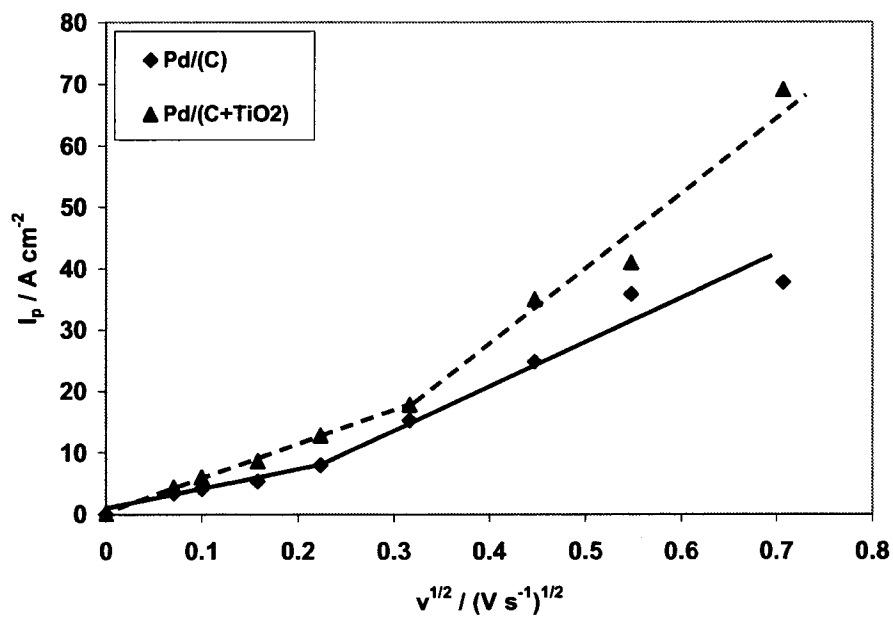


Fig. 4.7.11. The scan rate dependence of the peak current densities obtained on the colloidal Pd/(C-Black) and Pd/(C-Black+ TiO<sub>2</sub>) catalysts: NaBH<sub>4</sub> concentration 0.03 M, 298 K.

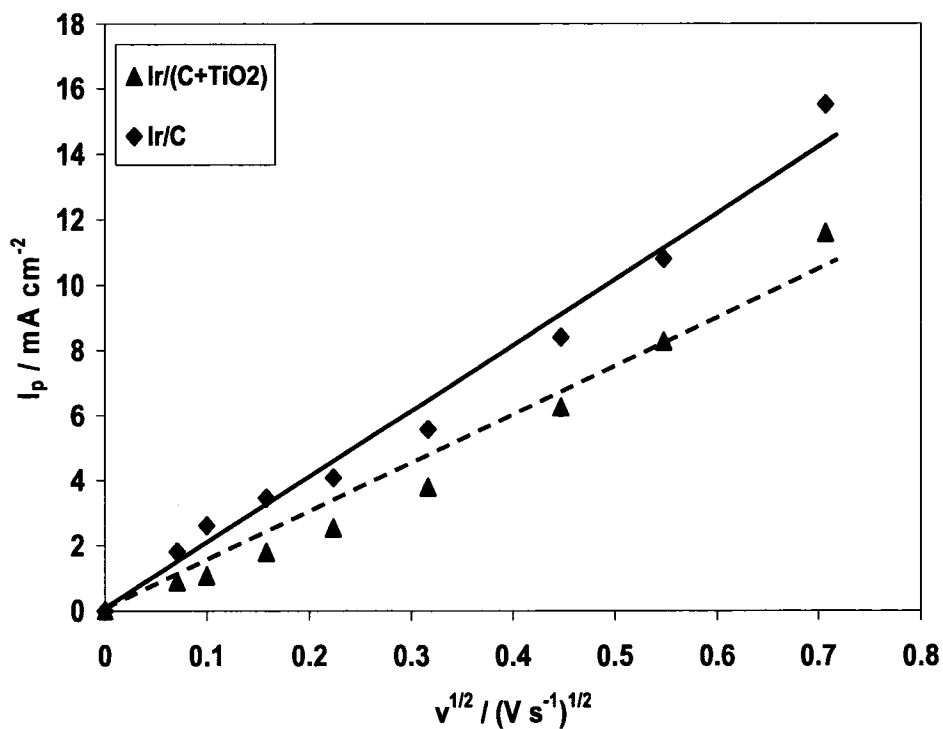


Fig. 4.7.12. The scan rate dependence of the peak current densities obtained on the colloidal Ir/(C-Black) and Ir/(C-Black+ TiO<sub>2</sub>) catalysts: NaBH<sub>4</sub> concentration 0.03 M, 298 K.



#### 4.7.2. Voltammetry of borohydride oxidation on rotating electrodes

The RDE results for colloidal Pt/(C-Black+TiO<sub>2</sub>), Pd/(C-Black+TiO<sub>2</sub>), Ir/(C-Black+TiO<sub>2</sub>), Pt/(C-Black), Pd/(C-Black), and Ir/(C-Black) catalysts are shown in Figures 4.7.13-4.7.15, 4.2.15, 4.5.9, and 4.4.11, respectively. The scan rate was 5 mV s<sup>-1</sup> in all cases, while the rotation speed range was between 500 and 3,000 rotations per minute (rpm). The BH<sub>4</sub><sup>-</sup> concentration was constant at 0.3 M. Again, a strong temperature effect and a weak rotation speed effect can be clearly seen.

On Pt and Pd, the TiO<sub>2</sub> addition slightly increases the peak current, but did not cause a change in the oxidation potential (Fig. 4.7.13 and 4.7.14). On Ir, on the other hand, the potential has shifted to a more positive value and the peak current is lowered due to the TiO<sub>2</sub> addition.

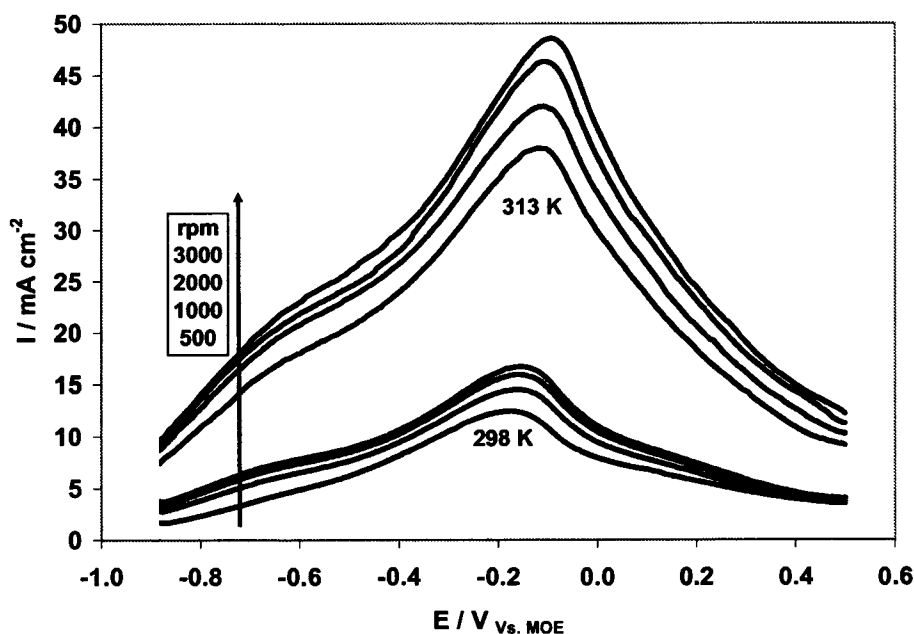


Fig. 4.7.13. Linear voltammetry of BH<sub>4</sub><sup>-</sup> oxidation on colloidal Pt catalysts using a rotating electrode showing the effect of rotation speed and temperature. The colloidal supported on 90wt% C-Black and 10wt% TiO<sub>2</sub>. Scan rate 5 mV s<sup>-1</sup>, 298 K and 313 K. NaBH<sub>4</sub> concentration 0.3 M in 2 M NaOH. Inset legend indicates the rotation speed per minute.

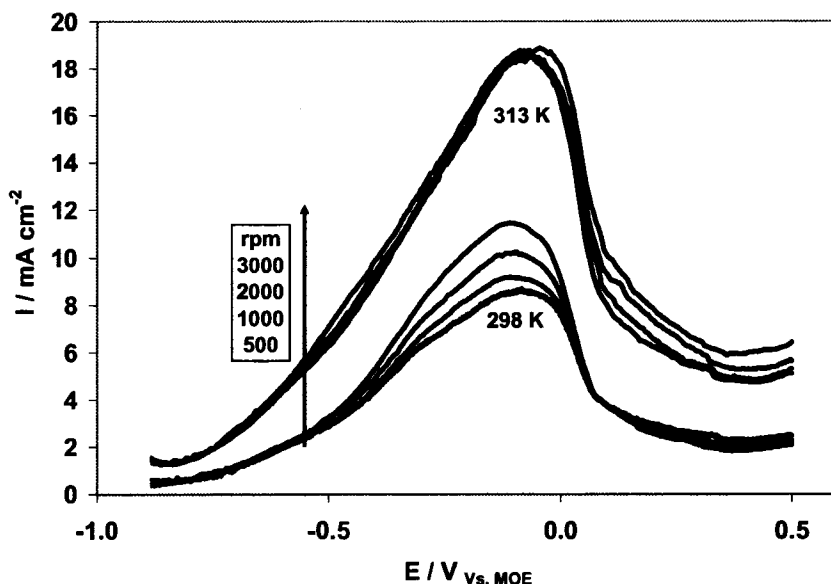


Fig. 4.7.14. Linear voltammetry of  $\text{BH}_4^-$  oxidation on colloidal Pd catalysts using a rotating electrode showing the effect of rotation speed and temperature. The colloidal supported on 90wt% C-Black and 10wt%  $\text{TiO}_2$ . Scan rate  $5 \text{ mV s}^{-1}$ , 298 K and 313 K.  $\text{NaBH}_4$  concentration 0.3 M in 2 M NaOH. Inset legend indicates the rotation speed per minute.

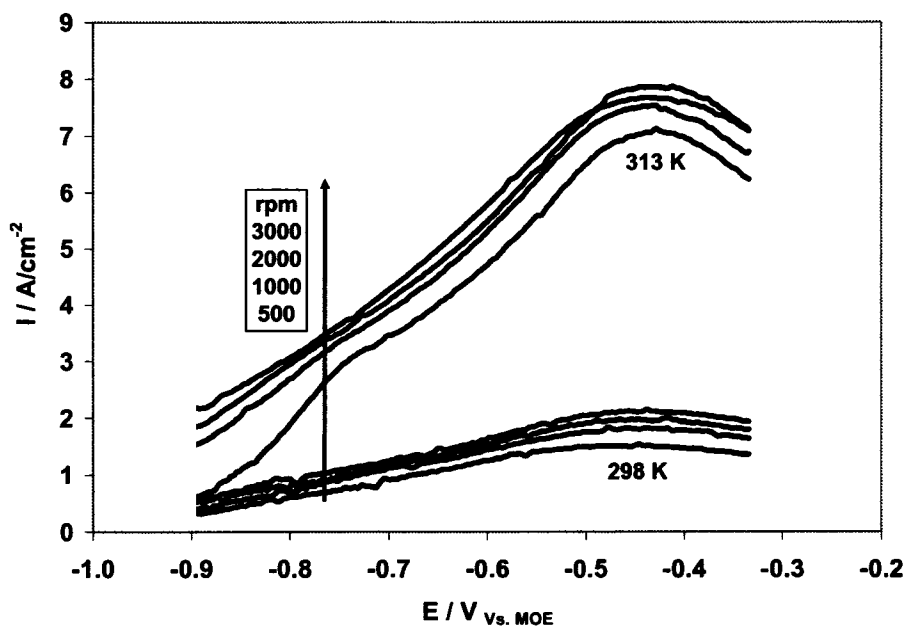


Fig. 4.7.15. Linear voltammetry of  $\text{BH}_4^-$  oxidation on colloidal Ir catalysts using a rotating electrode showing the effect of rotation speed and temperature. The colloidal supported on 90wt% C-Black and 10wt%  $\text{TiO}_2$ . Scan rate  $5 \text{ mV s}^{-1}$ , 298 K and 313 K.  $\text{NaBH}_4$  concentration 0.3 M in 2 M NaOH. Inset legend indicates the rotation speed per minute.

### Tafel slopes and the exchange current densities

The Tafel plots of  $\log i$  vs.  $\eta (= E - E_{oc})$  were made using the rising domain of Figs. 4.7.13-4.7.15 and are shown in Figs. 4.7.16-4.7.18.

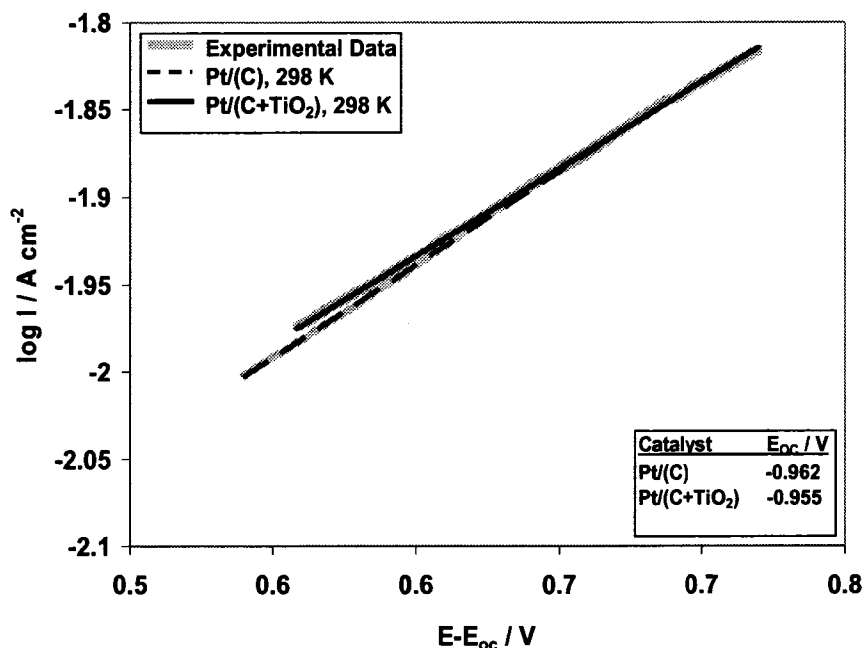


Fig. 4.7.16. Tafel plots for the supported colloidal Pt/(C-Black) and Pt/(C-Black+ TiO<sub>2</sub>) catalysts generated from the rotating disk electrode data. 298 K.

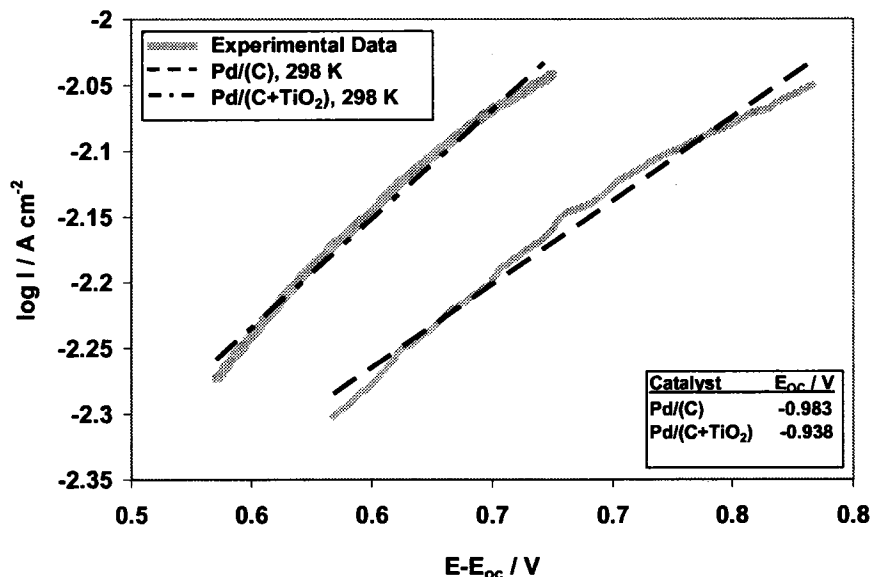


Fig. 4.7.17. Tafel plots for the supported colloidal Pd/(C-Black) and Pd/(C-Black+ TiO<sub>2</sub>) catalysts generated from the rotating disk electrode data. 298 K.

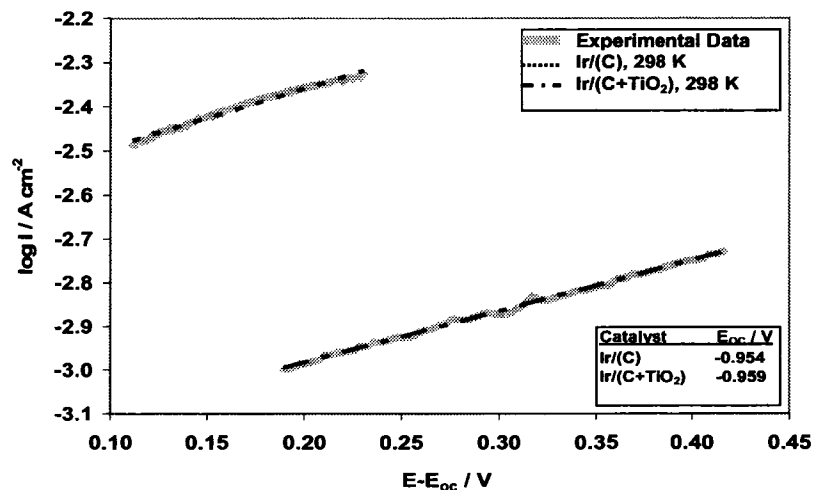


Fig. 4.5.18. Tafel plots for the supported colloidal Ir/(C-Black) and Ir/(C-Black+ TiO<sub>2</sub>) catalysts generated from the rotating disk electrode data. 298 K.

Table 4.7.1 summarizes the apparent Tafel slopes  $b_a$ , exchange current density  $i_{0,a}$ , and number of electrons transferred  $n$ , for Pt/(C-Black) and Pt/(C-Black+TiO<sub>2</sub>), Pd/(C-Black) and Pd/(C-Black+TiO<sub>2</sub>), and Ir/(C-Black) and Ir/(C-Black+TiO<sub>2</sub>) catalysts at 298 K. It can be clearly seen that the addition of TiO<sub>2</sub> has decreased the  $b_a$  value in the case of Pd and increased that of Pt and Ir, while  $i_{0,a}$  has slightly increased for Pt, slightly decreased for Pd, and significantly decreased for Ir.

Using the  $b_a$  values from Table 4.7.1 in conjunction with eq. (4.2.2), the number of electrons involved in the borohydride oxidation can be determined assuming that on pure Pt  $n$  is equal to 4 [6, 15]. For Pt, the TiO<sub>2</sub> addition has slightly increased the number of electrons transferred, while for Pd it has slightly decreased  $n$ , and for Ir has significantly decreased  $n$ .

Table 4.7.1. Apparent Tafel slopes, exchange current densities, total number of electrons exchanged,  $n$ , determined from RDE data using supported colloidal catalysts on Carbon and on Carbon+TiO<sub>2</sub> with Nafion 117 polymer electrolyte. Eq. (4.2.2) was used to calculate  $n$ .

Catalysts	$b_a$ (V dec <sup>-1</sup> ) 298 K	$i_{0,a}$ (A cm <sup>-2</sup> ) 298 K	$n$
Pd/C	0.787	$0.939 \times 10^{-3}$	4.5
Pd/C+TiO <sub>2</sub>	0.603	$0.70 \times 10^{-3}$	4.0
Pt/C	0.939	$2.64 \times 10^{-3}$	4.0
Pt/C+TiO <sub>2</sub>	1.00	$2.95 \times 10^{-3}$	4.3
Ir/C	0.755	$2.37 \times 10^{-3}$	1.5
Ir/C+TiO <sub>2</sub>	0.853	$0.60 \times 10^{-3}$	0.8

### 4.7.3. Chronopotentiometry

Figures 4.7.19-4.7.21 show the anode potentials and the open circuit values for the Pt/(C-Black) and Pt/(C-Black+TiO<sub>2</sub>), Pd/(C-Black) and Pd/(C-Black+TiO<sub>2</sub>), and Ir/(C-Black) and Ir/(C-Black+TiO<sub>2</sub>) catalysts operating at 10 mA cm<sup>-2</sup> and 298 K. It can be clearly seen that the overpotentials (=  $E - E_{oc}$ ) were affected by the addition of TiO<sub>2</sub>. The highest impact was on Pt where the overpotential about was 402 mV in contrast to the value of 640 mV in the absence of TiO<sub>2</sub> (Fig. 4.7.19). On Pd and Ir, on the other hand, the overpotential was increased slightly for Pd and significantly for Ir (Figs. 4.7.20 and 4.7.21).

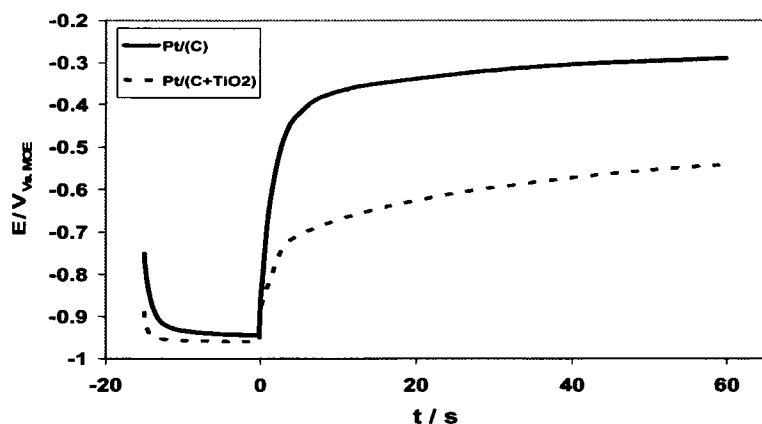


Fig. 4.7.19. Chronopotentiometry of BH<sub>4</sub><sup>-</sup> oxidation on colloidal Pt/(C-Black) and Pt/(C-Black+ TiO<sub>2</sub>) catalysts. Current step: from 0 to 10 mA cm<sup>-2</sup>. 0.5 M NaBH<sub>4</sub> in 2 M NaOH. 298 K.

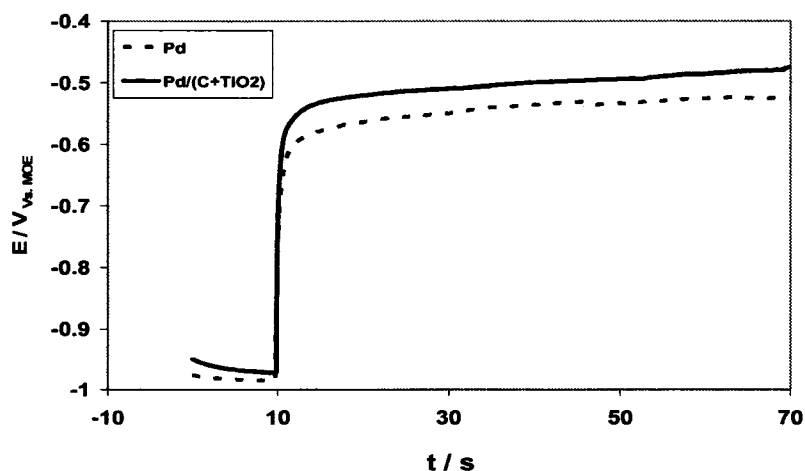


Fig. 4.7.20. Chronopotentiometry of BH<sub>4</sub><sup>-</sup> oxidation on colloidal Pd/(C-Black) and Pd/(C-Black+ TiO<sub>2</sub>) catalysts. Current step: from 0 to 10 mA cm<sup>-2</sup>. 0.5 M NaBH<sub>4</sub> in 2 M NaOH. 298 K.

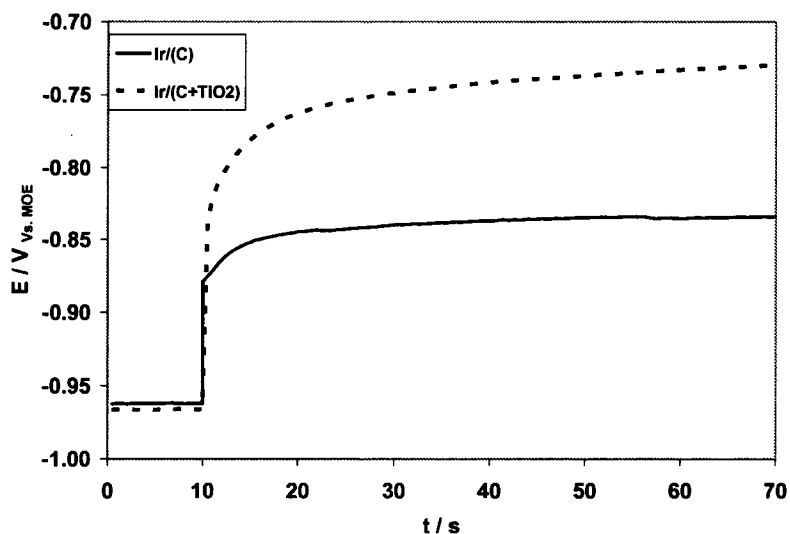


Fig. 4.7.21. Chronopotentiometry of  $\text{BH}_4^-$  oxidation on colloidal Ir/(C-Black) and Ir/(C-Black+  $\text{TiO}_2$ ) catalysts. Current step: from 0 to 10  $\text{mA cm}^{-2}$ . 0.5 M  $\text{NaBH}_4$  in 2 M  $\text{NaOH}$ . 298 K.

#### 4.7.4. Chronoamperometry and chronocoulometry

Figures 4.7.22-4.7.24 give the superficial current density transients for a step change from -0.9 V to 0.2 V vs. MOE on Pt/(C-Black) and Pt/(C-Black+ $\text{TiO}_2$ ), Pd/(C-Black) and Pd/(C-Black+ $\text{TiO}_2$ ), and Ir/(C-Black) and Ir/(C-Black+ $\text{TiO}_2$ ) catalysts, respectively. The superficial current density has increased significantly due to the  $\text{TiO}_2$  addition on Pt, decreased significantly on Ir, and remains unchanged on Pd.

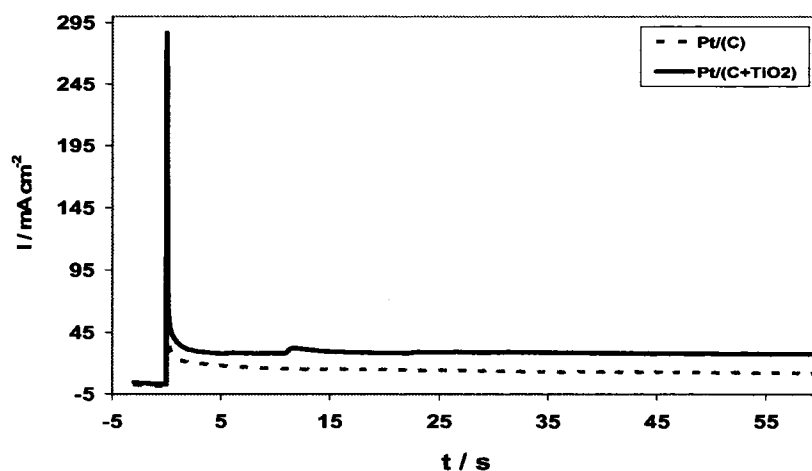


Fig. 4.7.22. Chronoamperometry of  $\text{BH}_4^-$  oxidation on Pt/(C-Black) and Pt/(C-Black+  $\text{TiO}_2$ ) catalysts. Potential steps from -0.9 V to -0.2 V vs. MOE. 0.5 M  $\text{NaBH}_4$  in 2 M  $\text{NaOH}$ . 298 K.

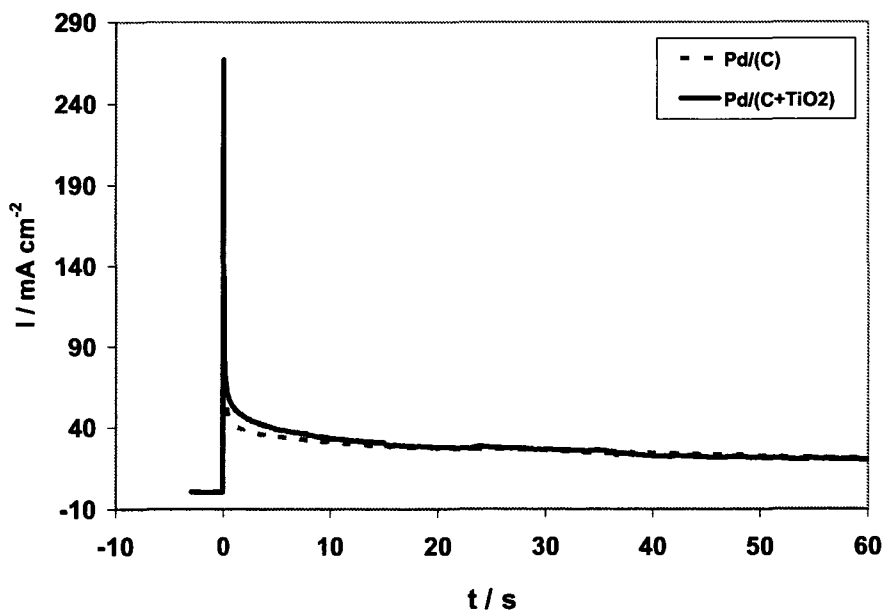


Fig. 4.7.23. Chronoamperometry of  $\text{BH}_4^-$  oxidation on Pd/(C-Black) and Pd/(C-Black+TiO<sub>2</sub>) catalysts. Potential steps from -0.9 V to -0.2 V vs. MOE. 0.5 M NaBH<sub>4</sub> in 2 M NaOH. 298 K.

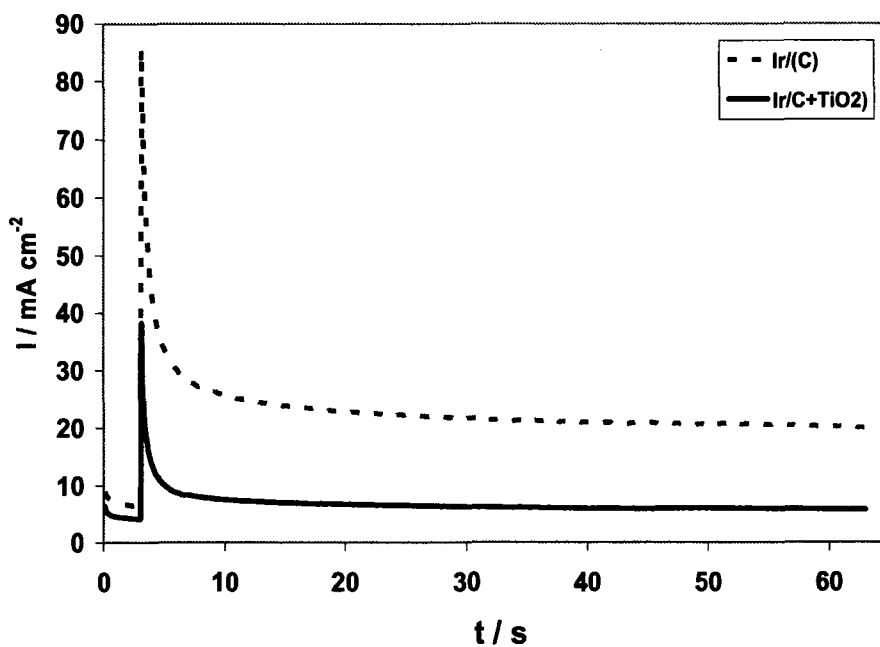


Fig. 4.7.24. Chronoamperometry of  $\text{BH}_4^-$  oxidation on colloidal Ir/(C-Black) and Ir/(C-Black+TiO<sub>2</sub>) catalysts. Potential steps from -0.9 V to -0.2 V vs. MOE. 0.5 M NaBH<sub>4</sub> in 2 M NaOH. 298 K.

### Cottrell Plot

Figures 4.7.25-4.7.27 show the Cottrell plots of  $i \cdot \sqrt{t}$  vs.  $t$  for Pt/(C-Black+TiO<sub>2</sub>), Pd/(C-Black+TiO<sub>2</sub>), and Ir/(C-Black+TiO<sub>2</sub>) catalysts, respectively. A non Cottrellian response (i.e. not purely diffusion controlled) is obvious for all cases, since  $It^{1/2}$  is not a constant value. For Ir, the TiO<sub>2</sub> addition has no effect compare to the Ir/C-Black (Figs. 4.7.27 and 4.4.25-4.4.27). For Pt has a significant impact for all potential steps compare to Pt/C-Black (Figs. 4.7.25 and 4.2.27-4.2.29). For Pd, on the other hand, the addition has affected the responses of -0.4 V and -0.6 V step changes in comparison with the response on Pd/C-Black (Figs. 4.7.26 and 4.5.25-4.5.27).

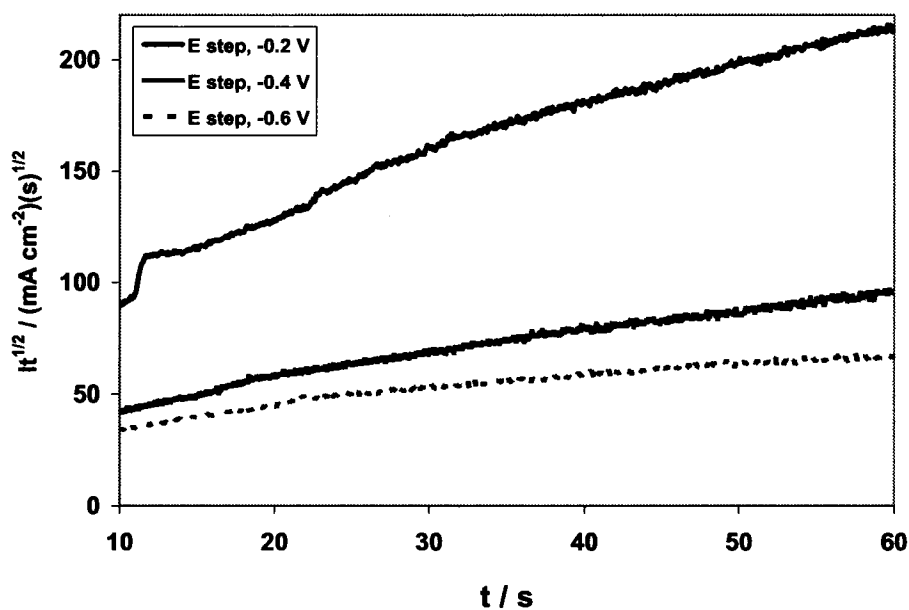


Fig. 4.7.25. Cottrell plot generated from the chronoamperometry data for colloidal Pt catalyst supported on 90wt% C-black and 10wt% TiO<sub>2</sub>. Potential steps from -0.9 V vs. MOE to -0.6, -0.4 and -0.2 V vs. MOE.



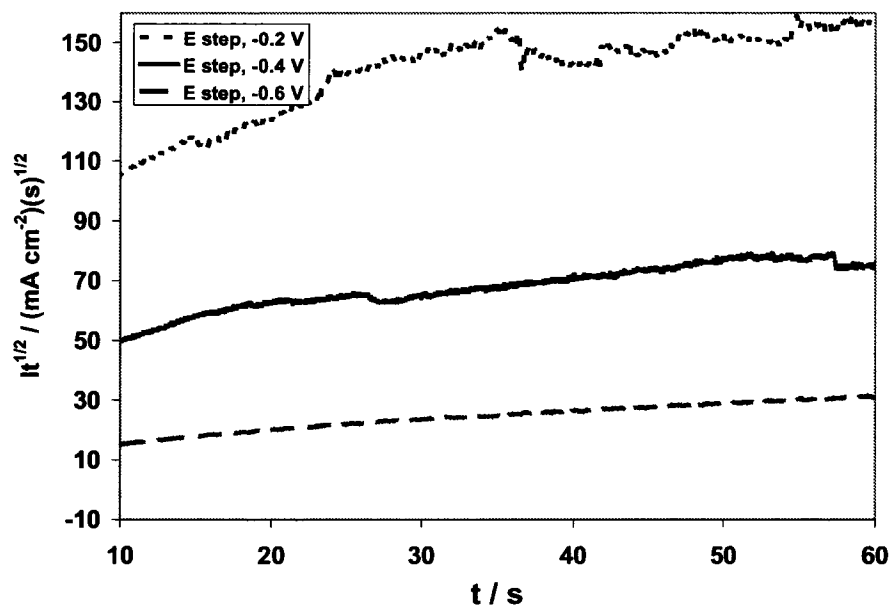


Fig. 4.7.26. Cottrell plot generated from the chronoamperometry data for colloidal Pd catalyst supported on 90wt% C-black and 10wt%  $\text{TiO}_2$ . Potential steps from  $-0.9 \text{ V}$  vs. MOE to  $-0.6$ ,  $-0.4$  and  $-0.2 \text{ V}$  vs. MOE.

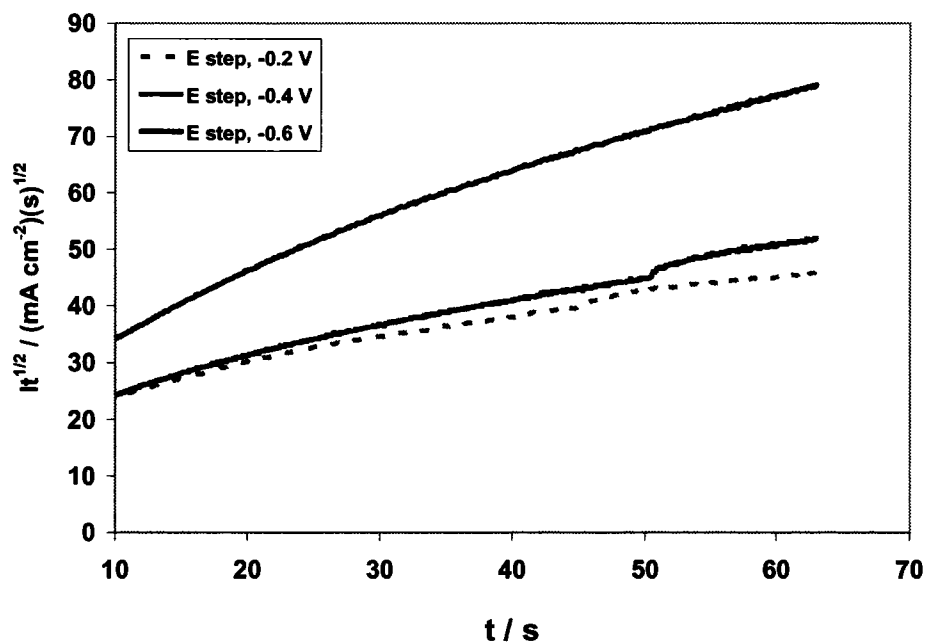


Fig. 4.7.27. Cottrell plot generated from the chronoamperometry data for colloidal Ir catalyst supported on 90wt% C-black and 10wt%  $\text{TiO}_2$ . Potential steps from  $-0.9 \text{ V}$  vs. MOE to  $-0.6$ ,  $-0.4$  and  $-0.2 \text{ V}$  vs. MOE.

### Chronocoulometry

Figures 4.7.28-4.7.30 show the Anson plots,  $Q$  vs.  $\sqrt{t}$ , obtained for the potential steps from  $-0.9$  V to  $-0.2$  V,  $-0.4$  V, and  $-0.6$  V vs. MOE, for Pt/(C-Black+TiO<sub>2</sub>), Pd/(C-Black+TiO<sub>2</sub>), and Ir/(C-Black+TiO<sub>2</sub>) catalysts respectively.

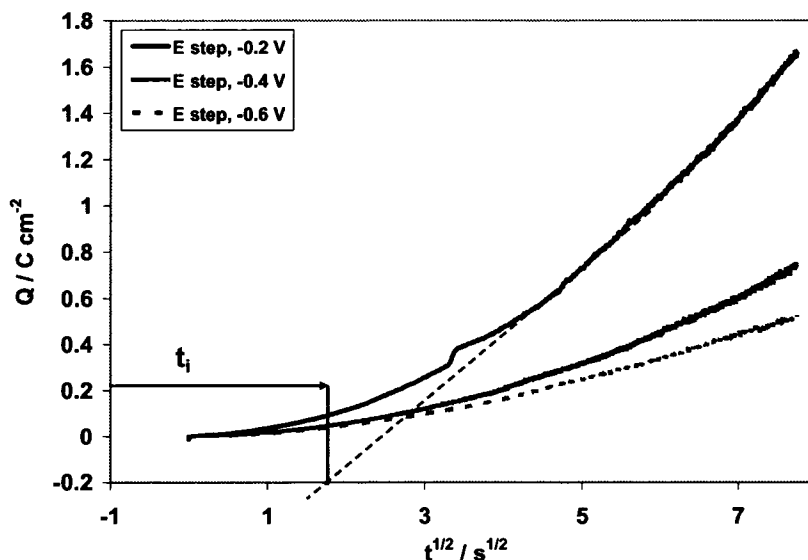


Fig. 4.7.28. Cumulative charge density as a function of square root of time (Anson plot) generated from the chronoamperometry data for colloidal Pt catalyst supported on 90wt% C-black and 10wt% TiO<sub>2</sub>. Potential steps from  $-0.9$  V vs. MOE to  $-0.6$ ,  $-0.4$  and  $-0.2$  V vs. MOE.

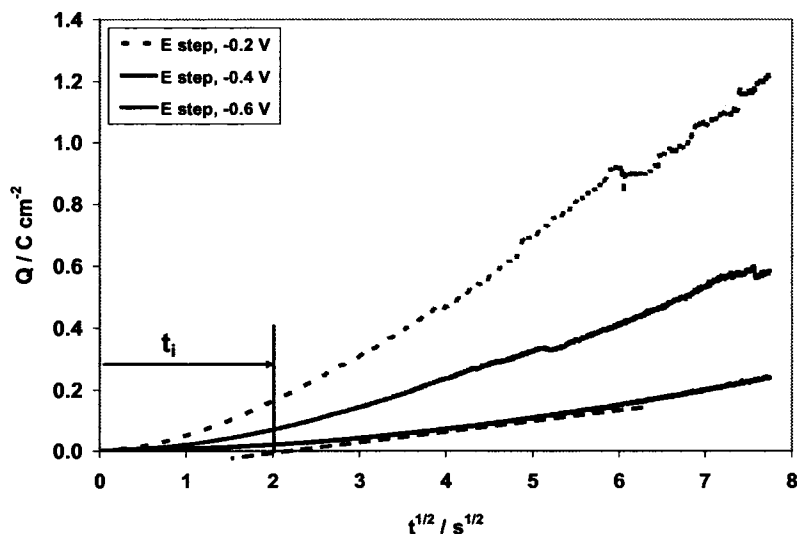


Fig. 4.7.29. Cumulative charge density as a function of square root of time (Anson plot) generated from the chronoamperometry data for colloidal Pd catalyst supported on 90wt% C-black and 10wt% TiO<sub>2</sub>. Potential steps from  $-0.9$  V vs. MOE to  $-0.6$ ,  $-0.4$  and  $-0.2$  V vs. MOE.

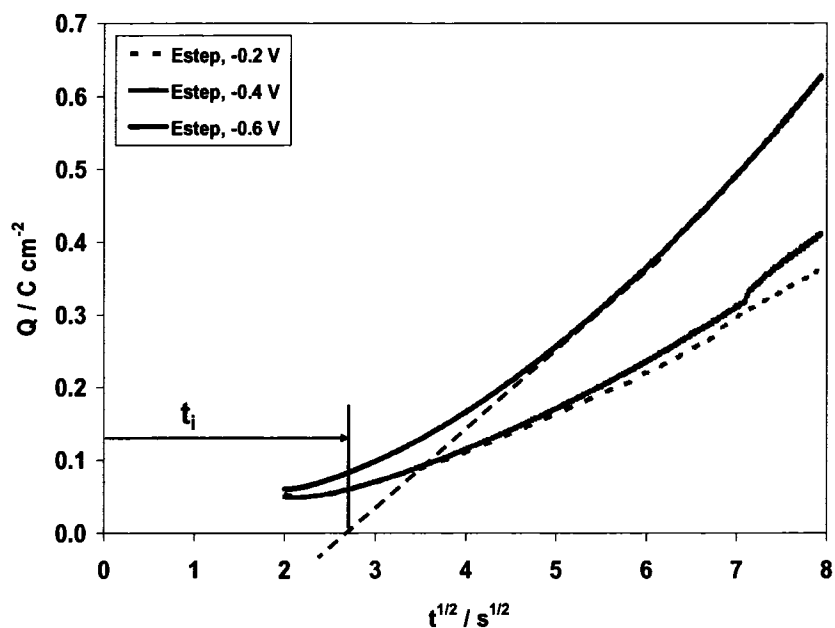


Fig. 4.7.30. Cumulative charge density as a function of square root of time (Anson plot) generated from the chronoamperometry data for colloidal Ir catalyst supported on 90wt% C-black and 10wt% TiO<sub>2</sub>. Potential steps from -0.9 V vs. MOE to -0.6, -0.4 and -0.2 V vs. MOE, respectively.

Again, by employing eqs.3.6.32 and 3.6.33 in conjunction with the extrapolation of the linear domain of these curves shown Figures 4.7.28-4.7.30 to  $Q = 0$ , the apparent heterogeneous rate constant  $k_h$  at -0.4 V can be determined [12]. Table 4.7.2 summarizes the  $k_h$  values at -0.4V at 298 K obtained from the slope of eq. (3.6.32) corresponding to the data from Figs. 4.7.28-4.7.30. The apparent heterogeneous rate constants for -0.4 V potential step show the following order of electrocatalytic activity: Ir/C > Ir/(C+TiO<sub>2</sub>) > Pd/(C+TiO<sub>2</sub>) > Pt/(C+TiO<sub>2</sub>) > Pd/C > Pt/C.

Table 4.7.2. Apparent heterogeneous rate constants for BH<sub>4</sub><sup>-</sup> oxidation at -0.4 V vs. MOE and 298 K calculated from chronocoulometry.

Catalyst	Pt/(C)	Pt/(C+TiO <sub>2</sub> )	Pd/(C)	Pd/(C+TiO <sub>2</sub> )	Ir/(C)	Ir/(C+TiO <sub>2</sub> )
$K_h$ (cm s <sup>-1</sup> )	5.84x10 <sup>-6</sup>	8.94x10 <sup>-6</sup>	6.72x10 <sup>-6</sup>	9.68x10 <sup>-6</sup>	35.5x10 <sup>-6</sup>	20.8x10 <sup>-6</sup>

It can be seen clearly from Table 4.7.2, that the addition of the promoter  $TiO_2$  has enhanced the heterogeneous rate constant for Pt and Pd significantly. This is in a good agreement with K-Minsker et al's [46] findings where the oxidation of propane was improved on Pt supported on  $TiO_2$  compared to pure Pt and Pt supported on other materials. It was also found by Eguchi et al [47], Widijaja et al [48], and Sekizawa et al [49] that supporting Pd on  $TiO_2$  enhanced methane oxidation in comparison with other supporting materials. However for Ir, the heterogeneous rate constant was decreased dramatically.

The surface electronic structure is highly affected by; the support type, add atom type and composition, and nanoparticle size [10-14]. Therefore, this could have contributed to the change in the electronic structure of the supported colloids due to the addition of such promoter, which in turn affects the catalytic activities of these colloids through changing (increasing or decreasing) the d-electron vacancies on the catalyst surfaces, which highly affects the reactants adsorption processes and their bonding energy to the catalyst's surface [10-14].

#### 4.7.5. Summary

In summary, a  $TiO_2$  addition to the support has a slightly positive impact on the activities of Pt and Pd, while it has a significant negative impact on the activity of Ir. CV studies showed an enhancement in the peak current of about 1.2 and 1.5 times in case of Pt and Pd, respectively, while a decrease of about 3.2 times was found in the case of Ir. This behaviour has been supported by the heterogeneous rate constant,  $k_h$ , calculations, where  $k_h$  was enhanced for Pt and Pd, respectively, but was decreased for Ir.

## 4.8. References

1. J. Kua and W.A. Goddard III, *J. Am. Chem. Soc.* 121 (1999) 10928-10941
2. G. Gökağaç and D.J. Kennedy, *Z. Naturforsch.* 57b (2002) 193-201.
3. J.T. Moore, D. Chu, R. Jiang, G.A. Deluga and C.M. Lukehart, *Chem. Mater.* 15 (2003) 1119-1124.
4. M. Pourbaix, *Atlas of Electrochemical Equilibria in Aqueous Solutions*, NACE, Houston (1974).
5. M. Yan, k. Liu, Z. Jiang, *J. Electroanal. Chem.* 408 (1996) 225-229.
6. E. Gyenge, *Electrochimica Acta* 49 (2004) 965-978.
7. B. Liu, Z. P. Li, S. Suda, *Electrochimica Acta*, 49 (2004) 3097-3105.
8. R. I. Masel, *Chemical Kinetics and Catalysis*, Wiley-Interscience, NY (2001) 689-755, 837-880, 667-743.
9. Y. Okinaka, *J. Electrochem. Soc.* 120 (1973) 739.
10. A. Wiekowski, E. Savinova, C. Vayenas, *Catalysis and Electrocatalysis at Nanoparticle Surfaces*, Marcel Dekkers Inc., NY (2003)
11. V. Ponec, *Applied Catalysis A: General*, 222 (2001) 31-45.
12. N. Toshima, T. Yonezawa, *New J. Chem.*, (1998) 1179-1201.
13. E. Antonlini, J. Salgado, M. Giz, E. Gonzalez, *Int. J. Hydrogen Energy*, 30 (2005) 1213-1220.
14. Yasuyuki Ishikawa, Meng-Sheng Liao and Carlos R. Cabrera, A theory-guided design of bimetallic nanoparticle catalysts for fuel cell applications, *Theor. Comput. Chem.*, 15, (2004) 325-365.
15. J. P. Elder, A. Hickling, *Trans. Faraday Soc.*, 58(1962)1852.
16. A.J. Bard and L. Faulkner, *Electrochemical methods*, Wiley, New York, (1980).
17. H. Obata, C. van den Berg, *Anal. Chem.*, 73 (2001) 2522-2528.
18. S. Çakır, E. Biçer, M. Odabaşoğlu, Ç. Albayrak, *J. Braz. Chem. Soc.*, 16 (4) (2005) 711-717.
19. B. Bonanni, D. Alliata, A. Bizzarri, S. Cannistraro, *CHEMPHYSCHEM*, 4 (2003) 1183- 1188.
20. J. Okada, J. Inukai, K. Itaya, *Phys. Chem. Chem. Phys.*, 3 (2001) 3297-3302.
21. H. Yao, N. Li, Y. Wei, J. Zhu, *Sensors*, 5 (2005) 277-283.
22. G. Zaitseva, Y. Gushikem, E. Ribeiro, S. Rosatto, *Electrochimica Acta*, 47 (2002) 1469-1474.
23. M.L. Perry, J. Newman and E.J. Cairns, *J. Electrochem. Soc.* 145, 5 (1998).
24. J. O'M. Bockris and S.U. M. Khan, *Surface electrochemistry: A molecular level approach*, Plenum Press, New York (1993), 280-283, 621.
25. E. Gileadi, *Electrode Kinetics*, VCH, NY (1993) 403-454.
26. S. H. Jordanov, P. Paunovic. O. Popovski, A. Dimitrov, D. Slavkov, *Bull. Chem. Tech. of Macedonia*, 23 (2) (2004) 101-112.
27. M.V. Mirkin, H. Yang and A.J. Bard, *J. Electrochem. Soc.* 139 (1992) 2212.
28. J. S. Newman, W. Tiedmann, *AIChE*, 21 (1) (1975) 25-41.
29. J.A. Drake, C. J. Radke, J. S. Newman, *J. Electrochem. Soc.* 145 (5) (1992) 1578-1585
30. J. S. Newman, *Electrochemical Systems*, Prentice Hall, NJ (1991) 454-495.
31. D. Bruggeman, *Ann. Physik.*, 24 (1935) 636.

32. R. Schofield, C. Dakshinamurti, *Discuss. Faraday Soc.*, 56 (3) (1948).
33. J. R. Selman, *AIChE*, 77 (204) (1981) 88-102.
34. M. V. Mirkin, A. J. Bard, *Anal. Chem.* 63 (1991) 532-533.
35. G. Denuault, M. V. Mirkin, A.J. Bard, *J. Electroanal. Chem.*, 308 (1991) 27-38.
36. R. Greef, P. Peat, L. Peter, D. Pletcher, J. Robinson, *Instrumental Methods in Electrochemistry*, JW, NY (1985) 229-250.
37. A. Wiekowski, E. Savinova, C. Vayenas, *Catalysis and Electrocatalysis at Nanoparticle Surfaces*, Marcel Dekkers Inc., NY (2003) 827-845.
38. G. C. Bond. *Catalysis by Metals*, Academic Press, NY (1962) 407-435.
39. A. Furstner, *Active Metals*, VCH, Germany (1996) 427-446.
40. Y. Iwasawa, *Tailored Metal Catalysis*, D. Reidel Publishing Company (1989) 87-269.
41. C. N. Rao, J. Gopolakrishnan, *New Directions in Solid State Chemistry*, Cambridge University Press (1997) 517-534.
42. V. Ponec, G. C. Bond, *Catalysis by Metals and Alloys*, Elsevier, Amsterdam (1995).
43. S.C. Amendola, P. Onnerud, M.T. Kelly, P.J. Petillo, S.L. Sharp-Goldman and M. Binder, *J. Power Sources* 84 (1999) 130.
44. A. Kinjo, *Diss. Abstr. B*, 29 (1969) 3235, and *Chem. Abstr.* 71 (1969) 18189.
45. R. Woods, "Chemisorption at Electrodes", *Electroanalytical Chemistry: A Series of Advances*, Edited by A. J. Bard, 9 (1976) 1-162.
46. L. K-Minsker, I. Yuranow, E. Slavinskaia, V. Zaikovskii, A. Renker, *Catalysis Today*, 59 (2000) 61-68.
47. K. Eguchi, H. Arai, *Applied Catalysis A: General*, 222 (2001) 359-367.
48. H. Widijaja, K. Sekizawa, K. Eguchi, H. Arai, *Catalysis Today*, 35 (1997) 197-202.
49. K. Sekizawa, H. Widjaja, S. Maeda, Y. Ozawa, K. Eguchi, *Catalysis Today*, 59 (2000) 69-74.

## CHAPTER 5

### CONCLUSIONS

Colloidal (1:1 atomic ratio) Os and Os-alloys, Pt and Pt-alloys, Au and Au-alloys, Ir and Ir-alloys, and Pd and Pd-alloys, supported on Vulcan XC-72 and prepared using a modified Bönnehan method, were investigated as anode electrocatalysts for direct borohydride fuel cells. They were all tested for  $BH_4^-$  oxidation, and in the case of the colloidal Os and Os-alloy catalysts for methanol oxidation. Cyclic voltammetry on static and rotating disk electrodes, chronopotentiometry, chronoamperometry and chronocoulometry techniques were used to evaluate their catalytic activity towards  $BH_4^-$  oxidation. Single fuel cell performance tests, using the most active catalysts as anode electrocatalysts, were also carried out.

The main conclusions to come from this study were as follows:

1. Os-based materials were catalytically inactive with respect to methanol oxidation in acid media. However, in case of borohydride, oxidation peaks were obtained at positive potentials. Thus, the fuel cell tests were not performed.
2. Colloidal Pt-Ni and Pt-Ir were the most active catalysts among the Pt-group. Pt-Ni showed the lowest Tafel slope,  $b_a$ , while Pt-Ir showed the highest exchange current density,  $i_o$ . The heterogeneous rate constant,  $k_h$ , was highest for Pt-Ir ( $28.7 \times 10^{-6} \text{ cm s}^{-1}$ ). The fuel cell performance of these catalysts at 298 K were about 1.8 times higher than that for pure Pt and 2.25 times higher than that for Pt-Ru the most popular commercial catalyst.
3. Amongst the Au-group, colloidal Au-Pt was the most active electrocatalyst. It showed the lowest  $b_a$  (0.662 V), and the highest  $i_o$  ( $1.180 \times 10^{-3} \text{ mA cm}^{-2}$ ) which are characteristics of a good electrocatalyst. The heterogeneous rate constant,  $k_h$ , was the highest for Au-Pt ( $6.26 \times 10^{-6} \text{ cm s}^{-1}$ ). These fundamental studies have been supported by the fuel cell tests where Au-Pt showed superior performance compared to the Au and Au-Pd catalysts.
4. Colloidal Ir-Ni showed the highest activity among the Ir-group, with a relatively low  $b_a$  (0.607 V) and a second highest  $i_o$  ( $7.906 \times 10^{-3} \text{ mA cm}^{-2}$ ). The heterogeneous rate

constant,  $k_h$ , for Ir-Ni was found to be three times lower than that of pure Ir. Fuel cell tests at 298 K, showed that Ir-Ni has the highest performance compared to the other group members.

5. Amongst the Pd-group, Pd-Ir was the most active, with the lowest  $b_a$  (0.757 V) and the highest  $i_o$  ( $13.06 \times 10^{-3} \text{ mA cm}^{-2}$ ). Pd-Ir also exhibited the highest heterogeneous rate constant,  $k_h$ , ( $25 \times 10^{-6} \text{ cm s}^{-1}$ ). The fuel cell tests showed that the performance of Pd-Ir was 165% better than pure Pd and 320% better than Pd-Au.

6. In general, the colloidal Ir-Ni, Pd-Ir, Pt-Ir and Pt-Ni catalysts were found to be the most electroactive. Their good fuel cell performance confirmed the basic electrochemical studies that were done on these electrocatalysts.

7. Although the oxidation of  $BH_4^-$  was incomplete on these catalysts (i.e.,  $n < 8$ ), they showed a relatively low Tafel slope and high exchange currents densities in the cases of Ir-Ni and Pd-Ir, which is indicative of a high electroactivity. The optimum Tafel slope ranking for the best four catalysts was Ir-Ni < Pt-Ni < Ir-Pd < Pt-Ir, while the exchange current densities ranking was Pd-Ir > Ir-Ni > Pt-Ir > Pt-Ni. This supports the idea that a lower Tafel slope and a higher exchange current density are required for an electrocatalyst to show a good activity for a specific reaction.

8. The heterogeneous rate constants were found to be the highest for Pt-Ir and Ir-Pd followed by Pt-Ni and Ir-Ni. The difference in their rate constants, (assuming almost constant particle size), is due the interactions between both the supported alloying elements themselves and with the conductive support. These interactions can lead to changes in the metal-metal distance (i.e, decreasing the distance enhances the close proximity catalyst action), changes in the surface structure, and changes in the surface electronic structure (i.e., an increase in metal(s) d-electron vacancies is favorable for adsorption controlled processes).

9. Fuel cell tests showed that had almost comparable performance characteristics. For Ir-Ni, Pd-Ir, Pt-Ir, and Pt-Ni as the anode catalysts, a cell operating at a voltage of 0.5 V can give a current density of about 51.28, 48.84, 46.39, and 44  $\text{mA cm}^{-2}$ , respectively at 298 K. At 333 K, the same catalysts can give a current density of about 83, 95, 105, and 105  $\text{mA cm}^{-2}$ , respectively at the same 0.5 V cell voltage. These anode electrocatalysts



showed superior performance compared to the commercial Pt-Ru catalyst. They were more active (higher performance) and more cost-effective.

10. A  $TiO_2$  addition to the support (the Vulcan XC-72 C-Black), was also investigated for the colloidal Pt, Pd and Ir catalysts. It was found that such an addition has a slightly positive impact on the activities of Pt and Pd, while it has a significant negative impact on the activity of Ir. CV studies showed an enhancement in the peak current of about 1.2 and 1.5 times in case of Pt and Pd respectively, while a decrease of about 3.2 times was found in the case of Ir. This behaviour has been supported by calculations of the heterogeneous rate constant,  $k_h$ , where  $k_h$  was enhanced 1.52 and 1.44 times for Pt and Pd, respectively, but was decreased by a factor of 1.7 for Ir.

The main contribution of this study is that for the first time a number of supported mono- and bi-metallic nanoparticle electrocatalysts were synthesized and investigated using fundamental electrochemical techniques and fuel cell station tests for anode electrocatalysts for direct borohydride fuel cells. The main findings are that the fuel cell test station experiments demonstrated the superior performance of the Ir-Ni, Pd-Ir, Pt-Ni, and Pt-Ir catalysts compared to both Pt and commercial Pt-Ru catalysts.

## CHAPTER 6

### RECOMENDATIONS FOR FUTURE WORK

This study has illuminated several areas that warrant further, more detailed study. These areas include, but are not limited, to the following list.

1. Would help to explain the differences in  $BH_4^-$  oxidation on the different surfaces, plus help in choosing the right add atom(s) to enhance the catalyst's activity, study the borohydride oxidation mechanisms. Knowing how  $BH_4^-$  and  $OH$  are adsorbed onto the different surfaces, whether by molecular or dissociative adsorption and the type of oxidation mechanism. X-ray Photoelectron Spectroscopy (XPS), Auger Electron Spectroscopy (AES), Infrared Spectroscopy (IR), and Secondary-Ion Mass Spectroscopy (SIMS) are the most popular techniques used to determine the chemisorbed species and the coverage rates. Investigation of the reaction mechanisms requires the determination of the overall reaction, the rate determining step, and the intermediate step(s). Electroanalysis, chromatography, and the tracer technique are useful tools for determining the overall reaction. For the stable electroadsorption species detection, in addition to the above mentioned non-electrochemical techniques, the chronoamperometric, chronopotentiometric, and potentiodynamic (cyclic voltammetry) are the most useful electrochemical methods. For the detection and identification of intermediates, in addition to the above mentioned non-electrochemical techniques, the transient, adsorption pseudocapacitance, and rotating disk with ring electrode methods are potentially the most useful methods.
2. Supporting the transition metals on a conductive surface and/or alloying with other elements can lead to a changes in the bulk surface electronic structures. Therefore, for better catalyst design, it is important to study the relationship between the catalyst activity and the bulk surface electronic structure. X-ray diffraction is the initial technique both to identify the crystalline phases inside the catalyst by means of lattice structural parameters, and to obtain an indication of particle size. X-ray Photoelectron Spectroscopy (XPS) is a useful tool in finding the elemental composition, the oxidation state of the elements, and the dispersion of one phase over another.

Extended X-ray Absorption Fine Structure (EXAFS) is another useful tool which can yield detailed structure information on the distance, number, and type of absorbing atoms, on the nanometer scale. Transmission Electron Microscopy (TEM) is a useful technique to determine the shape and size of the particles, which has an impact on the surface electronic structure. Mossbauer Spectroscopy is a special tool designed to be used in catalysis, which can yield important information on the oxidation state, the internal magnetic field, and the lattice symmetry of a limited number of elements. Finally, for the catalyst surface studies, Scanning Tunneling Microscopy (STM) and Atomic Force Microscopy (AFM) are potentially valuable techniques.

3. Adding  $TiO_2$  to the support has a positive impact on the activity of some of the electrocatalysts, and a negative impact on others. Providing that the borohydride oxidation mechanism is known, a study of the addition of different metal oxides to the support is of interest in order to help find an oxide that can significantly enhance the electrocatalyst activity by modifying the surface electronic structure. The chosen metal oxides should have a good chemical resistance in highly alkaline concentration solutions.
4. For a better evaluation of the supported catalysts, it is important to find the electrochemical surface area, which is limited to the metallic surfaces. The electrochemical surface area is a crucial parameter in determining the turnover frequency  $\{TOF = (\text{number of molecules of a given product})/(\text{number of active sites})(\text{time})\}$ , which yields information about the use of each catalyst site per second. The well established methods are the hydrogen desorption and CO adsorption methods. Electrochemical and surface techniques are being widely used for this purpose: examples include hydrogen desorption and CO stripping by combined cyclic voltammetry, IR and STM in order to identify the adsorbent bond and the layer on the metallic surface.
5. Investigation of different atomic ratios rather than 1:1, in order to optimize the alloy(s) composition.
6. Test Ni-Zr/(C-Black+ $TiO_2$ ), Ag-Ir, Ag-Pt, Pt/(C-Black+ $TiO_2$ ), and Os in the fuel cell.

## VITA AUCTORIS

**NAME:** Mohammed Hassan Atwan

**PLACE OF BIRTH** Iraq

**YEAR OF BIRTH** 1956

**EDUCATION** University of Baghdad, Baghdad, Iraq  
1975-1979 B.Sc.  
University of Baghdad, Baghdad, Iraq  
1983-1985 M.Sc.

**AFFILIATIONS** American Institute of Chemical Engineers (AIChE),  
National Association of Corrosion Engineers (NACE),  
The International Precious Metals Institute (IPMI).

## PUBLICATIONS AND PRESENTATIONS

### PRESENTATIONS

1. Mohammed H. Atwan, Derek O. Northwood, Elod L. Gyenge, Evaluation of Colloidal Os and Os-Alloys (Os–Sn, Os–Mo and Os–V) for electrocatalysis of methanol and borohydride oxidation, 16<sup>th</sup> Canadian Materials Science Conference, 5-8 Jun., 2004, Carleton University, Ottawa, Canada. Abstract only.
2. Mohammed H. Atwan, Derek O. Northwood, Elod L. Gyenge, Evaluation of Colloidal Ag and Ag-alloys as Anode Electrocatalysts for Direct Borohydride Fuel Cells, Invited paper presented at *INTERNATIONAL SYMPOSIUM ON SOLAR- HYDROGEN- FUEL CELLS -9* (INTERNATIONAL MATERIALS RESEARCH CONGRESS 2005), CANCUN, MEXICO, Aug. 21 – 25, 2005. Full paper submitted for publication in *Int. J. Hydrogen Energy*.

### PUBLICATIONS

1. Mohammed H. Atwan, Derek O. Northwood, Elod L. Gyenge, Evaluation of colloidal Os and Os-Alloys (Os–Sn, Os–Mo and Os–V) for electrocatalysis of methanol and borohydride oxidation, *Int. J. Hydrogen Energy*, 30 (2005) 1323-1331.
2. Elod L. Gyenge, Mohammed Atwan, Derek O. Northwood, Colloidal Pt and Pt-alloy catalysts for direct borohydride fuel cells: electrocatalysis and fuel cell performance, *J. Electrochem. Soc.*, 153 (1) (2006) (Accepted for publication, Oct. 11, 2005).
3. Mohammed H. Atwan, C. Macdonald, Derek O. Northwood, Elod L. Gyenge, Colloidal Au and Au-alloy catalysts for direct borohydride fuel cells: electrocatalysis and fuel cell performance, *J. Power Sources* (Accepted for publication, Oct. 7, 2005).
4. Mohammed H. Atwan, Derek O. Northwood, Elod L. Gyenge, Electro-oxidation of borohydride on colloidal Os and Os-alloys (Os–Sn, Os–Mo and Os–V), *J. of New Materials for Electrochemical Systems* (Accepted for publication, Oct. 19, 2005).
5. Mohammed H. Atwan, Derek O. Northwood, Elod L. Gyenge, Evaluation of Colloidal Ag and Ag-alloys as Anode Electrocatalysts for Direct Borohydride Fuel Cells (Submitted for publication in *Int. J. Hydrogen Energy*, Aug., 25, 2005).